An Optical Telemetry System For Wireless Transmission Of Biomedical Signals Across The Skin

by

Bruce C. Larson

B.S., Electrical Engineering
University of Houston, 1992

S.M., Electrical Engineering
Massachusetts Institute of Technology, 1996

SUBMITTED TO THE DEPARTMENT OF ELECTRICAL ENGINEERING
AND COMPUTER SCIENCE IN PARTIAL FULFILLMENT OF THE
REQUIREMENTS FOR THE DEGREE OF

DOCTOR OF PHILOSOPHY

AT THE

MASSACHUSETTS INSTITUTE OF TECHNOLOGY

FEBRUARY 1999

Signature of Author _____
Department of Electrical Engineering and Computer Science
January 29, 1999

Certified by _____
David J. Edell
Principle Research Scientist, Harvard-MIT Division of Health Sciences and Technology
Thesis Supervisor

Accepted by _____
Arthur C. Smith
Chairman, Department Committee on Graduate Students

An Optical Telemetry System For Wireless Transmission Of Biomedical Signals Across The Skin

by

Bruce C. Larson

Submitted to the Department Of Electrical Engineering and Computer Science
on January 29, 1999 in Partial Fulfillment of the Requirements for the Degree of
Doctor of Philosophy

ABSTRACT

A technology base for optically-coupled systems was developed that permits in-vivo transmission of biomedical signals across the skin. By complete implantation of sensors and instrumentation electronics, problems with percutaneous connectors were eliminated. Optical power and signal transmission was accomplished with smaller and lighter implant structures than previously achieved with radio frequency (RF) coupling techniques. This is particularly valuable in the field of neuroprosthetics, because it may be possible to implant an optical telemeter directly on the surface of the brain to make mechanically stable connections to microelectrode arrays for neuroelectric recordings.

Miniature optical power panels (2.5 mm x 2.5 mm) were developed from arrays of photodiodes. Infrared light of 880 nm wavelength was effective for delivering power across the skin. Panels composed of silicon photodiodes were 14% efficient at converting this light to electrical power, and GaAlAs panels were 41% efficient. Tissue heating experiments demonstrated the safety of optical power transmission. An LED was identified that was both electrically efficient (16%) and of appropriate wavelength (660 nm) for transmitting optical signals from the implant. Pulse period encoding was used for transmission of signals because it was robust and required less power than schemes with higher LED duty cycles. Specialized photodetector circuits were developed to receive pulse encoded data, and decoder circuits were built to reconstruct the transmitted signals.

Two prototype single-channel neural waveform telemeters (approx. 10 Hz to 7 kHz bandwidth) were constructed and implanted in the visual cortex of rabbits. Both implants successfully transmitted neuroelectric signals. The first implant survived for four weeks before failing due to a flaw in the encapsulation, and the improved second prototype continues to function properly 28 months after implantation.

Integrated circuits (ICs) were designed to record and transmit eight channels of neural waveforms. The first IC telemeter functioned properly, although the sensitivity was not as great as needed for the recording of neural waveforms. It required less than 50 μW of electrical power to operate. Efforts to improve this design introduced flaws in the next set of IC designs, so these problems were addressed, and a final set of designs was submitted for fabrication at the conclusion of this research project.

Thesis Supervisor: David J. Edell
Title: Principle Research Scientist
Harvard-MIT Division of Health Sciences and Technology

Summary

Biological information that cannot be acquired non-invasively has in the past typically necessitated the use of catheters or percutaneous connectors to cross the skin barrier. However, these catheters and percutaneous connectors are problematic. They introduce a considerable risk of infection, and are subject to marsupialization by epithelial downgrowth [1-8]. In addition, they are readily susceptible to damage and mechanical failure. Complete implantation of sensors and instrumentation electronics can eliminate the percutaneous devices and their inherent difficulties.

While radio frequency (RF) methods have been investigated to provide power and signal communication for implanted sensor systems, certain applications would benefit from a smaller and lighter implant than can be readily constructed for RF telemetry. In particular, the field of neuroprosthetics could benefit from an implantable telemeter that is small and light enough to be implanted on the surface of the brain and remain physically stable. This would enable long-term measurement of neuroelectric signals for basic neurophysiology research, and could possibly enhance the rehabilitation of spinal cord injury by providing a better source of control information for prosthetic and assistive devices. Light was investigated in this research as an alternative means of providing power to an implanted sensor system and for communicating information from the sensor to the external environment.

The primary objective of this research was the development of a technology base for optically-coupled systems that would permit in-vivo transmission of biomedical signals across the skin. It was also desired that the system be small and lightweight so that it could potentially be implanted on the surface of the brain to allow mechanically stable connections to microelectrode arrays.

The two most important goals for the design of the optical telemetry system were that it operate on the minimum amount of optical power, and that it be capable of transmitting information at the highest possible rate. These factors go together in the sense that decreasing the power needed by the implant electronics would allow more information to be acquired, encoded, and transmitted. The less power required by the implant for a given number of channels and bandwidth, the easier it is to provide the power optically. If a smaller optical power supply can be used, a smaller and lighter implant will result.

Thus these two considerations are foremost in the design of maximally useful telemeters.

Careful design of the complete system was necessary to accomplish these goals. The specific tasks involved in the system design were:

- Selection of an encoding scheme for efficient optical transmission of signals.
- Design of ultra low power implant electronics to acquire and encode desired biomedical signals.
- Identification of light wavelengths and sources for efficient transmission of power and signals across the skin.
- Specialized design of a photodetector system to receive the transmitted signals with the highest sensitivity, so that less power is required for signal telemetry by the implant.
- Development of optical power supplies optimized to provide the voltage and current requirements of the implant with as little incident light as possible for a given size.

These tasks were completed successfully. A pulse-period encoding technique was developed for the optical transmission of signals. This technique gave robust signal transmission with minimal power because the signal is encoded entirely in the timing between intense but brief pulses of light. Multiple channels of information were encoded in this technique by multiplexing the pulse periods, and by using a marker period that was different from the others to synchronize the receiver so that the transmitted signals could be decoded. This encoding was accomplished with less complicated and lower power electronics than necessary for traditional analog-to-digital conversion. Using a low power design methodology developed in prior work [90], integrated circuit input amplifiers were designed to measure biomedical signals with only as much power as necessary to achieve sufficiently low noise. An amplifier suitable for recording small neuroelectric potentials was developed that had less than 10 μV_{RMS} input-referred noise over a 10 kHz bandwidth while consuming only 625 nA.

A literature review and experiments with cadaver skin and in-vivo experiments led to the selection of LEDs with optimal performance for transmitting data and power. Skin was found to transmit light best at longer wavelengths and in the near infrared. An LED suitable for the telemeter output device was found that generates 660 nm red light with high efficiency. A mounting technique was developed for this chip LED that incorporates a reflector to increase light transmission across the skin. It provided up to 104% improvement over flat mounts. Power was transmitted at 880nm because it was less

absorbed than 660nm light, thereby minimizing tissue heating effects. The safety of optical power transmission at 880nm was demonstrated in an experiment that measured tissue heating when the power illumination was applied.

A design methodology for optimizing detection of the timing of light pulses from low amplitude sources was developed and applied to the problem of detection of pulses from an implanted multichannel neural signal telemeter. A transimpedance amplifier photodetector circuit was optimized for sensitive detection of pulse period encoded signals. Optical filters were found that reduced most background and powering illumination by a factor of more than 10,000 compared to the signal transmission wavelength. These improved photodetector performance by minimizing the interference and noise associated with the unwanted light.

Maximally efficient optical power supplies were designed similar to solar panels. The optimal number of photodiodes to connect in series was determined, and panels smaller than 2.5 mm x 2.5 mm were fabricated. A six-diode silicon panel provided 2.5 V and 75 μA when illuminated by 880 nm infrared light at 50 mW/cm^2 (half of overhead sunlight intensity). Its power conversion efficiency was up to 13.6%. GaAlAs panels were up to 41.3% efficient. A four-diode GaAlAs panel fitting in the same area would produce 3 V and 280 μA under the same illumination. Panel layouts that reduce the effects of non-uniform illumination were developed along with fabrication techniques.

The accomplishment of these individual, but interrelated, goals enabled the primary research objectives to be achieved. A technology base was developed enabling optical transmission of data from, and power to, implanted electronics for readout of biological information. As a demonstration, a prototype telemeter that recorded one channel of high-frequency extracellular neuroelectric signals was constructed and implanted in a rabbit. It was still functional at the time of this writing, more than 28 months after implantation. This telemeter was bulky and thus was subcutaneously placed because the integrated circuits developed in this research were not available when it was built. However, it incorporated many of the same low power signal detection, signal encoding, data transmission, and power transmission concepts.

Integrated circuits were fabricated using the developed technology concepts that can encode eight channels of biomedical information. These designs are expandable to an arbitrary number of channels, limited only by available power and signal bandwidth. The initial 8-channel design had approximately 10 mV_{p-p} input-referred noise when operated

at 15 kHz/channel sample rate. It consumed only 12.5 μA current from a 2.5 V supply for signal amplification, encoding, and multiplexing, and used another 7 μA for the optical output. Improved circuit designs were then developed and are now being fabricated which should permit much smaller signals to be encoded (limited by the noise level specified in the input amplifier design) with less power. Most subsystems of the improved designs were fabricated and verified in the laboratory indicating that the complete system for a free floating, multi-channel neural telemeter will likely be functional when the next set of fabricated devices is available. The technology base developed in this thesis work can now be exploited for many challenging applications. This optical telemetry technology will be especially useful whenever biological data must be acquired from small implanted sensors for long periods of time.

Contents

List of Figures

Chapter 1: Introduction

1.1 The Biomedical Information Optical Telemeter:

A biomedical information optical telemeter is a device which may be implanted in the body to monitor physiological variables and communicate this information across the skin, using light to provide wireless power and signal transmission. Examples of physiological variables that may be monitored are bioelectrical signals such as the neuroelectric potentials or *neural waveforms* that result from the "firing" or depolarizing of individual neurons, ElectroEncephaloGram (EEG) signals that arise from the spatial summation of neural signals, ElectroMyoGram (EMG) signals from the activation of muscle tissue, and ElectroCardioGram (ECG, or EKG) signals from the contractions of the heart. Other physiological variables which may be monitored, given a suitable implantable sensor, are temperature, pressure, glucose, pH, CO_2, PO_2, perfusion, etc.

1.2 Background and motivation

Monitoring of physiological variables for medicine and research has always presented unique problems, not the least of which involve the acquisition of this information inside the body and its transmission to the outside world where it may be utilized. Biological information that cannot be acquired non-invasively has typically necessitated the use of catheters or percutaneous connectors to cross the skin barrier. These allow direct access to the internal environment of the body, or carry wires that relay power and/or information to indwelling sensors. While this is a passable solution for some short-term applications, these catheters and percutaneous connectors must be assiduously maintained, as they create a significant potential for infection. Percutaneous connectors are in general not well tolerated by the body for extended periods of time, and may be subject to marsupialization by epithelial downgrowth [1-8]. In addition, percutaneous connectors with large numbers of electrical contacts tend to be fragile and difficult to work with. With only external instrumentation, this can limit the number of channels of sensor information that can be accessed. Implanting the instrumentation electronics along with the sensors may alleviate this problem by allowing data to be multiplexed and sent through fewer wires, but it does not eliminate the other difficulties associated with percutaneous connectors. Telemetry of power and data can be used to eliminate the percutaneous connector altogether. Batteries can be used to provide power without wires, and have been used with considerable success in implantable cardiac

pacemakers and defibrillators, but their useful lifetimes are limited without any means of recharging. Also, the size and mass of batteries would preclude their use in many potential applications.

Radio Frequency (RF) telemetry has been used to transmit power and/or information for a number of long-term biomedical applications [9-17]. Notable examples include cochlear prosthetics and Functional Neural Stimulation (FNS) muscle stimulators [18, 19]. Up to 22 channels of low frequency electrical stimulus information have been transmitted across the skin for cochlear implants [20]. Single channel muscle stimulators that are powered and controlled by an RF source have been developed that may be injected into muscle through a syringe [21]. However, for some applications, RF telemetry units may be too physically large or heavy. Additionally, RF telemetry devices are inherently sensitive to RF interference from the telecommunications industry, computers, microwave ovens, etc.

Research in the field of neuroprosthetics has long been hampered by the need for wires to access bioelectric signals from the nervous system, and percutaneous connectors to bring these signals out of the body. This application also places unique constraints on a telemetry system that make RF methods less than ideal. The signals that are typically of interest in neuroprosthetics are the small extracellular potentials that result from the minute currents that flow in the vicinity of a neuron when an action potential occurs. These signals are acquired with small electrodes implanted in the neural tissues of the central or peripheral nervous system, and have a bandwidth of approximately 100Hz to 7kHz. When using electrodes small enough to detect the activity of individual neurons, peak signal amplitudes are usually less than 250μV, and may extend down to the background neural noise floor of about 25μV [22-31].

When implanting electrodes in the brain, tethering of the electrodes to the skull by even the finest lead wires may result in damage to neurons as the normal movement of the brain in the skull places forces upon the electrodes. Destruction of nearby neurons will result in loss of information and signal strength, and the possible long-term drift of the electrodes will result in lack of stability and difficult interpretation of the received signals. It may be possible to make the electrodes mechanically stable in the brain by using telemetry to eliminate the wires, and by making the implant small and of the same density as the surrounding neural tissue. Then, acceleration of the head and motion of the brain relative to the skull should place minimal forces on the implant and its

electrodes. This requires that the implant incorporate amplifiers capable of detecting the small neural signals, circuitry for encoding them, a wireless means to transmit them, and a wireless power source that can continuously supply these electronics.

The size and mass limitations of this proposed free-floating brain implant make the use of RF power and signal transmission difficult. Allotting a few millimeter square area for the implant's electronics does not provide much room for RF coils. An example of an RF power source of this scale reported by Selvidge et al [32] generated 200μW in an integrated chip with a close coupled integrated RF coil using a 3 Watt RF source, under optimal conditions. Using this as a reference point, optical power sources can be evaluated as an alternative. Also, an LED may provide a smaller and more efficient output transmitter than an RF antenna. While light has occasionally been used as a means to communicate signals transcutaneously [33-35], or from an externally situated biological monitor [36-43], it does not appear to have been used for both power and signal transmission across the skin.

1.3 Goals of thesis

The primary objective of this research was the general development of an optically-coupled system, suitable for implantation, that would permit in-vivo transmission of biological signals across the skin without the use of wires or other percutaneous connectors. It was also desired that the system be small and lightweight so that it could potentially be implanted on the surface of the brain and be more physically/mechanically stable than a similar system tethered to the skull by power and communication wires. Optical telemetry of power and signals was investigated as an alternative to Radio-Frequency (RF) transmission, which has been studied elsewhere [44-54].

The issues that were addressed to develop the biomedical information optical telemeter are as follows. Sensors to acquire a biomedical signal for this prototype development research were selected, and circuits to amplify and condition these signals were designed. For telemeters that were to transmit more than one channel of signal information, a multiplexer circuit was devised to combine the signals for a single optical data output. A robust encoding scheme appropriate for optical transmission was found, and electronics to perform this encoding were designed. A light source that was small, efficient, and that was of an appropriate wavelength to transmit adequately across the skin was identified for use as the telemeter signal output device. Optical power supplies

that could sustain the operation of the amplifiers, multiplexer, encoder, and signal output device of a telemeter were developed. Externally, to complement the telemeter, a detector was designed to detect the optical transmission. A system was built to decode and demultiplex this transmission to reconstruct the original biomedical signal information. Also, a light source that could efficiently deliver power across the skin to the implant was found.

1.4 Layout of thesis

The numerous topics that were investigated in the creation of the biomedical information optical telemeter may be grouped into several main categories. Transmission of light through skin was studied to determine the feasibility of using this means of power and signal transmission for an implanted device. Experiments were conducted to empirically quantify light transmission through skin in the configuration proposed for the telemeter. This is the topic of Chapter 2, which also reviews the relevant literature regarding the absorption and scattering of light in skin and other tissues.

A suitable optical power supply had to be developed, and this is covered in Chapter 3. Available photodiodes that could be used to create a miniature power panel similar to a traditional silicon solar panel were investigated. The optimal number of photodiodes connected in series to achieve desired current and voltage characteristics was determined, and the physical layout of these diodes in the panel was considered in terms of the effects of non-uniform illumination. Based on the photodiode characteristics and the results from Chapter 2, the wavelength of light to use for power transmission was selected. Experiments to determine the fundamental limits of power transmission were conducted, and are described in this chapter as well.

Chapter 4 deals with the encoding of signals for optical transmission. Various encoding techniques were evaluated to find methods that were efficient in terms of circuit design (integrated circuit chip area and power consumption) and the output power required for signal transmission. Noise immunity during signal transmission and robustness of signal reception were considered in this evaluation of encoding methods, and led to the use of *pulse-period modulation*, a variant of pulse position modulation. The encoding and decoding of single and multiple channels of various physiological signals using this technique are discussed.

Transmission and reception of optical signals from the telemeter is discussed in Chapter 5. The wavelength of light for signal transmission was chosen based upon skin transmission properties and measurements of the efficiency of available LEDs. Photodetector devices were evaluated and an analysis of amplifier circuits was undertaken in order to develop receivers for the pulse-encoded signals. The trade-off between area of the photodetector and speed of the detector circuit is discussed for various applications, and lenses were considered as a possible means to increase sensitivity without sacrificing speed. Optical filters were tested in an effort to reduce the pickup of unwanted background light and the noise associated with it.

Two prototype neural signal optical telemeters were assembled from commercially available components to test the concepts developed in Chapters 2 through 5 *in vivo*, and are described in Chapter 6. Decoding circuits based on analog and digital techniques were built for these devices, and were interfaced to a computer for experimentation and data recording. The prototypes were implanted in the visual cortex of rabbits and tested by recording neuroelectric signals and *visual evoked potentials*, the disturbance in the normal neuroelectric activity that results from a flash of light in the eye contralateral to the implant site. The implant procedure and sample recordings are also presented.

Integrated circuits (ICs) to amplify and encode one or more channels of bioelectric signals were developed to operate on a minimum of electrical power. The designs detailed in Chapter 7 were optimized for the transduction of neural waveforms, since these signals generally required the greatest sensitivity and bandwidth. The results of a prior study of noise and power consumption in CMOS analog circuits were applied to design an optimized input amplifier for the neural waveform transmitter. Test results for the fabricated circuits are given along with a discussion of discrepancies from the computer simulations. Final IC designs that incorporate changes to address the flaws in the previous designs are presented. Decoder circuits built to work with the encoder chips are also described.

Chapter 2: Light transmission through skin

Relevant literature regarding the optical properties of skin and other tissues were reviewed [55-71], and light transmission tests of specific wavelengths of interest (i.e. from available LEDs) were conducted through skin samples of an animal model, in-vitro and in-vivo.

2.1 Absorption, scattering, and reflection

Literature on the subject of light absorption by tissue [55, 57, 63-66, 72-76] was useful in learning generally what to expect - that light is heavily scattered by tissue but not strongly absorbed in the visible and near infrared (IR) range, and that ultraviolet (UV) damage is limited to wavelengths below 400 nm or so.

Skin color and vascular perfusion were also obvious variables to consider. Fortunately, by choosing longer wavelengths for transmission of data and power, the effects of pigmentation and absorption by hemoglobin are minimized. In a comparison of transmission of light through dark black skin and white Caucasian skin, Wan et al [76] reported that at 660 nm dark black skin attenuated light by 60% more than Caucasian skin. At 800 nm, dark black skin attenuated light by 30% more than Caucasian skin. Reflection is also an important variable of skin color for the transmission of power [57]. Again, these losses are minimized by using longer wavelengths.

Because of the complexity of light absorption and scattering through the multilayered structure of the skin, and the relatively complex geometries involved, it was not easy to model the system mathematically. So in addition to the valuable information gathered from the literature, experiments were conducted with available LEDs and photodetectors to explore the specific issues of this application.

2.2 Tests of specific wavelengths

Figure 2.1 is a summary of initial experiments to test the feasibility of transcutaneous signal transmission by light, and to determine which diode is most power and skin transmission efficient.

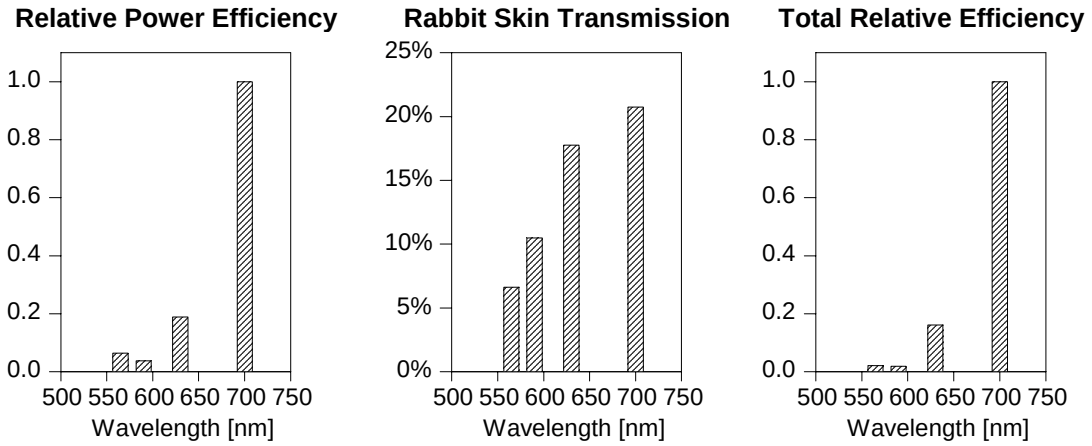

Figure 2.1: **Relative power efficiency (light output/current input normalized to highest), transmission through rabbit skin, and the total relative efficiency (relative power efficiency times transmission normalized to highest).**

Since Light Emitting Diodes (LEDs) were the most convenient, power efficient, and readily available devices for generating light for this application, many manufacturers were approached to find the most efficient sources. Diode selection was based on the total relative efficiency, which takes into account both the power efficiency of the LED and the transmission efficiency through the skin. Note that these measurements include the effects of reflection, absorption, and scattering. Relative power efficiency was computed by measuring the light output and dividing by the power input, and then normalizing to the highest measurement. Transmission through rabbit skin was determined using a broadband, large detector. The total relative efficiency was then computed by multiplying the relative power efficiency times transmission and normalizing to the highest. From this experiment it was possible to determine that longer wavelengths in this range transmit better (as the literature suggested), and power efficiencies for diodes varied greatly. Subsequent to these experiments, we became aware of a 660 nm photodiode that was nearly 10 times more power efficient than the 700 nm diode used in these experiments. Since the skin transmission is about the same as a 700 nm diode, the 660 nm LED was chosen for further evaluation *in-vivo.* Whether or not an LED would be adequate for transmitting data out depends also on the sensitivity of the photodetector used to receive the signal. Figure 2.2 is a copy of a graph from EG&G showing the sensitivity of a typical silicon PIN photodiode as a function of light wavelength. At 660 nm, this photodetector has about 75% quantum

efficiency (of carrier generation by incident photons), or radiant sensitivity of about 0.4 Amperes per Watt.

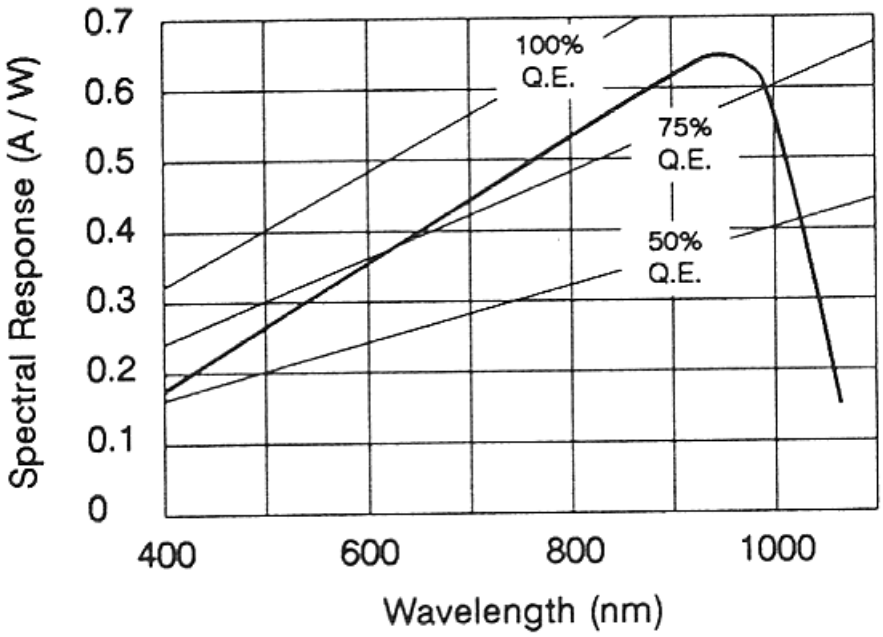

Figure 2.2: Radiant sensitivity of EG&G Vactec VTH2090 silicon PIN photodiode, in Amps per Watt. Includes quantum efficiency (Q.E.) reference lines.

Which wavelength of light would be most efficient for transmission of power was also investigated. Here the primary concern was tissue absorption and photo-electric efficiency. Power efficiency of the power LED was of secondary importance since the power on the outside is not as severely limited as the power on the inside. Because longer wavelengths are transmitted better than shorter wavelengths in the visible and near IR, IR diodes were of interest. Also, radiant sensitivity increases in proportion to wavelength until the photons do not have enough energy to reliably generate electron-hole pairs (above about 870 nm for this photodiode). Electron-hole pairs are generated when the absorbed photons have energy greater than the semiconductor bandgap. Because photon energy in excess of the bandgap energy is lost as heat, the longer wavelengths are more efficiently converted. However, beyond a certain wavelength, silicon photodiodes are inefficient because of the bandgap limitation, as can be seen in Figure 2.2. While this photodiode is optimized for light detection rather than power generation, it demonstrates the general spectral response characteristics of silicon diodes. The quantum efficiency of carrier generation is shown in Figure 2.2 by the

reference lines labeled “Q.E.”. The quantum efficiency drops to 50% at about 1200 nm for this photodiode, corresponding to photon energy of 1.034 eV.

Fortunately, high power IR light sources consisting of arrays of 880 nm LEDs are readily available from Opto-Diode, Inc. which are well suited to powering a subcutaneous silicon photodiode array power panel. This may be the optimal solution, because this wavelength is near the peak quantum efficiency for silicon photodiodes, and biological material becomes more highly absorptive at wavelengths longer than 1μm.

Figure 2.3 is a summary of *in-vitro* and *in-vivo* experiments to further develop our understanding of the use of LEDs to transmit power and data across skin.

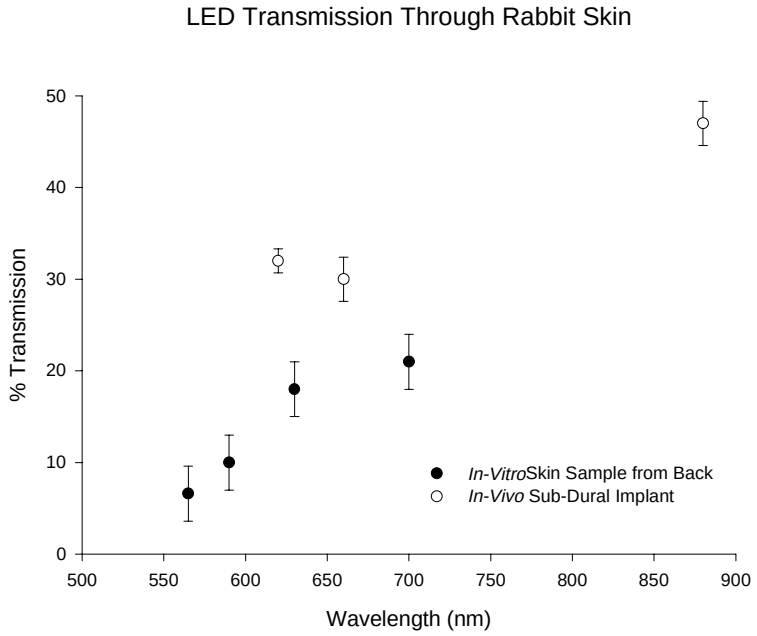

Figure 2.3: **Light transmission through New Zealand White rabbit skin, *in-vitro* and *in-vivo*.**

The *in-vitro* data was taken on skin samples from rabbit. The *in-vivo* data was taken during the thermal effects experiments outlined in the next chapter. A photodiode was implanted on the surface of the brain under the dura mater. A quartz window was placed in the skull over the photodiode, and the skin flap was closed with forceps. The 660 nm and 880 nm LEDs chosen for the first telemeter implementation were then used to illuminate the photodiode, both with and without the skin flap in place. Since this was

living, perfused skin, it is probably the most accurate assessment we have regarding the transmission of light through skin. As shown in Figure 2.3, the 660 nm light from the data transmission LED is attenuated to 30% of the original intensity by the presence of the skin. More importantly, the 880 nm light from the power transmission LED is only attenuated to about 45%.

Another part of the system being developed that was important to consider during the selection of LEDs was the encapsulation needed to protect the implanted devices from the body. From related work on insulating biomaterials for NIH [77], we only know of two materials that have a chance of protecting implanted micro-structures for long times: silicones and fluoropolymers. Silicones are the current choice because they are readily available and some have been approved for long term implantation. Teflon, while an excellent material for this application, cannot be used for medical implants because of legal restrictions by its manufacturer. Figure 2.4 shows the transmission spectrum of one of the silicones that has been tested extensively. Transmission losses (primarily absorption and reflection) in the region of interest between 600 nm and 900 nm are less than 10% for the 1mm thick section, which is negligible.

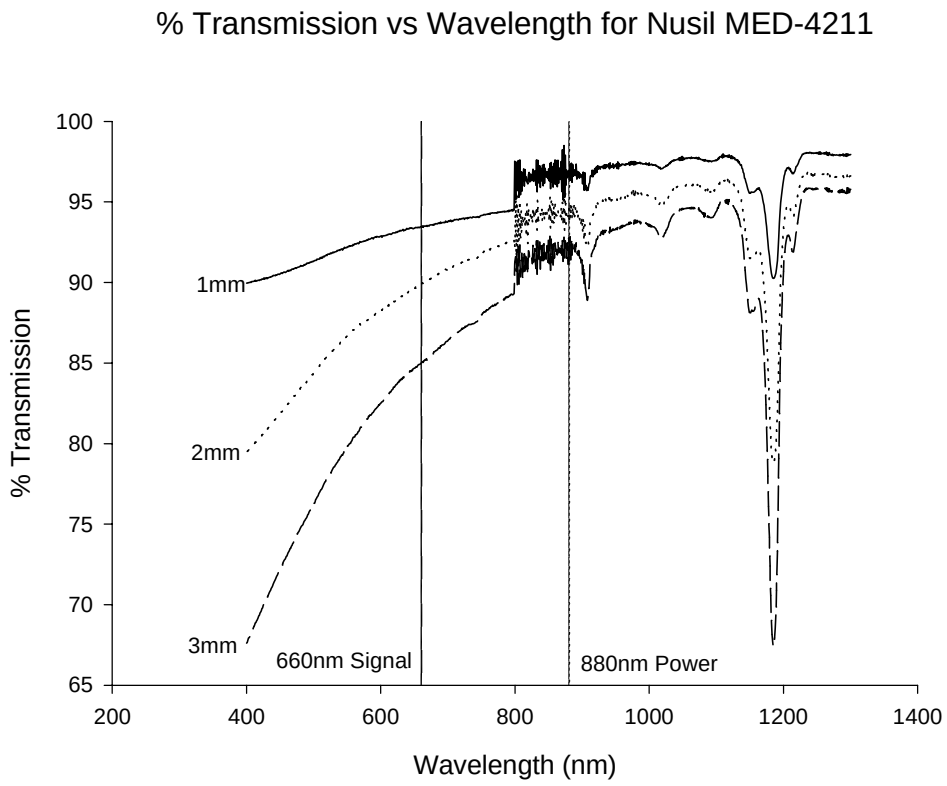

Figure 2.4: Percent transmission of light between 400 nm and 1400 nm through three depths of silicone encapsulant MED-4211 from Nusil. Note the high transmission for 1-3mm thick material above 600 nm. Noisy part of curve is detector artifact.

2.3 Human skin transmission measurements

Data from preliminary experiments to verify optical transmission through various colors of skin is presented in Figure 2.5.

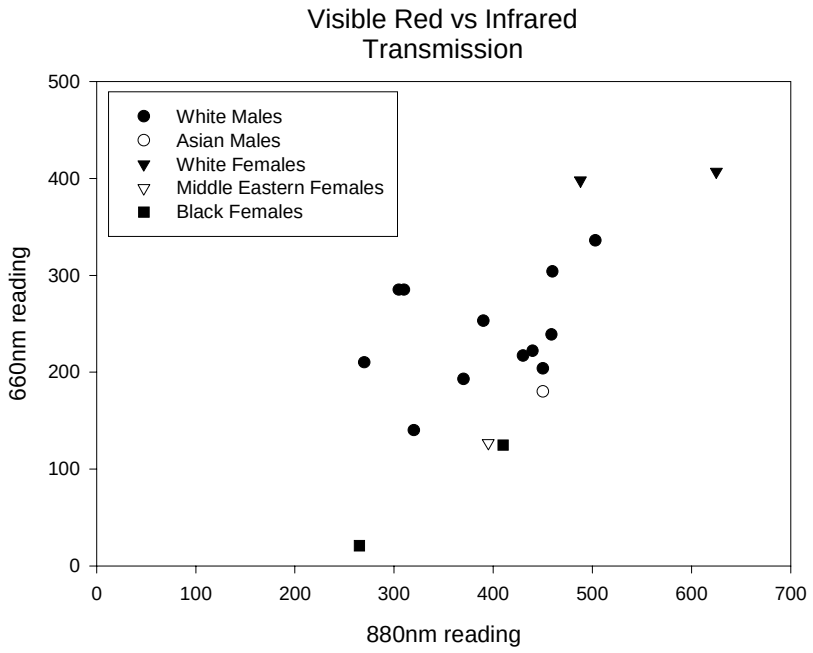

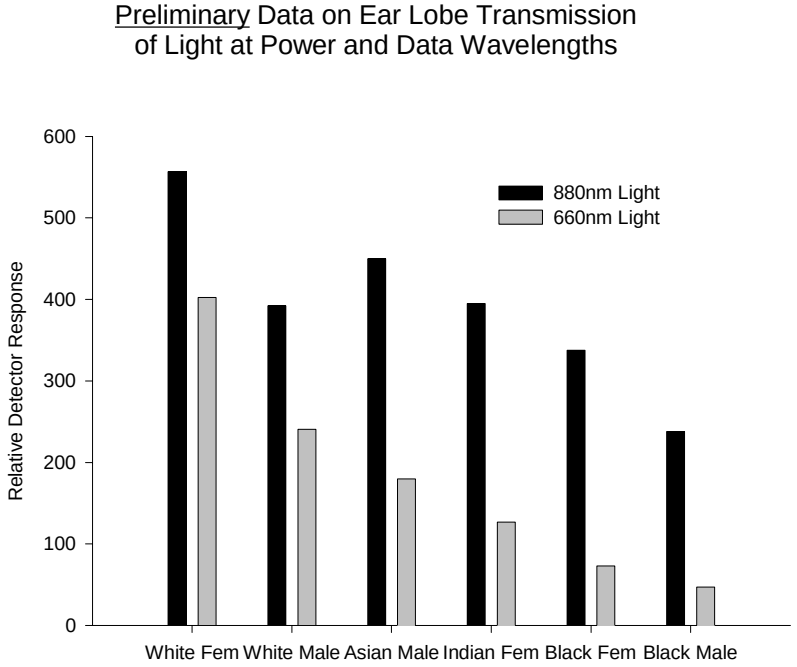

Figure 2.5: *Preliminary* data on human ear lobe transmission of light at two wavelengths. TOP: Scatter plot. BOTTOM: Bar graph.

This data was collected by placing optical emitters and detectors across the earlobes of individuals from different ethnic backgrounds. This data indicates that infrared transmission is relatively independent of skin color but the 660 nm red light is more strongly blocked by dark skin than white skin. Also, it confirms that the 880 nm light has higher transmission through skin than 660 nm in general, making it an appropriate choice for delivery of power to the telemeter. This is consistent with the literature [76]. The striking difference between males and females may be due to differences in the thickness of ear lobes between males and females, which may or may not be representative of other skin thickness.

Chapter 3: Optical power supplies

The basic principles behind traditional solar panels were adapted to create miniature optical power supplies. Since the performance of the micro-power panel constrains the design of the implanted telemeter system by determining the power available for the circuit, this was a critical aspect of the system design.

Micro-power panels can be designed as miniature versions of silicon solar panels. Basically, these are photodiodes connected in series to provide sufficient power for the application. By varying the type and doping levels of the photodiodes, more or less voltage or quantum efficiency can be obtained. For any given fabrication process, the number of diodes connected in series to make up the optical power panel is the most critical design parameter. Providing an excess number of diodes in series will ensure adequate voltage is available, but more light power will have to be provided to generate the required current for the circuit. If there are too few diodes in series, the current constraint could be more easily met, but more light power will have to be provided to generate the required voltage (if it can be generated at all). Because of the possibility of excessive tissue heating, we could not simply increase the illumination intensity to compensate for a poor design. Also, in order to maintain minimal size, the area of the panels could not be arbitrarily increased either. Thus, a design methodology was developed to allow optimization of the micro-power panels to operate the implanted circuits with minimal illumination.

3.1 Photodiodes

Photodiodes, such as regular silicon PN junction diodes and Gallium Arsenide (GaAs) diodes, develop a forward bias when illuminated by light of appropriate wavelengths. Electron-hole pairs are generated in the semiconductor by absorbed photons. When these carriers are formed within or near enough to diffuse to the depletion region of the junction, they are swept through it by the built-in potential gradient, producing a photo-induced current. The intensity of light incident on the diode and its active area determine the total amount of photocurrent generated. The photocurrent is a reverse current through the diode, flowing positive (according to the standard convention) from the cathode to the anode. In the open-circuit condition, this current is forced to flow back through the diode (from the anode to the cathode), forward biasing it. The open circuit voltage on the diode will be determined by the diode's forward current-voltage characteristic at the level of the photocurrent. If the diode is short-circuited, all of the

photocurrent flows (positive) out of the anode. When the diode has a load attached, the photocurrent will be divided into a current that flows internal to the diode and an external current that flows through the load. The balance between these currents is set by the current-voltage relationships of the load and the diode. A circuit model of the illuminated photodiode is given in Figure 3.1.

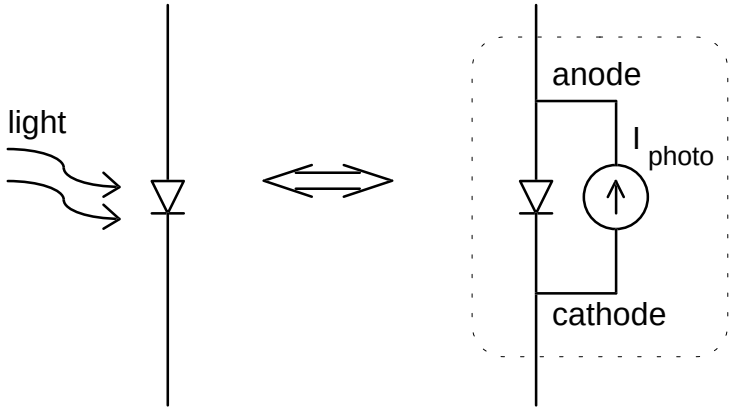

Figure 3.1: Circuit equivalent of illuminated photodiode.

The net current-voltage (I-V) characteristic of the illuminated photodiode is simply the I-V curve of the dark diode shifted along the current axis, as suggested by the circuit of Figure 3.1.

3.1.1 Silicon

Current-voltage curves representative of a silicon diode produced in a 2 μm CMOS process (specifically, the MOSIS 2 μm Orbit N-well CMOS offering) are plotted in Figure 3.2 for various levels of 880 nm infrared illumination. Note how the curves are shifted down the current axis by the photoinduced current. Slight differences in the shape of the curves are due to temperature changes during the course of the measurement, particularly as the photodiode was heated by the higher levels of illumination. Silicon diodes have a typical temperature coefficient of –2 mV/°C for their forward voltage.

The active area of this diode was 0.5 mm^2. Using a light meter as a reference, the radiant sensitivity of this diode at 880 nm was determined to be about 0.326 A/W.

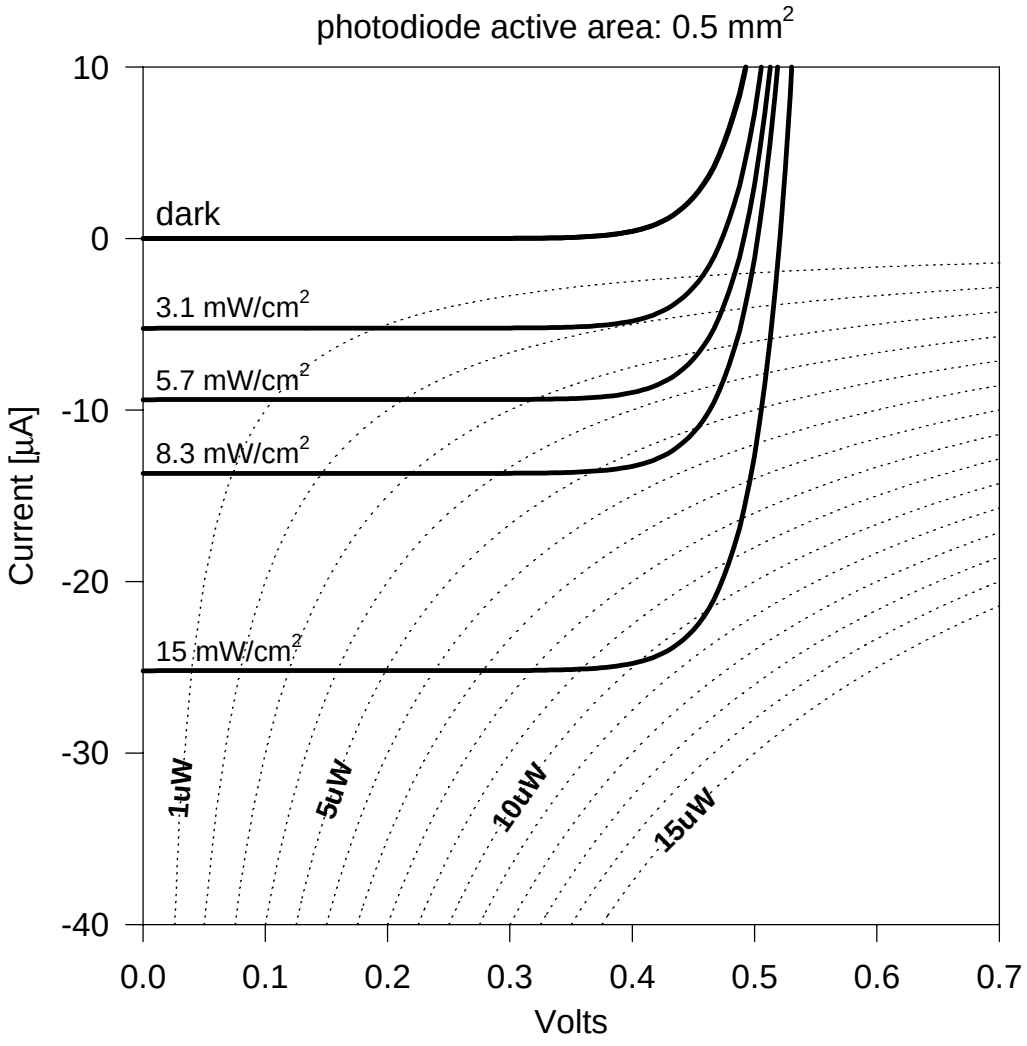

Figure 3.2: MOSIS diode I-V curves for various illumination levels, with isopower curves.

In this graph, and others of this type, the convention is positive *forward* current through the diode (anode to cathode). Thus the useful *output current* of the illuminated diode is negative in these plots. Curves of constant output power (output current times voltage), the "isopower lines", are also shown in Figure 3.2 and similar plots that follow.

Other silicon diodes designed specifically for photodetection were tested. The doping levels, junction depths, and depletion region thickness of these diodes were optimized for quantum efficiency and/or low capacitance, but the trade-off seemed to be lower voltage for a given forward current. Also, these diodes were available only in certain sizes, whereas diodes produced in the standard CMOS process could be fabricated in any desired geometry. One such photodetector diode, the EG&G VTS2086, was used in

some applications of this research. Figure 3.3 is a graph of the IV characteristic of this photodiode under dark and illuminated conditions.

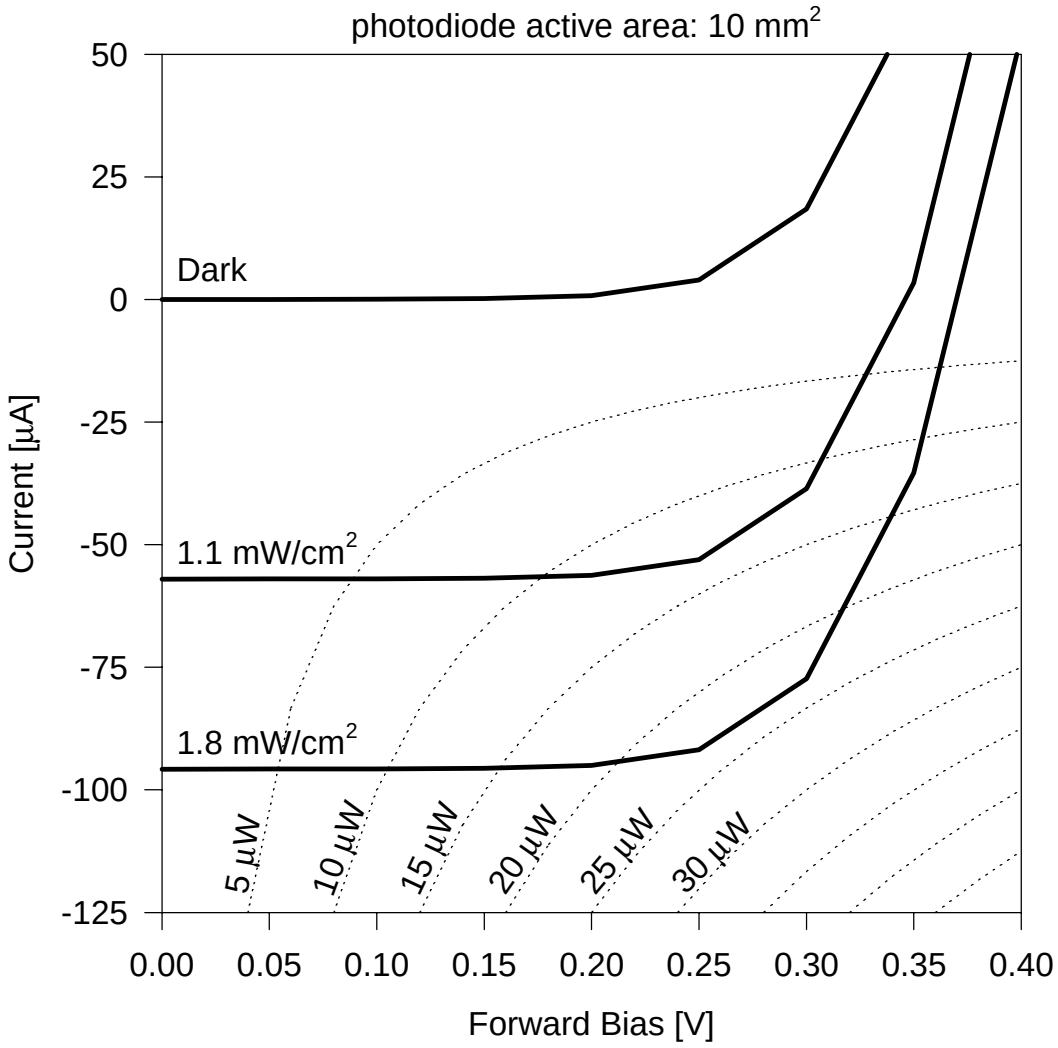

Figure 3.3: EG&G VTH2086 silicon photodiode I-V curves for various illumination levels.

Note the lower open circuit voltage than the MOSIS fabricated diode, for comparable illumination (corresponding to comparable current density through the area of the diode). However, the radiant sensitivity of this photodiode is considerably greater, about 0.525 A/W at 880 nm. Its active area is 10 mm^2 in a total area of 2.5 mm x 5 mm.

3.1.2 Gallium (Aluminum) Arsenide

A GaAlAs photodiode with response tuned to 880 nm light, the Opto Diode Corp. ODD-45W, was also investigated as a possible power panel component. Figure 3.4 is a plot

from the manufacturer's specification sheet showing its spectral response (radiant sensitivity) compared to typical silicon photodiodes, and Figure 3.5 shows how its response matches their high-power infrared emitters.

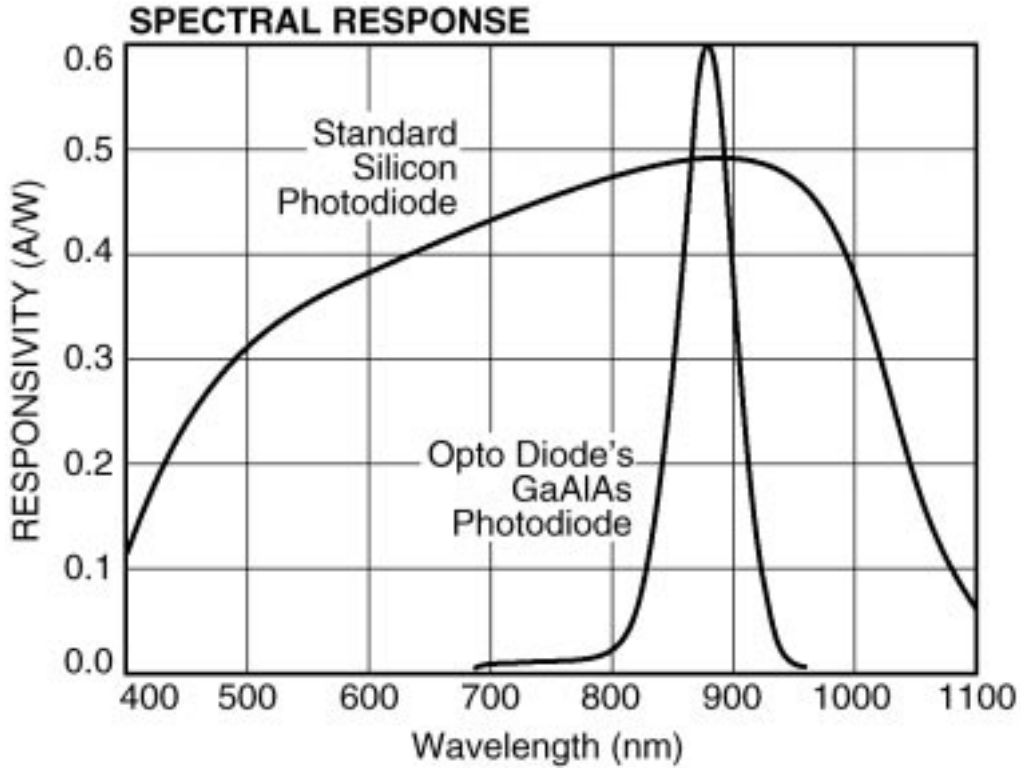

Figure 3.4: Radiant sensitivity of Opto Diode Corp. ODD-45W GaAlAs photodiode.

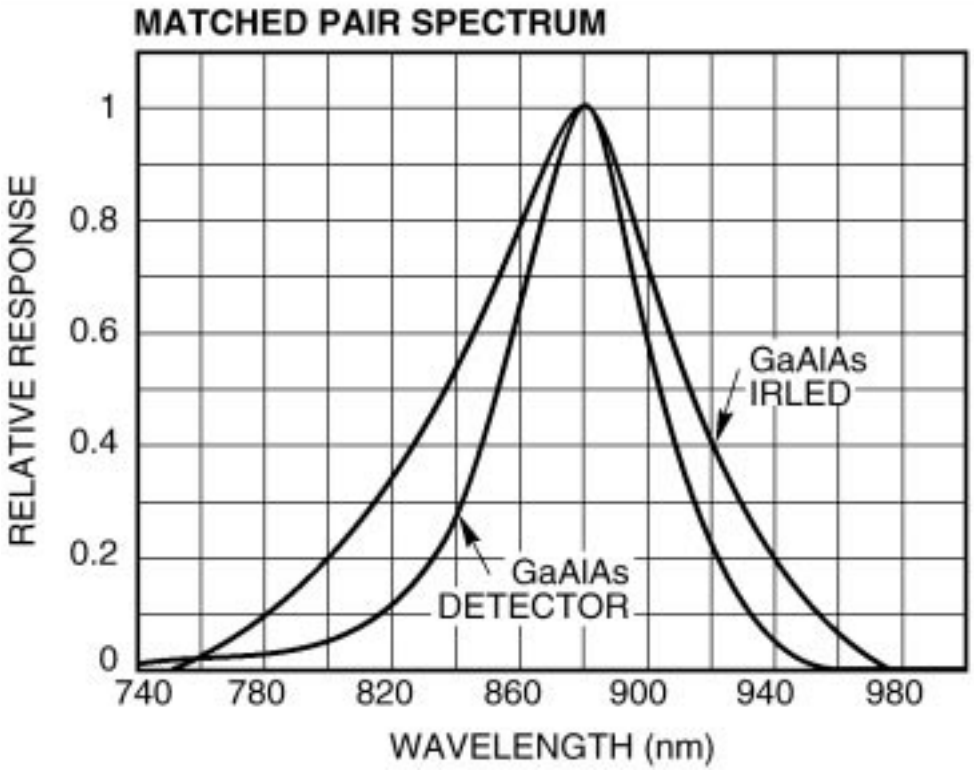

Figure 3.5: Matching of ODD-45W radiant sensitivity to GaAlAs 880 nm IR LEDs.

The current-voltage characteristic for this photodiode is plotted in Figure 3.6 for various levels of 880 nm illumination. The radiant sensitivity of this diode is typically 0.6 A/W at 880 nm. The area of this diode is 1 mm x 1 mm. Recently, a larger version of this photodiode has become available, the ODD-95W, which measures 5 mm x 5 mm.

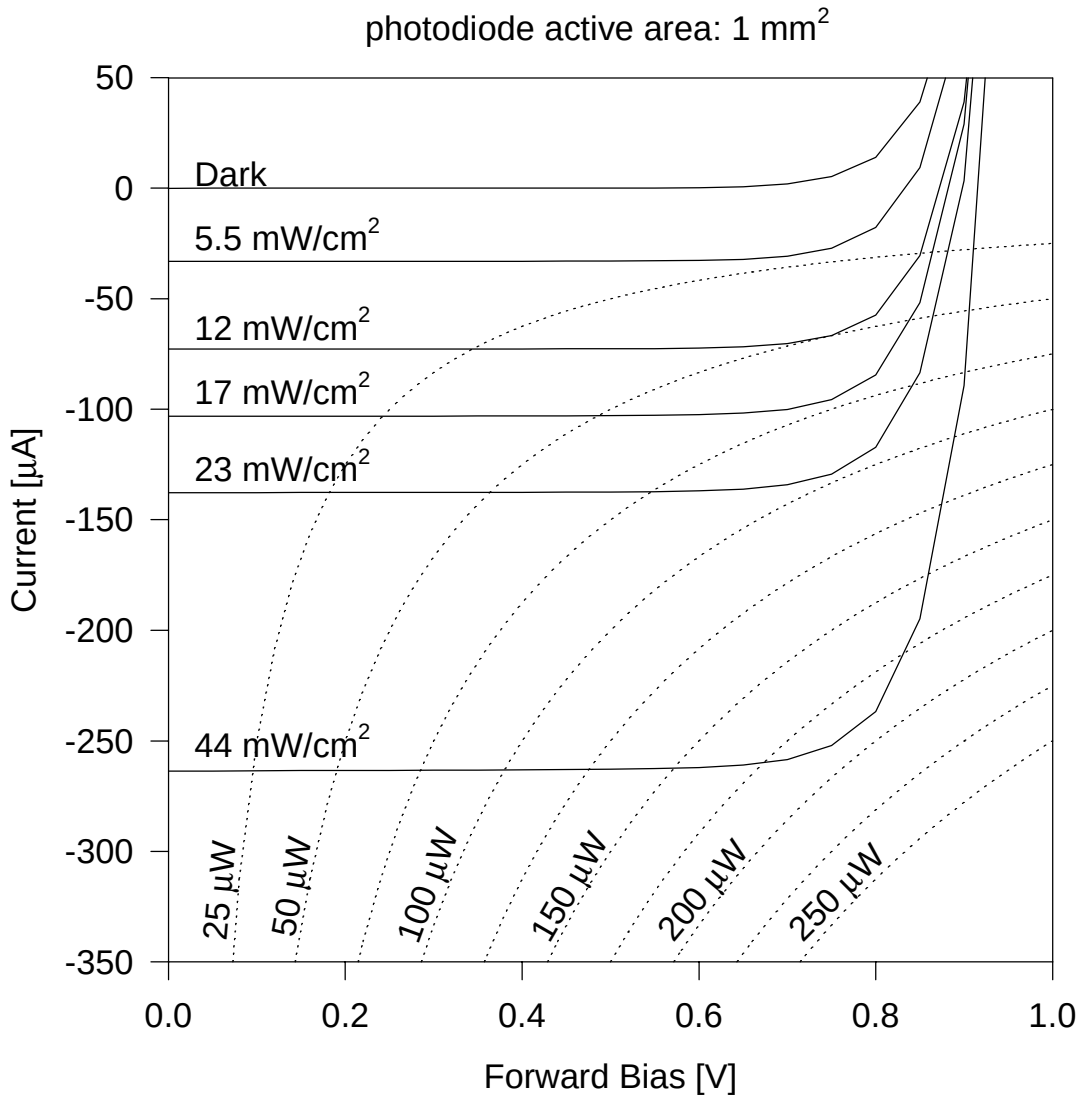

Figure 3.6: ODD-45W GaAlAs photodiode I-V curves for various illumination levels, with isopower curves.

Clearly, the GaAlAs photodiode would be a more efficient element to use for the power panels, because of its greater open circuit voltage and radiant sensitivity than silicon diodes. Figure 3.7 gives a direct efficiency comparison between the three diodes whose characteristics have been plotted. This table shows the open circuit voltage, short-circuit current per unit area, maximum power output per unit area, voltage at the maximum power point, and current per unit area at the maximum power point of each diode assuming 880 nm illumination at 10 mW/cm^2 intensity.

	V_{oc} [V]	$I_{sc/a}$ [$\mu A/mm^2$]	V_{mp} [V]	$I_{mp/a}$ [$\mu A/mm^2$]	$P_{max/a}$ [$\mu W/mm^2$]	%Eff [%]
CMOS	0.528	32.6	0.446	30.5	13.6	13.6
VTH2086	0.344	52.5	0.262	46.4	12.1	12.1
ODD-45W	0.871	60.0	0.734	56.3	41.3	41.3

Figure 3.7: Comparison of three photodiode types when illuminated by 880 nm light at 10 mW/cm^2 (= 100 μW/mm^2) intensity. Open circuit voltage (V_{oc}), short-circuit current per unit area ($I_{sc/a}$), current per unit area at the maximum power point ($I_{mp/a}$), voltage at the maximum power point (V_{mp}), maximum power output per unit area ($P_{max/a}$), and peak optical power conversion efficiency (%Eff) are listed.

A downside to using GaAlAs is the relatively lack of fabrication flexibility. While silicon diodes can be readily obtained from many sources in arbitrary sizes and shapes, the GaAlAs diodes are currently limited to a few options provided by a small number of manufacturers. Perhaps more significantly is the concern about implanting arsenic compounds in the body. While it is probably unavoidable to implant a small GaAs output LED, the use of much larger GaAlAs power panel diodes may present an unnecessary risk.

3.2 Wavelength of light for power transmission

As discussed in Chapter 2, near-infrared light is transmitted through all colors of skin better than visible wavelengths. It is also converted efficiently to electrical power by silicon and GaAlAs photodiodes. Since 880 nm illumination is appropriate for both semiconductors tested in this research, and high-power LEDs are available at this wavelength, it was used for this work. The Opto Diode Corp. OD-100 LEDs provide up to 100 mW continuous 880 nm light output at 12% electrical-to-light power conversion efficiency. The OD-663, OD-666, and OD-669 emitters provide 3, 6, and 9 diodes in a single package, respectively, for up to 500 mW light output capability. Using an LED rather than an incandescent light source minimizes heat transfer to the area of the telemeter implant, and the narrow range of wavelengths emitted is easier to block from the signal light receiver. Another possibility for powering the telemeters that merits future investigation is a fluorescent light source with phosphors tailored to produce near IR light.

3.3 Photodiode array power panel

In order to generate sufficient voltage with an optical power supply, it is likely that an array of photodiodes will have to be connected in series. The voltage available is determined primarily by the number of photodiodes in series and the illumination

intensity. The current available is determined by the area of the individual photodiodes and the illumination intensity.

3.3.1 Optimal number of diodes for power supply

For any given fabrication process, the number of diodes wired in series to make up the optical power panel is the most critical factor in its design. To know how many diodes are needed, one must first specify the voltage requirement of the circuit to be powered. Since the forward bias voltage on a diode determines how much of the photocurrent will flow through the external circuit and how much will flow internally to the diode, the maximum power will be delivered to an attached load when the operating voltage is set such that the product of the diode's output current and this voltage is maximum. If the minimum current and voltage required to operate a particular circuit is known, the dark I-V curve of a single diode may be shifted down the current axis to the necessary current level. It is important that the I-V curve of the diode is correct for the temperature that the power panel will be operated at, since the diode's negative temperature coefficient can lead to significant decrease in panel voltage when several diodes are placed in series. Isopower curves are then added to the I-V plot of the "illuminated" diode. The maximum power point can then be found at the intersection of the I-V curve with the maximum isopower line. If the output current of the diode at this point is less than desired, the I-V curve of the diode can be shifted down until the current output is sufficient at the (new) maximum power point. Now, the voltage required by the circuit is divided by the voltage of the single diode at this maximum power point, and the result is rounded up to determine the optimum number of diodes that will be connected in series to form the power panel. This panel will power the connected circuit with the minimum amount of illumination.

Because the current generated within the power panel is determined by the total number of photons incident on the solar panel (and the quantum efficiency of the diodes), the area of the panel is not a primary design consideration in terms of efficiency. The available space and acceptable power dissipation per unit area are factors that determine the size of the power panel, since the light beam can usually be focused onto the area of the panel.

3.3.1.1 2.5 V, 25 μA integrated silicon power panel

Most of the telemeter circuits were designed to operate from a 2.5 V power supply with less than 25 μA current. To design a power panel for these applications in a commercially available fabrication process, the MOSIS service 2 μm Orbit N-well CMOS process, the I-V curves of Figure 3.2 were consulted, since these measurements were taken from a diode produced in this process. As seen in this plot, for 25 μA output, the maximum power point (about 10.3 μW) occurs at about 0.44 V forward bias on the diode. So at this current level, six diodes in series would provide just over 2.5 V with the maximum efficiency.

A six diode power panel was fabricated[1] in this technology on the "Tinychip" die, which measures less than 2.5 mm x 2.5 mm (usable area 2.2 mm x 2.2 mm). Each diode had an active area of 0.5 mm^2. The I-V characteristics of this power panel are plotted in Figure 3.8 for several illumination levels.

[1]Fabricated by The MOSIS Service, Information Sciences Institute, University of Southern California

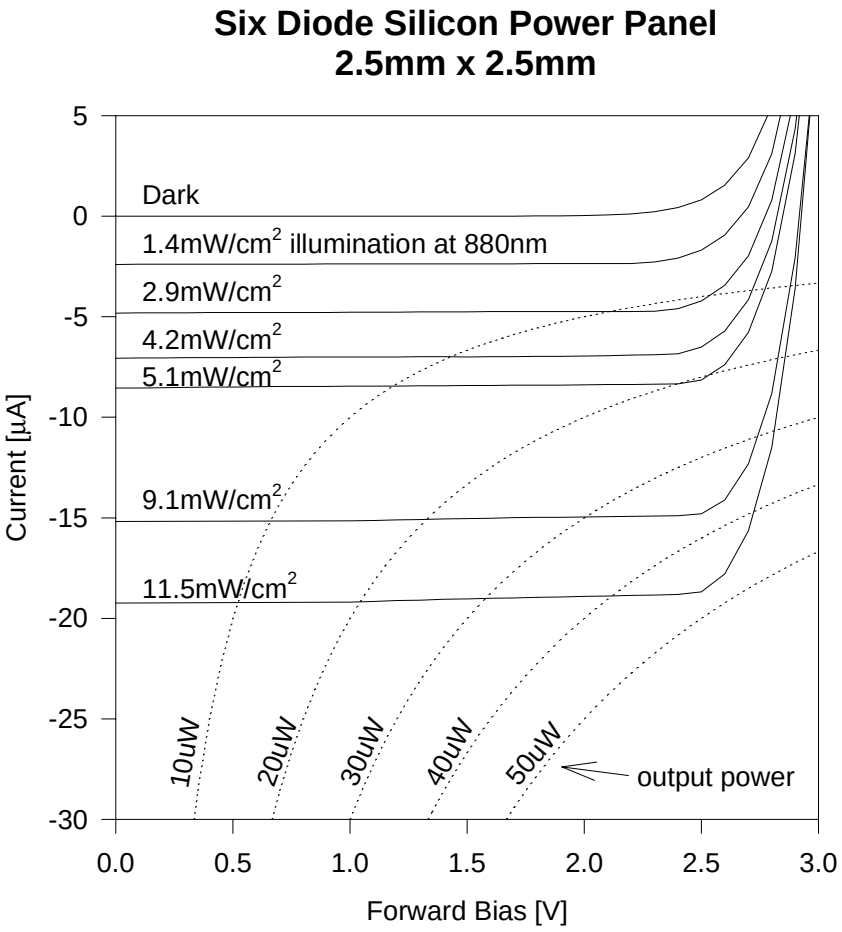

Figure 3.8: Six diode, 2.5 V integrated silicon power panel I-V curves

3.3.1.2 5 V, 25 µA integrated silicon power panel

A silicon power panel to provide 5 V output at 25 µA was also designed for the MOSIS service 2 µm Orbit N-well CMOS process. Since the single diode in this process was found in the preceding section to be maximally efficient operating at 0.44 V for 25 µA output current, 12 diodes were necessary for a 5 V power panel. To fit this design on the Tinychip die, the individual diodes had active areas of 0.65 mm x 0.45 mm. Figure 3.9 is a plot of this panel's I-V characteristics for several levels of illumination. While these curves should be identical in shape, some variability can be seen. Some of the curves have a sharper "knee" than others, such as the curve at 14.4 mW/cm^2 compared to the dark curve. This change is attributable to non-uniformity of the illumination, which

is discussed later in this chapter in the context of measurements from a 10-diode GaAlAs panel where the effect was much more pronounced. Some of this effect can also be seen in Figure 3.8, but it is more subtle. The illumination level labels in these figures give the *minimum* intensity on the panel, so the measured voltage and power output may be slightly higher than expected.

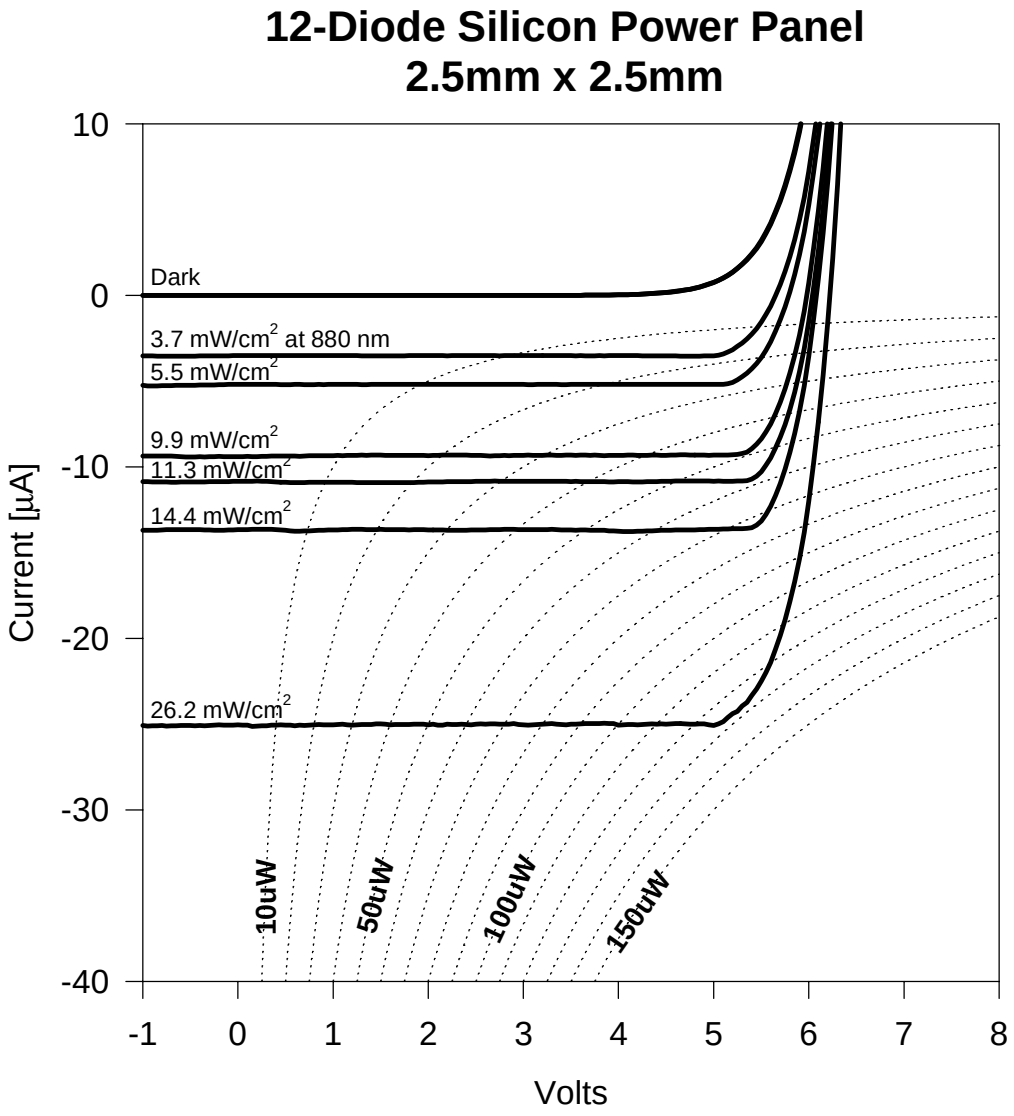

Figure 3.9: Twelve diode, 5 V integrated silicon power panel I-V curves.

3.3.1.3 2 V, 75 µA discrete silicon power panel

A large area power panel was assembled from EG&G VTS2086 photodiodes for the prototype single channel neural waveform telemeter, before the power panel design

methodology was developed. The desired output was 75 μA at 2.5 V. The design of this panel was based on the manufacturer's open circuit voltage specification of 0.33 V (which was at an illumination level that produced 85 μA short-circuit current). This crude approach indicated that eight diodes in series would therefore yield slightly more than 2.5 V. However, when the power panel design method described in this chapter is applied, it is evident from Figure 3.3 that these photodiodes are maximally efficient at 0.26 V when generating 75 μA output photocurrent. Thus the eight diode panel would be better suited as a 2 V, 75 μA power supply.

The I-V characteristics of this panel are plotted in Figure 3.10, which also shows the effect of heating on the illuminated power panel. The I-V curves of the panel measured in the dark and under 1.6 mW/cm^2 880 nm illumination are plotted along with the theoretical illuminated curve, which is simply the dark I-V curve shifted down the current axis by 85 μA. The measured illuminated I-V curve is shifted approximately 250 mV to the left of the theoretical curve. This can be explained by the fact that the temperature of the panel was not controlled, so it was inadvertently heated by the illumination. Dividing the 250 mV total shift by 8 gives the change in voltage of each diode, -31 mV. Since the temperature coefficient of this diode is –2 mV/°C, a rise in panel temperature of 15.6 °C (28 °F) would account for the shift in the I-V curve. If the panel was at 68 °F room temperature for the dark measurement, it is quite possible that it rose to 96 °F when illuminated. This example demonstrates the importance of taking temperature into account when designing a power panel.

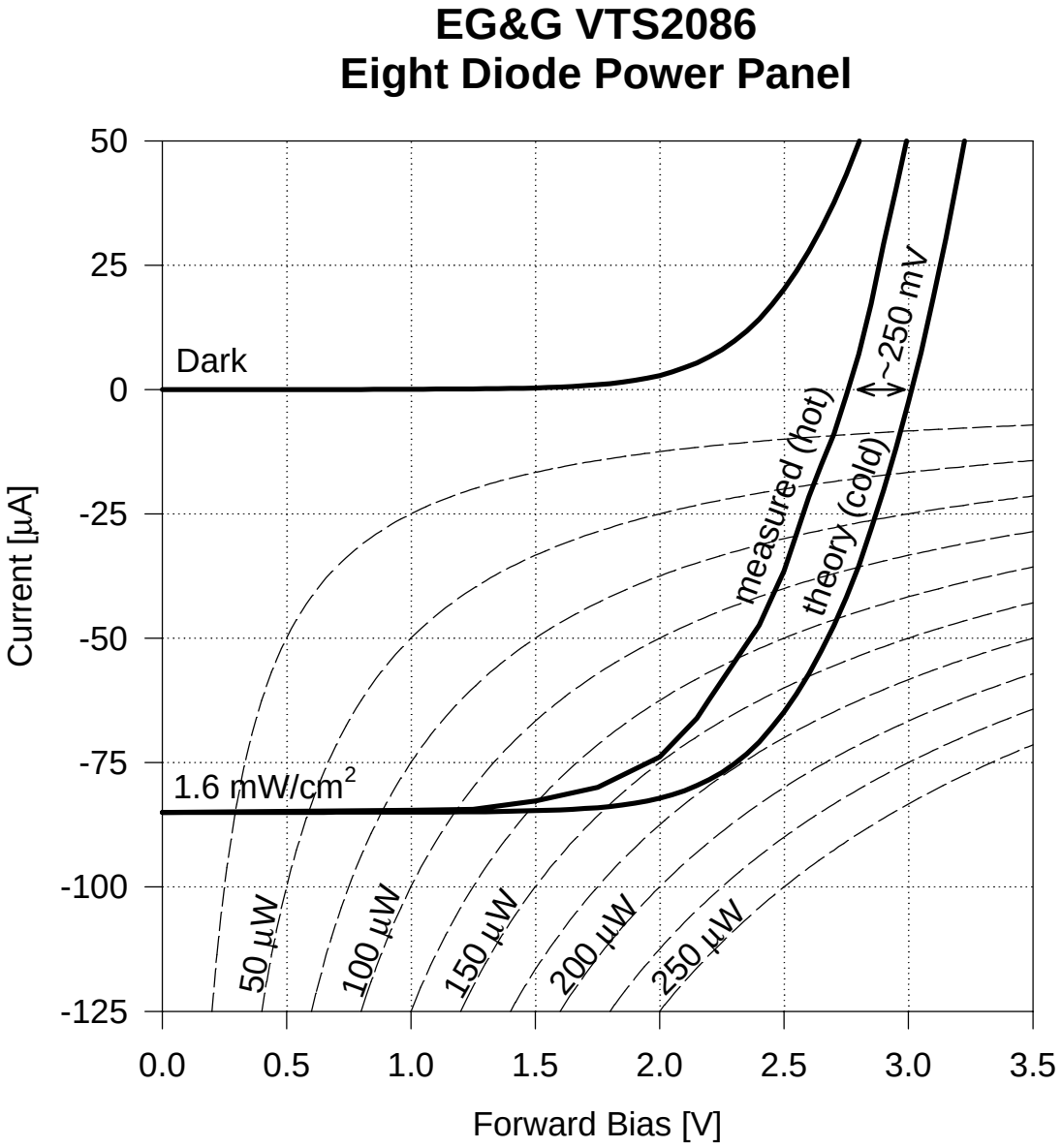

Figure 3.10: Eight diode, 2 V discrete silicon power panel I-V curves. Shows reduction of forward voltage due to panel heating (measured vs theory).

To see the benefit of operating at 2 V versus 2.5 V in terms of current output, we note that the photocurrent that flows internally to the diodes is equal to the difference between the short-circuit current and the current at the operating point. Only 10 μA of photocurrent is lost to the diodes when the power panel is operated at its design specification (2 V and 75 μA output), where it is maximally efficient with 150 μW output power. But at 2.5 V, almost 50 μA of photocurrent must flow through the diodes to provide this much forward voltage, leaving only 37μA current and 92 μW power output capacity.

3.3.1.4 GaAlAs power panels

To implement the 2.5 V, 25 μA power panel with GaAlAs photodiodes (Opto Diode Corp. ODD-45), the operating curves of Figure 3.6 were used to find the maximum power point at 25 μA output current. This falls near 0.7 V forward bias, so four diodes in series will be necessary to provide at least 2.5 V with maximum efficiency. Since the ODD-45 measures 1 mm x 1 mm, this panel could be assembled in less area than the 2.5 V silicon panel described above. Because the area of each diode in the panel is twice the area of the diodes in the silicon panel, and the radiant sensitivity is about 0.6 A/W vs 0.326 A/W for the silicon, this panel would be 3.7 times as effective at converting 880 nm light to electrical power!

One application called for a 7 V power supply, so ten ODD-45 diodes were connected in series to create this power panel[2]. When this panel was illuminated with an 880 nm LED, the I-V curves plotted in Figure 3.11 were recorded.

[2] Assembled by Cynthia Vanaria at MIT Lincoln Laboratory

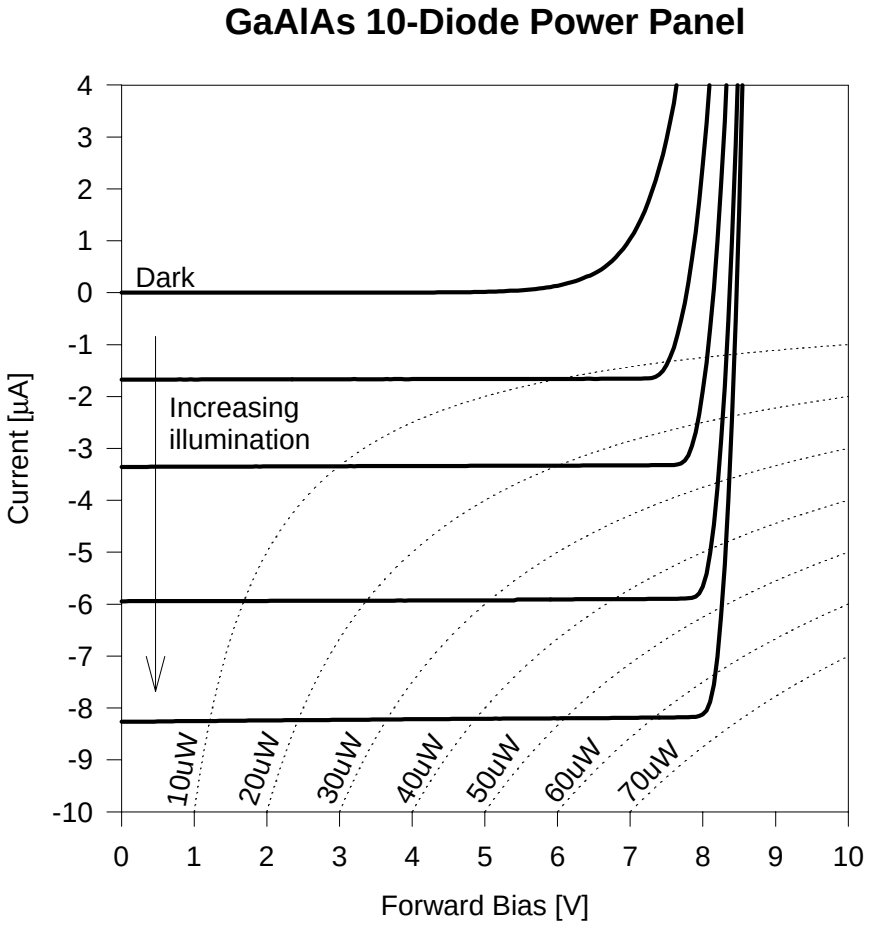

Figure 3.11: Ten diode, 7 V GaAlAs power panel I-V curves showing effect of non-uniform illumination.

The strange sharpening of the knee in the I-V characteristic at higher illumination levels was surprising at first, but then attributed to non-uniform illumination. Because a single LED was used at close range to illuminate the whole panel, some of the diodes in the panel were more strongly illuminated than others. This observation revealed an important design consideration that is the topic of the following section.

3.3.2 Array geometry and effects of non-uniform illumination

Figure 3.12 LEFT shows the circuit equivalent of an evenly illuminated power panel. The I-V curve of this panel should be identical to the I-V curve of a single diode, except the voltage axis is scaled by the number of diodes in the panel, as sketched in Figure 3.12 RIGHT.

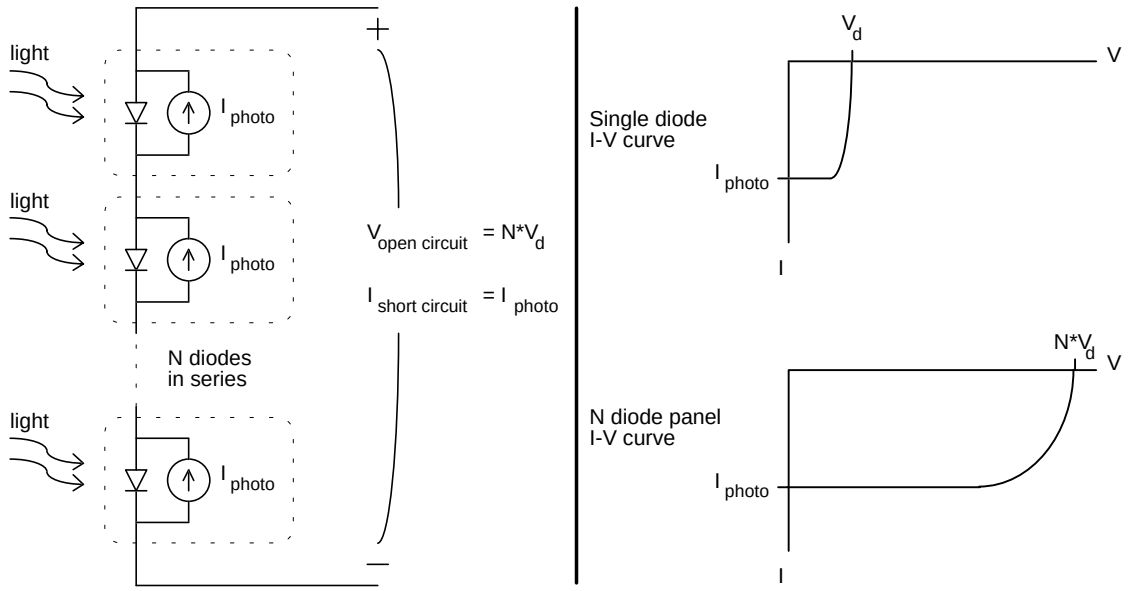

Figure 3.12: LEFT: Evenly illuminated power panel circuit equivalent. RIGHT: I-V curve of evenly illuminated panel is curve of single diode scaled on volt axis.

What happens to the I-V curve of the panel when some diodes are more highly illuminated than others is most easily understood by considering the case that one diode is illuminated at a lower level than the others. The circuit equivalent of this case is shown in Figure 3.13.

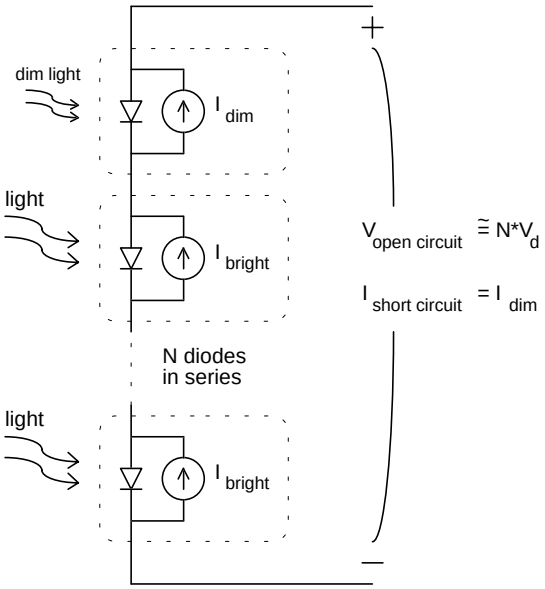

Figure 3.13: Power panel circuit with one diode less brightly lit than others.

In the extreme that the diode is completely dark, it is simply a reverse-biased diode in series with the others, cutting off the panel output current entirely. When the diode is

shadowed to a small fraction of the illumination level of the others, it limits the current through the whole panel. The majority of the photocurrent generated in the other diodes is forced to flow back through them. The strongly illuminated diodes are thus forward biased at a fairly constant level, and can be approximated by voltage sources in series with the darkened diode, as shown in Figure 3.14 LEFT. The I-V curve of the panel in this condition, shown in Figure 3.14 RIGHT, would look approximately like the I-V curve of the darkened diode shifted along the voltage axis by the sum of the (constant) forward voltages of the other diodes. Note how the "knee" of the curve is sharpened compared to the evenly lit panel. This is also evident in the experimental data of Figure 3.11.

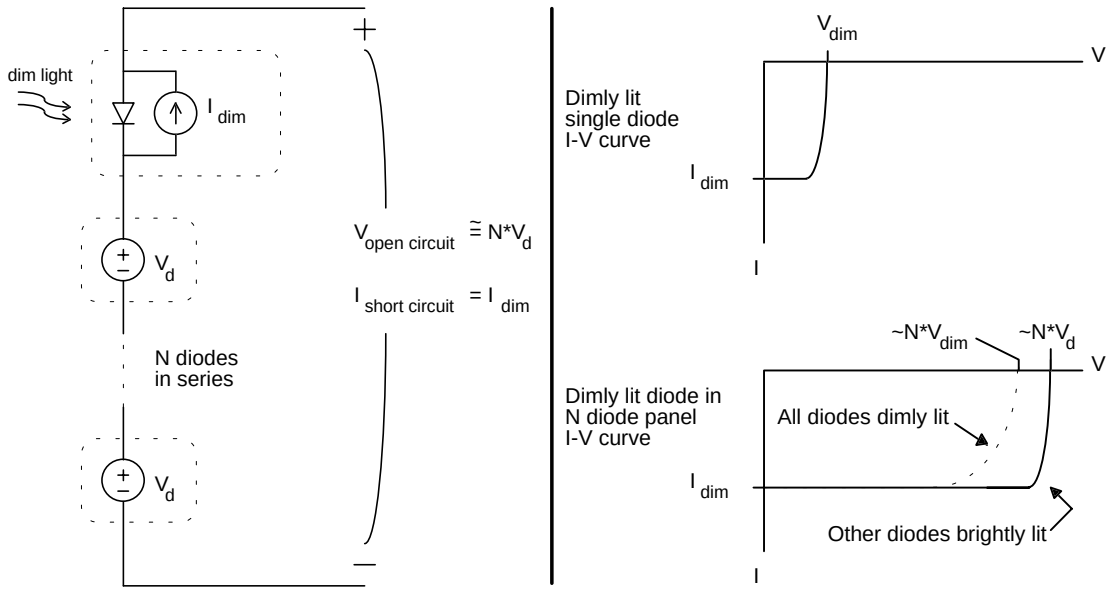

Figure 3.14: LEFT: Circuit approximation for one dimly lit diode in brightly lit panel. RIGHT: I-V curve of this circuit is curve of dimly lit diode shifted on volt axis. Dotted curve is for dimly lit panel.

The layout of the power panel can be designed to minimize the detrimental effects of uneven illumination. If the panel is divided into the series-parallel arrangement depicted in Figure 3.15, the effect of shadowing one diode is less severe, since it disables only one of several "mini-panels" that act in parallel to provide the output.

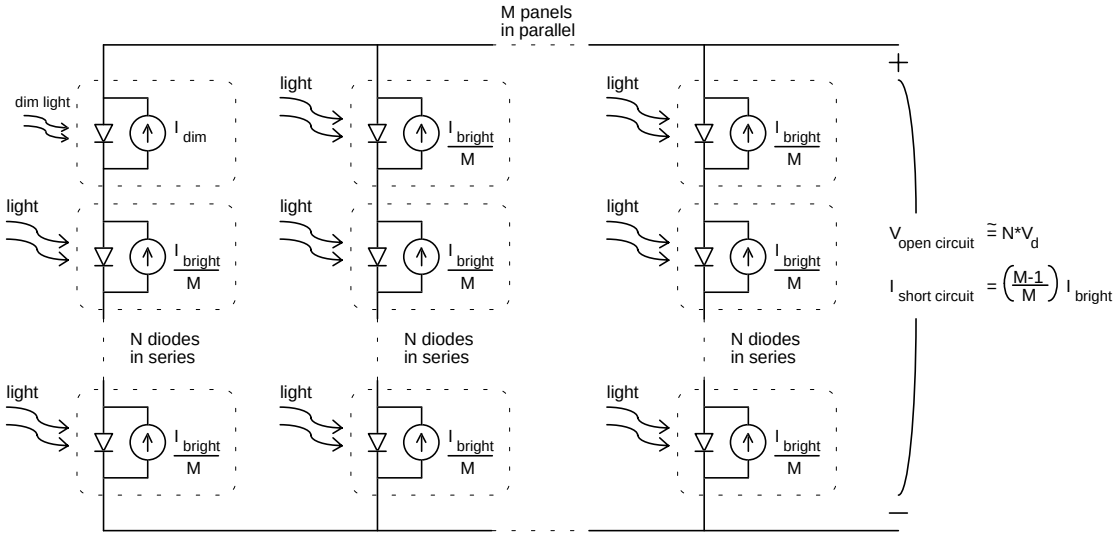

Figure 3.15: Series-parallel layout of panel to minimize effect of shadowing.

A similar benefit can be obtained by shaping the diodes in the panel into long stripes rather than compact squares, so that a shadow will be less likely to block any one diode completely. This arrangement is easier to manufacture than the series-parallel layout, and wastes less area for isolation.

3.3.3 Fabrication techniques

A number of different techniques for constructing implantable photodiode power panels were investigated. Originally it was planned to use micromachined integrated circuit silicon photodiode arrays. While conceptually the plan was simple, there were problems in isolating the photodiodes that required extensive process development to solve. A true integrated, micromachined panel would be a valuable part of the biological information telemeter, but hand-assembled or partially integrated units were developed in order to make progress until the more efficient and robust integrated circuit versions are realized.

3.3.3.1 Integrated circuit implementation

Most of the requirements of integrated power panels are met by standard foundry processes. However, standard isolation wells formed by PN junctions that are used in integrated circuits do not properly isolate the diodes in an optical power panel. Figure 3.16 illustrates the inherent fault with fabrication of diode arrays using the substrate diode isolation typically found in commercial processes. The top picture shows p-diffusion to n-well diodes that are intended to form the power panel, and the parasitic

well-to-substrate diodes that become conductive when the panel is illuminated. The lower picture shows the other failure mode of this implementation, where each well forms the base of a parasitic bipolar junction transistor. In either case, all but one of the series panel diodes is shorted out, so the integrated power supply appears to have only one photodiode.

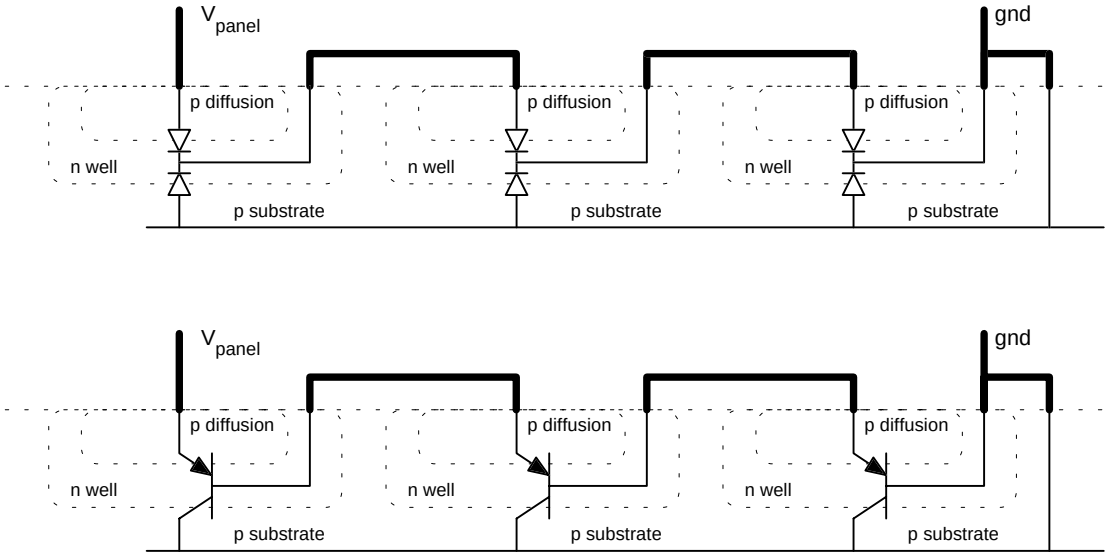

Figure 3.16: Failure of standard CMOS integrated circuit implementation of power panel. TOP: Well-to-substrate diodes become conductive when illuminated along with panel diodes. BOTTOM: Parasitic vertical bipolar transistors formed by the isolation wells shunt diode currents.

A silicon-on-insulator (SOI) process would eliminate these defects by using true dielectric isolation between the diodes. Each panel diode could be fabricated in its own silicon island on an insulating substrate. The diodes could be wired together using the standard process interconnects, yielding a true integrated power panel. If a thin, transparent substrate was used, the panel could be illuminated from the backside for even greater efficiency because the metal interconnects would not block incident light.

3.3.3.2 Manual assembly of discrete photodiodes

Functioning power panels have been produced by soldering small discrete diodes together. This approach is certainly reliable, and relatively inexpensive. However, the resulting power panels are relatively large and are tedious to assemble. They were used as subcutaneous power systems for prototype work, but they were too large to use as part of a system implanted on the surface of the brain. The panel whose I-V characteristics were given in Figure 3.10 was produced in this manner.

3.3.3.3 Post-processing of CMOS fabricated power panels

A combination of mechanical sawing and plasma etching was used to dielectrically (air) isolate diodes fabricated in a standard foundry process for integrated circuits[3]. This process was not as straightforward as originally anticipated. The process sequence requires gluing a glass front on the photodiode array and then sawing nearly through the array from the backside. The process is then completed by plasma etching down to the glass surface from the back of the device without damaging the thin metal interconnects on the front of the array. It turns out that although semiconductor wafer saws can perform the sawing operation, it is difficult to align the devices from the backside because of irregularities in the dice. This was overcome by first marking the locations for sawing on the sides of the device using a laser, and then flipping the device over for sawing. However, even then, variations in the thickness of the glue used to hold the quartz window on the front surface made it very difficult to accomplish the sawing process without destroying the front surface interconnects. Interaction between the plasma etching system and the glue tended to crack the front surface interconnects as well, adding to the difficulties. In spite of these difficulties, one of these devices was fabricated and used to test the integrated power panel concepts. This was the 12-diode device that produced the I-V curves of Figure 3.9.

This basic approach was reduced to a more robust process for producing these partially integrated power panels. This process involves creating an array of silicon photodiodes using the MOSIS foundry service, as before, but gluing a thin quartz support to the *back* of the array. The diodes were then dielectrically isolated in one step by sawing completely through the array from the front side. The separated diodes, still held together by the insulating quartz support, were then wire-bonded in series to create the panel. Lead wires were attached, and this structure was then encapsulated in silicone to complete the assembly. This design approach was developed after the realization that the series-parallel effect could be accomplished by making the diodes long rectangles rather than squares or groups of very small cells. Also, from the power panel optimization work and circuit design efforts, we learned that we could construct optimal panels with relatively few diodes to power low voltage systems.

[3] Backside sawing and etching performed by Terry Herndon at MIT Lincoln Laboratory

The six diode power panel characterized in Figure 3.8 was created by this process[4]. The mask layout[5] for this particular integrated circuit (IC) design is shown in Figure 3.17. Note that with fewer saw cuts (fewer diodes) afforded by the optimization, the area per diode can be greatly increased, further optimizing the assembly. The efficient use of space in this rectangular design has the advantages of the series-parallel arrangement while maximizing usable chip area. Each of the six diodes has an active area of 250 μm by 2,000 μm. However, an area equivalent to 0.5 mm x 2 mm (28%) is lost to the saw cuts, which would not be lost in an SOI process implementation. Individual cells were wire bonded together to form the active array, which was capable of supplying at least 25 μA at 2.5 V with relatively low-level illumination. Bond pad straps were included in the IC layout, in case the backside sawing process was perfected. Normally, these are sawn apart and re-bonded using 0.007" gold bond wire.

[4] Process conceived by Bruce Larson and David Edell, performed by Cynthia Vanaria at MIT Lincoln Laboratory

[5] Layout artwork by David Edell

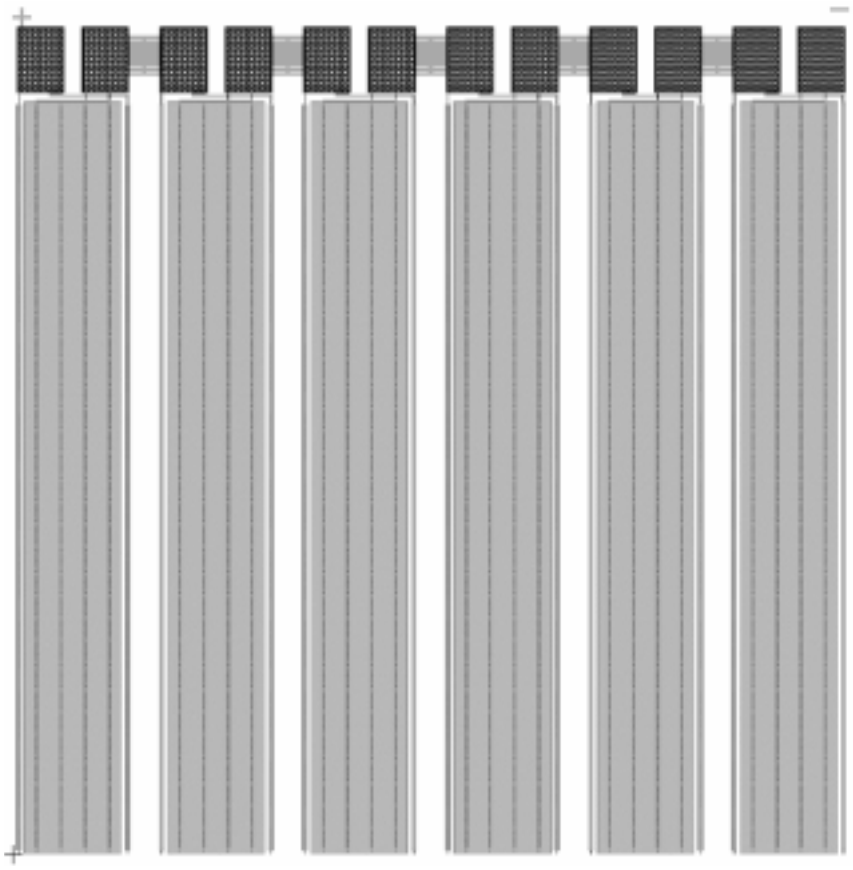

Figure 3.17: Integrated circuit layout of 6 cell micropower panel. Bond pads at top are to be wire bonded after sawing between each of the cells. Active cells are 2 mm long and 0.25 mm wide. Die area equivalent to 0.5mm x 2mm (28%) is lost to the five saw cuts.

3.4 Limitations

3.4.1 Physical size and optical power density

The specific application will set the size limits for the optical power supply. Then the efficiency of light transmission and conversion to electrical power combined with the maximum safe optical power density determine the maximum amount of power that may be supplied by the panel. Since non-ionizing radiation is used to illuminate the power panel, the limit on the optical power density is set by tissue heating due to the power dissipation of the implant and direct absorption of light by the tissues. Experiments were performed to quantify these tissue heating effects.

3.4.1.1 Tissue heating

Tissue heating is one possible limitation with any transmitted power source that is partially absorbed. It is a problem with RF sources as well as optical sources. This potential limitation to the optical technology was evaluated to determine some bounds. The maximum power density from the sun onto the earth's surface is 100 mW/cm^2 when the sun is directly overhead [78]. As a starting point, this power density can be considered as a conservative estimate of the upper limit that could be used for the power transmission system. It should be noted that the long wavelength light used for optical telemetry is not damaging to the skin as is UV from sunlight. The analogy is made for putting the power density level of the optical power transmitter into a familiar perspective. And because only non-damaging wavelengths are used, and the power dissipated in the optical transducer system will be localized and will not lead to overall body temperature elevation (as does full body sunlight), this estimate is particularly conservative.

Most of the circuits for biomedical information telemetry that were designed in the course of this research required less than 100 μW of electrical power from a 2.5 V supply to operate. As shown in the preceding section on micro-power panel development, this can be generated using less than 25 mW/cm^2 of incident light power with even a relatively inefficient photoelectric transducer (the six diode integrated silicon power panel). Since tissue losses were only about 50% across the skin for the power transmission wavelength of 880 nm, only roughly 50 mW/cm^2 need be applied to the implanted transducer to satisfy the power requirements. This should be well under damage limits for skin. For many applications, a power panel made from GaAlAs photodiodes or with greater area could be used to reduce the optical power density requirement to even lower levels.

To further determine if the incident power densities in the range anticipated for this application were within reasonable bounds for the safety of the biological system, tissue temperatures were monitored during illumination of an implanted photodiode with an active area approximately the same as that expected for a free floating neural waveform telemeter, 2mm x 2mm. Miniature thermocouples were fixed to the top and bottom surfaces of the photocell. Under heavy anesthesia, a rabbit was implanted with the photocell on the brain surface[6]. First, an incision was made in the rabbit's scalp creating

[6] Surgery performed by David Edell assisted by Bruce Larson at the West Roxbury VAMC

a flap of skin that was lifted back to reveal the skull. A hole was cut into the skull, just large enough to fit the photocell. An incision was then made in the dura mater so that the photocell, with the thermocouples mounted above and below, could be slipped under it onto the surface of the brain. The leads were fixed to the skull with bone cement, and a 3mm thick quartz window was cemented in place to close the hole in the skull over the dura and photocell. A third thermocouple was placed over the quartz window, and the skin flap was closed with forceps. A fourth thermocouple was placed on the skin surface directly over the quartz window. A high intensity 880 nm LED was finally aimed at the skin over the implanted photodiode (and thermocouples) to serve as the illumination source for the experiment.

The infrared LED was powered on and off while the thermal excursions at each level were monitored. Power was left on until the readings stabilized and remained unchanged for 5 minutes or longer.

Figure 3.18 is a summary of the thermal effects experiments. The largest excursions were on the surface of the skin, heating from approximately 97 °F to 107 °F with the maximum power input of 50 mW/cm^2. The brain surface - bottom of photocell interface, however, only increased from 101 °F to 102 °F at the highest setting. Since the power input from sunlight is twice that used in this experiment, it is unlikely that this level of heating will cause adverse effects. It would also be expected that perfusion of the tissues was compromised in these experiments by the bulk of the implant occluding the subdural space, by interruption of the bone by the quartz plate, and by interruption of a substantial area of the skin's blood supply. Additionally, the animal's thermal regulation was undoubtedly impaired by the anesthesia. Thus, it seems that a reasonable margin of safety exists for the proposed operation of the optical power system.

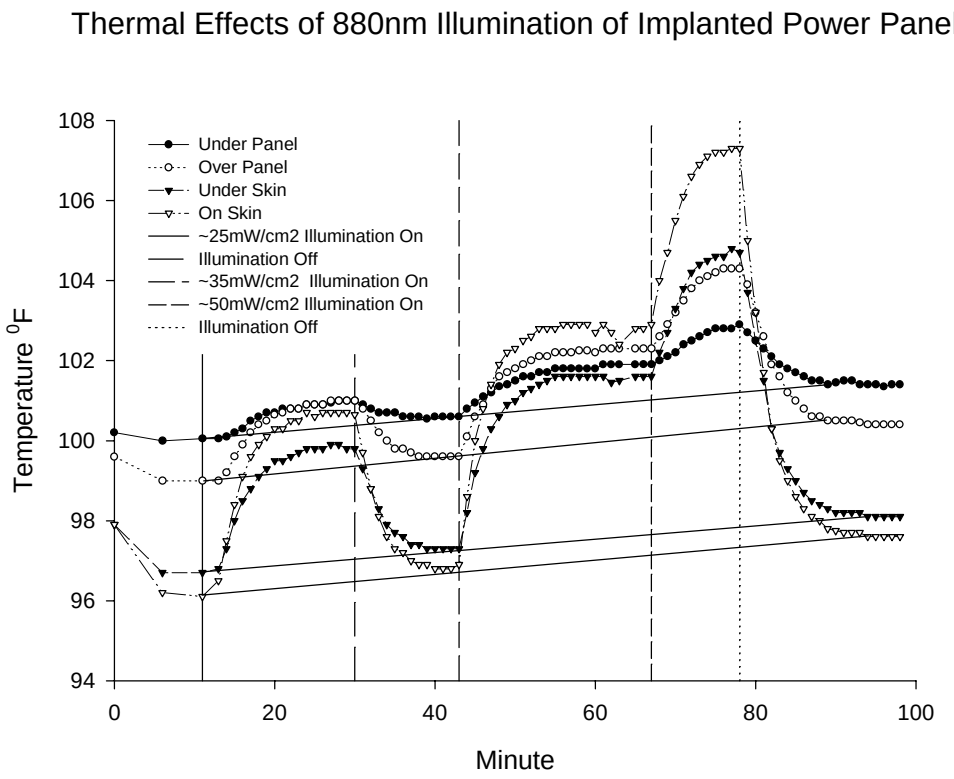

Figure 3.18: Thermal excursions due to focused light on skin. Note that the animal was being warmed slowly by hot water blanket to maintain temperature under anesthesia. This accounts for slow drift of data over the course of the experiment as illustrated by the four lines connecting the off-time temperatures.

Chapter 4: Signal encoding for optical transmission

4.1 Biomedical signals

The type of biological signals being telemetered will influence much of the implant design. Small signals, and high bandwidths and channel counts will naturally present the greatest design challenges. For this reason, the multi-channel neural waveform transmitter is an ambitious and useful goal, since the signals involved are both small (10 to 250 μV) and of large bandwidth (7kHz) compared to most other biological signals. For comparison: 1) electroencephalogram (EEG) signals have typical peak amplitudes of 10 to 100 μV on the surface of the scalp with a bandwidth of DC to 100 Hz; 2) electromyogram (EMG) signals have 50 μV to 1 mV peak amplitudes and a bandwidth of about 10 Hz to 3 kHz; and 3) electrocardiogram (ECG, or EKG) signals have peak amplitudes from 0.1 to 1 mV and a bandwidth of DC to 100 Hz [79]. Other physiological variables of common interest, including temperature, pressure, glucose, pH, CO_2, PO_2, and perfusion, all have much lower bandwidths. So a system that could transmit multiple channels of neural waveform data would be capable of transmitting most other physiological signals, and could probably be modified to transmit many more channels of these signals.

Various encoding techniques were evaluated to find methods that are efficient in terms of circuit design (chip area and power consumption) and the power required for signal transmission. Noise immunity during signal transmission and robustness of signal reception were considered in this evaluation of encoding methods. A single channel neural waveform transmitter was developed first, and development of a multiple channel telemeter was subsequently begun.

4.2 Encoding techniques

In order to transmit the biomedical signals (neural recordings, in this particular application) from the implant using light, they had to be encoded in some manner.

4.2.1 Amplitude modulation (AM)

The simplest encoding scheme might be direct amplitude modulation of the output light of the LED. This could be achieved by varying the LED drive current about some average bias value in proportion to the signal level. More than one channel could be transmitted by time-division multiplexing. Unfortunately, this method entails continuous

operation of the LED at power levels high enough to overcome light losses in the tissue, background illumination, and the noise of the photodetector circuit. It is certainly not the most power-conservative method. Another reason that this technique is not well suited to the biomedical information telemeter is that the transmission is highly subject to corruption by movement of the photodetector receiver relative to the telemeter. This movement would cause changes in the received signal amplitude that could be hard to distinguish from the transmitted signal information. Automatic gain control could be used to correct for some of the changes in received signal amplitude caused by movement, but only if the low-frequency content of the transmitted signals could be ignored.

4.2.2 Frequency modulation (FM)

Traditional frequency modulation of a carrier signal would overcome the movement problem associated with pure amplitude modulation. This could be accomplished with a voltage-controlled oscillator (VCO) that drives the output LED with a periodic waveform whose frequency is proportional to the biomedical signal. Again, time-division multiplexing could be used to encode several channels of signal information before the voltage-to-frequency conversion. This technique is more robust than amplitude modulation, but could still require a good deal of power for signal transmission, depending on the carrier waveform utilized.

4.2.3 Analog vs digital transmission

If the analog biomedical signals were converted to digital, they could be transmitted more robustly because it would only be necessary to detect two levels of light output. These could be two easily distinguished intensity levels, or simply “on” and “off”. In the latter case, only the duration or time of occurrence of the “on” pulses would need to be determined, depending on the digital transmission scheme used. Hence the signal-to-noise ratio of the received optical signal can be much lower than, for example, an amplitude modulated analog signal. Consequently, less power is required for signal transmission. The cost of digital conversion and encoding for serial transmission is increased telemeter circuit complexity, and the associated increase in electrical power consumption.

4.2.4 Pulse encoding

4.2.4.1 Pulse position encoding

A technique that offers the much of the circuit simplicity of analog methods, along with the transmission efficiency and robustness of digital signals, is *pulse position* encoding. With this technique, the input signal information is encoded in the relative timing of pulses in a sequence. In typical pulse position encoding, two pulses are required for each data sample. The time between the two pulses in each pair is proportional to the encoded signal, but the first pulse of each pair occurs at a constant rate. Pulse position encoding of this type is very similar to *pulse width modulation* (PWM), except that the transitions (on and off) are marked by short pulses. Figure 4.1 illustrates a pulse position encoded waveform.

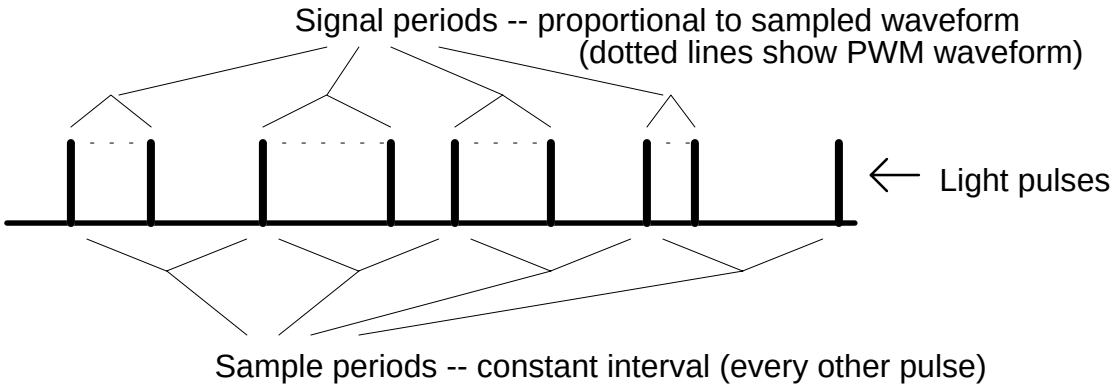

Figure 4.1: Pulse position encoded waveform.

4.2.4.2 Pulse period encoding

A variation of pulse position encoding, which may be more aptly referred to as *pulse period* encoding, was used for the biomedical information telemeters developed in this research. Pulse period encoding requires only one pulse per sample, because the time between one pulse and the next is proportional to a sample of the encoded signal, as shown in Figure 4.2. While the sampling rate of a single channel of information encoded in this fashion is somewhat variable, the savings in transmission power is almost 50%. The average pulse rate must be made high enough to meet the Nyquist criterion for the sampled signals despite the rate variations intrinsic to this encoding scheme.

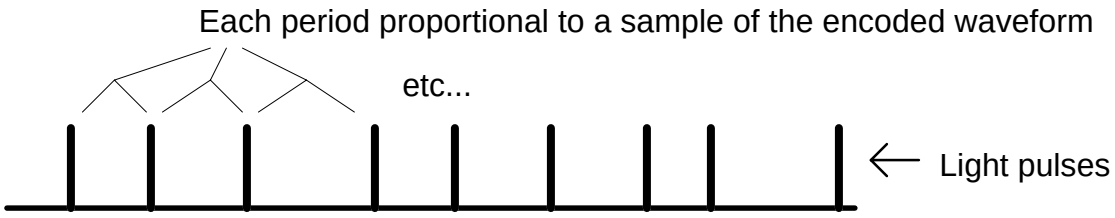

Figure 4.2: Pulse *period* encoded waveform.

Pulse encoding had the advantage that short but intense flashes of light from the output LED could be used to mark the pulses. These pulses require less average power and are easier to detect than, for instance, a continuous amplitude- or frequency-modulated light output. And since only the occurrence of a light pulse needs to be detected, and not its amplitude, pulse period encoding is largely immune to changes in the physical arrangement of the emitter and detector. Also, the very minimum amount of light needed to overcome background illumination and the noise of the detection system is required for successful reception of the signal.

A trade-off with pulse period encoding is that the encoder and detector circuits must have greater bandwidth than some techniques, because the signal information is encoded entirely in the timing of the pulses, as the amplitude of the pulses carries no information. In contrast, an amplitude-modulated signal contains the same frequency content as the original signal, and requires only this bandwidth to transmit. The penalty associated with increased detector circuit bandwidth is that the sensitivity of the most detector circuits goes down as bandwidth is increased (as discussed next in Chapter 5), so pulse amplitudes must be correspondingly larger. However, it appeared that under normal circumstances, the amount of light required to overcome background illumination would make a continuous amplitude- or frequency-modulated light output impracticable, while pulse transmission could be achieved. The encoder circuit will generally require more power to operate at higher speed as well, but the necessary bandwidth was achieved in our designs with little additional power consumption by the circuitry.

4.2.4.2.1 Multiplexed data transmission

Multiple channels of biomedical signal information can be pulse period encoded by sequencing through the channels to form a cycle of signal periods. Each period in the sequence corresponds to one channel, and the cycle of channel sample periods can be separated from the next by a marker period that is either longer or shorter than any

signal period. An example pulse sequence for an 8-channel multiplexed system is given in Figure 4.3.

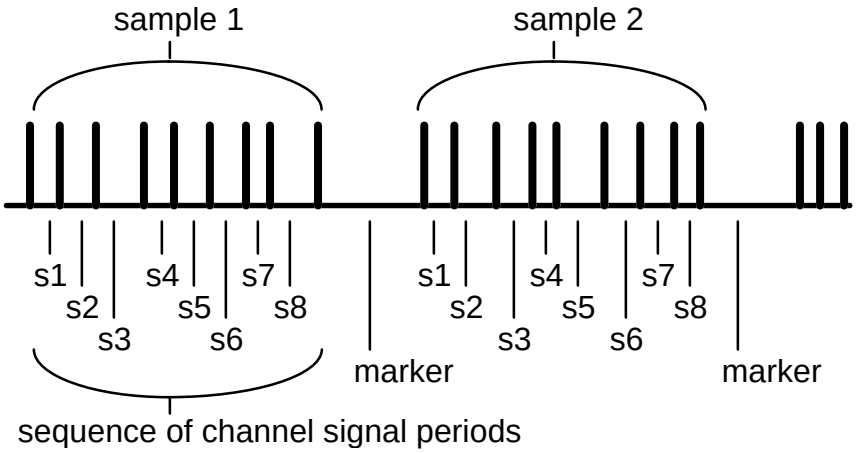

Figure 4.3: Multiplexing of signals in pulse period encoding.

4.3 A simple pulse period encoder circuit

A pulse period encoder circuit was developed for a single channel neural waveform telemeter. In its simplest discrete component form, the single channel telemeter is sketched in Figure 4.4. This circuit is somewhat different from subsequent integrated circuit designs, in that it produces a sequence of pulses where the time between pulses is varied in *inverse* proportion to the input signal (i.e. the instantaneous frequency of pulses is linearly related to the input signal).

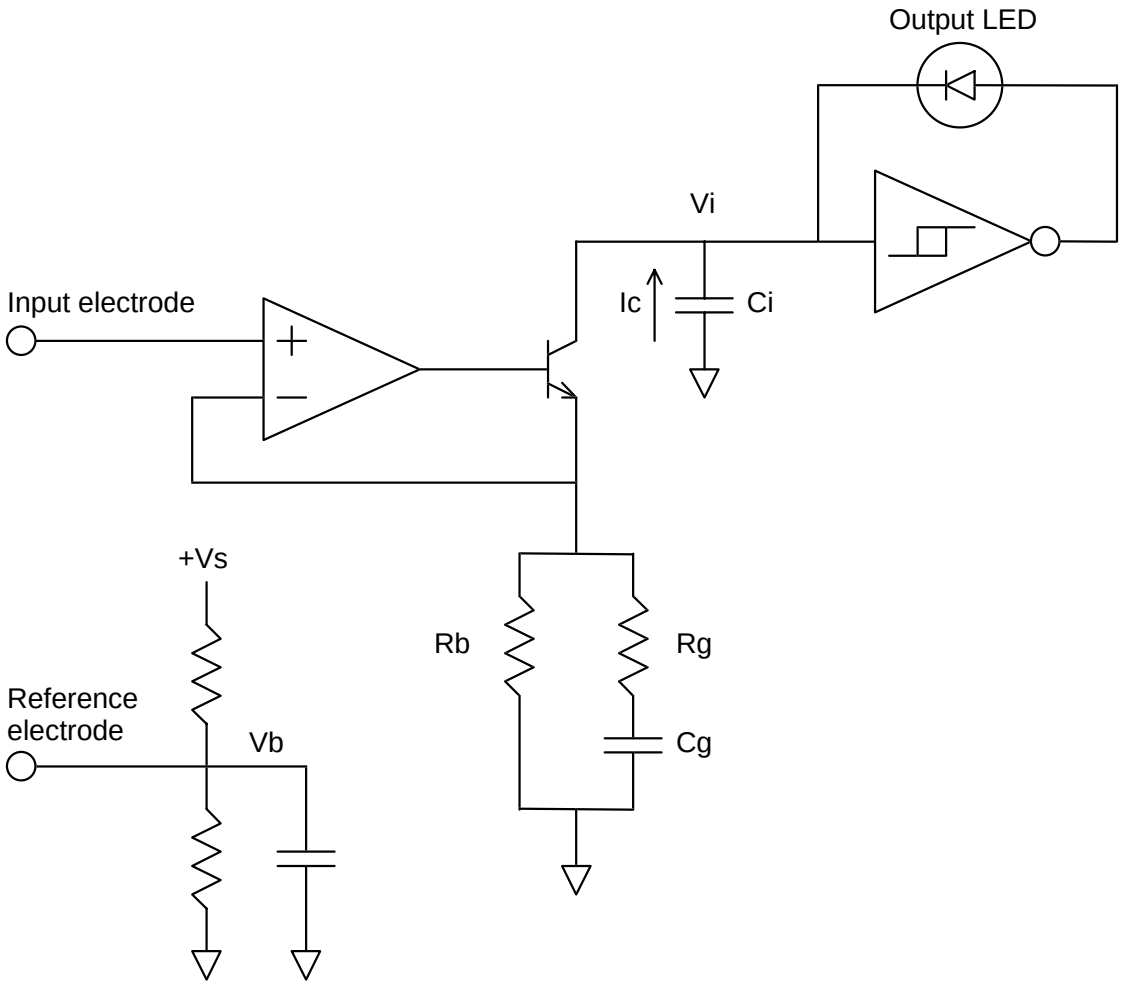

Figure 4.4: Pulse period encoder circuit.

This circuit encodes the differential voltage waveform on its electrodes into a continuous sequence of short pulses of light that are spaced apart in time according to the instantaneous potential between the electrodes. It performs this function as follows. The resistor network on the reference electrode references the circuit to the animal, which also sets the DC bias on the input electrode to the same voltage V_b relative to circuit ground. The operational amplifier sets the voltage at the transistor emitter to the input electrode voltage, causing a current to flow through the transistor collector. This current has a DC component equal to V_b/R_b, and an AC component approximately equal to v_{in}/R_g for $R_g << R_b$, where v_{in} is the potential difference between the electrodes. The bandwidth of the circuit is limited on the low end by the time constant $R_g C_g$ and at the high end by the speed of the op-amp. Normally the inverting Schmitt

trigger connected to the transistor drain will be in the low state, so the drain current will flow through the integrating capacitor C_i, whose voltage will drop according to:

$$\Delta V_i = -\frac{1}{C_i}\int I_c dt\,,$$

where

$$I_c = \frac{V_b}{R_b} + \frac{v_{in}}{R_g}\,.$$

When the capacitor voltage V_i drops below the low threshold, the inverting Schmitt trigger output changes to the high state. The LED connected from its output to its input then flows current onto the integrating capacitor until V_i exceeds the Schmitt trigger hysteresis level and it switches back to the low state, and the integration process starts over. While the reset current flows through the LED, it emits a pulse of light. Since the reset process occurs very quickly, a short but intense pulse of light is emitted.

Because V_i ramps between the hysteresis limits of the Schmitt trigger, the total voltage excursion on the integrating capacitor will be the same for every cycle. The effect of changing the current flow through the transistor drain must then be to change the time required for the capacitor voltage to make the transition from the lower hysteresis limit to the upper one. The time it takes for the capacitor voltage to be reset from the high state to the low state it relatively constant (and very short) because of the large current that flows through the LED when it is forward biased.

If the change in v_{in} occurs slowly compared to the cycle time of the integrator, it may be treated as a constant to determine I_c during each integrating cycle, so that

$$\Delta V_h \approx \frac{1}{C_i} I_c \Delta t$$

where ΔV_h is equal to the hysteresis width and Δt is the duration of the integration cycle. Thus, the time between light pulses is related to the input voltage by:

$$\Delta t = \frac{C_i \Delta V_h}{I_c} = \frac{C_i \Delta V_h}{\left(\frac{V_b}{R_b} + \frac{v_{in}}{R_g}\right)}.$$

To decode the differential electrode voltage from the pulse period, the input voltage is extracted from the measured time between each sequential pulse:

$$v_{in} = \left(\frac{C_i \Delta V_h}{\Delta t} - \frac{V_b}{R_b} \right) R_g .$$

If the Schmitt trigger has some time delay before it changes state, as is often the case, this must be taken into account to determine the true integration time:

$$\Delta t_{true} = \Delta t_{measured} - T_{delay}$$

where T_{delay} is the sum of the low-to-high and high-to-low transition delay times. This is used to find the real input voltage:

$$\begin{aligned} v_{in} &= \left(\frac{C_i \Delta V_h}{\Delta t_{true}} - \frac{V_b}{R_b} \right) R_g \\ &= \left(\frac{C_i \Delta V_h}{\left(\Delta t_{measured} - T_{delay} \right)} - \frac{V_b}{R_b} \right) R_g \end{aligned}$$

which can also be expressed in terms of the measured base period Δt_{base} by solving for the case when $v_{in} = 0$ and performing the substitution:

$$v_{in} = \left(\frac{\left(\Delta t_{base} - T_{delay} \right)}{\left(\Delta t_{measured} - T_{delay} \right)} - 1 \right) \frac{R_g}{R_b} V_b .$$

Capacitor C_i and resistor R_b are selected along with V_b to give a minimum period that is sufficiently fast to avoid aliasing of the encoded signal, and resistor R_g is chosen to give easily measurable changes in the pulse period for the expected range of input voltages v_{in}. Capacitor C_g is selected in conjunction with R_g to set the low frequency cut-off of encoded signals. The bandwidth of interest for neural signals is approximately 10 Hz to 7 kHz, so the single-channel encoder was designed to have a base period of 30 μs and a maximum period of 70 μs when $v_{in} = -1\text{mV}$.

4.4 Decoding

Decoding of the pulse-period-encoded signals was accomplished by a number of different methods during the development of this technology. The basic technique for decoding these signals is to measure the time between the pulses of light received by the photodetector, and to reverse the transformation that related the original input signals to time. For multiplexed data, the pulse sequence must be sorted out to decode the individual signal channels. Since the details of these transformations were

somewhat specific to the various encoder circuits, the decoders will be discussed in the context of the telemeters for which they were designed. This also makes for a more clear presentation of the increased sophistication of circuits and techniques that were developed as the research progressed.

Chapter 5: Optical signal transmitters and receivers

5.1 LED for transmitter

5.1.1 Wavelength for signal transmission

5.1.1.1 Skin transmission efficiency

As discussed in Chapter 2, longer wavelengths of light were found to cross skin more efficiently that shorter wavelengths, and longer wavelength light emitting diodes (LEDs) were more efficient as well (Figure 2.1 and Figure 2.3). Since infrared light was already selected for power transmission, red LEDs were investigated for use as telemeter signal output devices. Using a visible wavelength of light for the telemeter output had the added advantage of providing a visual aid to receiver alignment.

5.1.1.2 Electrical efficiency

Assorted commercially available LEDs were evaluated at appropriate (low) current levels in order to find the most efficient one. Figure 5.1 shows the relative light output of some of the LEDs that were tested. Logarithmic scales are used because of the dramatic differences in efficiency of the diodes.

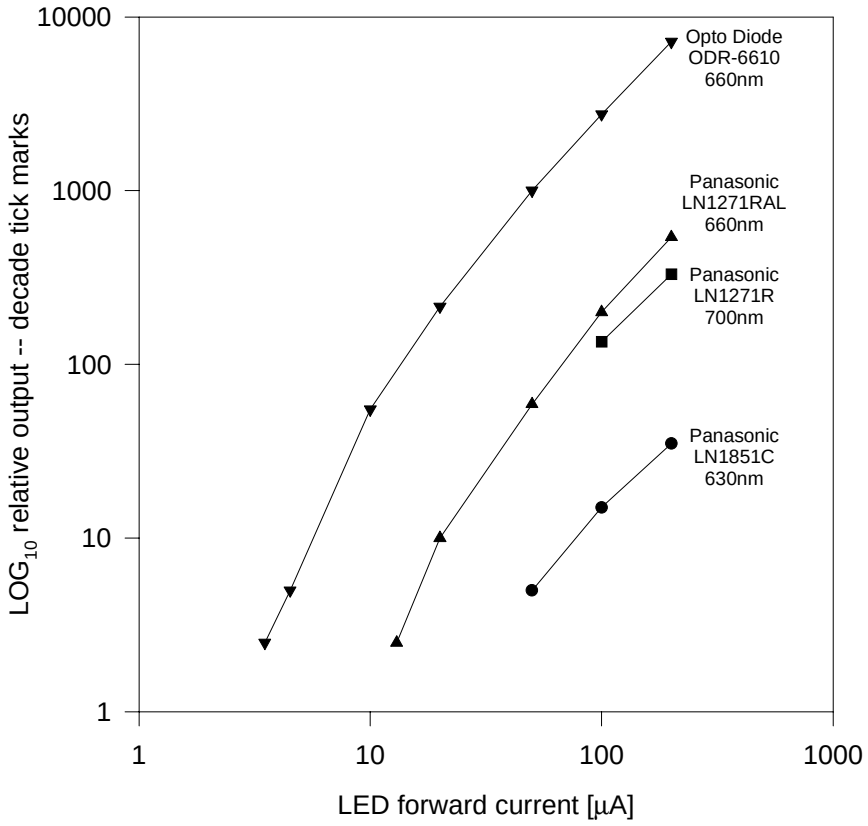

Figure 5.1: Relative light output of various LEDs.

By a significant margin, the best LED found was the ODR-6610 produced by Opto Diode Corp. The peak emission wavelength of this LED is 660 nm, with a 50% spectral bandwidth of 20 nm. Calculated from the published specifications, its power efficiency (defined as the percentage of power dissipated by the LED that is output as light) is about 15.8%. This corresponds to a quantum efficiency (the percentage of electrons flowing through the diode that produce a photon that is emitted from the LED) of 16%. In addition to high output power capability, this LED had the most efficient output measured at low current levels. It was obtained in both packaged and die form. For some applications in this research, packaged diodes were utilized by grinding the plastic lens to minimize the size of the package.

5.1.2 Reflector

In order to use the unpackaged (chip) LEDs, they were mounted to platinum reflectors[7] that also served as one of the electrical contacts to the diode. A lead was wire-bonded

[7] Micro-assembly work performed by Cynthia Vanaria at MIT Lincoln Laboratory

to the top of the diode to form the other electrical connection. A comparison was made between reflector mounts which were simply flattened platinum balls and ones which had been flattened and dented with a polished 45° conical tip center-punch to hold the LED. The LEDs were driven by a current source, and the light output directly above the diodes was measured by two techniques: a large area photodiode and a portable light power meter. A piece of white paper placed directly over the LEDs was used to simulate tissue scattering, to see if the advantage of the conical reflector was reduced. Figure 5.2 gives the results of the measurements with the light power meter, and Figure 5.3 lists the results of measurements made with the photodiode. Under these conditions, the conical reflector gave at least a 42% increase in detected light output, and as much as 104% improvement.

Test condition (LEDs 5mm from sensor)	Power meter reading, uW/cm^2			Percent improvement with conical reflector
	Dark	Flat reflector LED	Cone reflector LED	
no scattering	0	2.14	3.84	79%
paper scattering	0	0.662	1.08	63%

Figure 5.2: LED reflector comparison made with light power meter.

Test condition and distance from sensor	Photodiode detector current, nA			Percent improvement with conical reflector
	Dark	Flat reflector LED	Cone reflector LED	
no scattering, 3mm	49.5	2885	4362	52%
no scattering, 13mm	48	485	796	71%
no scattering, 31mm	48	214	387	104%
no scattering, 50mm	47	127	198	89%
paper scattering, 13mm	46	174	228	42%

Figure 5.3: LED reflector comparison made with photodiode detector.

5.2 Receiver

5.2.1 Transimpedance amplifier photodetector circuit

The fundamental limitation to decreasing the power requirement of the implant may be the power required for the optical transmission of signals off the implant. Hence this power limit may be the final limiting factor in the number of channels of information that can be encoded by a given implant. The more sensitive the receiver/detector, the less power per pulse is required from the implant, so a thorough investigation of receiver sensitivity was undertaken.

5.2.1.1 Basic circuit dynamics and need for compensation

Several circuit approaches were initially considered, but the basic transimpedance amplifier photo-detector circuit shown in Figure 5.4 was the most promising. The noise/speed design tradeoffs for this circuit were studied in detail to determine the optimal design.

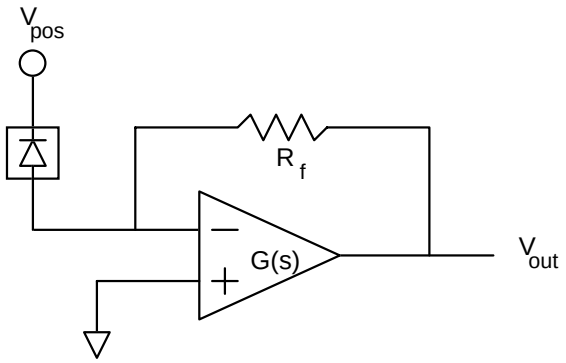

Figure 5.4: A typical transimpedance amplifier photo-detector circuit.

To study the dynamics of the detector circuit, the photodetector diode may be modeled by capacitance C_d in parallel with a current source I_d as shown in Figure 5.5.

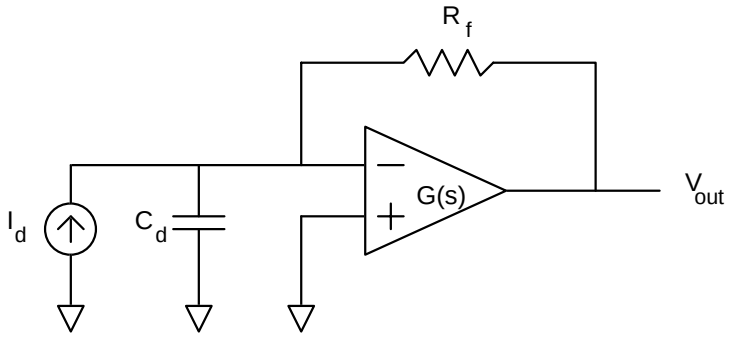

Figure 5.5: Transimpedance amplifier detector with photodiode modeled by a capacitor and a current source.

The block diagram of Figure 5.6 was constructed to study the dynamics of this circuit.

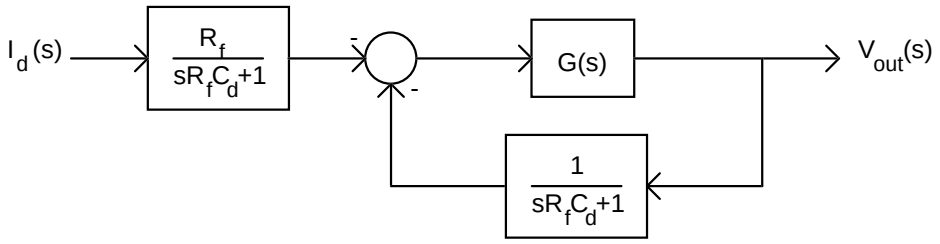

Figure 5.6: Block diagram of the transimpedance amplifier photo-detector circuit.

The dynamics of the operational amplifier were approximated by

$$G(s) = \frac{K}{s\tau + 1},$$

so the loop transmission is

$$L(s) = \frac{K}{(s\tau + 1)(sR_f C_d + 1)}.$$

The magnitude of the loop transmission is sketched in Figure 5.7, where it has been assumed that the pole from the op-amp is at a lower frequency than the pole from the resistor and diode capacitance.

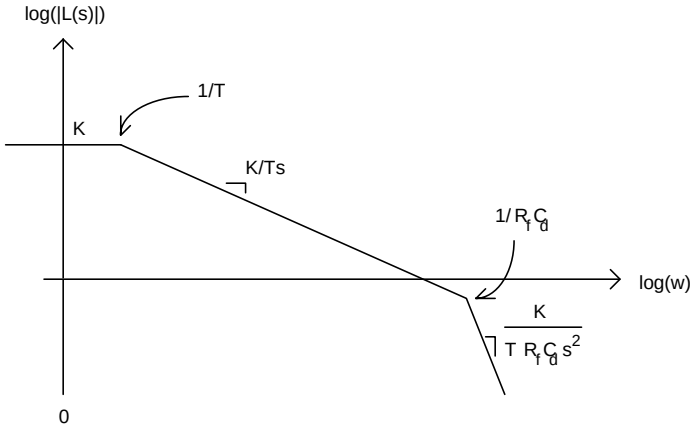

Figure 5.7: Bode magnitude plot of loop transmission of system in Figure 5.6.

For this system to have reasonable stability, the magnitude of the loop transmission must be less than one before the phase approaches -180°. This will be the case if the pole due to the diode capacitance and the feedback resistor occurs at a frequency higher than the unity gain frequency of the operational amplifier, or

$$\frac{1}{R_f C_d} \geq \frac{K}{\tau},$$

ensuring a phase margin of at least 45°. The transimpedance of the photodetector circuit is approximately R_f for frequencies below K/τ. According to this analysis, it would be better to leave out the op-amp altogether, because the bandwidth achieved by directly loading the photodiode with the resistor is $1/R_f C_d$, which is greater!

5.2.1.2 Feedback capacitor compensation

When the circuit of Figure 5.5 was frequency compensated with a capacitor across the feedback resistor as shown in Figure 5.8, the benefits of the transimpedance amplifier were revealed.

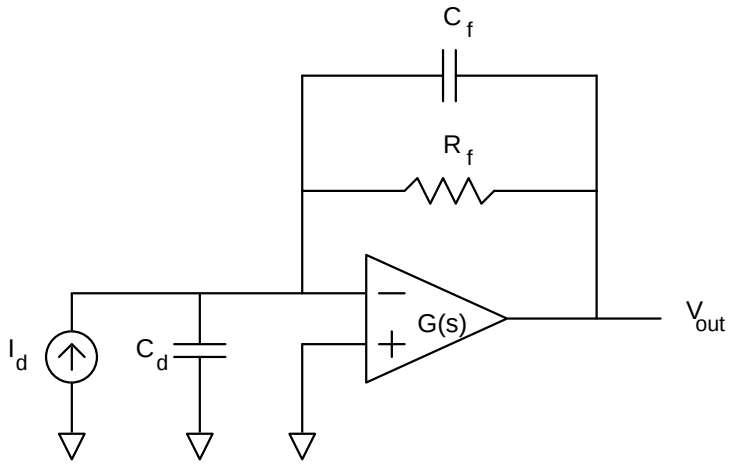

Figure 5.8: Transimpedance amplifier detector with frequency-compensation capacitor.

The block diagram was revised to include the dynamics of the compensation capacitor for Figure 5.9.

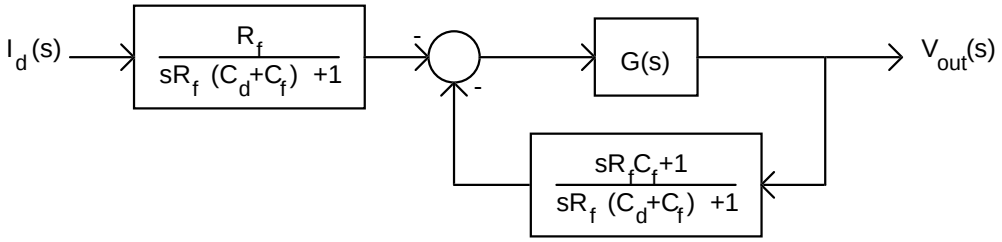

Figure 5.9: Block diagram of the transimpedance amplifier photo-detector circuit with frequency compensation capacitor.

The loop transmission of the capacitor-compensated circuit is

$$L(s) = \frac{K(sR_f C_f + 1)}{(s\tau + 1)(sR_f(C_d + C_f) + 1)},$$

and the Bode magnitude plot of the loop transmission of this system is sketched in Figure 5.10, where the compensation is seen to add a transfer function zero and shift the second pole to a lower frequency.

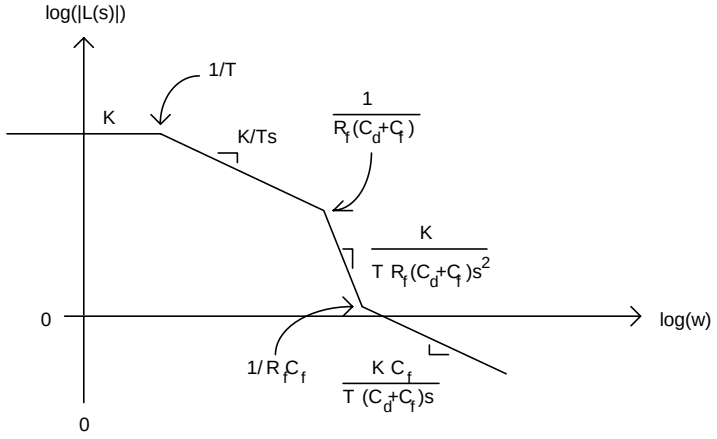

Figure 5.10: Bode magnitude plot of loop transmission of capacitor-compensated system.

Provided that the loop transmission at angular frequency $1/R_f C_f$ is equal to or greater than unity, this system will be reasonably stable. Using the asymptotic approximation of Figure 5.10, this means that

$$\frac{1}{R_f C_f} \le \frac{KC_f}{\tau\left(C_d + C_f\right)}.$$

Typically the compensation capacitance C_f is much smaller than the diode capacitance C_d, so the stability criteria is satisfied if

$$C_f \ge \sqrt{\frac{\tau C_d}{KR_f}}.$$

The bandwidth of this detector system (for which the transimpedance is approximately equal to R_f) is $1/R_f C_f$, and there is not an arbitrary limit on the size of R_f as before. However, the bandwidth is limited to a fraction of the unity gain frequency of the op-amp by:

$$\omega_B = \frac{1}{R_f C_f} \le \left(\frac{C_f}{C_d + C_f}\right)\frac{K}{\tau},$$

which has a maximum of

$$\omega_{Bmax} = \sqrt{\frac{K}{\tau R_f C_d}}$$

for good stability. It is interesting to note that this is the geometric mean of the unity gain frequency of the op-amp and the bandwidth of a passive detector made by loading the diode with resistor R_f.

While a capacitor may be used to frequency-compensate the transimpedance amplifier as discussed above, it may be difficult to implement in many practical cases. When high bandwidth and large transimpedance are desired, the necessary capacitance can be impracticably small. For example, a system with a 1 MHz bandwidth and feedback resistance of 1 MΩ would require a compensation capacitor of 0.16 pF, which is difficult to achieve reliably with discrete components.

5.2.1.3 Series resistor compensation

Another means of compensating the transimpedance amplifier is shown in Figure 5.11, where resistor R_c is placed in series with the photodiode (which has been modeled by its small-signal capacitance and a current-source as before).

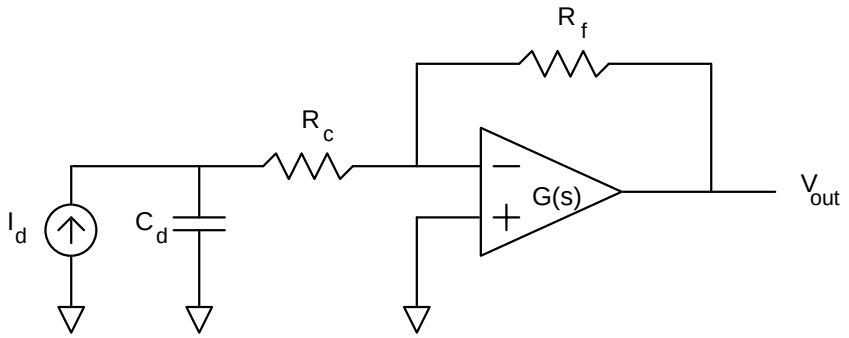

Figure 5.11: Transimpedance amplifier detector with frequency-compensation resistor.

The block diagram of this circuit is shown in Figure 5.12,

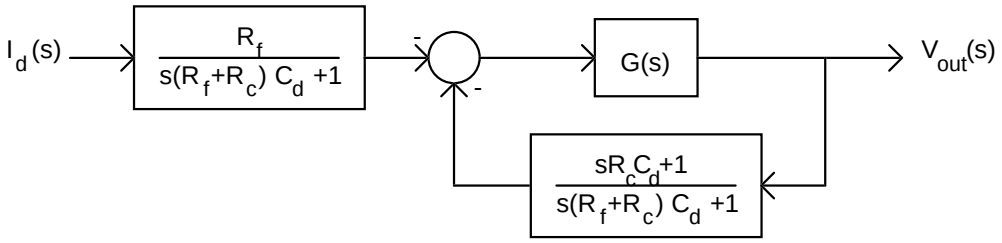

Figure 5.12: Block diagram of the transimpedance amplifier photo-detector circuit with frequency compensation resistor.

and the loop transmission is:

$$L(s) = \frac{K(sR_cC_d + 1)}{(s\tau + 1)(s(R_f + R_c)C_d + 1)}.$$

The Bode magnitude plot of the loop transmission is quite similar to that of Figure 5.10, but the zero is introduced by the compensation resistor R_c as shown in Figure 5.13.

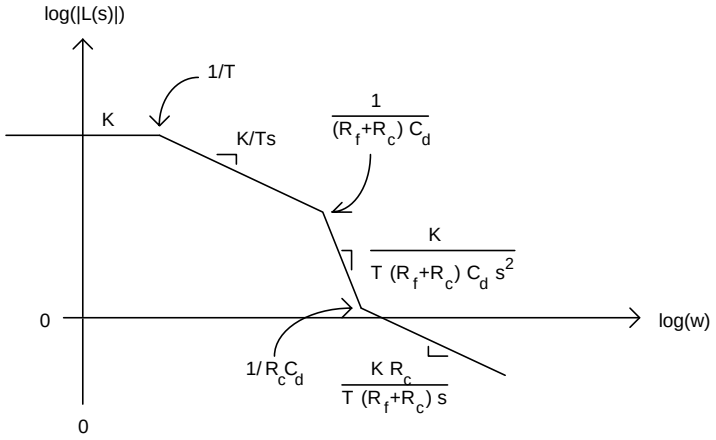

Figure 5.13: Bode magnitude plot of loop transmission of resistor-compensated system.

This system will be reasonably stable if the loop transmission magnitude is greater than or equal to unity at angular frequency $1/R_cC_d$. Approximating from the asymptotes of Figure 5.13, this stability criterion means that:

$$\frac{1}{R_cC_d} \le \frac{KR_c}{\tau(R_f + R_c)}.$$

Given a particular op-amp and a desired transimpedance for the photodetector circuit, the compensation resistor is therefore set by

$$R_c \ge \sqrt{\frac{\tau R_f}{KC_d}},$$

provided that $R_f >> R_c$. Since the bandwidth for which the transimpedance is close to R_f is $1/R_cC_d$, this places an upper bound on it:

$$\omega_{Bmax} = \sqrt{\frac{K}{\tau R_f C_d}}$$

when R_c is set to its minimum value. Note that this is the same as when the system was compensated by a capacitor.

Since the bandwidth of the photodetector circuit is often the primary design consideration, it is useful to know the maximum possible transimpedance since this will yield the most sensitive system. Rearranging terms in the equation for maximum bandwidth gives the maximum transimpedance as a function of bandwidth:

$$R_{f\,\max} = \frac{K}{\tau C_d \omega_B{}^2},$$

for a system compensated by resistance

$$R_c = \frac{1}{C_d \omega_B}.$$

5.2.2 Noise of the transimpedance amplifier photodetector

5.2.2.1 Input-referred current noise of detector circuit

The noise sources associated with the photodiode, operational amplifier, and resistors were added in Figure 5.14 in order to determine the equivalent input current noise of the detector circuit.

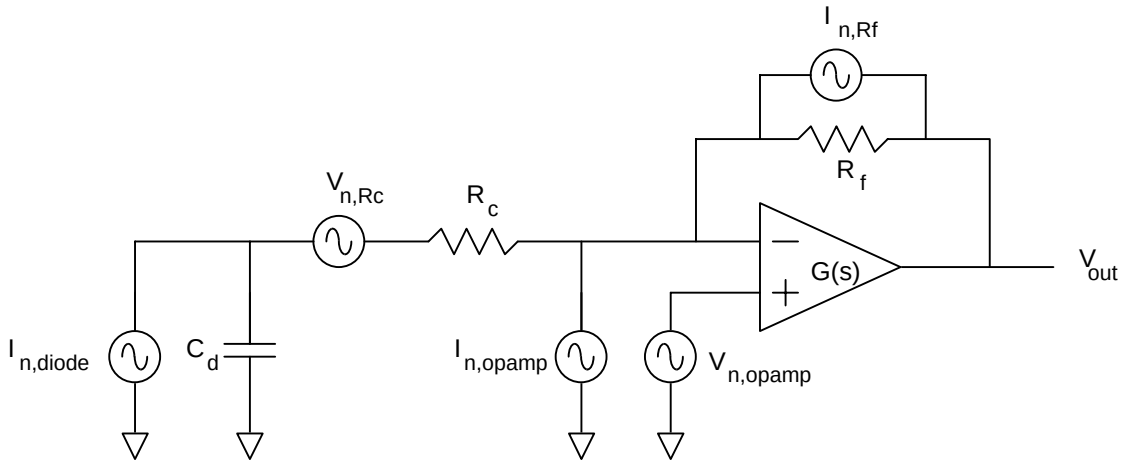

Figure 5.14: Detector circuit with noise sources.

The total equivalent input current noise of the detector circuit is computed by finding the contribution of each noise source independently. Once the equivalent input currents of all the sources are known, their power spectral densities are added, and the square root of the result is the total equivalent input current noise of the detector circuit. The equivalent input current for each noise source in Figure 5.14 can be determined by finding the output voltage associated with each and dividing by the transimpedance. For

each source, a block diagram can be made in the form of Figure 5.15 that relates it to the output voltage.

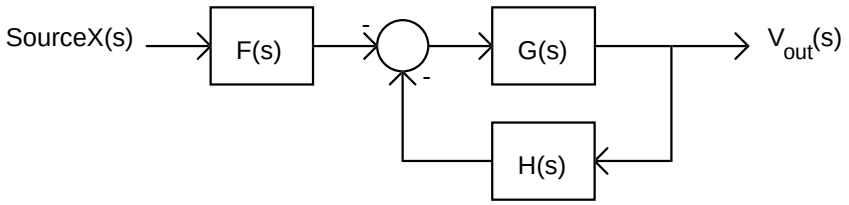

Figure 5.15: General block diagram relating signal and noise sources to the output voltage.

5.2.2.1.1 Technique for referring noise sources to the input

The forward gain $G(s)$ and the feedback $H(s)$ are the same for all cases, and only the input transfer function $F(s)$ changes with the different noise sources. The forward gain and feedback are the same as in Figure 5.12:

$$G(s) = \frac{K}{s\tau + 1}$$

and

$$H(s) = \frac{sR_cC_d + 1}{s(R_f + R_c)C_d + 1}.$$

The transimpedance function of the photodetector circuit can be found from the diagram of Figure 5.15 with the input block

$$F_{I_{diode}}(s) = \frac{R_f}{s(R_f + R_c)C_d + 1}.$$

Multiplying this by the transfer function of the feedback loop yields the transimpedance (inverting) exactly:

$$\frac{V_{out}}{I_{diode}} = -F_{I_{diode}}(s) \cdot \frac{G(s)}{1 + G(s)H(s)},$$

but it is usually sufficient to approximate this within the passband of the photodetector circuit $(\omega \le 1/R_cC_d)$ where $|G(s)H(s)| > 1$ by:

$$\frac{V_{out}}{I_{diode}} \approx -F_{I_{diode}} \cdot \frac{1}{H(s)} = -\frac{R_f}{sR_cC_d + 1}.$$
$$\approx -R_f$$

Similarly, the output voltage due to each noise source is found by substituting the appropriate input block $F_{SourceX}(s)$:

$$V_{outSourceX} = -F_{SourceX}(s) \cdot \frac{G(s)}{1+G(s)H(s)} \cdot (SourceX).$$

Dividing this by the transimpedance yields the equivalent input current for each noise source:

$$I_{eqSourceX} = \frac{V_{outSourceX}}{(V_{out}/I_{diode})} = \frac{F_{SourceX}(s)}{F_{I_{diode}}(s)} \cdot (SourceX).$$

Thus only the input transfer functions associated with each noise source must be determined to compute its contribution to the total equivalent input noise current.

5.2.2.1.2 Equivalent input-referred current noise sources

Clearly, since the current noise of the detector enters the system at the same location as the signal current, its input transfer function is the same, so the “equivalent” input current is exactly the current noise of the detector. The power spectral density of this source adds directly to the total equivalent input current noise power spectral density. The input blocks in the diagrams associated with the current noise of the op-amp and the current noise of the feedback resistor are identical:

$$F_{I_{n,R_f}}(s) = F_{I_{n,opamp}}(s) = \frac{(sR_cC_d+1)R_f}{s(R_f+R_c)C_d+1},$$

so their equivalent input currents are

$$I_{eqI_{n,opamp}} = (sR_cC_d+1) \cdot I_{n,opamp}$$

and

$$I_{eqI_{n,R_f}} = (sR_cC_d+1) \cdot I_{n,R_f}.$$

The noise of the compensation resistor, which is most easily interpreted as the voltage source V_{n,R_c}, enters the system block diagram through

$$F_{V_{n,R_c}}(s) = \frac{sR_fC_d}{s(R_f+R_c)C_d+1},$$

and is equivalent to input current

$$I_{eqV_{n,R_c}} = sC_d \cdot V_{n,R_c}.$$

It is instructive to note that this could have been obtained by finding the Norton equivalent of the voltage source in series with the diode capacitance. Finally, the

equivalent input voltage noise of the op-amp V_{opamp} is simply inverted at the summing junction of the block diagram, meaning

$$F_{V_{n,opamp}}(s) = -1,$$

so the equivalent input current is

$$I_{eqV_{n,opamp}} = -\frac{s(R_f + R_c)C_d + 1}{R_f} \cdot V_{n,opamp}\ .$$

5.2.2.1.3 Total power spectral density of input-referred noise

Squaring the magnitude of the equivalent input currents gives their power spectral density functions,

$$S_{I_{eqSourceX}}(\omega) = \left(I_{eqSourceX}(s)\right) \cdot \left(I_{eqSourceX}(s)\right)^*\Big|_{s=j\omega} = \left|I_{eqSourceX}(j\omega)\right|^2,$$

which can be summed to determine the total equivalent input current noise power spectral density:

$$S_{I_{eqTotal}}(\omega) = S_{I_{n,diode}}(\omega) + \left(\omega^2 R_c{}^2 C_d{}^2 + 1\right) \cdot S_{I_{n,opamp}}(\omega) + \left(\omega^2 R_c{}^2 C_d{}^2 + 1\right) \cdot S_{I_{n,R_f}}(\omega)$$
$$+ \left(\omega^2 C_d{}^2\right) \cdot S_{V_{n,R_c}}(\omega) + \left(\frac{\omega^2 (R_f + R_c)^2 C_d{}^2 + 1}{R_f{}^2}\right) \cdot S_{V_{n,opamp}}(\omega) \quad .$$

The noise from the photodiode is typically dominated by shot noise on the current that flows through it, which is a combination of its reverse leakage current and the optically-induced current resulting from the signal and background illumination. Thus,

$$S_{I_{n,diode}}(\omega) = 2qI_{diode}$$

If metal film resistors are used, the noise of R_f and R_c will be primarily thermal (Johnson), so

$$S_{I_{n,R_f}}(\omega) = \frac{4kT}{R_f},$$

and

$$S_{V_{n,R_c}}(\omega) = 4kTR_c\ .$$

Substituting these noise components into the total equivalent input noise current formula yields:

$$S_{I_{eqTotal}}(\omega) = 2qI_{diode} + \left(\omega^2 {R_c}^2 {C_d}^2 + 1\right) \cdot S_{I_{n,opamp}}(\omega) + \left(\omega^2 {R_c}^2 {C_d}^2 + 1\right) \cdot \frac{4kT}{R_f}$$
$$+ \left(\omega^2 {C_d}^2\right) \cdot 4kTR_c + \left(\frac{\omega^2 \left(R_f + R_c\right)^2 {C_d}^2 + 1}{{R_f}^2} \right) \cdot S_{V_{n,opamp}}(\omega) \quad .$$

5.2.2.1.3.1 Minimum detectable optical power within bandwidth of photodetector circuit

Usually, the output of the detector circuit will be low-pass filtered, and only the noise within its useful signal bandwidth is of concern. Since this bandwidth is $\omega \le 1/R_c C_d$, the power spectral density of the total equivalent input noise current can be approximated by:

$$S_{I_{eqTotal}}(\omega) \approx S_{I_{n,diode}}(\omega) + S_{I_{n,opamp}}(\omega) + S_{I_{n,R_f}}(\omega)$$
$$+ \left(\omega^2 {C_d}^2\right) \cdot S_{V_{n,R_c}}(\omega) + \left(\frac{\omega^2 \left(R_f + R_c\right)^2 {C_d}^2 + 1}{{R_f}^2} \right) \cdot S_{V_{n,opamp}}(\omega) \quad .$$

Substituting the diode and resistor noise components yields:

$$S_{I_{eqTotal}}(\omega) \approx 2qI_{diode} + S_{I_{n,opamp}}(\omega) + \frac{4kT}{R_f}$$
$$+ \left(\omega^2 {C_d}^2\right) \cdot 4kTR_c + \left(\frac{\omega^2 \left(R_f + R_c\right)^2 {C_d}^2 + 1}{{R_f}^2} \right) \cdot S_{V_{n,opamp}}(\omega) \quad .$$

The minimum optical power per unit area that can be detected by the circuit is equal to the equivalent input noise current over the system bandwidth (in Hertz, $\omega_B/2\pi$) divided by the area A_{diode} and the radiant sensitivity γ_{diode} (in Amps/Watt) of the diode:

$$P_{optical,min} = \frac{1}{A_{diode}\gamma_{diode}} \sqrt{\int_0^{\omega_B} \left[\begin{array}{l} 2qI_{diode} + S_{I_{n,opamp}}(\omega) + \frac{4kT}{R_f} + \left(\omega^2 {C_d}^2\right) \cdot 4kTR_c \\ + \left(\frac{\omega^2 \left(R_f + R_c\right)^2 {C_d}^2 + 1}{{R_f}^2} \right) \cdot S_{V_{n,opamp}}(\omega) \end{array} \right] \frac{d\omega}{2\pi}}$$

This is also called the “noise equivalent power” (NEP) of the photodetector circuit. The sensitivity of the detector circuit is maximized by using a large feedback resistor, R_f , and a large area photodiode that has low capacitance C_d .

5.2.2.1.4 Photodiode selection criteria

Since the maximum value of R_f is inversely proportional to C_d for a given photodetector circuit bandwidth, the noise equivalent power suggests that a reasonable figure of merit to compare photodiodes is $A_{diode}\gamma_{diode}/C_d^{\,2}$. A photodiode for which this quantity is large is desirable because it will tend to maximize the signal-to-noise ratio of the photodetector circuit.

5.2.3 Threshold detection of signal pulses

Since a pulse position encoding scheme was chosen for low-power signal transmission, the photodetector circuit must be designed to accurately measure timing of the light pulses. A threshold detector set to trigger on the fast-rising edge of a received light pulse provides a robust yet simple means to determine the relative timing of pulses. The broadband noise and slope of the signal as it crosses threshold determine the error in the time measurement obtained with a threshold detector.

5.2.3.1 Pulse detection timing error

Provided that the slope of the signal (without noise) from the photodetector is relatively constant near threshold, the rms uncertainty in the time measurement will be equal to the rms voltage noise divided by the slope of the rising edge of the pulse as it crosses threshold, $dV/dt\big|_{V_{threshold}}$. The rms voltage noise is calculated over the entire frequency spectrum because the threshold detector is assumed to trigger the instant that the signal crosses its threshold voltage. Thus the shape of the pulse at the photodetector output is critical to the function of the decoder circuit. A fast-rising pulse will have less timing error than a slow-rising pulse for a given rms noise level, but the rms noise usually increases with the bandwidth, and hence speed, of the photodetector circuit. Both the frequency response and total noise of the photodetector must be considered to achieve the lowest rms noise in the pulse time measurement.

5.2.3.1.1 Analysis of a first-order photodetector circuit

Computation of broadband noise at the output of a practical photodetector such as the resistor-compensated circuit of Figure 5.11 is much more amenable to numerical methods than symbolic analysis, so it is useful to consider simpler hypothetical systems to develop intuitive feel for the fundamental design issues. For example, a photodetector circuit whose closed-loop response is dominated by a single pole at

angular frequency ω_p and has transimpedance equal to R_f will have unit impulse response equal to

$$v_{out,impulse} = R_f \omega_p e^{-\omega_p t} u(t),$$

and unit step response equal to

$$v_{out,step} = R_f \left(1 - e^{-\omega_p t}\right) u(t),$$

where $u(t)$ is the unit step function.

Since the pulses of light are usually produced by switching an LED on for a short period of time, it is easiest to find the photodetector response by superimposing two step response functions which represent the onset and offset of the light flash. Thus a pulse of current from the photodiode of amplitude I_p and duration T_f produces the response:

$$\begin{aligned} v_{out,pulse} &= I_p R_f \left(1 - e^{-\omega_p t}\right) u(t) - I_p R_f \left(1 - e^{-\omega_p (t - T_f)}\right) u(t - T_f) \\ &= \begin{cases} I_p R_f \left(1 - e^{-\omega_p t}\right), & 0 < t < T_f \\ I_p R_f \left(e^{\omega_p T_f} - 1\right) e^{-\omega_p t}, & t > T_f \end{cases} \end{aligned},$$

which has a slope versus time of:

$$\begin{aligned} \frac{dv_{out,pulse}}{dt} &= I_p R_f \omega_p e^{-\omega_p t} u(t) - I_p R_f \omega_p e^{-\omega_p (t - T_f)} u(t - T_f) \\ &= \begin{cases} I_p R_f \omega_p e^{-\omega_p t}, & 0 < t < T_f \\ I_p R_f \omega_p \left(1 - e^{\omega_p T_f}\right) e^{-\omega_p t}, & t > T_f \end{cases} \end{aligned}.$$

The output pulse is rising for $0 < t < T_f$, and its slope is maximum near $t = 0$. If the input-referred current noise is "white", or has uniform power spectral density:

$$S_{I_{eq}}(\omega) = {I_{n,eq}}^2$$

where $I_{n,eq}$ is in units of $A/\sqrt{Hz}$, then the power spectral density of the photodetector output voltage is:

$$\begin{aligned} S_{V_{out}}(\omega) &= S_{I_{eq}}(\omega) \cdot \left| \frac{R_f}{(s/\omega_p) + 1} \right|^2 \\ &= \frac{{I_{n,eq}}^2 {R_f}^2}{(\omega/\omega_p)^2 + 1} \end{aligned}.$$

Integration of this power spectral density over the full spectrum (in Hertz) yields the mean-square voltage noise at the output of the photodetector circuit:

$$
\begin{aligned}
V_{\substack{n,out \\ rms}}^{\ 2} &= \int_0^\infty S_{V_{out}}(\omega)df \\
&= \int_0^\infty \frac{I_{n,eq}^{\ 2}R_f^{\ 2}}{(\omega/\omega_p)^2+1}df = I_{n,eq}^{\ 2}R_f^{\ 2}\cdot\int_0^\infty \frac{1}{(2\pi f/\omega_p)^2+1}df \\
&= I_{n,eq}^{\ 2}R_f^{\ 2}\cdot\left[\left(\frac{\omega_p}{2\pi}\right)\cdot\arctan\left(\frac{2\pi f}{\omega_p}\right)\right]\Bigg|_0^\infty \\
&= I_{n,eq}^{\ 2}R_f^{\ 2}\cdot\left(\frac{\omega_p}{4}\right)
\end{aligned}
$$

Accordingly, the rms voltage noise at the output of the photodetector is

$$V_{\substack{n,out \\ rms}} = \frac{I_{n,eq}R_f}{2}\sqrt{\omega_p}\ .$$

It is interesting to note that the single pole low-pass filtering results in about 25% more rms noise than if the noise were perfectly bandlimited at $\omega_p/2\pi$. Dividing the rms voltage noise at the output of the photodetector by the slope of the rising edge of the pulse gives the approximate rms noise in the time of pulse detection:

$$
\begin{aligned}
\Delta T_{\substack{noise \\ rms}} &= \frac{V_{\substack{n,out \\ rms}}}{(dv_{out,pulse}/dt)} \\
&= \left(\frac{I_{n,eq}R_f}{2}\sqrt{\omega_p}\right)\left(\frac{1}{I_pR_f\omega_pe^{-\omega_pt}}\right) \\
&= \frac{I_{n,eq}}{2I_pe^{-\omega_pt}\sqrt{\omega_p}}
\end{aligned}
$$

At first glance, this suggests that the uncertainty in the time at which the pulse is detected would be minimized by using a fast photodetector circuit (large ω_p) and a low detection threshold (so as to trigger at the very beginning of the pulse where its slope is greatest). However, there are other factors that contradict these simple rules. First, the occurrence of spurious threshold crossings due to noise fluctuations must be minimized by setting the threshold higher than the peak output noise level. There will always be some probability that the instantaneous noise voltage will be high enough to cross the threshold, so the threshold must be set high enough that the frequency of spurious crossings is acceptably low compared to the frequency of signal pulses. A treatment of this aspect of simple threshold detection is presented in Clark [29] (pp. 154-159) which

can be used to estimate a reasonable threshold for a particular application. The second failing of the simple conclusions drawn above is that the equivalent input current noise power spectral density of real photodetector circuits generally increases with the bandwidth of the circuit. For example, if the bandwidth of this hypothetical photodetector circuit is inversely proportional to R_f, and the noise is dominated by this resistor, then $I_{n,eq}$ is proportional to $1/\sqrt{R_f}$ which is proportional to $\sqrt{\omega_p}$. In this case the advantage of the fast photodetector circuit is lost. Furthermore, the bandwidth of higher performance photodetector circuits such as the second-order circuit of Figure 5.14 can be inversely proportional to the *square root* of R_f, so that $I_{n,eq} \propto \omega_p$ and there is a penalty for increased bandwidth. Also, the noise power spectral density often *increases* with frequency as it is dominated by other noise sources, as was revealed in the analysis of the circuit of Figure 5.14.

5.2.3.1.2 Analysis of a critically-damped second-order photodetector circuit

Another hypothetical photodetector circuit that is instructive to analyze symbolically is a second-order system whose closed-loop response is critically damped, with two poles at angular frequency ω_p and transimpedance R_f. This has considerable practical significance because the circuits of Figure 5.8 and Figure 5.11 can be designed to have this closed-loop response. Unit impulse response of this system would be

$$v_{out,impulse} = R_f \omega_p{}^2 t e^{-\omega_p t} u(t),$$

and its unit step response would be

$$v_{out,step} = R_f \left(1 - e^{-\omega_p t}\left(1 + \omega_p t\right)\right) u(t).$$

A pulse of current from the photodiode of amplitude I_p and duration T_f produces the response:

$$\begin{aligned} v_{out,pulse} &= I_p R_f \left(1 - e^{-\omega_p t}\left(1 + \omega_p t\right)\right) u(t) - I_p R_f \left(1 - e^{-\omega_p (t - T_f)}\left(1 + \omega_p (t - T_f)\right)\right) u(t - T_f) \\ &= \begin{cases} I_p R_f \left(1 - e^{-\omega_p t}\left(1 + \omega_p t\right)\right), & 0 < t < T_f \\ I_p R_f \left(\left(1 + \omega_p t\right)\left(e^{\omega_p T_f} - 1\right) - \omega_p T_f e^{\omega_p T_f}\right) e^{-\omega_p t}, & t > T_f \end{cases} \end{aligned},$$

which has a slope versus time of:

$$\frac{dv_{out,pulse}}{dt} = I_p R_f \omega_p{}^2 t e^{-\omega_p t} u(t) - I_p R_f \omega_p{}^2 (t - T_f) e^{-\omega_p (t - T_f)} u(t - T_f)$$
$$= \begin{cases} I_p R_f \omega_p{}^2 t e^{-\omega_p t}, & 0 < t < T_f \\ -I_p R_f \omega_p{}^2 \left(t\left(e^{\omega_p T_f} - 1\right) - T_f e^{\omega_p T_f}\right) e^{-\omega_p t}, & t > T_f \end{cases}.$$

The output pulse is rising for

$$0 < t < \left(\frac{e^{\omega_p T_f}}{e^{\omega_p T_f} - 1}\right) T_f ,$$

and its slope is maximum at $t = 1/\omega_p$:

$$\left.\frac{dv_{out,pulse}}{dt}\right|_{\max} = I_p R_f \omega_p e^{-1}$$
$$\approx 0.368 \cdot I_p R_f \omega_p .$$

If the input-referred current noise has both a “white” spectral component that is independent of frequency and a “blue” spectral component that increases with frequency (as seen in the analysis of the circuit of Figure 5.14):

$$S_{I_{eq}}(\omega) = I_{\substack{n,eq \\ white}}{}^2 + \omega^2 I_{\substack{n,eq \\ blue}}{}^2$$

where $I_{\substack{n,eq \\ white}}$ is in units of $A/\sqrt{Hz}$ and $I_{\substack{n,eq \\ blue}}$ is in units of $A \cdot s/\sqrt{Hz}$, then the power spectral density of the photodetector output voltage is:

$$S_{V_{out}}(\omega) = S_{I_{eq}}(\omega) \cdot \left| \frac{R_f}{\left((s/\omega_p) + 1\right)^2} \right|^2$$
$$= \frac{I_{\substack{n,eq \\ white}}{}^2 R_f{}^2}{\left((\omega/\omega_p)^2 + 1\right)^2} + \frac{\omega^2 I_{\substack{n,eq \\ blue}}{}^2 R_f{}^2}{\left((\omega/\omega_p)^2 + 1\right)^2} .$$

Integration of this power spectral density over the full spectrum (in Hertz) yields the mean-square voltage noise at the output of the photodetector circuit:

$$V_{\substack{n,out\\rms}}^{\ 2} = \int_0^\infty S_{V_{out}}(\omega)df$$

$$= \int_0^\infty \frac{I_{\substack{n,eq\\white}}^{\ 2} R_f^{\ 2}}{\left((\omega/\omega_p)^2+1\right)^2} + \frac{\omega^2 I_{\substack{n,eq\\blue}}^{\ 2} R_f^{\ 2}}{\left((\omega/\omega_p)^2+1\right)^2} df \quad .$$

$$= \underbrace{I_{\substack{n,eq\\white}}^{\ 2} R_f^{\ 2} \cdot \int_0^\infty \frac{1}{\left((2\pi f/\omega_p)^2+1\right)^2} df}_{V_{\substack{n,out\\white,rms}}^{\ 2}} + \underbrace{I_{\substack{n,eq\\blue}}^{\ 2} R_f^{\ 2} \cdot \int_0^\infty \frac{(2\pi f)^2}{\left((2\pi f/\omega_p)^2+1\right)^2} df}_{V_{\substack{n,out\\blue,rms}}^{\ 2}}$$

These integrals are solved by substituting $\tan\theta = (2\pi f/\omega_p)$:

$$V_{\substack{n,out\\white,rms}}^{\ 2} = I_{\substack{n,eq\\white}}^{\ 2} R_f^{\ 2} \cdot \int_0^{\pi/2} \frac{1}{\left(\tan^2\theta+1\right)^2} \underbrace{\left(\frac{\omega_p}{2\pi}\sec^2\theta d\theta\right)}_{df}$$

$$= I_{\substack{n,eq\\white}}^{\ 2} R_f^{\ 2} \left(\frac{\omega_p}{2\pi}\right) \cdot \int_0^{\pi/2} \frac{\sec^2\theta}{\left(\sec^2\theta\right)^2} d\theta = I_{\substack{n,eq\\white}}^{\ 2} R_f^{\ 2} \left(\frac{\omega_p}{2\pi}\right) \cdot \int_0^{\pi/2} \cos^2\theta d\theta \quad ,$$

$$= I_{\substack{n,eq\\white}}^{\ 2} R_f^{\ 2} \left(\frac{\omega_p}{2\pi}\right) \cdot \left[\frac{1}{2}\theta + \frac{1}{4}\sin 2\theta\right]_0^{\pi/2} = I_{\substack{n,eq\\white}}^{\ 2} R_f^{\ 2} \left(\frac{\omega_p}{2\pi}\right) \cdot \left[\frac{\pi}{4}\right]$$

$$= I_{\substack{n,eq\\white}}^{\ 2} R_f^{\ 2} \left(\frac{\omega_p}{8}\right)$$

and

$$V_{\substack{n,out\\blue,rms}}^{\ 2} = I_{\substack{n,eq\\blue}}^{\ 2} R_f^{\ 2} \cdot \int_0^{\pi/2} \frac{\omega_p^{\ 2}\tan^2\theta}{\left(\tan^2\theta+1\right)^2} \underbrace{\left(\frac{\omega_p}{2\pi}\sec^2\theta d\theta\right)}_{df}$$

$$= I_{\substack{n,eq\\blue}}^{\ 2} R_f^{\ 2} \left(\frac{\omega_p^{\ 3}}{2\pi}\right) \cdot \int_0^{\pi/2} \frac{\tan^2\theta \cdot \sec^2\theta}{\left(\sec^2\theta\right)^2} d\theta = I_{\substack{n,eq\\blue}}^{\ 2} R_f^{\ 2} \left(\frac{\omega_p^{\ 3}}{2\pi}\right) \cdot \int_0^{\pi/2} \sin^2\theta d\theta \quad .$$

$$= I_{\substack{n,eq\\blue}}^{\ 2} R_f^{\ 2} \left(\frac{\omega_p^{\ 3}}{2\pi}\right) \cdot \left[\frac{1}{2}\theta - \frac{1}{4}\sin 2\theta\right]_0^{\pi/2} = I_{\substack{n,eq\\blue}}^{\ 2} R_f^{\ 2} \left(\frac{\omega_p^{\ 3}}{2\pi}\right) \cdot \left[\frac{\pi}{4}\right]$$

$$= I_{\substack{n,eq\\blue}}^{\ 2} R_f^{\ 2} \left(\frac{\omega_p^{\ 3}}{8}\right)$$

Accordingly, the rms voltage noise at the output of the photodetector is

$$V_{\substack{n,out\\rms}} = \sqrt{V_{\substack{n,out\\white,rms}}^{\ 2} + V_{\substack{n,out\\blue,rms}}^{\ 2}} = \frac{R_f}{2\sqrt{2}} \sqrt{I_{\substack{n,eq\\white}}^{\ 2}\omega_p + I_{\substack{n,eq\\blue}}^{\ 2}\omega_p^{\ 3}} \quad .$$

The second-order low-pass filtering results in about 11% less rms white noise and 53% more rms "blue" noise than perfect bandlimiting at $\omega_p/2\pi$. Dividing the rms voltage noise at the output of the photodetector by the slope of the rising edge of the pulse gives the approximate rms noise in the time of pulse detection. Assuming $T_f \geq 1/\omega_p$ and that the threshold is set so detection is made near the maximum slope (at $t = 1/\omega_p$):

$$\begin{aligned}\Delta T_{\substack{noise \\ rms}} &= \frac{V_{\substack{n,out \\ rms}}}{\left(dv_{out,pulse}/dt\right)} \\ &= \left(\frac{R_f}{2\sqrt{2}}\sqrt{I_{\substack{n,eq \\ white}}{}^2\omega_p + I_{\substack{n,eq \\ blue}}{}^2\omega_p{}^3}\right)\left(\frac{1}{I_p R_f \omega_p{}^2 t e^{-\omega_p t}}\right). \\ &= \frac{\sqrt{I_{\substack{n,eq \\ white}}{}^2\omega_p + I_{\substack{n,eq \\ blue}}{}^2\omega_p{}^3}}{2\sqrt{2}I_p\omega_p{}^2 t e^{-\omega_p t}}\end{aligned}$$

The pulse detection timing error is minimized by setting the threshold at the point of maximum rising slope:

$$\begin{aligned}v_{threshold,optimal} &= \left(1-2e^{-1}\right)I_p R_f \\ &\approx 0.26 \cdot I_p R_f\end{aligned}$$

and has the value:

$$\begin{aligned}\Delta T_{\substack{noise \\ rms,\min}} &= \frac{\sqrt{I_{\substack{n,eq \\ white}}{}^2\omega_p + I_{\substack{n,eq \\ blue}}{}^2\omega_p{}^3}}{2\sqrt{2}I_p\omega_p e^{-1}} \\ &\approx \frac{0.961}{I_p}\cdot\sqrt{\frac{I_{\substack{n,eq \\ white}}{}^2}{\omega_p} + I_{\substack{n,eq \\ blue}}{}^2\omega_p}\end{aligned}.$$

5.2.3.1.3 Analysis of a second-order photodetector circuit with high-pass filter

Since the threshold pulse detector triggers on the rapidly rising edge of the light pulse signal, it seems reasonable that the low frequency content of the signal is not as important as the higher-frequency content. By putting a low-frequency zero in the photodetector system response, low-frequency gain would be reduced. This has the benefit of decreasing low frequency noise, possibly reducing the timing measurement error. Also, it can eliminate any DC offset resulting from leakage and background light generated currents through the photodiode. A simple implementation of the system zero

is to place a high-pass RC filter on the output of the photodetector op-amp, as illustrated in Figure 5.16.

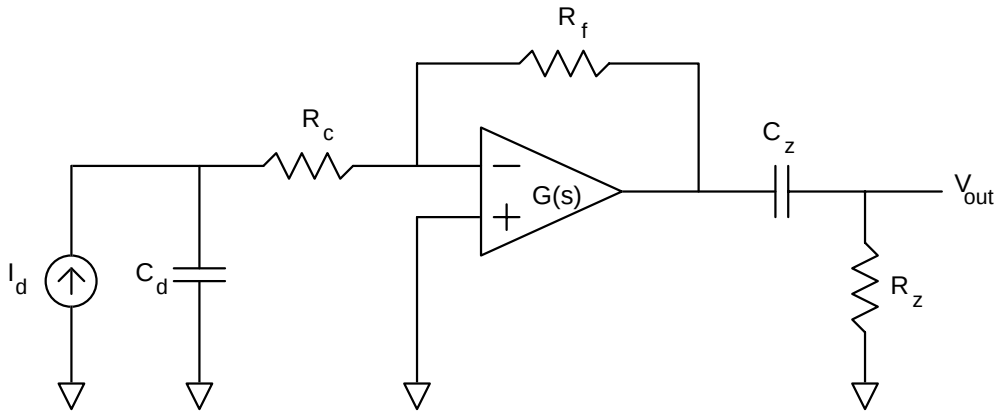

Figure 5.16: Photodetector circuit with high-pass RC filter.

This filter will add a transfer function zero at zero frequency, and a pole at $1/R_zC_z$. To be certain that this pole does not introduce a slow-settling component to the pulse response of the system, it should occur above the system bandwidth. In order to avoid amplifying noise at frequencies above the system bandwidth, it is convenient to make the pole equal to the system bandwidth. For the hypothetical critically-damped two pole closed loop system previously studied, this will yield a complete transfer function of:

$$\frac{V_{out}}{I_{diode}} = \left(\frac{R_f}{\left((s/\omega_p)+1\right)^2} \right) \left(\frac{sR_zC_z}{sR_zC_z+1} \right)$$
$$= \frac{R_f (s/\omega_p)}{\left((s/\omega_p)+1\right)^3}$$

It is easiest to find the unit step response of this system first, then differentiate to obtain the unit impulse response. The Laplace transform of the step response is:

$$V_{out,step}(s) = \frac{R_f (1/\omega_p)}{\left((s/\omega_p)+1\right)^3}.$$

Recognizing that the Laplace transform of the unit impulse response of the two-pole system without the high-pass filter is

$$V_{\substack{out,impulse \\ two-pole \\ system}}(s) = \frac{R_f}{\left((s/\omega_p)+1\right)^2},$$

and that its derivative with respect to s is:

$$\frac{d}{ds}V_{\substack{out,impulse\\two-pole\\system}}(s)=\frac{-2R_f\left(1/\omega_p\right)}{\left(\left(s/\omega_p\right)+1\right)^3}$$
$$=-2\cdot V_{\substack{out,step\\high-pass\\system}}(s),$$

the following Laplace operational transform property may be applied to advantage:

$$-t\cdot f(t)\overset{L}{\Leftrightarrow}\frac{d}{ds}F(s).$$

Thus,

$$V_{\substack{out,step\\high-pass\\system}}(s)=-\frac{1}{2}\left(\frac{d}{ds}V_{\substack{out,impulse\\two-pole\\system}}(s)\right),$$

and

$$v_{\substack{out,step\\high-pass\\system}}(t)=-\frac{1}{2}\left(-t\cdot v_{\substack{out,impulse\\two-pole\\system}}(t)\right).$$

Recalling that the impulse response of the two-pole system without the high-pass filter was

$$v_{\substack{out,impulse\\two-pole\\system}}=R_f{\omega_p}^2te^{-\omega_p t}u(t),$$

the step response of the high-pass filtered two-pole system is:

$$v_{\substack{out,step\\high-pass\\system}}=\frac{1}{2}R_f{\omega_p}^2t^2e^{-\omega_p t}u(t).$$

Taking the time derivative of the unit step response yields the impulse response:

$$v_{\substack{out,impulse\\high-pass\\system}}=\frac{1}{2}R_f{\omega_p}^2\left(2-\omega_p t\right)te^{-\omega_p t}u(t).$$

A pulse of current from the photodiode of amplitude I_p and duration T_f produces the response:

$$v_{out,pulse} = \frac{1}{2} I_p R_f \omega_p{}^2 t^2 e^{-\omega_p t} u(t) - \frac{1}{2} I_p R_f \omega_p{}^2 (t - T_f)^2 e^{-\omega_p (t - T_f)} u(t - T_f)$$

$$= \begin{cases} \frac{1}{2} I_p R_f \omega_p{}^2 t^2 e^{-\omega_p t}, & 0 < t < T_f \\ \frac{1}{2} I_p R_f \omega_p{}^2 \left(t^2 - (t - T_f)^2 e^{\omega_p T_f} \right) e^{-\omega_p t}, & t > T_f \end{cases},$$

which has a slope versus time of:

$$\frac{dv_{out,pulse}}{dt} = \frac{1}{2} I_p R_f \omega_p{}^2 (2 - \omega_p t) t e^{-\omega_p t} u(t) - \frac{1}{2} I_p R_f \omega_p{}^2 \left(2 - \omega_p (t - T_f)\right)(t - T_f) e^{-\omega_p (t - T_f)} u(t - T_f)$$

$$= \begin{cases} \frac{1}{2} I_p R_f \omega_p{}^2 (2 - \omega_p t) t e^{-\omega_p t}, & 0 < t < T_f \\ \frac{1}{2} I_p R_f \omega_p{}^2 \left(2t - \omega_p t^2 - \left(2t - 2T_f - \omega_p (t - T_f)^2 e^{\omega_p T_f}\right)\right) e^{-\omega_p t}, & t > T_f \end{cases}$$

The output pulse is rising (at the onset of the light pulse) for $t < 2/\omega_p$ provided that $T_f > 2/\omega_p$, and its slope is maximum at $t = (2 - \sqrt{2})/\omega_p \approx 0.586/\omega_p$:

$$\left.\frac{dv_{out,pulse}}{dt}\right|_{\max} = \frac{1}{2} I_p R_f \omega_p{}^2 \left(2 - \omega_p \left(\frac{2 - \sqrt{2}}{\omega_p}\right)\right)\left(\frac{2 - \sqrt{2}}{\omega_p}\right) e^{-\omega_p \left(\frac{2 - \sqrt{2}}{\omega_p}\right)}$$

$$\approx 0.231 \cdot I_p R_f \omega_p .$$

Again, if the input-referred current noise is modeled by a white component and a blue component:

$$S_{I_{eq}}(\omega) = \underset{white}{I_{n,eq}{}^2} + \omega^2 \underset{blue}{I_{n,eq}{}^2}$$

then the power spectral density of the photodetector output voltage is:

$$S_{V_{out}}(\omega) = S_{I_{eq}}(\omega) \cdot \left| \frac{R_f (s/\omega_p)}{((s/\omega_p) + 1)^3} \right|^2$$

$$= \frac{\underset{white}{I_{n,eq}{}^2} R_f{}^2 (\omega/\omega_p)^2}{((\omega/\omega_p)^2 + 1)^3} + \frac{\omega^2 \underset{blue}{I_{n,eq}{}^2} R_f{}^2 (\omega/\omega_p)^2}{((\omega/\omega_p)^2 + 1)^3} .$$

Integration of this power spectral density over the full spectrum (in Hertz) yields the mean-square voltage noise at the output of the photodetector circuit:

$$V_{\substack{n,out\\rms}}^{\ 2} = \int_0^\infty S_{V_{out}}(\omega)df$$

$$= \int_0^\infty \frac{I_{\substack{n,eq\\white}}^{\ 2} R_f^{\ 2}(\omega/\omega_p)^2}{\left((\omega/\omega_p)^2+1\right)^3} + \frac{\omega^2 I_{\substack{n,eq\\blue}}^{\ 2} R_f^{\ 2}(\omega/\omega_p)^2}{\left((\omega/\omega_p)^2+1\right)^3} df \quad .$$

$$= \underbrace{I_{\substack{n,eq\\white}}^{\ 2} R_f^{\ 2} \cdot \int_0^\infty \frac{(2\pi f/\omega_p)^2}{\left((2\pi f/\omega_p)^2+1\right)^3} df}_{V_{\substack{n,out\\white,rms}}^{\ 2}} + \underbrace{I_{\substack{n,eq\\blue}}^{\ 2} R_f^{\ 2} \cdot \int_0^\infty \frac{(2\pi f)^2(2\pi f/\omega_p)^2}{\left((2\pi f/\omega_p)^2+1\right)^3} df}_{V_{\substack{n,out\\blue,rms}}^{\ 2}}$$

These integrals are solved by substituting $\tan\theta = (2\pi f/\omega_p)$:

$$V_{\substack{n,out\\white,rms}}^{\ 2} = I_{\substack{n,eq\\white}}^{\ 2} R_f^{\ 2} \cdot \int_0^{\pi/2} \frac{\tan^2\theta}{\left(\tan^2\theta+1\right)^3} \underbrace{\left(\frac{\omega_p}{2\pi}\sec^2\theta d\theta\right)}_{df}$$

$$= I_{\substack{n,eq\\white}}^{\ 2} R_f^{\ 2} \left(\frac{\omega_p}{2\pi}\right) \cdot \int_0^{\pi/2} \frac{\tan^2\theta\sec^2\theta}{\left(\sec^2\theta\right)^3} d\theta = I_{\substack{n,eq\\white}}^{\ 2} R_f^{\ 2} \left(\frac{\omega_p}{2\pi}\right) \cdot \int_0^{\pi/2} \sin^2\theta\cos^2\theta d\theta \quad ,$$

$$= I_{\substack{n,eq\\white}}^{\ 2} R_f^{\ 2} \left(\frac{\omega_p}{2\pi}\right) \cdot \left[\frac{1}{2}\theta + \frac{1}{4}\sin 2\theta - \frac{1}{4}\cos^3\theta\sin\theta - \frac{3}{8}\cos\theta\sin\theta - \frac{3}{8}\theta\right]_0^{\pi/2}$$

$$= I_{\substack{n,eq\\white}}^{\ 2} R_f^{\ 2} \left(\frac{\omega_p}{32}\right)$$

and

$$V_{\substack{n,out\\blue,rms}}^{\ 2} = I_{\substack{n,eq\\blue}}^{\ 2} R_f^{\ 2} \cdot \int_0^{\pi/2} \frac{\omega_p^{\ 2}\tan^4\theta}{\left(\tan^2\theta+1\right)^3} \underbrace{\left(\frac{\omega_p}{2\pi}\sec^2\theta d\theta\right)}_{df}$$

$$= I_{\substack{n,eq\\blue}}^{\ 2} R_f^{\ 2} \left(\frac{\omega_p^{\ 3}}{2\pi}\right) \cdot \int_0^{\pi/2} \frac{\tan^4\theta\sec^2\theta}{\left(\sec^2\theta\right)^3} d\theta = I_{\substack{n,eq\\blue}}^{\ 2} R_f^{\ 2} \left(\frac{\omega_p^{\ 3}}{2\pi}\right) \cdot \int_0^{\pi/2} \sin^4\theta d\theta \quad .$$

$$= I_{\substack{n,eq\\blue}}^{\ 2} R_f^{\ 2} \left(\frac{\omega_p^{\ 3}}{2\pi}\right) \cdot \left[-\frac{1}{4}\sin^3\theta\cos\theta - \frac{3}{8}\sin\theta\cos\theta + \frac{3}{8}\theta\right]_0^{\pi/2}$$

$$= I_{\substack{n,eq\\blue}}^{\ 2} R_f^{\ 2} \left(\frac{3\omega_p^{\ 3}}{32}\right)$$

Accordingly, the rms voltage noise at the output of the photodetector is

$$V_{\substack{n,out\\rms}} = \sqrt{V_{\substack{n,out\\white,rms}}^{\ 2} + V_{\substack{n,out\\blue,rms}}^{\ 2}} = \frac{R_f}{4\sqrt{2}} \sqrt{I_{\substack{n,eq\\white}}^{\ 2}\omega_p + 3I_{\substack{n,eq\\blue}}^{\ 2}\omega_p^{\ 3}} \quad .$$

The addition of high-pass filtering to the second-order system results in about 56% less rms white noise and 33% more rms blue noise than perfect bandlimiting at $\omega_p/2\pi$. Dividing the rms voltage noise at the output of the photodetector by the slope of the rising edge of the pulse gives the approximate rms noise in the time of pulse detection. Assuming $T_f > \left(2-\sqrt{2}\right)/\omega_p \approx 0.586/\omega_p$ and that the threshold is set so detection is made near the maximum slope ($t = \left(2-\sqrt{2}\right)/\omega_p$), the time measurement noise is:

$$\begin{aligned}\Delta T_{\substack{noise\\rms}} &= \frac{V_{\substack{n,out\\rms}}}{\left(dv_{out,pulse}/dt\right)} \\ &= \left(\frac{R_f}{4\sqrt{2}}\sqrt{I_{\substack{n,eq\\white}}{}^2\omega_p + 3I_{\substack{n,eq\\blue}}{}^2\omega_p{}^3}\right)\left(\frac{1}{\frac{1}{2}I_p R_f \omega_p{}^2\left(2-\omega_p t\right)te^{-\omega_p t}}\right). \\ &= \frac{\sqrt{I_{\substack{n,eq\\white}}{}^2\omega_p + 3I_{\substack{n,eq\\blue}}{}^2\omega_p{}^3}}{2\sqrt{2}I_p\omega_p{}^2\left(2-\omega_p t\right)te^{-\omega_p t}}\end{aligned}$$

This pulse detection timing error is minimized by setting the threshold at the point of maximum rising slope:

$$\begin{aligned}v_{threshold,optimal} &= \frac{1}{2}\left(2-\sqrt{2}\right)^2 e^{-\left(2-\sqrt{2}\right)}I_p R_f \\ &\approx 0.096\cdot I_p R_f\end{aligned}$$

and has the value:

$$\begin{aligned}\Delta T_{\substack{noise\\rms,\min}} &= \frac{\sqrt{I_{\substack{n,eq\\white}}{}^2\omega_p + 3I_{\substack{n,eq\\blue}}{}^2\omega_p{}^3}}{2\sqrt{2}I_p\omega_p\left(\sqrt{2}\right)\left(2-\sqrt{2}\right)e^{-2+\sqrt{2}}} \\ &\approx \frac{0.767}{I_p}\cdot\sqrt{\frac{I_{\substack{n,eq\\white}}{}^2}{\omega_p} + 3I_{\substack{n,eq\\blue}}{}^2\omega_p}\end{aligned}.$$

Thus the high-pass filtering yields a 20% decrease in the rms error due to white noise and 38% increase in the rms error due to blue noise in the pulse time measurement by threshold detection for the two-pole photodetector system. If the rms noise is dominated by the white component, then the high-pass filter improves the pulse time detection. But if the rms noise is dominated by the blue component, then the high-pass filter does not

improve pulse detection performance. However, the elimination of the DC offset at the output of the photodetector circuit is a significant practical advantage of the high-pass filtered system for threshold detection. For this reason the photodetector circuit of Figure 5.16 was used in this research.

5.2.3.2 False pulse detection

In addition to error in the time that a pulse crosses threshold, noise on the photodetector output can cause purely random threshold crossings not associated with light pulses. The frequency of these spurious threshold crossings must be considered in comparison to the frequency of actual light pulses. The expected number of positive threshold crossings per unit time is (adapted from Clark [29]):

$$\overline{N}_{\uparrow V_{th}} = \left(\frac{\int_0^\infty f^2 S_{V_{out}}(f)\,df}{{V_{\substack{n,out \\ rms}}}^2} \right)^{\frac{1}{2}} e^{-V_{th}^2 / 2{V_{\substack{n,out \\ rms}}}^2},$$

where V_{th} is the threshold voltage. For the case of the high-pass filtered critically-damped second-order photodetector circuit, the only part of this expression that remains to be evaluated is the integral:

$$\begin{aligned}\int_0^\infty f^2 S_{V_{out}}(f)\,df &= \int_0^\infty \frac{f^2 {I_{\substack{n,eq \\ white}}}^2 {R_f}^2 (2\pi f/\omega_p)^2}{\left((2\pi f/\omega_p)^2+1\right)^3} + \frac{f^2 (2\pi f)^2 {I_{\substack{n,eq \\ blue}}}^2 {R_f}^2 (2\pi f/\omega_p)^2}{\left((2\pi f/\omega_p)^2+1\right)^3} df \\ &= {I_{\substack{n,eq \\ white}}}^2 {R_f}^2 \cdot \int_0^\infty \frac{f^2 (2\pi f/\omega_p)^2}{\left((2\pi f/\omega_p)^2+1\right)^3} df + {I_{\substack{n,eq \\ blue}}}^2 {R_f}^2 \cdot \int_0^\infty \frac{f^2 (2\pi f)^2 (2\pi f/\omega_p)^2}{\left((2\pi f/\omega_p)^2+1\right)^3} df\end{aligned}.$$

The first term in the sum has the same form as the integral for the mean-square blue noise of this circuit, so by inspection it is simply:

$$\begin{aligned}{I_{\substack{n,eq \\ white}}}^2 {R_f}^2 \cdot \int_0^\infty \frac{f^2 (2\pi f/\omega_p)^2}{\left((2\pi f/\omega_p)^2+1\right)^3} df &= \left(\frac{1}{2\pi}\right)^2 {I_{\substack{n,eq \\ white}}}^2 {R_f}^2 \left(\frac{3{\omega_p}^3}{32}\right) \\ &= {I_{\substack{n,eq \\ white}}}^2 {R_f}^2 \left(\frac{3{\omega_p}^3}{128\pi^2}\right)\end{aligned}.$$

The second term is solved by substituting $\tan\theta = (2\pi f/\omega_p)$:

$$I_{\substack{n,eq\\blue}}^{\ 2} R_f^{\ 2} \cdot \int_0^{\infty} \frac{f^2 (2\pi f)^2 \left(2\pi f/\omega_p\right)^2}{\left(\left(2\pi f/\omega_p\right)^2+1\right)^3} df = I_{\substack{n,eq\\blue}}^{\ 2} R_f^{\ 2} \cdot \int_0^{\pi/2} \frac{\left(\frac{\omega_p^{\ 4}}{4\pi^2}\right)\tan^6\theta}{\left(\tan^2\theta+1\right)^3} \underbrace{\left(\frac{\omega_p}{2\pi}\sec^2\theta d\theta\right)}_{df}$$

$$= I_{\substack{n,eq\\blue}}^{\ 2} R_f^{\ 2} \left(\frac{\omega_p^{\ 5}}{8\pi^3}\right) \cdot \int_0^{\pi/2} \frac{\sin^6\theta}{\cos^2\theta} d\theta$$

$$= I_{\substack{n,eq\\blue}}^{\ 2} R_f^{\ 2} \left(\frac{\omega_p^{\ 5}}{8\pi^3}\right) \cdot \int_0^{\pi/2} \frac{1-3\cos^2\theta+3\cos^4\theta-\cos^6\theta}{\cos^2\theta} d\theta$$

$$= I_{\substack{n,eq\\blue}}^{\ 2} R_f^{\ 2} \left(\frac{\omega_p^{\ 5}}{8\pi^3}\right) \cdot \int_0^{\pi/2} \left(\sec^2\theta-3+3\cos^2\theta-\cos^4\theta\right) d\theta$$

$$= I_{\substack{n,eq\\blue}}^{\ 2} R_f^{\ 2} \left(\frac{\omega_p^{\ 5}}{8\pi^3}\right) \cdot \left[\begin{matrix}\tan\theta-3\theta+\frac{3}{2}\theta+\frac{3}{4}\sin 2\theta-\frac{3}{8}\theta\\ -\frac{1}{4}\cos^3\theta\sin\theta-\frac{3}{8}\cos\theta\sin\theta\end{matrix}\right]_0^{\pi/2}.$$

This integral has an infinite result, which is misleading because the photodetector model only included one zero and three poles:

$$\frac{V_{out}}{I_{diode}} = \frac{R_f\left(s/\omega_p\right)}{\left(\left(s/\omega_p\right)+1\right)^3}.$$

Squaring the magnitude of the transfer function, and multiplying it by f^2 and a noise power spectral density that is proportional to f^2 yields a function that is constant at high frequencies. Clearly, when this is integrated over the infinite frequency spectrum, the result is infinite. However, in any real physical system there are extra poles at high frequencies that are usually neglected. In fact, most op-amps have a second pole in their transfer function near their unity gain frequency, and many more at higher frequencies. If we add just the pole near the unity gain frequency of the op-amp:

$$\frac{V_{out}}{I_{diode}} = \frac{R_f\left(s/\omega_p\right)}{\left(\left(s/\omega_p\right)+1\right)^3\left(\left(s/\omega_{pu}\right)+1\right)},$$

the integral above will converge. Unfortunately, the trigonometric substitution does not result in a tidy analytical solution to the integral. A conservative estimate of the integral can be made by breaking it into two segments separated by the high-frequency pole. For frequencies below the pole, the integral will neglect its effect, and above the pole the transfer function will be approximated by the net number of poles:

$$I_{\substack{n,eq\\blue}}{}^2 R_f{}^2 \cdot \int_0^{\infty} \frac{f^2 (2\pi f)^2 (2\pi f/\omega_p)^2}{\left((2\pi f/\omega_p)^2+1\right)^3 \left((2\pi f/\omega_{pu})^2+1\right)} df \approx I_{\substack{n,eq\\blue}}{}^2 R_f{}^2 \cdot \int_0^{\omega_{pu}/2\pi} \frac{f^2 (2\pi f)^2 (2\pi f/\omega_p)^2}{\left((2\pi f/\omega_p)^2+1\right)^3} df$$
$$+ I_{\substack{n,eq\\blue}}{}^2 R_f{}^2 \cdot \int_{\omega_{pu}/2\pi}^{\infty} \frac{f^2 (2\pi f)^2}{(2\pi f/\omega_p)^4 (2\pi f/\omega_{pu})^2} df$$

The first segment has already been solved by trigonometric substitution. Changing the limits of integration, the first segment has the value:

$$I_{\substack{n,eq\\blue}}{}^2 R_f{}^2 \cdot \int_0^{\frac{\omega_{pu}}{2\pi}} \frac{f^2 (2\pi f)^2 (2\pi f/\omega_p)^2}{\left((2\pi f/\omega_p)^2+1\right)^3} df = I_{\substack{n,eq\\blue}}{}^2 R_f{}^2 \left(\frac{\omega_p{}^5}{8\pi^3}\right) \cdot \left[\begin{array}{l} \tan\theta - \frac{15}{8}\theta \\ -\frac{1}{4}\cos^3\theta \sin\theta \\ +\frac{9}{8}\cos\theta \sin\theta \end{array}\right]_0^{\arctan\left(\frac{\omega_{pu}}{\omega_p}\right)}$$
$$= I_{\substack{n,eq\\blue}}{}^2 R_f{}^2 \left(\frac{\omega_p{}^5}{8\pi^3}\right) \cdot \left[\begin{array}{l} \frac{\omega_{pu}}{\omega_p} - \frac{15}{8}\arctan\left(\frac{\omega_{pu}}{\omega_p}\right) \\ -\frac{(\omega_{pu}/\omega_p)}{4\left((\omega_{pu}/\omega_p)^2+1\right)^2} \\ +\frac{9(\omega_{pu}/\omega_p)}{8\left((\omega_{pu}/\omega_p)^2+1\right)} \end{array}\right]$$

The second segment may be integrated directly:

$$I_{\substack{n,eq\\blue}}{}^2 R_f{}^2 \cdot \int_{\omega_{pu}/2\pi}^{\infty} \frac{f^2 (2\pi f)^2}{(2\pi f/\omega_p)^4 (2\pi f/\omega_{pu})^2} df = I_{\substack{n,eq\\blue}}{}^2 R_f{}^2 \frac{\omega_p{}^4 \omega_{pu}{}^2}{(2\pi)^4} \cdot \int_{\omega_{pu}/2\pi}^{\infty} \frac{1}{f^2} df$$
$$= I_{\substack{n,eq\\blue}}{}^2 R_f{}^2 \frac{\omega_p{}^4 \omega_{pu}{}^2}{(2\pi)^4} \cdot \left[\frac{-1}{f}\right]_{\frac{\omega_{pu}}{2\pi}}^{\infty}$$
$$= I_{\substack{n,eq\\blue}}{}^2 R_f{}^2 \frac{\omega_p{}^4 \omega_{pu}}{(2\pi)^3}$$

Finally, the white and blue noise components are all combined,

$$\int_0^\infty f^2 S_{V_{out}}(f)df = I_{\substack{n,eq\\white}}^{\ 2} R_f^{\ 2}\left(\frac{3\omega_p^{\ 3}}{128\pi^2}\right) + I_{\substack{n,eq\\blue}}^{\ 2} R_f^{\ 2}\left(\frac{\omega_p^{\ 5}}{8\pi^3}\right)\cdot\left[\begin{array}{l}\dfrac{\omega_{pu}}{\omega_p} - \dfrac{15}{8}\arctan\left(\dfrac{\omega_{pu}}{\omega_p}\right)\\ -\dfrac{\left(\omega_{pu}/\omega_p\right)}{4\left(\left(\omega_{pu}/\omega_p\right)^2+1\right)^2}\\ +\dfrac{9\left(\omega_{pu}/\omega_p\right)}{8\left(\left(\omega_{pu}/\omega_p\right)^2+1\right)}\end{array}\right], + I_{\substack{n,eq\\blue}}^{\ 2} R_f^{\ 2}\left(\frac{\omega_p^{\ 4}\omega_{pu}}{8\pi^3}\right)$$

so that the expected number of positive threshold crossings per unit time can be calculated. For the case that $\omega_{pu} >> \omega_p$, the preceding integral can be simplified to:

$$\int_0^\infty f^2 S_{V_{out}}(f)df \approx I_{\substack{n,eq\\white}}^{\ 2} R_f^{\ 2}\left(\frac{3\omega_p^{\ 3}}{128\pi^2}\right) + I_{\substack{n,eq\\blue}}^{\ 2} R_f^{\ 2}\left(\frac{\omega_p^{\ 4}\omega_{pu}}{4\pi^3}\right),$$

and the expected number of positive threshold crossings per unit time is approximately:

$$\overline{N}_{\uparrow V_{th}} \approx \left(\frac{I_{\substack{n,eq\\white}}^{\ 2} R_f^{\ 2}\left(\frac{3\omega_p^{\ 3}}{128\pi^2}\right) + I_{\substack{n,eq\\blue}}^{\ 2} R_f^{\ 2}\left(\frac{\omega_p^{\ 4}\omega_{pu}}{4\pi^3}\right)}{\frac{R_f^{\ 2}}{32}\left(I_{\substack{n,eq\\white}}^{\ 2}\omega_p + 3I_{\substack{n,eq\\blue}}^{\ 2}\omega_p^{\ 3}\right)}\right)^{\frac{1}{2}} e^{-V_{th}^2/2V_{\substack{n,out\\rms}}^2},$$

$$\approx \left(\frac{3I_{\substack{n,eq\\white}}^{\ 2} + (32/\pi)\omega_p\omega_{pu}I_{\substack{n,eq\\blue}}^{\ 2}}{I_{\substack{n,eq\\white}}^{\ 2} + 3\omega_p^{\ 2}I_{\substack{n,eq\\blue}}^{\ 2}}\right)^{\frac{1}{2}} \frac{\omega_p}{2\pi} e^{-V_{th}^2/2V_{\substack{n,out\\rms}}^2}$$

where

$$V_{\substack{n,out\\rms}}^{\ 2} = \frac{R_f^{\ 2}\omega_p}{32}\left(I_{\substack{n,eq\\white}}^{\ 2} + 3I_{\substack{n,eq\\blue}}^{\ 2}\omega_p^{\ 2}\right).$$

5.2.3.3 Application of hypothetical circuit analyses to transimpedance amplifier design

The design of a practical photodetector circuit that is suited to a particular application now depends on the actual noise of the system and the bandwidth required for successful signal decoding/reconstruction. In order to apply the preceding noise

analysis to practical photodetector circuit design, it is useful to know how to compensate the circuit of Figure 5.11 to have critically damped second-order closed-loop response with pass-band transimpedance R_f and poles at angular frequency ω_p. While no compelling reason has yet been given for having the system critically damped, it is a reasonable place to start the system design for threshold detection because the output will exhibit no overshoot or ringing. Ringing in the photodetector output could lead to extra threshold crossings and thus false pulse detections, and should be avoided. It may be possible to decrease the system damping slightly to achieve faster rise time and thus improved slope (for more accurate pulse time measurement) without extra threshold crossings, but the mathematics of the critically damped system is more manageable.

5.2.3.3.1 Design for critically-damped second-order closed-loop response

5.2.3.3.1.1 Series resistor compensated photodetector circuit

To the extent that the op-amp can be modeled by its dominant pole, the closed-loop response of the series resistor compensated circuit in Figure 5.11 was shown to be:

$$\frac{V_{out}}{I_{diode}} = -\left(\frac{R_f}{s\left(R_f + R_c\right)C_d + 1}\right)\cdot\left(\frac{\left(\frac{K}{s\tau + 1}\right)}{1 + \left(\frac{K}{s\tau + 1}\right)\left(\frac{sR_cC_d + 1}{s\left(R_f + R_c\right)C_d + 1}\right)}\right),$$

which reduces to:

$$\frac{V_{out}}{I_{diode}} = \frac{-R_f}{s^2\left(\frac{\tau}{K}\left(R_f + R_c\right)C_d\right) + s\left(R_cC_d + \frac{\left(R_f + R_c\right)C_d}{K} + \frac{\tau}{K}\right) + 1 + \frac{1}{K}}.$$

When the system is critically damped, the poles will be identical (and real). Applying the quadratic formula to the denominator, this means that the poles will be at:

$$s = \frac{-\left(R_cC_d + \frac{\left(R_f + R_c\right)C_d}{K} + \frac{\tau}{K}\right)}{2\left(\frac{\tau}{K}\left(R_f + R_c\right)C_d\right)},$$

when

$$\left(R_cC_d+\frac{(R_f+R_c)C_d}{K}+\frac{\tau}{K}\right)^2-4\left(\frac{\tau}{K}(R_f+R_c)C_d\right)\left(1+\frac{1}{K}\right)=0\,.$$

For $K>>1$ the critical damping condition may be approximated by:

$$\left(R_cC_d+\frac{(R_f+R_c)C_d}{K}+\frac{\tau}{K}\right)^2=4\left(\frac{\tau}{K}(R_f+R_c)C_d\right).$$

Substituting the pole frequency

$$\omega_p=\frac{\left(R_cC_d+\frac{(R_f+R_c)C_d}{K}+\frac{\tau}{K}\right)}{2\left(\frac{\tau}{K}(R_f+R_c)C_d\right)}$$

into this equation and rearranging yields the following relationships:

$$R_f+R_c=\left(\frac{K}{\tau C_d}\right)\left(\frac{1}{\omega_p}\right)^2$$

and

$$R_c=\left(\frac{2}{C_d}\right)\left(\frac{1}{\omega_p}\right)-\frac{R_f}{K}-\frac{\tau}{KC_d}\,.$$

Substituting the latter relationship into the former, and again approximating for $K>>1$ gives the transimpedance resistor value as a function of ω_p:

$$R_f\approx\left(\frac{K}{\tau C_d}\right)\left(\frac{1}{\omega_p}\right)^2-\left(\frac{2}{C_d}\right)\left(\frac{1}{\omega_p}\right)+\frac{\tau}{KC_d}\,,$$

so that

$$R_c\approx-\left(\frac{1}{\tau C_d}\right)\left(\frac{1}{\omega_p}\right)^2+\left(\frac{2}{C_d}\right)\left(\frac{1}{\omega_p}\right)-\frac{\tau}{KC_d}\,.$$

The last two expressions for R_f and R_c permit the design of a critically damped second-order system with bandwidth ω_p. It is a simple matter to implement the high-pass filter shown in Figure 5.16 by adding R_z and C_z such that $1/R_zC_z=\omega_p$.

5.2.3.3.1.2 Feedback capacitor compensated photodetector circuit

Alternatively, the closed-loop response of the feedback capacitor compensated circuit in Figure 5.8 was shown to be:

$$\frac{V_{out}}{I_{diode}} = -\left(\frac{R_f}{sR_f\left(C_d + C_f\right)+1}\right)\cdot\left(\frac{\left(\frac{K}{s\tau+1}\right)}{1+\left(\frac{K}{s\tau+1}\right)\left(\frac{sR_fC_f+1}{sR_f\left(C_d+C_f\right)+1}\right)}\right) \quad .$$

$$= \frac{-R_f}{s^2\left(\frac{\tau}{K}R_f\left(C_d+C_f\right)\right)+s\left(R_fC_f+\frac{R_f\left(C_d+C_f\right)}{K}+\frac{\tau}{K}\right)+1+\frac{1}{K}}$$

Applying the quadratic formula to the denominator to find the identical, real poles for critical damping yields:

$$s = \frac{-\left(R_fC_f+\frac{R_f\left(C_d+C_f\right)}{K}+\frac{\tau}{K}\right)}{2\left(\frac{\tau}{K}R_f\left(C_d+C_f\right)\right)},$$

when

$$\left(R_fC_f+\frac{R_f\left(C_d+C_f\right)}{K}+\frac{\tau}{K}\right)^2-4\left(\frac{\tau}{K}R_f\left(C_d+C_f\right)\right)\left(1+\frac{1}{K}\right)=0\,.$$

For $K >> 1$ the critical damping condition may be approximated by:

$$\left(R_fC_f+\frac{R_f\left(C_d+C_f\right)}{K}+\frac{\tau}{K}\right)^2 = 4\left(\frac{\tau}{K}R_f\left(C_d+C_f\right)\right).$$

Substituting the pole frequency

$$\omega_p = \frac{\left(R_fC_f+\frac{R_f\left(C_d+C_f\right)}{K}+\frac{\tau}{K}\right)}{2\left(\frac{\tau}{K}R_f\left(C_d+C_f\right)\right)}$$

into this equation and rearranging yields the following relationships:

$$C_d + C_f = \left(\frac{K}{\tau R_f}\right)\left(\frac{1}{\omega_p}\right)^2$$

and

$$C_f = -\left(\frac{1}{\tau R_f}\right)\left(\frac{1}{\omega_p}\right)^2+\left(\frac{2}{R_f}\right)\left(\frac{1}{\omega_p}\right)-\frac{\tau}{KR_f}\,.$$

Substituting the latter relationship into the former, and again approximating for $K >> 1$ gives the transimpedance resistor value as a function of ω_p:

$$R_f \approx \left(\frac{K}{\tau C_d}\right)\left(\frac{1}{\omega_p}\right)^2 - \left(\frac{2}{C_d}\right)\left(\frac{1}{\omega_p}\right) + \frac{\tau}{KC_d},$$

which is, of course, the same as for the series resistor compensated circuit. The expression for the compensation capacitance can be simplified by eliminating R_f:

$$C_f = \left(\left(1 - \frac{\tau}{K}\omega_p\right)^{-2} - 1\right) \cdot C_d .$$

The last two expressions for R_f and C_f permit the design of a critically damped second-order system with bandwidth ω_p. Again, the high-pass output filter as in Figure 5.16 is easily implemented by adding R_z and C_z such that $1/R_z C_z = \omega_p$.

5.2.3.4 Optimal photodetector bandwidth

As long as R_z is smaller than R_f, it can be neglected in the calculation of input-referred noise of this system, which is:

$$S_{I_{eqTotal}}(\omega) = 2qI_{diode} + \left(\omega^2 R_c{}^2 C_d{}^2 + 1\right) \cdot S_{I_{n,opamp}}(\omega) + \left(\omega^2 R_c{}^2 C_d{}^2 + 1\right) \cdot \frac{4kT}{R_f}$$
$$+ \left(\omega^2 C_d{}^2\right) \cdot 4kTR_c + \left(\frac{\omega^2 \left(R_f + R_c\right)^2 C_d{}^2 + 1}{R_f{}^2}\right) \cdot S_{V_{n,opamp}}(\omega) .$$

For most of the applications considered in this thesis research, this sum was dominated by the thermal noise of the resistors or the voltage noise of the op-amp. Also, it was found that R_f was approximately proportional to $1/\omega_p{}^2$. Consequently, the pulse detection timing error was usually minimized by making ω_p as small as possible.

5.2.3.4.1 Interaction between received light pulses

The factors that determine the minimum value of ω_p are the maximum rate of light pulses and the amount of interaction between pulses that can be tolerated. The response of the photodetector circuit to each light pulse must decay to the point that it does not significantly affect the time of detection of the subsequent pulse. A light pulse

that generates photodiode current I_p for time $t = 0 \rightarrow T_f$ in the critically damped second-order photodetector circuit with high-pass output filter produces the response:

$$v_{out,pulse}(t) = \frac{1}{2} I_p R_f {\omega_p}^2 \left(t^2 - \left(t - T_f \right)^2 e^{\omega_p T_f} \right) e^{-\omega_p t}, \quad t > T_f .$$

If the next light pulse occurs at time T_i, the previous pulse will have decayed to:

$$v_{out,pulse}(T_i) = \frac{1}{2} I_p R_f {\omega_p}^2 \left(T_i^2 - \left(T_i - T_f \right)^2 e^{\omega_p T_f} \right) e^{-\omega_p T_i} .$$

Dividing this by the slope of the next pulse at threshold crossing will give the approximate change in the time of its threshold crossing. Assuming that it still crosses threshold near the maximum slope, which is

$$\left. \frac{dv_{out,pulse}}{dt} \right|_{\max} \approx 0.231 \cdot I_p R_f \omega_p ,$$

the time shift caused by the tail of the previous pulse will be:

$$\begin{aligned} \Delta T_{interaction} &= \frac{v_{out,pulse}(T_i)}{dv_{out,pulse}/dt} \approx \frac{\frac{1}{2} I_p R_f {\omega_p}^2 \left(T_i^2 - \left(T_i - T_f \right)^2 e^{\omega_p T_f} \right) e^{-\omega_p T_i}}{0.231 \cdot I_p R_f \omega_p} \\ &\approx 2.16 \cdot \omega_p \left(T_i^2 - \left(T_i - T_f \right)^2 e^{\omega_p T_f} \right) e^{-\omega_p T_i} \end{aligned} .$$

The maximum slope used here is valid only if $T_f > \left(2 - \sqrt{2}\right)/\omega_p \approx 0.586/\omega_p$, or rather $\omega_p > 0.586/T_f$. For photodetector circuit bandwidths less than this value, the pulse time measurement noise and pulse interaction would have to be calculated without the benefit of the analysis presented earlier in this chapter.

5.2.3.4.2 Relationship between pulse interaction and signal decoding

The pulse-position modulation scheme that was used for the optical telemeter encodes the signal information in the time between each light flash. The average interval between flashes, $T_{i,ave}$, is increased or decreased by an amount, ΔT, that is proportional to the encoded signal (voltage). The timing error due to pulse interactions ($\Delta T_{interaction}$) and photodetector noise (ΔT_{noise}) must be less than the period change corresponding to the smallest signal that it is desired to encode, $\Delta T_{\min}$. If the largest signal that can be encoded produces a maximum change in the inter-pulse period of

$\pm\Delta T_{\max}$, then the dynamic range of the system is $2\Delta T_{\max}/\Delta T_{\min}$. The dynamic range may also be expressed in terms of the number of bits resolution, N:

$$N = \text{int}^{-}\left(\frac{\log\left(2\Delta T_{\max}/\Delta T_{\min}\right)}{\log(2)}\right),$$

where $\text{int}^{-}(\ )$ denotes integer rounding down.

The worst-case pulse interaction will occur after the shortest possible pulse period, $T_{i,ave} - \Delta T_{\max}$. In this case, the resulting error in the time of detection of the second pulse will be

$$\Delta T_{\substack{interaction \\ \max}} \approx 2.16\cdot\omega_p\left(\left(T_{i,ave} - \Delta T_{\max}\right)^2 - \left(T_{i,ave} - \Delta T_{\max} - T_f\right)^2 e^{\omega_p T_f}\right)e^{-\omega_p\left(T_{i,ave}-\Delta T_{\max}\right)},$$

which must be less than $\Delta T_{\min}$. With N bits resolution, $\Delta T_{\min} = \Delta T_{\max}/2^{N-1}$, so

$$2.16\cdot\omega_p\left(\left(T_{i,ave} - \Delta T_{\max}\right)^2 - \left(T_{i,ave} - \Delta T_{\max} - T_f\right)^2 e^{\omega_p T_f}\right)e^{-\omega_p\left(T_{i,ave}-\Delta T_{\max}\right)} < \frac{\Delta T_{\max}}{2^N}$$

for less than ½ LSB (Least Significant Bit) pulse interaction. This relationship can be solved to find the minimum value of ω_p (keeping in mind that this derivation has assumed that $\omega_p > 0.586/T_f$) to permit the design of a photodetector circuit for a particular telemeter.

5.2.4 Practical design example: photodetector for 8-channel neural waveform telemeter

A practical example from this thesis research that demonstrates the design process for a photodetector circuit is the 8-channel neural waveform telemeter. In this application, eight neural waveform signals of 7kHz bandwidth each were to be sequentially pulse-position encoded. In addition to the eight signal periods in each sampling cycle, a marker period that was twice as long as the average signal period was used.

5.2.4.1 Bandwidth based on signal encoding

A 20kHz sampling rate was chosen to minimize aliasing, so the average period between signal pulses was:

$$\begin{aligned} T_{i,ave} &= \left(\frac{1}{20[kHz]}\right)\left(\frac{1}{8+2}\right), \\ &= 5[\mu s] \end{aligned}$$

in order to cycle through all eight signal periods and the double-length marker period every 50 μs. The encoder was designed to produce a maximum period variation of $\pm\Delta T_{\max} = \pm T_{i,ave}/2 = \pm 2.5[\mu s]$ corresponding to ±1 mV input signals. It was desired to encode signals as small as 10 μV_{rms}, which was well below the measured background neural noise level of 23 μV_{rms}, so 8 bits of resolution were required of the photodetector circuit. The shortest light flash that could be produced by the low power telemeter electronics was $T_f = 0.5[\mu s]$. The pulse interaction condition with these values:

$$\omega_p\left(\left(6.25\cdot 10^{-12}\right) - \left(4\cdot 10^{-12}\right)e^{\omega_p\left(5\cdot 10^{-7}\right)}\right)e^{-\omega_p\left(2.5\cdot 10^{-6}\right)} < 4.52\cdot 10^{-9},$$

is satisfied for $\omega_p \geq 4\cdot 10^6$. Verifying that $\omega_p > 0.586/T_f \approx 1.2\cdot 10^6$ shows that the choice of $\omega_p = 4\cdot 10^6$ is acceptable.

5.2.4.2 Component selection

For this photodetector circuit, the EG&G VTH2090 silicon PIN photodiode was selected for its large active area and particularly low capacitance. According to the published specifications, the active area of this diode is 9.2 x 9.2 mm (0.8464 cm^2), its radiant sensitivity γ_{diode} is about 0.4 A/W at 660 nm, its capacitance is about 70 pF when reverse-biased at 30 Volts, and the leakage current is less than 10 nA. The Burr-Brown OPA655 operational amplifier was used because of its high speed and low noise. This op-amp has a 240 MHz gain-bandwidth product, less than 30 fA/√Hz input-referred current noise up to 1 MHz, and 6 nV/√Hz input-referred voltage noise above 10 kHz. Its transfer function can be approximated by:

$$G_{OPA655}(s) = \frac{1000}{s\left(8\cdot 10^{-7}\right)+1},$$

so $K = 1000$ and $\tau = 8\cdot 10^{-7}$. The feedback resistor for the circuits of Figure 5.8 and Figure 5.10 is then

$$\begin{aligned} R_f &\approx \left(\frac{K}{\tau C_d}\right)\left(\frac{1}{\omega_p}\right)^2 - \left(\frac{2}{C_d}\right)\left(\frac{1}{\omega_p}\right) + \frac{\tau}{KC_d}. \\ &\approx 1.11[M\Omega] \end{aligned}$$

The feedback capacitor required for compensation with critical damping would be

$$C_f = \left(\left(1 - \frac{\tau}{K} \omega_p \right)^{-2} - 1 \right) \cdot C_d ,$$
$$\approx 0.45[pF]$$

which is impracticably small for discrete components. Instead, series resistor compensation can be used with

$$R_c = \left(\frac{2}{C_d} \right) \left(\frac{1}{\omega_p} \right) - \frac{R_f}{K} - \frac{\tau}{K C_d} .$$
$$\approx 6.02[k\Omega]$$

The high-pass filter in Figure 5.16 can be implemented by $R_z = 500[\Omega]$ and $C_z = 500[pF]$.

5.2.4.3 Input-referred current noise

In the dark, the input-referred noise of this photodetector is

$$S_{I_{eqTotal}}(\omega) \approx 2qI_{diode} + \left(\omega^2 {R_c}^2 {C_d}^2 + 1\right) \cdot S_{I_{n,opamp}}(\omega) + \left(\omega^2 {R_c}^2 {C_d}^2 + 1\right) \cdot \frac{4kT}{R_f}$$
$$+ \left(\omega^2 {C_d}^2\right) \cdot 4kTR_c + \left(\frac{\omega^2 \left(R_f + R_c\right)^2 {C_d}^2 + 1}{{R_f}^2} \right) \cdot S_{V_{n,opamp}}(\omega)$$
$$\approx 3.2 \cdot 10^{-27} + 1.6 \cdot 10^{-40} \omega^2 + 9 \cdot 10^{-28} + 2.65 \cdot 10^{-39} \omega^2 + 1.49 \cdot 10^{-26} .$$
$$+ 4.88 \cdot 10^{-37} \omega^2 + 1.78 \cdot 10^{-37} \omega^2 + 2.92 \cdot 10^{-29}$$
$$\approx 1.90 \cdot 10^{-26} + 6.70 \cdot 10^{-37} \omega^2$$

This quantity is dominated by the noise of R_f at low frequency, and by the noise of R_c and the op-amp voltage noise at frequencies greater than about 170 krad/s, or 27 kHz. The significance of R_c in the noise total suggests that capacitor compensation (as in Figure 5.8) should be used whenever feasible.

5.2.4.4 Output rms voltage noise

To find the voltage noise at the output of the photodetector circuit, we can apply the previously derived expression:

$$V_{\substack{n,out \\ rms}} = \frac{R_f}{4\sqrt{2}} \sqrt{{I_{\substack{n,eq \\ white}}}^2 \omega_p + 3 {I_{\substack{n,eq \\ blue}}}^2 {\omega_p}^3} ,$$

where $I_{\substack{n,eq \\ white}}^{\ 2} \approx 1.90 \cdot 10^{-26}$, $I_{\substack{n,eq \\ white}}^{\ 2} \approx 6.70 \cdot 10^{-37}$, $\omega_p = 4 \cdot 10^6$, and $R_f = 1.11[M\Omega]$. This yields

$$V_{\substack{n,out \\ rms}} \approx 2.22[mV].$$

5.2.4.5 Pulse detection timing error

If the pulse detector threshold is set at the point of maximum slope,

$$\begin{aligned} v_{threshold,optimal} &\approx 0.096 \cdot I_p R_f \\ &\approx 1.07 \cdot 10^5 \cdot I_p \end{aligned},$$

then the rms error in the time of threshold crossing is approximately:

$$\begin{aligned} \Delta T_{\substack{noise \\ rms,\min}} &= \frac{V_{\substack{n,out \\ rms}}}{0.231 \cdot I_p R_f \omega_p} \approx \frac{0.767}{I_p} \cdot \sqrt{\frac{I_{\substack{n,eq \\ white}}^{\ 2}}{\omega_p} + 3 I_{\substack{n,eq \\ blue}}^{\ 2} \omega_p} \\ &\approx \frac{2.17 \cdot 10^{-15}}{I_p} \end{aligned}.$$

5.2.4.5.1 Minimum photocurrent for proper signal decoding

In order for the noise-induced error in pulse timing to be less than ½ LSB of the decoded signal, i.e.

$$\Delta T_{\substack{noise \\ rms,\min}} \leq \frac{T_{\max}}{2^N},$$

or

$$\frac{2.17 \cdot 10^{-15}}{I_p} \leq \frac{2.5 \cdot 10^{-6}}{2^8},$$

the minimum photocurrent in the diode must be:

$$I_p \geq 0.22[\mu A].$$

Dividing by the radiant sensitivity $\gamma_{diode} = 0.4[A/W]$ and the active area of the photodiode $A_{diode} = 0.8464[cm^2]$ yields the minimum average light intensity at the detector:

$$L_{p,\min} = 6.5 \cdot 10^{-7} \left[\frac{W}{cm^2}\right].$$

5.2.4.6 Rate of spurious pulse detections

In addition to ensuring that pulses can be detected with sufficient timing accuracy, we must make certain that random threshold crossings are sufficiently rare. The expected number of random positive threshold crossings per unit time was given by:

$$\overline{N}_{\uparrow V_{th}} \approx \left(\frac{3 I_{\substack{n,eq \\ white}}^{\ 2} + (32/\pi)\omega_p \omega_{pu} I_{\substack{n,eq \\ blue}}^{\ 2}}{I_{\substack{n,eq \\ white}}^{\ 2} + 3\omega_p^{\ 2} I_{\substack{n,eq \\ blue}}^{\ 2}} \right)^{\frac{1}{2}} \frac{\omega_p}{2\pi} e^{-V_{th}^{\ 2} / 2V_{\substack{n,out \\ rms}}^{\ 2}},$$

so with the high frequency pole at the unity gain frequency of this op-amp, $\omega_{pu} \approx 2.5 \cdot 10^9$,

$$\overline{N}_{\uparrow V_{th}} \approx 2.94 \cdot 10^7 \cdot e^{-\frac{1}{2}\left(\frac{V_{th}}{2.22 \cdot 10^{-3}} \right)^2}.$$

With the threshold set to the optimal value for the minimum photocurrent given above, $V_{th} = 23.4[mV]$, this is:

$$\overline{N}_{\uparrow V_{th}} \approx 1.79 \cdot 10^{-17}.$$

Accordingly, a very long time would be expected between false pulse detections, even for the weakest acceptable signal in this design example.

5.2.4.7 Complete circuit schematic with threshold detector

The complete schematic of the photodetector circuit for the 8-channel neural waveform telemeter is given in Figure 5.17.

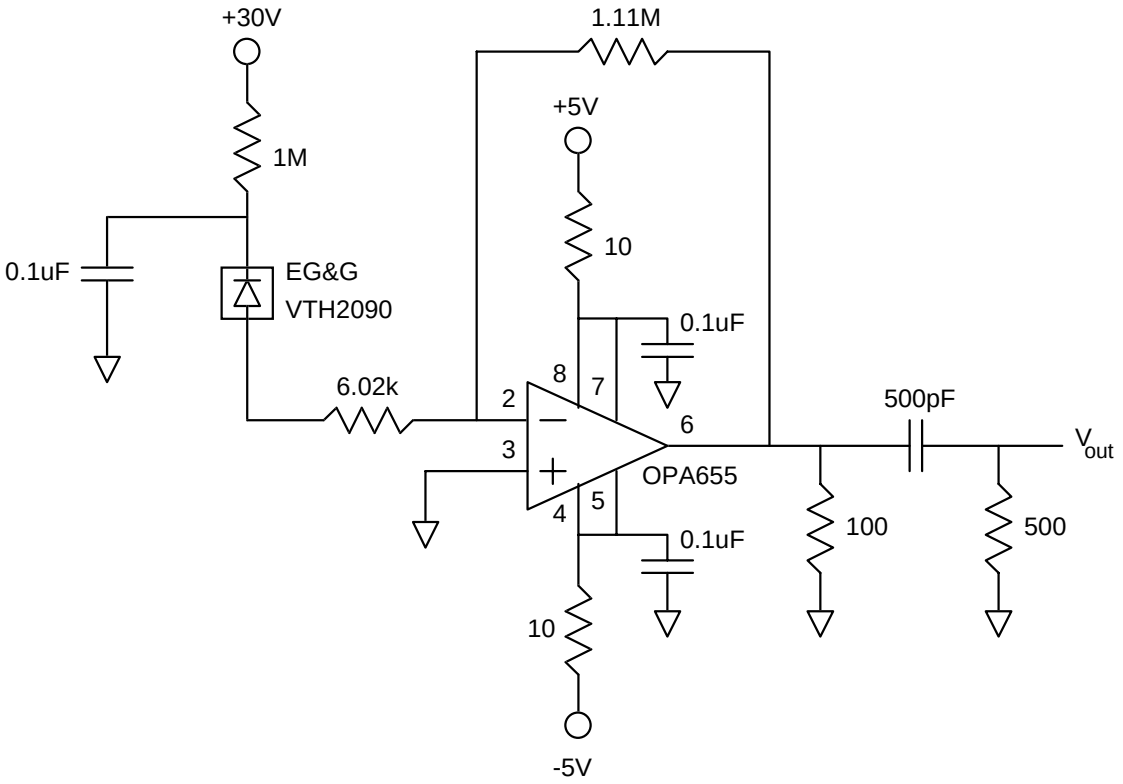

Figure 5.17: Photodetector circuit schematic for design example.

A threshold pulse detection circuit with active threshold setting is sketched in Figure 5.18. For clarity, the power supply decoupling has been omitted from this schematic, and all power supply pins should be decoupled with at least a 10 Ω resistor and 0.1 μF capacitor.

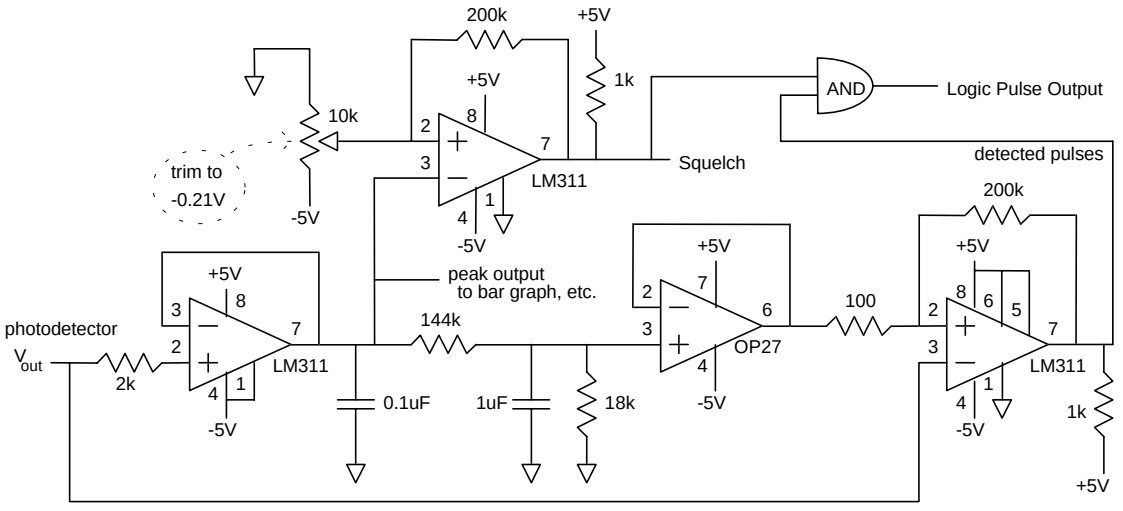

Figure 5.18: Threshold detector circuit for design example.

This circuit incorporates a precision peak detector that sets the threshold to the optimal level based on the received pulse amplitude. Pulse detection is disabled when the signal is too weak for accurate pulse timing (i.e. the pulse amplitude is less than the calculated minimum level). The response of the photodetector circuit is at its maximum amplitude (negative) on the rising edge of the pulse when $t = 2/\omega_p$, provided that $T_f \geq 2/\omega_p$. Since $T_f = 0.5[\mu s]$ and $\omega_p = 4 \cdot 10^6$ in this design example, this just works out. Thus the peak output voltage will be:

$$\begin{aligned} v_{out,peak} &= -I_p R_f \left(1 - e^{-2}\right) \\ &= -(0.865) I_p R_f \end{aligned} .$$

In order to trigger at the optimal threshold, $v_{threshold,optimal} \approx -0.096 \cdot I_p R_f$, the threshold should be set in relation to the peak at:

$$\begin{aligned} v_{threshold,optimal} &\approx 0.111 \cdot v_{out,peak} \\ &\approx \frac{v_{out,peak}}{9} \end{aligned} .$$

The variation in received pulse amplitude will result mostly from movement of the photodetector in relation to the telemeter, and these changes should occur relatively slowly. A bandwidth of about 10 Hz should be adequate to track the important fluctuations in pulse amplitude, so the peak detector and the comparator threshold are low-pass filtered at approximately this frequency to provide a steady threshold voltage. A small amount of hysteresis is used with the comparator to prevent multiple or ambiguous threshold crossings. Finally, the pulse detector output is disabled by a second comparator if the peak detector voltage indicates that the pulses are below the minimum desired value of $I_p = 0.22[\mu A]$, or:

$$\left| v_{out,peak} \right| \leq 0.211[V].$$

The peak detector output can be used to provide feedback for manual positioning of the photodetector by connecting it to an audible or visible output device. For example, the peak voltage can be connected directly to a meter or an LED bar graph display, or it could be voltage-to-frequency converted for output through a speaker or flashing LED.

5.2.4.8 Suggestion for improving photodetector circuit

Recently, a clever yet simple technique was suggested for improving the photodetector circuit of Figure 5.17 [80]. It allows feedback capacitor compensation to be implemented

with workable component values. This eliminates the compensation resistor in series with the photodiode, and the noise that goes along with it. The technique is to use a voltage divider circuit to attenuate the output signal before the feedback capacitor, so that the feedback capacitor can be made correspondingly larger. If capacitors or sufficiently small resistors are used to construct the voltage divider, the noise contribution from this compensation circuit can be negligible. Figure 5.19 shows the improved photodetector circuit.

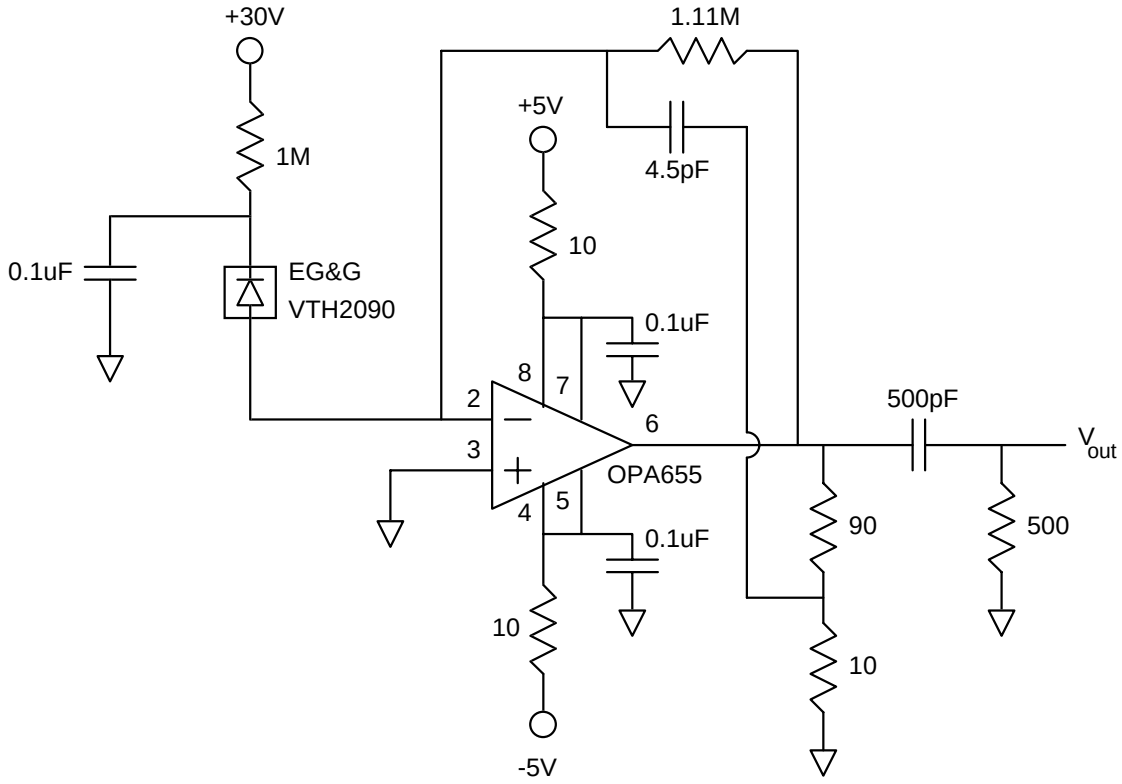

Figure 5.19: Photodetector circuit with improved frequency compensation feedback.

The input-referred current noise of this improved photodetector is approximately:

$$S_{I_{eqTotal}}(\omega) \approx 2qI_{diode} + S_{I_{n,opamp}}(\omega) + \frac{4kT}{R_f} + \left(\omega^2 C_d{}^2 + \frac{1}{R_f{}^2}\right) \cdot S_{V_{n,opamp}}(\omega)$$

$$\approx 3.2 \cdot 10^{-27} + 9 \cdot 10^{-28} + 1.49 \cdot 10^{-26} + 1.76 \cdot 10^{-37}\omega^2 + 2.92 \cdot 10^{-29},$$

$$\approx 1.90 \cdot 10^{-26} + 1.76 \cdot 10^{-37}\omega^2$$

so the rms voltage noise at its output is:

$$V_{\substack{n,out \\ rms}} = \frac{R_f}{4\sqrt{2}}\sqrt{I_{\substack{n,eq \\ white}}{}^2\omega_p + 3I_{\substack{n,eq \\ blue}}{}^2\omega_p{}^3}$$
$$= \frac{1.11\cdot 10^6}{4\sqrt{2}}\sqrt{\left(1.90\cdot 10^{-26}\right)\left(4\cdot 10^6\right)+3\left(1.76\cdot 10^{-37}\right)\left(4\cdot 10^6\right)^3}\ .$$
$$\approx 1.14[mV]$$

With the pulse detector threshold set at the point of maximum slope, the rms error in the time of threshold crossing will be approximately:

$$\Delta T_{\substack{noise \\ rms,\min}} = \frac{V_{\substack{n,out \\ rms}}}{0.231\cdot I_p R_f \omega_p}\ .$$
$$\approx \frac{1.11\cdot 10^{-15}}{I_p}$$

In order for the noise-induced error in pulse timing to be less than ½ LSB of the decoded signal, the minimum photocurrent in the diode must be:

$$I_p \geq 0.11[\mu A].$$

Dividing by the radiant sensitivity $\gamma_{diode} = 0.4[A/W]$ and the active area of the photodiode $A_{diode} = 0.8464[cm^2]$ yields the new minimum average light intensity at the detector:

$$L_{p,\min} = 3.4\cdot 10^{-7}\left[\tfrac{W}{cm^2}\right].$$

Since this photodetector is more sensitive than the series resistor compensated circuit discussed before, the level at which the output of the threshold pulse detector circuit (Figure 5.18) should be disabled can be reduced. The "output disable" level should be set to cut off for pulse amplitudes less than:

$$\left|v_{out,peak}\right| \leq 0.106[V].$$

5.2.5 Optical filters for removing ambient and powering light

In order to minimize the photodiode shot noise term in the photodetector circuit noise sum, and to prevent the photodetector circuit from saturating on non-signal light, optical filters can be used to block unwanted wavelengths. The most critical wavelength to block from the detector is the light used to power the telemeter. Filters were evaluated at the signal light wavelength of 660 nm and the power light wavelength of 880 nm. Provided that the attenuation at 660 nm was not enough to require significantly increased telemeter output, the ratio between the attenuation at 660 nm to the attenuation at 880 nm was used to compare the efficacy of the various filters. Several

absorption color filters (mostly red glass and plastic) were tested, but none were found to block the 880 nm infrared light. Interference filters selective to wavelengths near 660 nm gave the best results They had the added advantage of blocking most ambient room light in addition to 880 nm. The absolute and relative transmittances of two interference filters and an IR cutoff filter are presented in Figure 5.20.

Filter	660 nm Transmittance	880 nm Transmittance	660 nm / 880 nm
Edmund A53,709 IR cutoff	94%	0.34%	275
Ealing 42-5504 interference	55%	0.0044%	12400
CVI F40-670.0-04 interference	50%	0.0048%	10400

Figure 5.20: Optical filters for blocking unwanted light from photodetector.

5.2.6 Optics

Lenses and mirrors were investigated as means to increase signal light collection at the photodetector. The issue of maximizing the collected light is complicated, and a rigorous study of this problem would be warranted in future work. The research on this topic that was performed as part of this thesis did not yield definite answers, but did suggest a general strategy.

Conventional imaging optics were not found to be particularly useful, because imaging optics are designed to exclude scattered light. In this application, it is desired to collect as much light from the telemeter output LED as possible, including the scattered light. And the tissue between the telemeter and the photodetector is a highly scattering medium, so a significant fraction of the light is scattered. In fact, the light source as seen by the photodetector can be modeled as a random collection of light sources spread over some volume of the tissue. Since each one of these light sources emits light in all directions, it is difficult to focus this light onto the detector as would be done in an imaging application.

Light collecting optics (as opposed to imaging optics) should be used, and a parabolic reflector seemed to be appropriate for this application. The penalty in using any optics between the telemeter and the photodetector is an increase in the distance between the two, and it became apparent that placing the photodetector as close to the emitter as possible (i.e. against the skin) would yield the strongest signal. But with the detector

close against the skin, there was significant lateral position sensitivity. The sensitivity to position was decreased by using a large area photodetector, which simply covered a larger area of skin. Of course, the noise of the photodetector circuit is strongly dependent on the capacitance of the photodiode, so this limits the maximum beneficial size.

5.2.7 Other photodetectors and circuit configurations

5.2.7.1 GaAs-family photodiodes

Photodiodes made in GaAs and related technologies were considered as alternatives to silicon PIN photodiodes, since they can be obtained with different spectral response ranges. For example, the Hamamatsu G1738 GaAsP photodiode has a spectral response range of 400 to 760 nm. It has virtually no response at the 880 nm infrared wavelength used in this research to provide power to the telemeter devices. In the absence of other background illumination, no optical filtering would be necessary with this photodiode. This is a significant advantage in terms of eliminating filter losses and decreasing the distance between the photodetector and the telemeter. Unfortunately, the capacitance was quite high for all of the diodes of this type that were found. The figure of merit defined in section 5.2.2.1.4, $A_{diode}\gamma_{diode}/C_d^{\,2}$, can be used to compare this GaAsP photodiode with the silicon photodiode that was used, the EG&G VTH2090. The specifications for the Hamamatsu G1738 are $A_{diode} = 1.66[mm^2]$, $\gamma_{diode} = 0.35[A/W]$ at 660 nm, and $C_d = 250[pF]$, so

$$\frac{A_{diode}\gamma_{diode}}{C_d^{\,2}} \approx 9.3 \cdot 10^{12}\left[\frac{m^2 \cdot A}{W \cdot F^2}\right].$$

The EG&G VTH2090 values are: $A_{diode} = 84.64[mm^2]$, $\gamma_{diode} = 0.4[A/W]$ at 660 nm, and $C_d = 70[pF]$, so

$$\frac{A_{diode}\gamma_{diode}}{C_d^{\,2}} \approx 6.9 \cdot 10^{15}\left[\frac{m^2 \cdot A}{W \cdot F^2}\right].$$

The score of the silicon PIN diode is a factor of 740 higher than the GaAsP diode on this figure of merit. The silicon photodiode should result in a much more sensitive photodetector, even though some signal loss will be incurred by optical filters needed to block the infrared powering light.

5.2.7.2 Photodiode bootstrap amplifier

The circuit of Figure 5.21 was considered as a possible means to improve the noise / bandwidth tradeoff of the photodetector circuit.

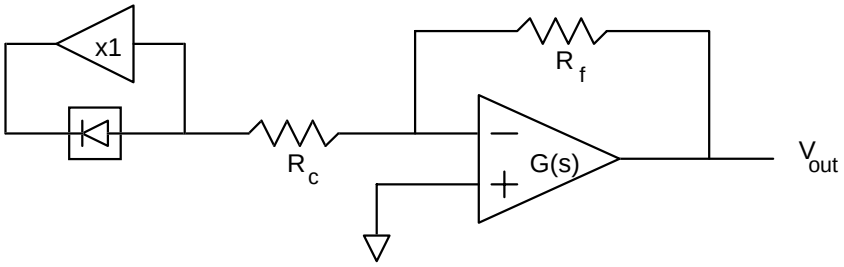

Figure 5.21: Transimpedance amplifier with bootstrapped photodiode.

A unity-gain voltage follower is used to "bootstrap" the photodiode, forcing the voltage across it to stay close to zero. To the extent that a constant potential (zero volts) is maintained across the diode, its capacitance cannot store any charge, so the photocurrent is forced to flow into the transimpedance amplifier. In other words, the photodiode capacitance seen by the transimpedance amplifier is greatly decreased. Substituting the effective photodiode capacitance into the noise equations for the transimpedance amplifier shows the apparent benefit of this technique. Unfortunately, a new noise source has been added. The input-referred current noise of the buffer amp will be added to the input-referred current noise of the transimpedance amplifier. Worse yet, the input-referred voltage noise of the buffer amp is divided by the magnitude of the impedance of the photodiode $\left(1/\omega C_d\right)$ to determine its contribution to the input-referred current noise of the transimpedance amplifier. Unless a buffer amplifier with lower voltage noise *and* current noise than the transimpedance amplifier op-amp can be found, the total noise of this configuration is likely to be greater than the basic transimpedance amplifier circuit analyzed previously. Also, with real components, the dynamics of this circuit are considerably more complex, making it more difficult to implement in practice.

5.2.7.3 Photomultiplier tubes

For some applications it may be advantageous to use a photomultiplier tube (PMT) for the photodetector circuit. While PMTs are larger than photodiode-type detectors, much more costly, probably less mechanically robust, and require high-voltage power supplies, their sensitivity and speed can be much greater. The quantum detection efficiency of PMTs is not as good as silicon PIN photodiodes (which have typical quantum

efficiencies of 85% over most of their spectral response range), but they can be much more sensitive because the electron multiplication in the tube pre-amplifies the signal, reducing the effect of post-amplifier noise. Also, PMTs can have large active areas, and speed is virtually independent of sensitivity. The output of the PMT is typically its anode current, which is equal to the photoelectric current from the cathode multiplied by the gain provided by the electron multiplier dynodes. The input-referred current noise power spectral density of the PMT in the dark is given by:

$$S_{I_{eq}}(f) = \frac{2qI_{db}}{\mu},$$

where I_{db} is the anode (output) dark current, and μ is the current amplification of the tube. The noise equivalent power of the PMT over bandwidth β is equal to the rms input-referred current noise divided by the cathode radiant sensitivity γ_c (in A/W):

$$NEP = \frac{1}{\gamma_c}\sqrt{\int_0^{\beta} S_{I_{eq}}(f)df} = \frac{1}{\gamma_c}\sqrt{\frac{2qI_{db}}{\mu}\beta}.$$

Since the input-referred current noise of the subsequent amplifier stage is divided by μ to refer it to the input of the photodetector, it can usually be neglected. This is the principal noise advantage of the PMT.

A suitable photomultiplier tube module manufactured by Hamamatsu, the H6780-01, incorporates a high-voltage power supply in a package measuring 50x22x22 mm. Its spectral response range is 300 to 820 nm, its cathode radiant sensitivity is $\gamma_c = 0.017[A/W]$ at 660 nm, and it has an 8 mm diameter active area. The anode pulse rise time is 0.65 ns, corresponding to a bandwidth of about 540 MHz. The current amplification of this tube is adjustable over four orders of magnitude, with a maximum value of $\mu_{\max} = 1.2 \cdot 10^6$. At the recommended maximum operating gain of about $\mu = 3 \cdot 10^5$, the typical anode dark current is $I_{db} = 1[nA]$. The input-referred current noise of this PMT is thus:

$$I_{n,eq} \approx 3.3 \cdot 10^{-17}\left[A/\sqrt{Hz}\right].$$

To roughly compare this to the practical photodetector example of section 5.2.4, we can calculate the noise equivalent power of both circuits. If we divide the rms voltage noise

at the output of the photodiode detector by its transimpedance and the radiant sensitivity of the diode (at 660 nm), the NEP is:

$$NEP_{\substack{photodiode \\ circuit}} = \frac{(2.22[mV])}{(1.11\cdot 10^{6}[\Omega])(0.4[A/W])} . \\ = 5\cdot 10^{-9}[W]$$

The noise equivalent power of the PMT circuit, assuming perfect bandlimiting at $\beta = \omega_p / 2\pi = 640[kHz]$, is:

$$NEP_{\substack{PMT \\ circuit}} = 1.5\cdot 10^{-12}[W].$$

Dividing the NEP by the active area of the detectors gives the most direct comparison, since this gives the light flux necessary to equal the noise in the systems:

$$\frac{NEP}{area}_{\substack{photodiode \\ circuit}} = \frac{5\cdot 10^{-9}[W]}{0.8464[cm^2]} = 5.9\cdot 10^{-9}\left[\frac{W}{cm^2}\right],$$

and

$$\frac{NEP}{area}_{\substack{PMT \\ circuit}} = \frac{1.5\cdot 10^{-12}[W]}{0.50[cm^2]} = 3\cdot 10^{-12}\left[\frac{W}{cm^2}\right].$$

If the cost and relative inconvenience of the PMT can be tolerated, it gives a factor of almost 2000 improvement in sensitivity over the photodiode detector circuit in this high-speed application. The improvement becomes even greater for higher bandwidth applications.

Chapter 6: Single-channel neural waveform telemeters

Initially, it appeared that circuit simulations had to be relied upon until the first integrated circuit was designed and fabricated. However, there were many subtle issues of the biomedical information optical telemeter that needed to be tested in animals prior to fully investing the time and expense of generating an integrated circuit. A prototype assembly of discrete components was not optimal, but was possible to implement to gain valuable experience with the many different aspects of the complete system.

As a test of the concepts developed for the optically-linked biomedical information telemeter, a pulse-encoded neural waveform transmitter was developed from commercially available electronic components and implanted in a rabbit. In particular, it was desired to demonstrate the efficacy of optical power and signal transmission, the low power circuits, and the encoding technique.

6.1 A biomedical signal to test the telemeter -- the Visual Evoked Potential

6.1.1 Overview of the origin of neuroelectric signals

Nerve cells generally have three main functional parts: dendrites which receive information from other neurons, a cell body that contains the nucleus and other supporting structures, and the axon which serves as an information conduit to communicate with other cells. The most readily observable phenomena during neuron communication are transient electrical signals called action potentials. Action potentials consist of transient ionic currents that flow across the cell membrane and propagate along the length of the axon. Action potentials are generated by the discharge of a "resting potential" created by charge stored across the cell membrane. The resting potential is an electrochemical potential difference resulting from ionic concentration differences between the inside of the cell and its surrounding environment. The resting potential is maintained by the selective permeability of the cell membrane and active ionic transport mechanisms, as described by the Goldman equation [81]. Active transport mechanisms pump sodium out of the cell, and potassium into the cell. Resting potentials are generally between –60 mV and –100 mV depending on the type of cell, with –70 mV being typical of neurons [79].

When a neuron is excited by an appropriate stimulus, sodium-specific channels in the cell membrane open to allow sodium ions to flow into the cell, driven by the electric field

and the concentration gradient across the membrane. The membrane potential is quickly neutralized, and is said to be depolarized. The membrane potential actually continues to rise above neutral, going positive to approximately +20 mV. This brief positive membrane potential, called the action potential, results from the concentration imbalance of potassium ions. The membrane potential is reset by the opening of potassium channels in the membrane that allow potassium ions to flow out of the cell. A second process triggered by the membrane depolarization causes the ion channels to close, so that the cell will return to its resting condition. The repolarizing ionic flows are slower than the depolarizing flows, but the entire process can happen in as little as one millisecond for some nerve cells. Following an action potential, there is a refractory period of several milliseconds or more during which the cell cannot at first respond to any new stimulus and then requires a stronger stimulus to depolarize again.

Less strictly speaking, the term “action potential” is often used to refer to the entire depolarization event of a neuron. Action potentials can be triggered by depolarizing the cell membrane of the neuron by electrical, chemical, or mechanical stimuli, depending on the type of nerve cell involved. The action potential can stimulate or inhibit the activity of other neurons and cells of other types through direct electrical activation or by modulating the release of neurotransmitters [79].

6.1.2 Recording of individual action potentials and gross neuroelectric signals

Although the transmembrane action potentials of certain nerve cells can be directly recorded with special electrodes, this requires precise placement of an electrode inside the cell and is not suitable for long-term observation of neural activity. More commonly, the biopotentials in the extracellular environment due to the combined effect of many action potentials are recorded at some location on the surface of the body or between a pair of electrodes placed inside or near the brain or a nerve bundle. The recorded bioelectric signal patterns result from the summation of the potentials developed by the ionic currents associated with the individual action potentials. Depending on the size, spacing, and placement of the electrodes, it is possible to observe individual action potential spikes on these extracellular recordings as well.

During the flow of the positively charged sodium ions into the cell during action potentials, potential gradients are generated in the extracellular space near the neuron. Placement of electrodes within the gradients allows detection of the action potentials

using differential amplifiers. The closer an electrode is to the active site, the larger will be the amplitude of the recorded action potential. Since the positive sodium ions flow into the cell during the initial phase and peak of the action potential, this portion of the recorded waveform is negative relative to a distant reference electrode. This negative waveform or "spike" is usually on the order of 250 μs in duration at its half-amplitude point, and has a characteristic gaussian-like shape followed by a slower, lower amplitude positive waveform that is often lost in the noise encountered with extracellular recordings. When the potential measurement is made between two electrodes of similar size that are both placed near active neurons, one of the electrode signals is inverted by the differential amplifier, so spikes of both negative and positive polarity may be observed, as illustrated in Figure 6.1.

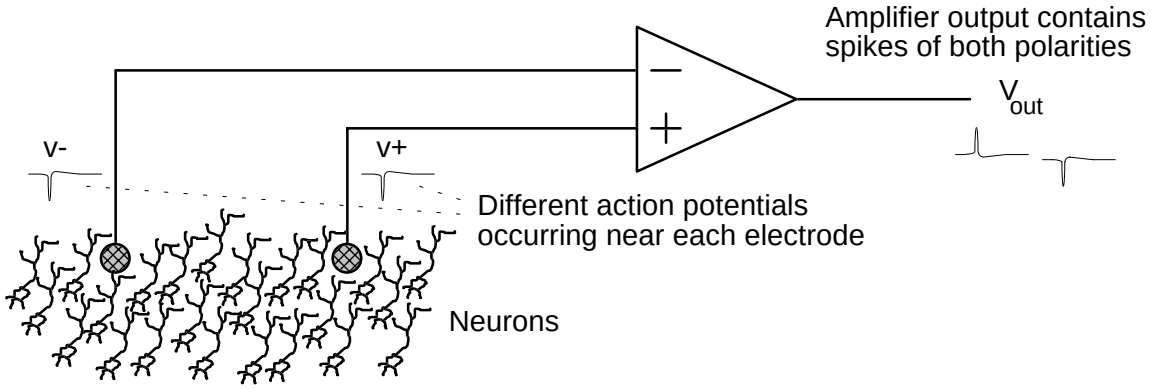

Figure 6.1: Action potential spikes are negative relative to a distant reference in the body, but differential measurements show positive and negative spikes.

6.1.2.1 The electroencephalogram (EEG)

A recording of the bioelectric signals generated by the cerebral cortex and deep brain structures is called the electroencephalogram, or EEG. The term EEG is normally used in reference to a relatively low-frequency signal (up to about 100 Hz) that can be measured on the scalp with skin surface electrodes. This signal is produced by the slow settling of ionic currents associated with the action potentials of many neurons. As different cognitive processes occur, the neurons in different regions of the brain are preferentially activated or suppressed, causing changes in the net ionic flows through the tissue. These ionic currents create the potential changes that can be measured on the scalp. But if small penetrating electrodes are inserted in the brain for the EEG recording, it is possible to observe the individual action potentials from nearby neurons as well. The EEG recorded with penetrating electrodes is still the summation of the

effects of innumerable action potentials occurring throughout the brain at different times, but it can be described by two semi-random components: a high frequency component (up to several thousand Hertz) that may include some distinguishable individual action potentials, and the relatively low frequency component (normally measured with scalp surface electrodes) that can be of large amplitude depending on the spacing of the electrodes between which the potential measurement is made. To distinguish it from the normal low-frequency EEG that can be measured on the scalp, the term "neural waveform" is generally used in this work to identify the complete signal recorded from the nervous system with penetrating electrodes. The high frequency component is due to the stochastic occurrence of action potentials in neurons near enough to the electrodes to produce signals large enough to be distinguishable combined with those from neurons farther away. So even in the absence of discernable action potential spikes, a high frequency "neural noise" signal will be present in most EEG recordings made with penetrating electrodes, provided that the amplifiers have sufficient bandwidth. Since the neural noise is composed of many small action potential spikes, it covers the same frequency spectrum as the identifiable action potential spikes. The spectral density of the neural noise is fairly flat out to about 7 kHz, where it begins to roll off. Thus while it is possible to separate the EEG signal from the high-frequency "noise" and action potential spikes in the neural waveform recording, filtering cannot be used to reduce the background neural noise to enhance detection of individual action potentials.

Both the normal EEG and the action potential spike signals are valuable for understanding the nervous system and its processing of information. Considerable attention has been given to the EEG since it is readily accessible, and it has been used to identify various states of mental activity, particularly in regard to epileptic seizures and sleep. However, EEG signals vary widely among people and lack consistent repeatability even in particular individuals, so specific relationships are difficult to establish. EEG patterns are in general quite complex, and become increasingly "desynchronized" and unpredictable when a person is alert or "thinking" [79, 82]. Neural waveform recordings that include distinguishable action potentials from one or more neurons have more recently led to considerable advances in the understanding of the nervous system. These recordings require the use of invasive electrodes, so most of the research has been conducted with animals. Since the neuron is the fundamental element of the nervous system's ability to communicate and process information, observation of individual neural signals is a key part of the study of its basic operation.

Much has been learned about the basic input and output of information from the brain through these studies, particularly in the visual, auditory, somatic, and motor systems [81].

6.1.2.2 The evoked response

An EEG recording taken while some stimulus is applied can reveal an *evoked response*. The evoked response is the "disturbance" in the EEG signal that results from the stimulus. When a stimulus such as a flash of light to the eye or an audible click is used, the disturbance in the EEG can be quite repeatable. Multiple recordings which are time-locked to the occurrence of the stimulus can be averaged together to extract the evoked response from the ongoing EEG activity and noise because these parts of the EEG signal will not be well correlated from recording to recording. Only the repeatable evoked response in the EEG will not tend to average out [79]. On recordings made with penetrating electrodes placed in the appropriate area of the brain, the evoked response may be large enough to be seen on single recordings. Furthermore, it may be possible to distinguish some of the individual action potentials that make up the evoked response, or at least changes in the firing rate (frequency of action potentials) of certain neurons that is related to the stimulus. In other words, neurons affected by the stimulus may have a tonic firing rate that is either increased or decreased by the stimulus, or they may be relatively inactive until the stimulus is applied. If the recording electrodes are located near such neurons, this activity may be recorded as part of the evoked response neural waveform. Synchronous averaging of these recordings is unlikely to bring out the individual action potential responses because of normal variability in the timing of the action potentials.

The visual evoked response (also called a visual evoked potential), elicited by a flash of light in the eye, has been studied extensively in various animals and in man [83-89]. Because it is easily elicited, and the strongest response is obtained in the occipital-parietal cortex which is readily accessible in the rabbit for surgical implantation of recording electrodes, the visual evoked response was chosen for the prototype testing in this research. It was expected that the normal EEG evoked response could be recorded by the prototype telemeter implant, and it was hoped that individual action potentials from one or more neurons could be observed as well. In the primary visual cortex, it is possible to strobe a localized area of the retina and repeatedly activate specific cortical neurons [85]. Although action potentials related to the evoked response would be

convenient for testing purposes, any action potential spikes would be useful for verifying the proper operation of the telemeter and to see whether the neurons in the vicinity of the microelectrodes were still functional and generating the same signals on the microelectrodes. Because Visual Evoked Potentials (VEPs) are generated in the visual cortex in response to a flash of light on the retina, behavioral issues are largely eliminated, simplifying the experiments needed to study the function of the implant and waveform stability over time.

6.1.3 Preliminary VEP recordings without telemeter

Though Choudhury [84] presented a thorough paper on the cortical projections of the albino rabbits they had bred in their colony, we needed to verify the location of the center of the visual field in the New Zealand White albino rabbits that we typically work with. A simple set of experiments were thus conducted to verify Choudhury's work and to refine the cortical coordinates for the center of the visual field. Briefly, the experiment consisted of anesthetizing the animal with an acepromazine, xylazine, ketamine cocktail and exposing the visual cortex. Using bregma (the point on top of the skull where the coronal and sagittal suture lines between the skull plates join) as a reference, microelectrodes were positioned at various locations while the center of the visual field was strobed with brief (100 μs) pulses of light from an LED. Synchronous potential recordings were then taken relative to a "distant" reference electrode placed outside the skull, and the magnitude of the evoked response was noted on a coordinate map. The evoked responses we observed were consistent with those reported by other researchers [83, 88, 89]. We found that the largest responses were obtained 11 mm caudal and 6 mm lateral to bregma in the contralateral cortex. This location was approximately 2 mm more caudal than the center located by Choudhury. Our measurement, however, was not meant to find the center of the visual field but rather to find the location of the maximum response to an LED flashed at the center of the eye using our setup. The difference in location could probably be accounted for by the relatively crude nature of our light spot system. Nonetheless, the location of interest for these tests was the site of the greatest evoked response using the LED strobe.

In order to verify that local neuron activity could be observed following a visual stimulus from an LED, VEPs were recorded using an eight-electrode silicon microelectrode array obtained from the University of Michigan - NIH Neural Communication Center. The

animal was anesthetized, and the primary visual cortex was exposed[8]. The eight-electrode array was lowered 2 mm into the cortex at various locations relative to bregma and VEPs were recorded in response to 100 μs light flashes in the contralateral eye[9]. A typical recording taken using the eight-electrode University of Michigan silicon array is shown Figure 6.2. The response is shown for the 100 ms following a single flash of the LED in the contralateral eye. Individual action potentials (the sharp spikes of about 150 μV amplitude) can be seen clearly on the trace for electrode 2 after 35 ms. The timing of these action potential spikes coincides with a large negative peak in the EEG evoked response seen on electrodes 3-8 and a small positive peak on electrode 1. This was repeatable, indicating that it may be possible to monitor these action potentials over time for evaluation of the stability of long term implants. In the case of chronic implants, the experiments would be similar except that the LED would be moved around to elicit neural responses near particular microelectrode contacts.

[8] Surgery performed by David Edell assisted by Bruce Larson at the West Roxbury VAMC

[9] Instrumentation and software developed by Bruce Larson

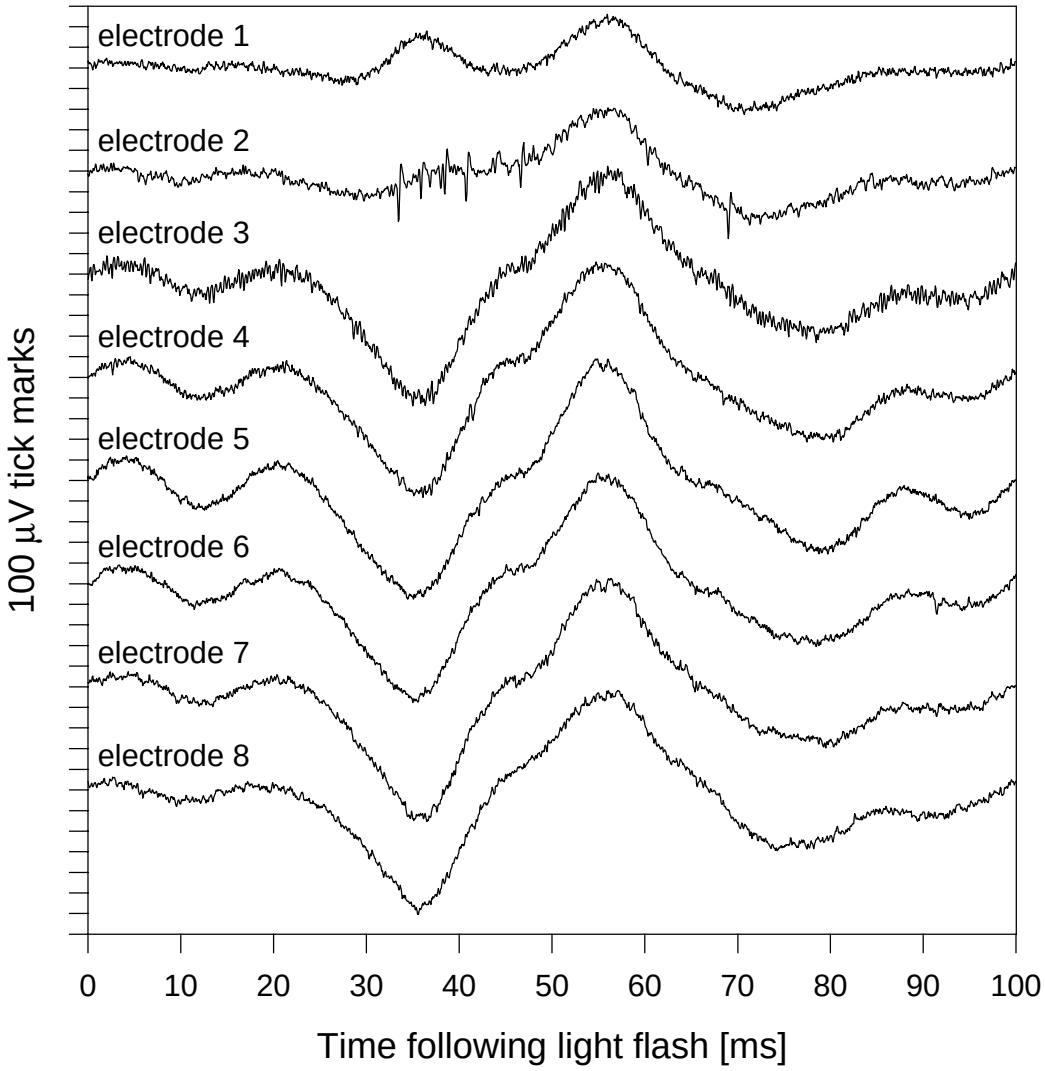

Figure 6.2: Visual evoked potential recorded acutely with UM array. Note the large action potential spikes in the evoked response recorded on electrode 2, which could be monitored over time to assess implant stability.

Since the low-frequency EEG evoked potential is produced by the activity of many neurons too far from the electrodes to yield individually distinguishable responses, differential measurements between closely-spaced electrodes can be made to decrease the amplitude of this neural waveform component. These differential recordings are useful when it is desired to observe only the activity of neurons near to the electrodes. To illustrate this benefit the recordings shown in Figure 6.2, which were measured relative to a distant reference electrode placed outside the skull, have been paired and subtracted to generate the software-differential traces presented in Figure 6.3. The vertical scale has been changed in this plot to show the relative increase in the individual

neuron activity component of the recording compared to the low-frequency EEG component.

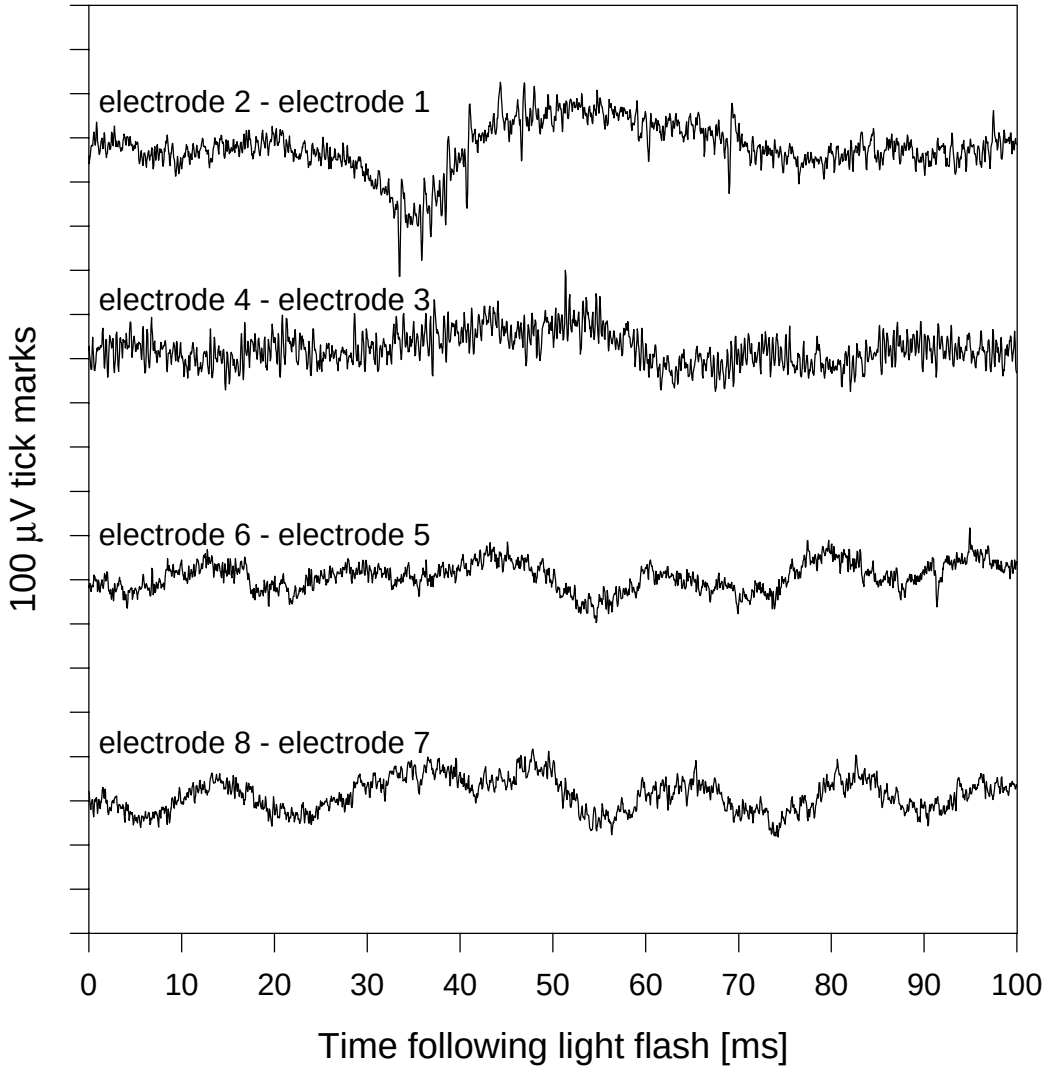

Figure 6.3: Software-subtracted recordings from UM electrode array to illustrate how differential measurements reduce amplitude of EEG, highlighting the activity of individual neurons in the evoked response.

The first trace in the plot of Figure 6.3 has been expanded in Figure 6.4 to show the individual action potentials visible in this evoked response neural waveform. If action potentials such as these can be seen in recordings made with a prototype telemeter, they can be used to further verify the high-frequency operation of the telemeter.

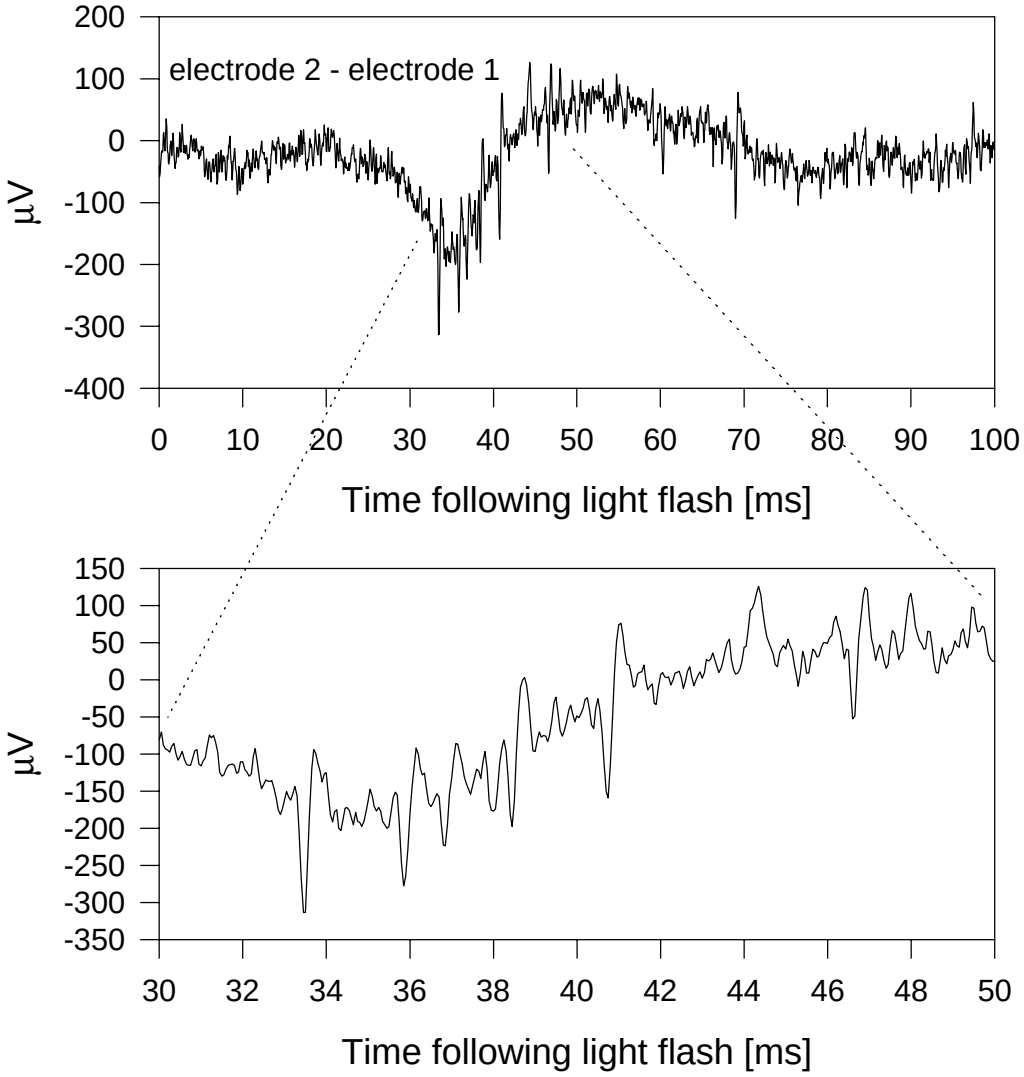

Figure 6.4: Detail view of individual action potential spikes in evoked response neural waveform recording.

6.2 Prototype telemeters

6.2.1 Rabbit VA18 implant

6.2.1.1 Circuit design and operation

True micropower operational amplifiers and comparators have recently become available as IC manufacturers target the low power portable electronics market. These components made it possible to assemble a pulse position encoded, optically linked neural waveform transmitter that was capable of encoding one channel of data with a

bandwidth of 20 Hz to 6 kHz while consuming less than 150 μW of electrical power[10]. Surface-mount technology provided miniature IC packages and micro-components such as resistors and capacitors that allowed the final assembly to be sufficiently small for implantation. The telemeter circuit was based on the design presented in Chapter 4. However, certain aspects of the design were changed in order to take advantage of components that gave the practical implementation lower power consumption.

The circuit of the first prototype telemeter is given in Figure 6.5.

[10] Implant developed and assembled jointly by Bruce Larson and David Edell

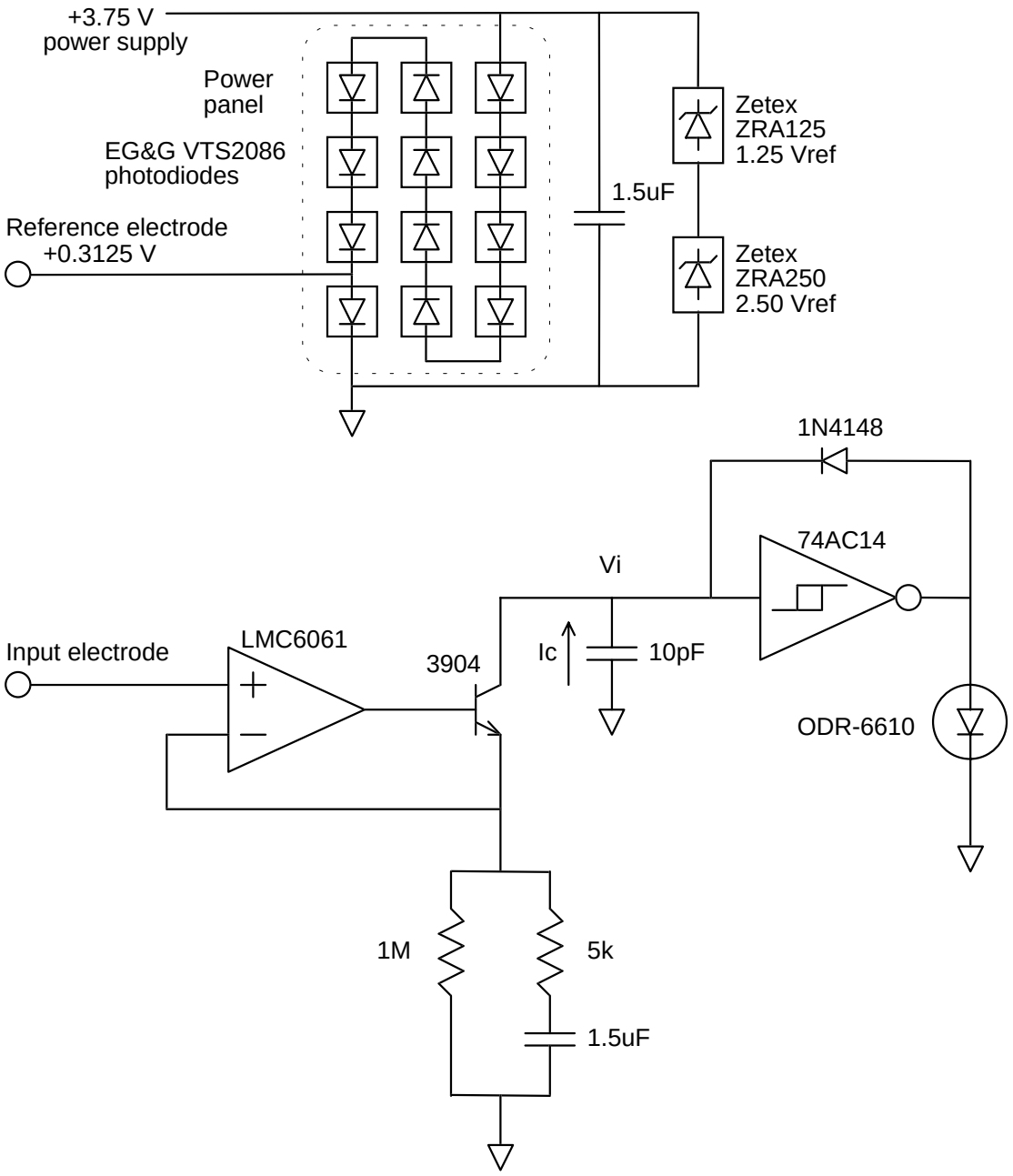

Figure 6.5: Schematic of VA18 telemeter with power supply.

The LMC6061 low power op-amp produced by National Semiconductor is specified to operate at 4.5 V with approximately 20 μA current, but we found that it had adequate performance at 3.75 V, which was easier to generate with the prototype power panel. The circuit potentials were referenced to the body of the rabbit by the reference electrode, which was a tap off of the power panel. This gave a relatively low impedance reference that did not require additional power. The input electrode was biased at the reference potential (0.3125 V, in the reference frame of the circuit) through the

conductive fluids of the body, since no DC current could flow between the electrodes. The feedback around the op-amp created a 0.3125 V DC drop across the 1 MΩ resistor, causing an average current of 0.31 μA to flow from the 10 pF integrating capacitor. The total capacitance at the integrating node and the hysteresis of the 74AC14 Schmitt trigger inverter was such that the average cycle rate of the pulse period encoder was 33 kHz. Since the sample period of the encoder is defined by:

$$\Delta t_{measured} - T_{delay} = \frac{C_i \Delta V_h}{I_c} = \frac{C_i \Delta V_h}{\left(\frac{V_b}{R_b} + \frac{v_{in}}{R_g} \right)},$$

and we know that $T_{delay} \le 20[ns]$ for the 74AC14, we can solve for $C_i \Delta V_h$:

$$C_i \Delta V_h \approx \left(\frac{1}{33[kHz]} \right) \left(\frac{0.3125[V]}{1[M\Omega]} \right) \approx 9.375[pC].$$

Thus the instantaneous period of this encoder is related to the AC component of the input electrode voltage (v_{in}) by:

$$\Delta t \approx \frac{9.375 \cdot 10^{-12}}{\left(0.3125 \cdot 10^{-6} + \frac{v_{in}}{5000} \right)}.$$

For example, a +250 μV input signal gave a period of about 25.9 μs, and a -250 μV input signal gave a period of about 35.7 μs for this encoder circuit. The capacitor reset takes only as long as the Schmitt trigger propagation delay, which is about 10 ns. In a departure from the circuit design presented in Chapter 4, a standard silicon diode was used for the capacitor reset switch, and the output LED was connected directly to ground. While this added a component to the assembly, it increased the intensity of the light flash, making detection easier. The output LED is strongly forward biased during the capacitor reset phase; it probably flows almost 30 mA. But since the duty cycle is very low, the average current through the LED is only 10 μA.

The bandwidth of the encoded signals was limited on the low frequency end to about 21 Hz by the 5 kΩ resistor and 1.5 μF capacitor network. The high frequency cut-off can be determined with the aid of the block diagram given in Figure 6.6, which represents the small-signal feedback loop around the op-amp for frequencies greater than 21 Hz.

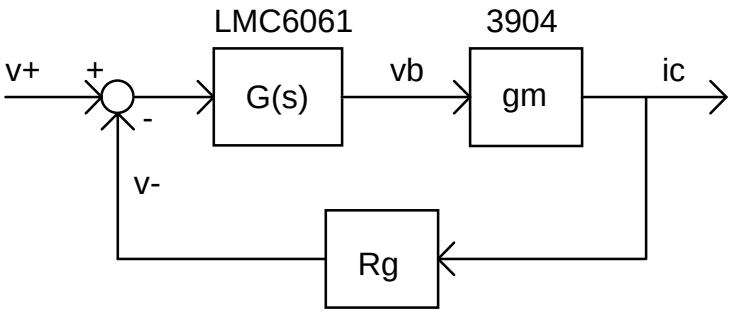

Figure 6.6: Block diagram for ascertaining high frequency cut-off of VA18 encoder.

The relationship between the small signal input voltage and collector current (which determines the signal component of the integration period) is relatively constant at $1/R_g$ as long as the loop gain is greater than unity. The transfer function of the op-amp can be approximated by $G(s) \approx 2\pi \cdot 10^5 / s$, and the transconductance of the transistor is about $12[\mu A/V]$ (with $0.3125[\mu A]$ DC bias current). Since $R_g = 5[k\Omega]$, the loop gain cross-over occurs at about 6 kHz, setting the high frequency limit for encoded signals.

Three-terminal voltage regulators were tested as possible means to provide a stable supply voltage for the encoder circuit. Unfortunately, they either required too much quiescent current or start-up current to operate. Instead, a series of two-terminal bandgap voltage references (the Zetex ZRA125 and ZRA250) were used in parallel with the panel to limit its output voltage to 3.75 V. This arrangement simply shunted excess current through the references. These references did require approximately 27 μA current in order to function properly, which the power panel had to provide in addition to the 40 μA current needed by the encoder circuit. A low-power bandgap reference was later designed with the integrated circuit telemeters to reduce this additional current requirement. The integrated bandgap reference provided adequate regulation for the IC telemeter circuits while requiring less than 3 μA current.

6.2.1.2 Physical assembly

A surface mount device implementation of this circuit was assembled, packaged, and connected to a pair of sharpened platinum-iridium wire electrodes for implantation into the visual cortex of a rabbit. It is important to note that typically only one electrode from the Michigan probe study showed substantial single unit activity at any particular implant location. Since the implant was only a single channel device, relatively large electrode areas were used (~5,000μm^2) in an attempt to improve the odds of successfully

recording from active neurons. While this reduces the amplitude of individual action potential recordings, it increases the likelihood of observing them. The electrode pair (reference and input electrodes) between which the biopotential measurement is made were spaced about 4 mm apart. This spacing is wide in terms of the dimensions of the rabbit visual cortex, and was chosen so that the low frequency EEG component of the neural waveform would be readily detected. The EEG component would be useful for evaluation of the prototype implant, particularly if no single action potential spikes were observed.

Implementation of the micropower panel for the prototype was also possible with commercially available technology. An array of 12 photodiodes capable of providing the 3.75 V and 67 μA required for operation of the prototype circuit (including the 27 μA needed by the shunt voltage regulator) was hand-assembled from EG&G VS2086 photodiode chips. While this panel was quite large (0.5"x1.5"), there was adequate room for it under the skin along the dorsal surface of the nose of the rabbit. It should be noted that the photodiodes used were optimized for optical detection rather than power generation, but they were the only devices available to us at that time.

The plastic package of an Opto Diode ODR-6610 high-efficiency 660 nm red LED was machined down to the minimum possible size for use in this telemeter. This enabled us to take advantage of the parabolic reflector that was part of this package, before we had developed the platinum reflector mount for chip LEDs discussed in Chapter 5. The encoder circuit, output LED, power panel, and supply conditioning circuit were finally wired together and encapsulated in silicone to complete the first prototype neural waveform optical telemeter. This implant had greater power consumption and larger overall dimensions than the integrated versions being developed, but the system function was equivalent, particularly in regard to the optical coupling issues.

6.2.1.3 Implantation and in-vivo testing

This first optically linked neural waveform transmitter was implanted March 1, 1996[11] and functioned for four weeks. It was implanted in a rabbit, VA18, under the skin over the cranium. While the proposed brain implants will be on the pia mater (the absolute surface of the brain), the transmitted light to and from the circuit will pass through the skin and a quartz window in the skull as demonstrated in earlier tests (Chapters 2 and

[11] Surgery performed by David Edell assisted by Bruce Larson at the West Roxbury VAMC

3). Figure 6.7 is an X-ray image of the implant in place on the animal's head just after surgery. Large, multiunit intracortical recording electrodes (5,000 μm^2 elliptical facets) were implanted in the visual cortex (occipital), spaced 4 mm apart. The encoding circuitry and output LED were located just behind the eyes over the cranium. The conditioning circuitry and power panel were located on the nasal bone. Immediately following implantation, the animal was tested using visual evoked potential methods to drive neurons in the visual cortex. A flashlight provided sufficient illumination to power the circuit fully through the skin, but an 880nm infrared LED was used for this purpose. The infrared LED minimizes background illumination near the wavelength used for data transmission (660 nm). In addition, the photodetector was fitted with a narrow band optical filter to minimize interference from ambient lighting and the infrared illuminator.

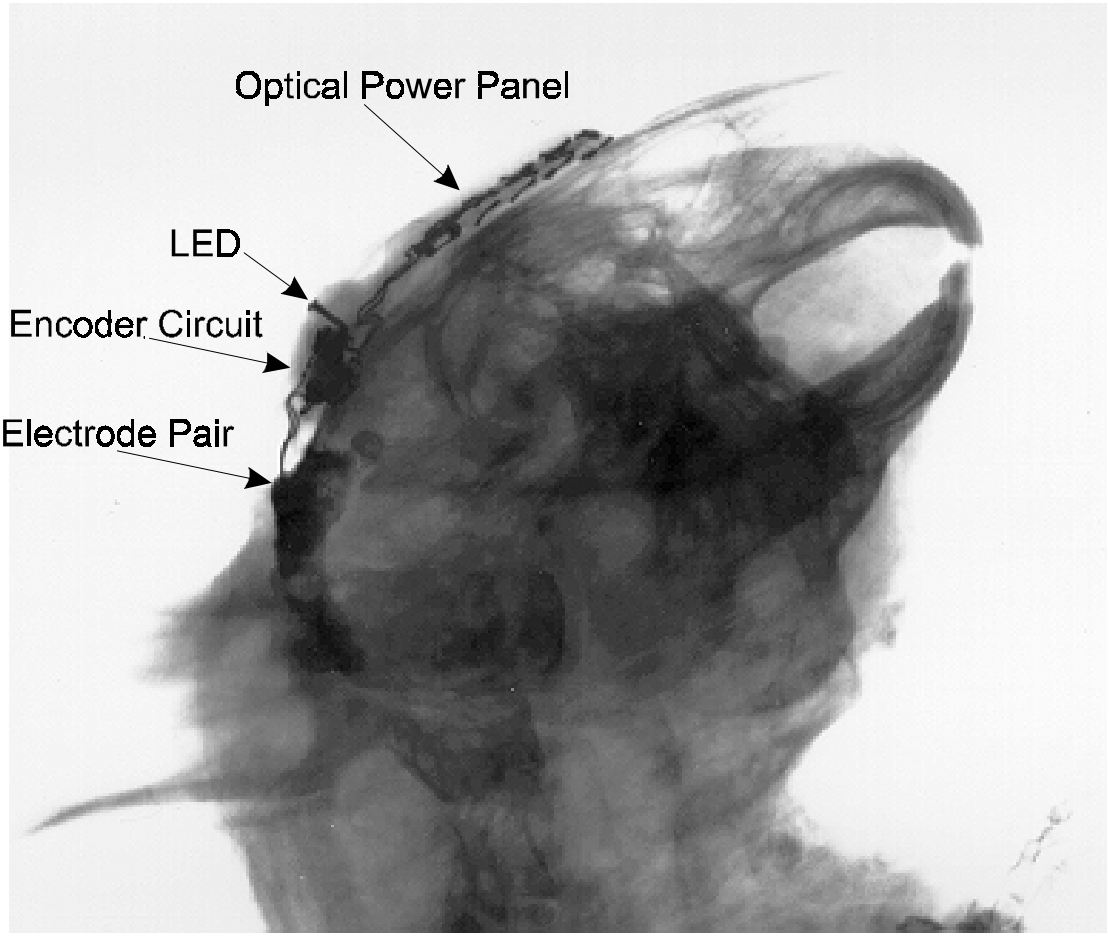

Figure 6.7: Lateral X-ray view of first implanted optically based neural waveform transducer, showing electrode insertion area, encoding circuit, output LED, power conditioning circuit, and optical power panel. Top of rabbit's nose is at upper right of image, ear is at lower left.

Reasonably clean post-operative multi-unit VEP recordings were obtained as shown in

Figure 6.8. These VEPs are consistent with our previous acute recordings and those reported in the literature. Individual action potentials, though small from the large electrodes used, are visible on the evoked responses. The burst of action potential spikes between 30 ms and 45 ms after the light flash stimulus is similar to the neural activity observed in the acute microelectrode experiment (Figure 6.4) that coincides with an early peak in the evoked EEG response. When the area of the implant fully healed, much cleaner appearing action potentials were observed. The equivalent input noise of the complete system post-implantation (including the normal, ongoing EEG activity) is approximately 25 μV_{rms}. There was no motion artifact, radio frequency or 60 cycle electromagnetic interference, since the electronics of the telemeter were shielded by the conductive fluids of the animal and completely isolated from ground potentials by virtue of the wireless design. Attempts to create these problems by placing laboratory equipment that normally produced these types of interference in previous experiments with external amplifiers were unsuccessful with the implanted telemeter system (as desired). To further rule out the possibility that the observed waveforms were due to some artifact of the experimental setup, a piece of opaque paper was inserted between the LED strobe and the rabbit's eye to block the light during VEP experiments. This eliminated the evoked response in the neural waveform recordings, and only the ongoing EEG and neural activity was then observed.

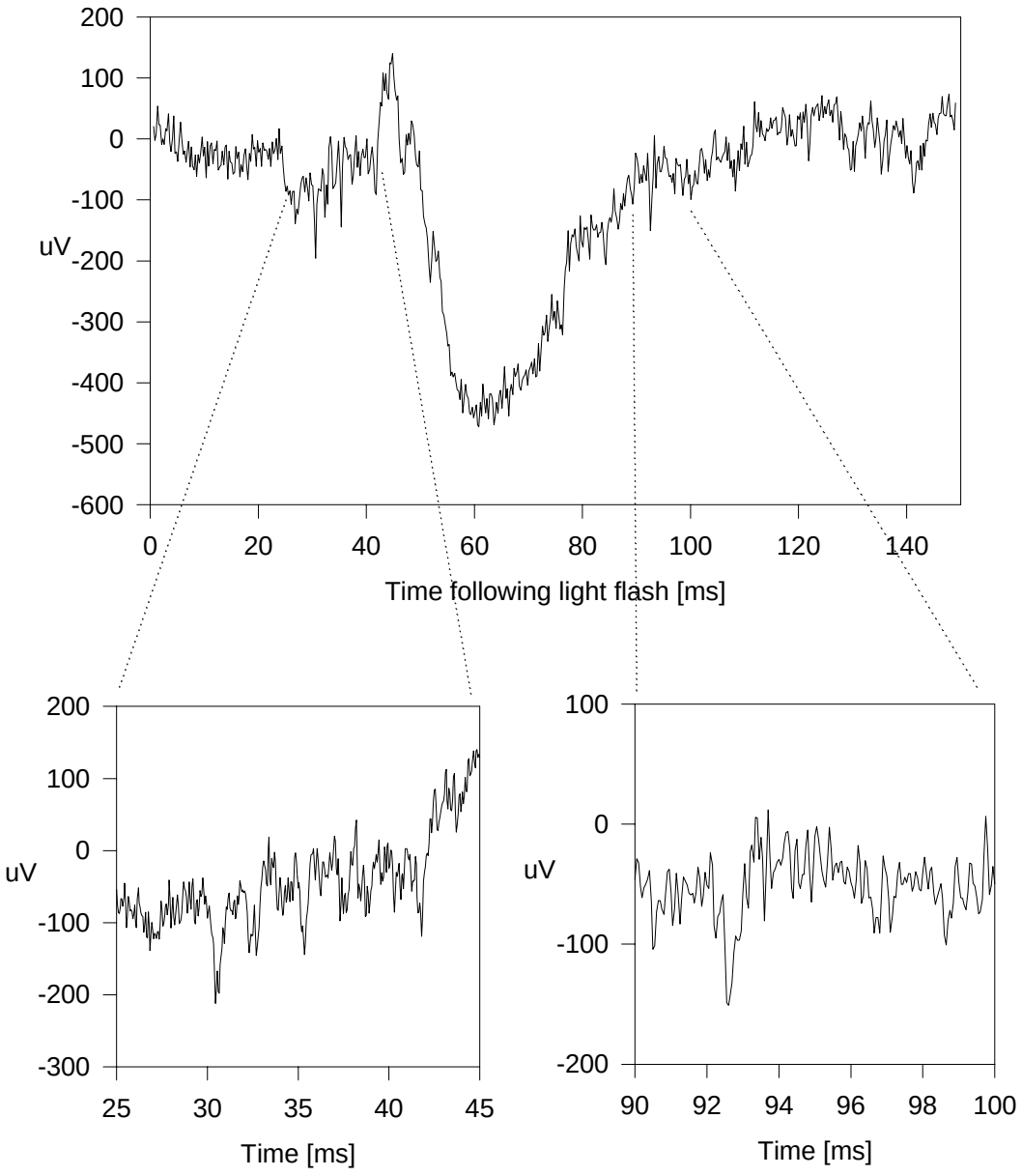

Figure 6.8: Recordings of visual evoked potentials from rabbit VA18 made with the first optically linked neural waveform transmitter, showing likely individual action potentials superimposed on evoked EEG waveform.

The implant in rabbit VA18 became intermittent in its operation due to encapsulation failure after four weeks. Figure 6.9 shows results taken from VA18 just prior to sacrifice for removal of the optical transmitter. Under anesthesia, efforts were made to repair the encoder, but only temporary operation could be restored. When the repair attempt failed, a final recording session was performed by attaching a laboratory amplifier to the

implanted electrodes and recording VEPs. The top trace shows encoded signals with essentially the same characteristics as those observed with direct amplifier connection. The neural noise observed for the lower trace was less than that observed with the encoder, presumably due to the anesthesia.

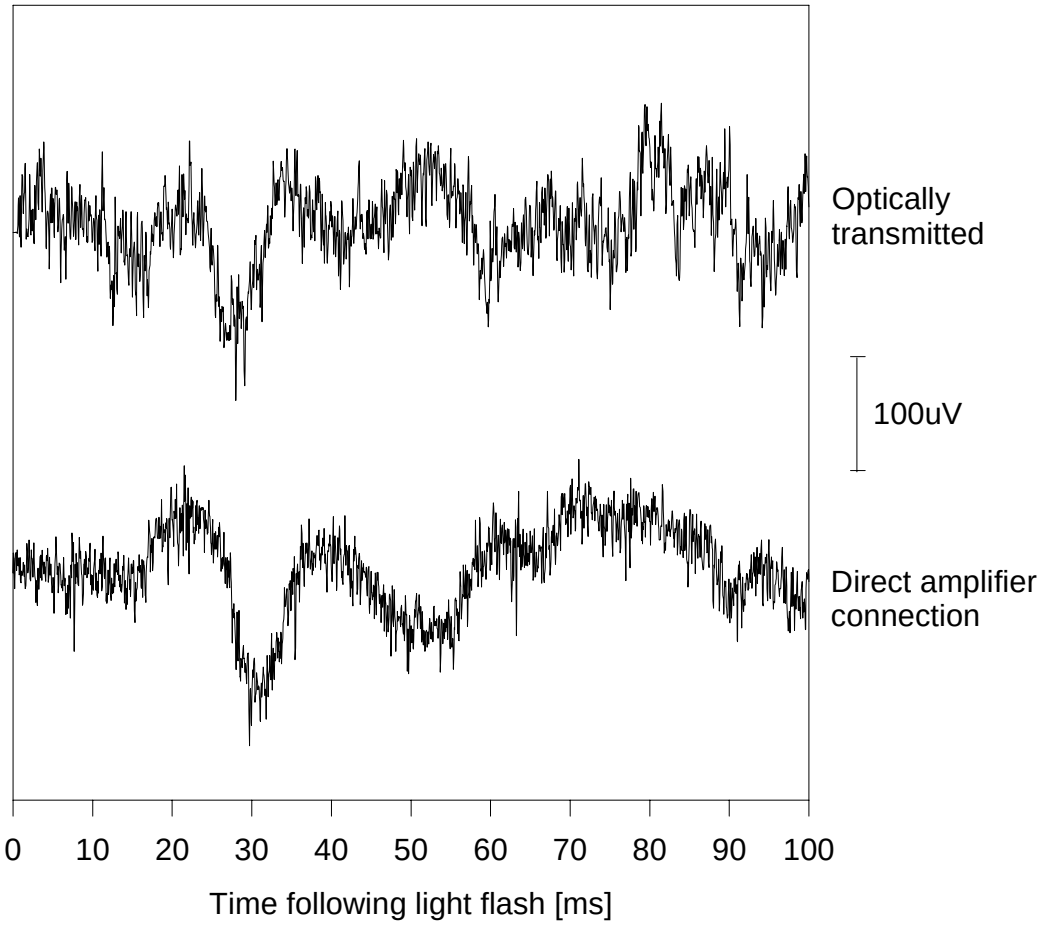

Figure 6.9: Final experiment just prior to removal of optical transmitter from VA18 due to encapsulation failure. Note similarity of waveforms, especially the action potential spikes. The direct connection recordings were taken with the animal under anesthesia and thus are slightly quieter.

A fabrication error led to the failure of the first neural waveform optical telemeter. Part of the problem was related to the number of discrete components that had to be assembled. In addition, the silicone encapsulant used in the first implant was chosen for optical clarity, but suffered from poor mechanical properties. This led to the opening of a pathway along Teflon-insulated wires leading to the microelectrodes. Saline intrusion reached a solder joint, thereby setting up a galvanic cell that added sufficient electrical offset to drive the circuit out of its operating range. By drying the leaky area of the

implant at the time of removal, proper function was returned to the circuit, enabling us to make the final recordings.

6.2.2 Rabbit VA19 implant

A second optically linked neural waveform transmitter was designed and improved based on results from the first implant[12]. It was implanted in rabbit VA19 on August 19, 1996[13], and continues to function flawlessly as of December, 1998. This second implant was constructed with far fewer parts and was encapsulated with a more flexible, more adhesive silicone. In addition, it was saline soaked for 2 weeks prior to implantation to test the encapsulation.

6.2.2.1 Improved circuit design, operation, and assembly

The improved encoder circuit used for VA19 is shown in Figure 6.10.

[12] Implant developed and assembled jointly by Bruce Larson and David Edell

[13] Surgery performed by David Edell assisted by Bruce Larson at the West Roxbury VAMC

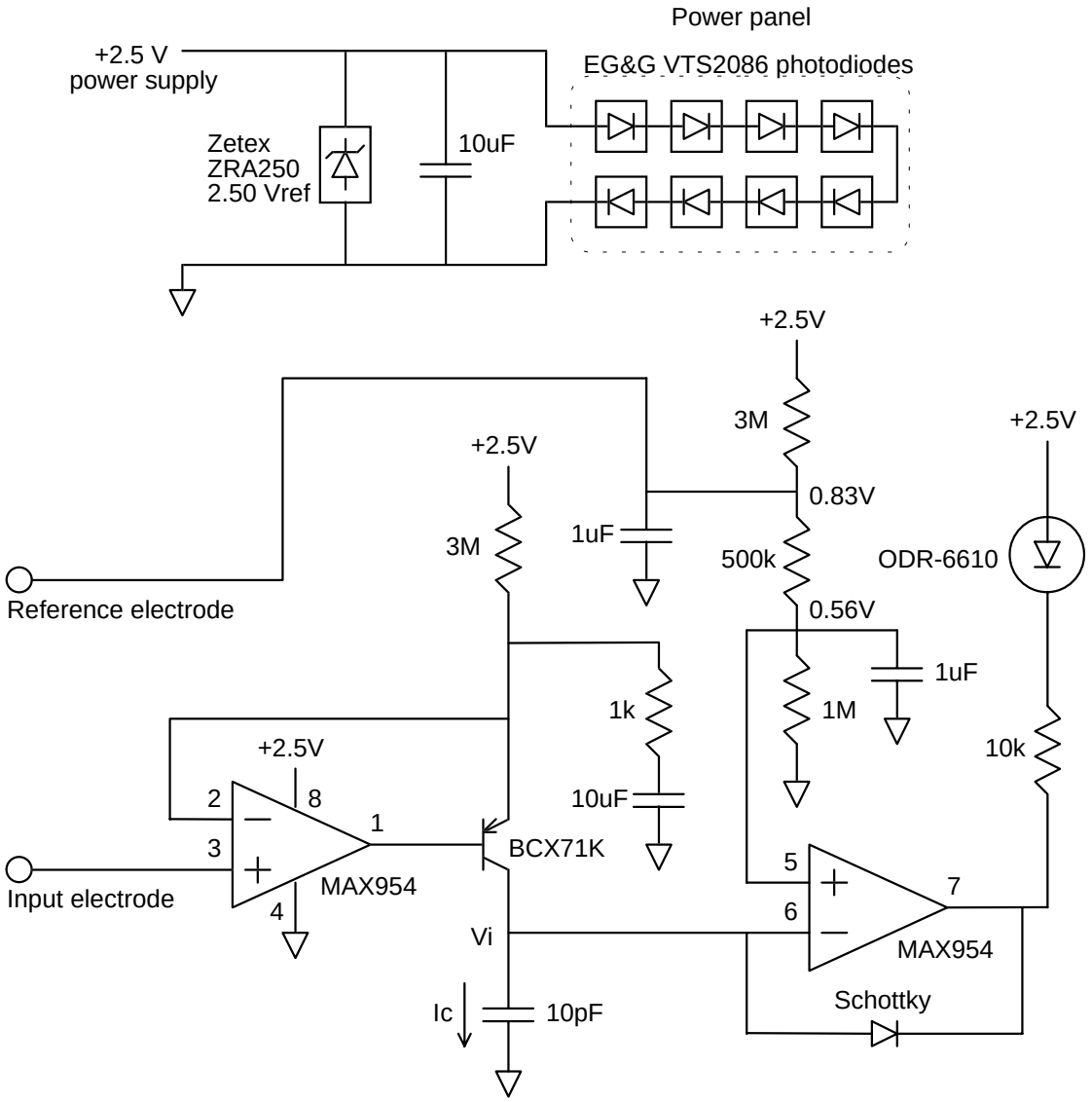

Figure 6.10: Improved circuit design of second telemeter prototype.

A combined operational amplifier and comparator, the Maxim Integrated Products MAX954, was key to this new design, allowing operation of the circuit at 2.5 volts with less than 30 μA current. Because of the limited common-mode input ranges of the op-amp and comparator (0 V to 0.9 V with the 2.5 V supply), it was convenient to "invert" the circuit. A PNP transistor designed for low current operation was used to flow positive current onto the integrating capacitor, so that its voltage rises during the integration phase. When the integrating capacitor voltage reaches the 0.56 V reference level set by the resistor divider, the comparator output goes low. The comparator takes the place of the Schmitt trigger in the previous design, and its transition delay eliminates the need for hysteresis. Since the comparator exhibited a 3.5 μs delay before changing from the low

output state to high, the capacitor voltage has time to settle to 0.3 V, the sum of the comparator low output voltage and the Schottky diode drop. During this time, the output LED flows 66 μA. The average pulse frequency of this encoder was 37.7 kHz, so the average current through the LED is only 8.7 μA.

Operation of this circuit is otherwise similar to implant VA18, with changes in the bias and signal pathways to increase signal "gain", the conversion between input voltage and pulse period. The bias resistor divider references the circuit to the body of the animal so that the input electrode will be at 0.83 V DC relative to the circuit ground in the schematic. The feedback loop around the op-amp thus creates a 1.67 V drop across the 3 MΩ resistor at the emitter of the PNP transistor, causing 0.55 μA to flow from the collector onto the integrating capacitor. The average period of this encoder circuit is 26.5 μs. Since the comparator exhibited a 4.5 μs transition delay from the high output state to low, in addition to the 3.5 μs delay for the other transition, the actual time that the integrator takes to go from the reset voltage of 0.3 V to the comparator threshold of 0.56 V was only 18.5 μs. This indicates that the total capacitance at the integration node, including the 5 pF discrete capacitor, is about 40 pF. However, there appeared to be considerable charge injection from the Schottky diode capacitance when the comparator output switched high, which invalidates this simplistic analysis to some extent. Because of the small signals and capacitances involved, direct measurement of the voltage waveform at the integrating node was unsatisfactory with the equipment available. The scope probe impedance was low enough to significantly interfere with the measurement. So instead of selecting the integrating capacitor analytically, the 5 pF discrete capacitor was chosen empirically to trim the average pulse period.

The relationship between the instantaneous period of this encoder and the AC component of the input electrode voltage (v_{in}) is approximately given by:

$$\Delta t_{measured} - T_{delay} = \frac{C_i \Delta V_h}{I_c} = \frac{C_i \Delta V_h}{\left(\frac{V_b}{R_b} - \frac{v_{in}}{R_g} \right)},$$

where $C_i \approx 40[pF]$ and the hysteresis voltage is replaced by the measured capacitor integration range so that $\Delta V_h \approx 0.256[V]$. Solving for the observed period of the encoder then yields

$$\Delta t_{measured} \approx \frac{10.2 \cdot 10^{-12}}{\left(0.55 \cdot 10^{-6} - \frac{v_{in}}{1000}\right)} + 8 \cdot 10^{-6}.$$

For example, the pulse period of this encoder circuit is about 42 μs for a +250 μV input signal, and about 20.8 μs for a -250 μV input.

The low frequency cut-off of encoded signals is set to about 16 Hz by the 1 kΩ resistor and 10 μF capacitor network. Applying the same analysis as for VA18, the high frequency cut-off is equal to the unity gain frequency of the feedback loop of the op-amp. The block diagram of Figure 6.6 can be used by substituting the approximate transfer function of the MAX954 op-amp, $G(s) \approx 2\pi \cdot 125000/s$, and the transconductance of the transistor, $21[\mu A/V]$. The MAX954 is not unity-gain compensated, but is stable with feedback less than 1/10. Fortunately, in this circuit, the high-frequency feedback from the output of the op-amp to its inverting input is approximately $g_m R_g$, which is about 1/47. Since $R_g = 1[k\Omega]$, the loop gain cross-over occurs at about 2.6 kHz, setting the high frequency limit for encoded signals. While this high-frequency cut-off is lower than desired for neural waveforms, the bandwidth could only be improved by increasing DC current through the transistor or increasing R_g. These solutions either increased power consumption, increased the low-frequency cut-off, or decreased signal gain. It was decided that it was preferable to have low power consumption and high gain (voltage-time conversion) over this bandwidth, and that corrective filtering could be used to flatten the spectral response of the received and decoded signals out to 7 kHz if desired. This can be done with the understanding that the signal-to-noise ratio will be lower above 2.6 kHz, since the encoded signal "gain" rolls off with a single pole response.

A power panel capable of providing 75 μW to the encoder circuit was needed to power this prototype. An 8 cell power panel was constructed from EG&G VTS2086 photodiodes that was 2/3 the size of the previous implementation. A two-terminal 2.5 V reference was used in parallel with the panel to stabilize its output voltage. This bandgap reference requires at least 27 μA to properly regulate the voltage. Since this is almost as much current as the encoder circuit consumes, a more efficient reference could decrease the total optical power requirement significantly. Also, as the subsequent analysis of power panel design revealed in Chapter 3, this panel would have

been more efficient as a 2.5 V supply if it had 10 diodes in series. However, the smaller size of this panel and encoder circuit reduced the overall dimensions of the implant to less than 50% of the first implant, which was a substantial improvement.

Once again, to ensure that neural waveforms would be accessed by the microelectrodes, a pair of large contact area platinum-iridium wire electrodes, 2.5 mm long and 2 mm apart, were fabricated in a silicone pad. The contacts of the electrode wires were elliptical facets approximately 5,000 μm^2 in area. The closer spacing of these electrodes reduces the magnitude of the slow wave VEP response in order to minimize the possibility of saturating the amplifier with a signal that is too large. Action potentials and neural noise, however, are not attenuated by this spacing since they are from much more localized sources.

6.2.2.2 Implantation and testing

Figure 6.11 shows the implant in place in rabbit VA19. Note the thinner overall height of the implant, the shorter power panel and more compact circuit. The silicone encapsulation visible in this X-ray was Nusil 2186 material which is more adhesive and flexible than that used for the VA18 implant. The electrodes are not visible, but are located just caudal to the circuit.

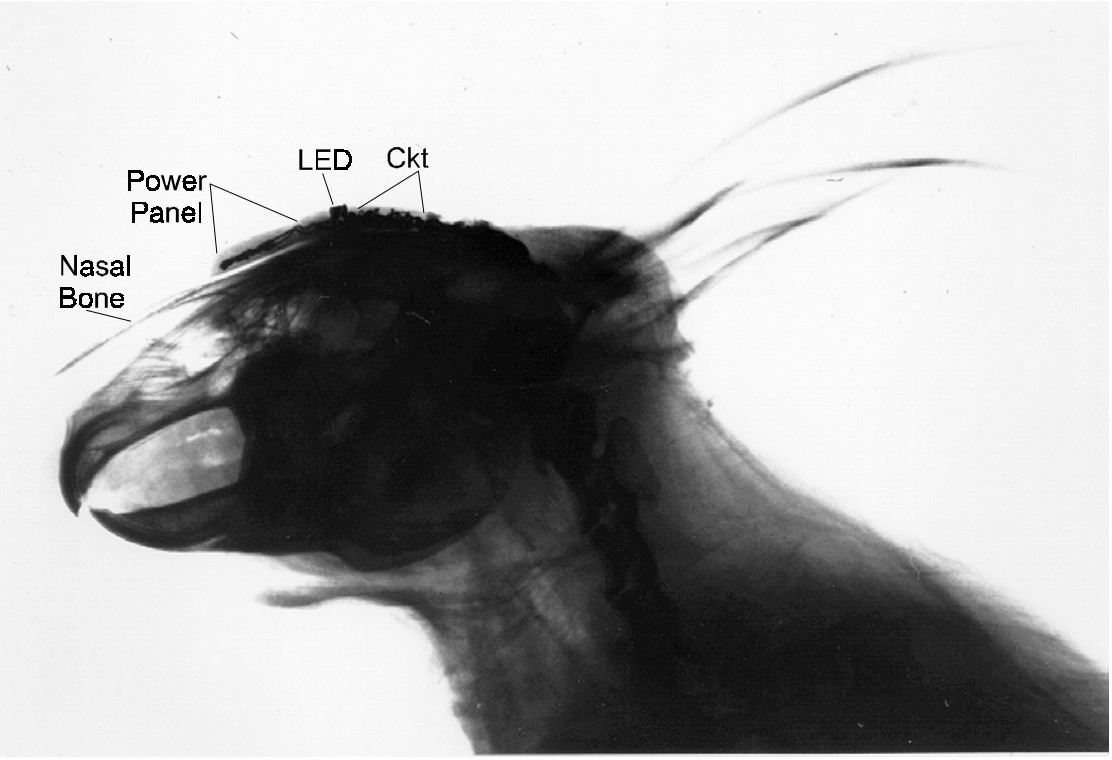

Figure 6.11: Lateral X-ray view of VA19 implant. Note smaller sized power panel and lower profile compared to VA18 implant.

6.2.2.2.1 Noise

The noise of the encoder is summarized in Figure 6.12, which plots representative noise data acquired during implant assembly and before and after implantation. Before the implant was encapsulated in silicone, the input-referred noise of the encoder circuit was 8.5 μV_{rms}. Over the bandwidth of the encoder, the RMS noise from the op-amp was approximately 8 μV_{rms}. Thus, nearly all of the noise of the encoder was due to the input operational amplifier. Under saline soak, the total RMS noise was 18 μV_{rms}. Thus the electrode noise (in saline soak) was 16 μV_{rms}. Once implanted, while under anesthesia, the RMS noise dropped to 14 μV_{rms} which is a combination of neural, electrode, and amplifier noise. Recall that the term "neural noise" refers to the summation of innumerable action potential spikes that occur too far from the recording electrodes to produce individually identifiable waveforms. In this work, it will also be used more generally to describe all of the ongoing neuroelectric (EEG) activity that is not an evoked response. The reduction in total noise immediately after implantation compared to the saline soak condition was most likely due to lower electrode impedance in the tissue fluids. Subtracting the noise under anesthesia, when neural activity was greatly

reduced, from the noise of a typical wakeful neural recording (about 27 μV_{rms}) gave an estimate of the background neural noise of 23 μV_{rms} over the encoded signal bandwidth.

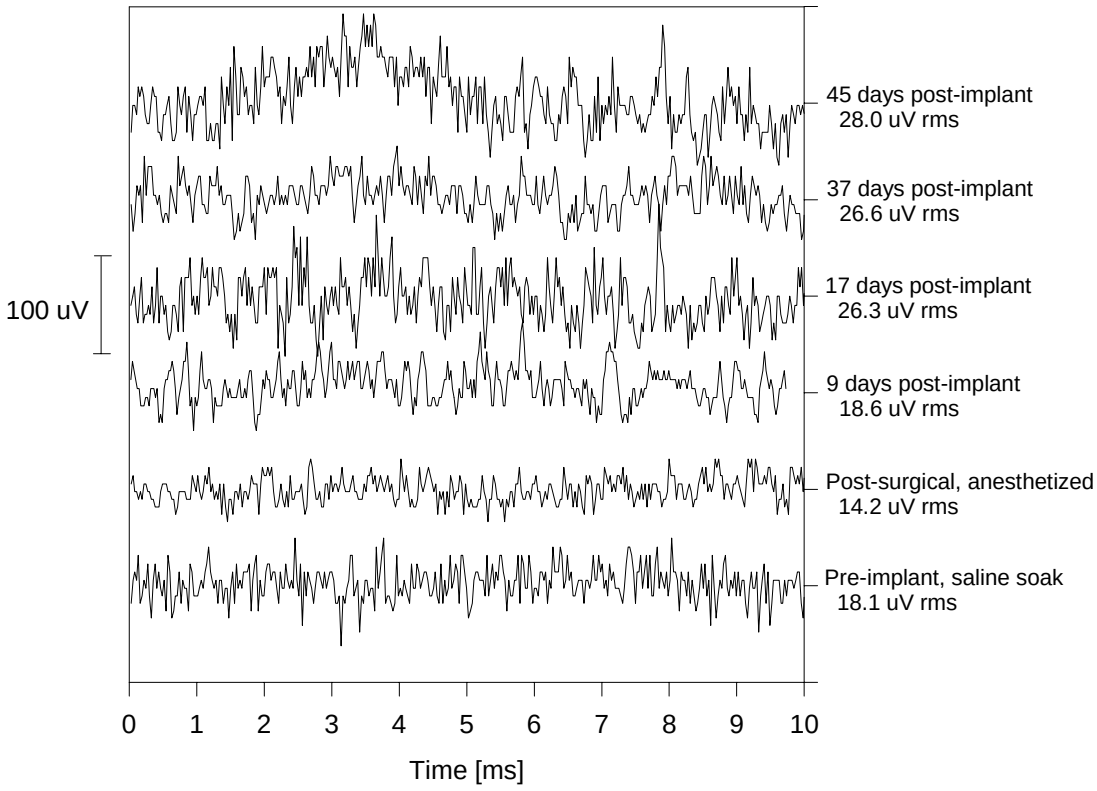

Figure 6.12: Sample recordings of VA19 encoder noise and ongoing neuroelectric signals (neural noise).

6.2.2.2.2 Visual evoked potential testing

Post-operative VEPs were recorded while the animal was recovering from anesthesia and thereafter. The VEP waveforms from VA19 were consistent with those previously observed in our research, and with those published in the literature. Blocking the light flash from the eye with a piece of dark paper eliminated the observed evoked response, so that neural waveforms such as those presented in the top four traces of Figure 6.12 were then observed. Figure 6.13 shows example VEPs recorded at various times since the implant was accomplished. These VEPs were elicited by flashing a green LED in the center of the visual field for 100 μs at the beginning of each recording. Not only did the elicited waveforms become more distinct with time, they were more reproducible from recording to recording as the animal recovered from the telemeter implant surgery. An interesting observation that merits further investigation is that the background neural activity appears to be different from day to day.

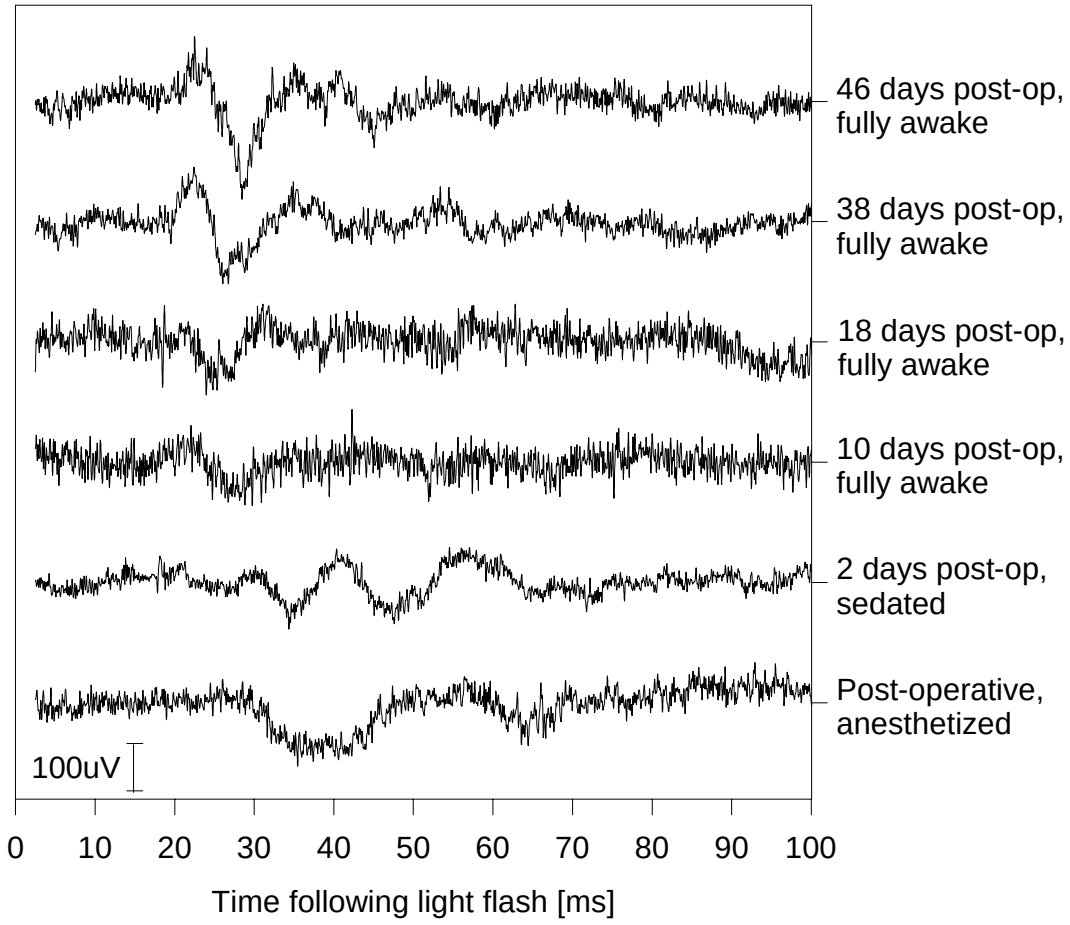

Figure 6.13: History of evoked potential data transmitted from VA19 from post-op to 46 days. Single LED strobe of light at center of visual field was used to elicit all responses.

Figure 6.14 shows four different evoked potential recordings taken with an improved decoder that allows longer data acquisition times before the memory buffers are full. This data could also be taken continuously, but would rapidly fill available storage space. Clearly observable features of the evoked response are the initial excitatory effects of the light flash from 20-100 ms followed by a period of suppressed activity, enhanced activity at 200 ms, then a return to baseline activity.

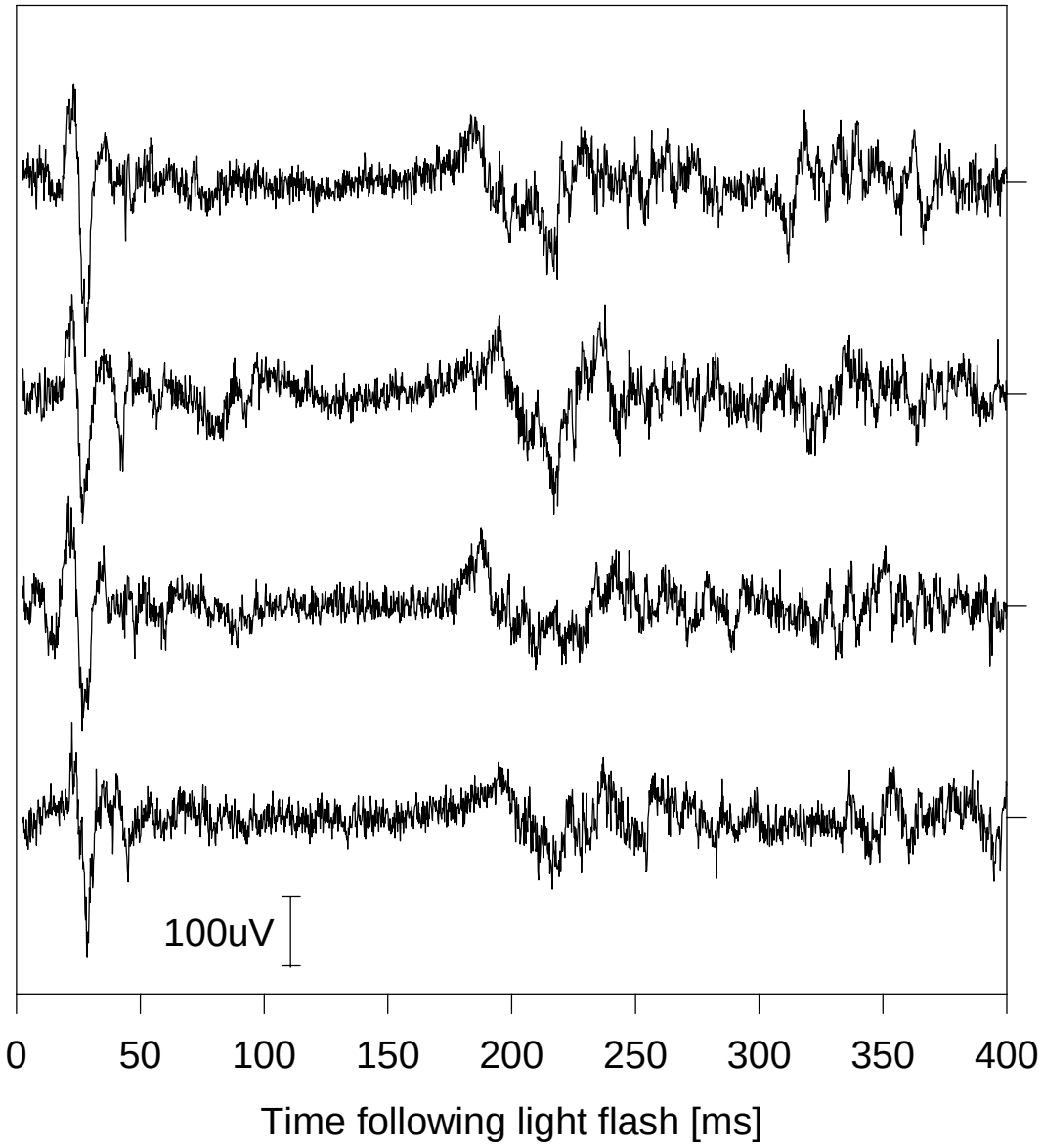

Figure 6.14: Four optically telemetered VEP recordings taken from rabbit VA19, six weeks after implant surgery. Improved decoder system allowed longer data records.

Control experiments were performed routinely to test the telemeter and VEP experiments. To verify that the evoked responses were due to the light stimulus on the retina, VEP recordings were made with a piece of dark paper between the LED strobe and the rabbit's eye to block the light stimulus. All other aspects of the experiment were the same. These produced recordings without the evoked response. When the light was blocked, recordings had the same type of EEG activity as those made without any stimulus. Another good control experiment was to flash the light in the eye ipsilateral to the location of the electrodes in the brain. Normally the light flash stimulus is presented

to the eye contralateral to the electrodes, since the left and right optic nerves cross the midline so that the left visual field is represented in the right hemisphere of the brain, and vice-versa. As expected, stimulation of the ipsilateral eye evoked no observable response. Example recordings of these control experiments (six weeks after surgery) are presented in Figure 6.15 for comparison with the normal VEP.

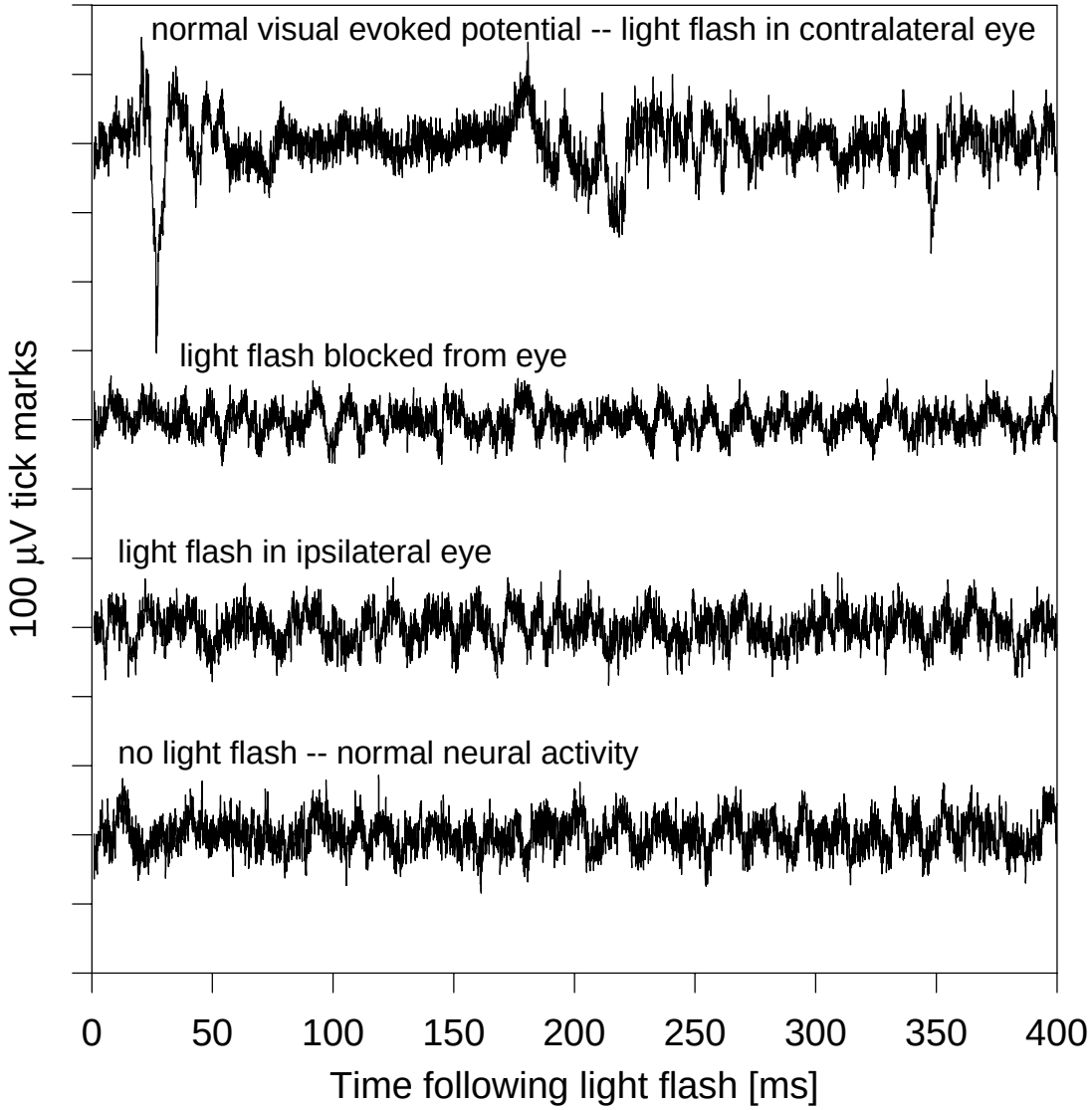

Figure 6.15: Control experiments used to verify VEP recordings. When the visual stimulus was blocked by paper or presented to the wrong eye, the recordings showed only the normal background neural activity.

To more clearly show the EEG evoked response, and to identify possible individual action potentials in the VEP recordings, the filtering and averaging techniques discussed previously were applied. As mentioned, the traditional EEG component of the

recordings can be separated from the high-frequency action potential spikes and neural noise by frequency selective filtering. The spectral content of the EEG component is mostly below 100 Hz, while the action potentials and neural noise can be adequately represented by the neural waveform signal content from about 100 Hz to 6 kHz. Because the neural noise is of the same bioelectric origin as the action potential spikes, these signals can only be distinguished by their amplitudes.

The EEG evoked response can be extracted from the ongoing neuroelectric activity by synchronously averaging many VEP recordings time-locked to the occurrence of the light flash stimulus. The top trace of Figure 6.16 shows the average of 85 VEP recordings taken on July 10, 1998. Also shown in this figure are the EEG signal component below 100 Hz, and the remaining signal above 100 Hz. As predicted, most of the neural noise and action potential signals have been averaged out because of the variability in the timing of individual action potentials, leaving only the low-frequency ensemble response of the nervous system. The shape of this average evoked response is slightly different from the evoked response seen in the recordings presented in Figure 6.14 because of differences in the positioning of the LED strobe. The location of the LED strobe determines which part of the visual field is stimulated, and therefore which areas of the visual cortex are activated. When the light flash stimulus was blocked with dark paper, the average of the recordings simply approached a flat zero response.

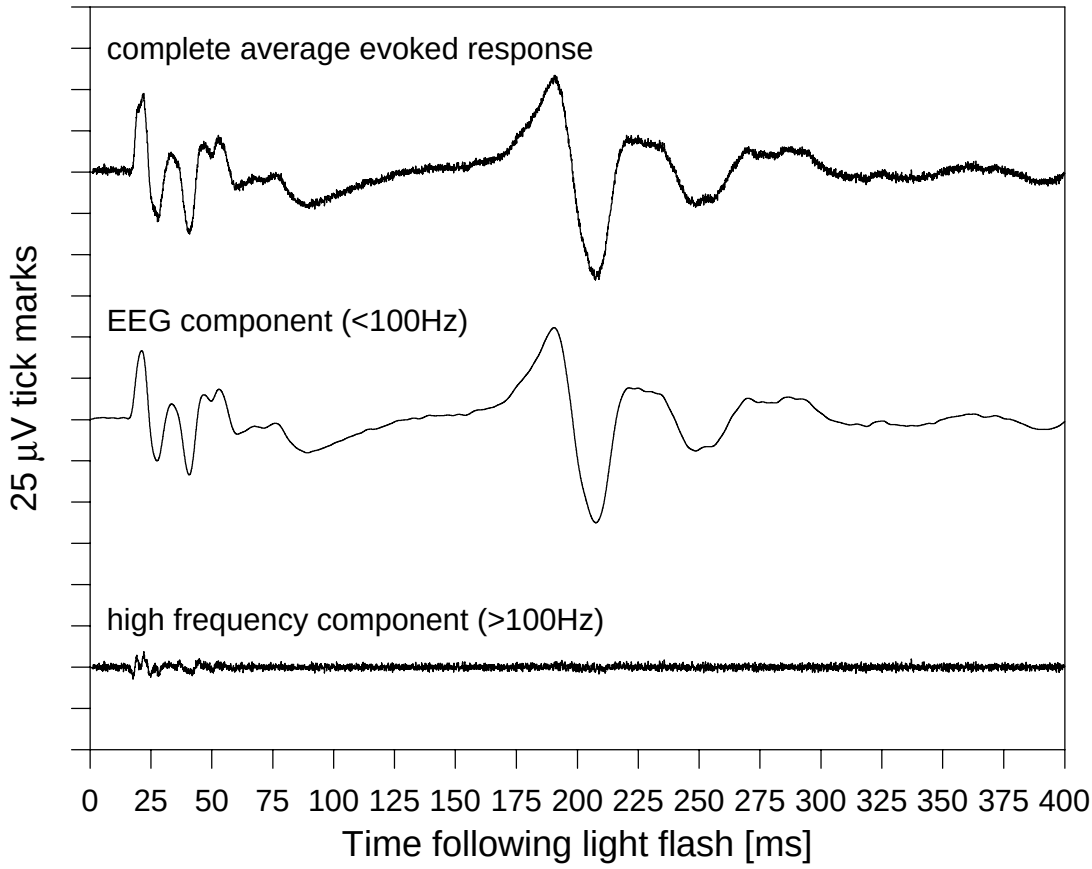

Figure 6.16: Average of 85 VEP recordings extracts the EEG evoked response from the ongoing neuroelectric activity. High frequency content of individual recordings is mostly averaged out.

Separation of the EEG component from the high frequency content of a single VEP recording can help to reveal individual action potential waveforms. In Figure 6.17, a 250^{th}-order finite impulse response digital filter (also used for the data of Figure 6.16) has been applied to a single VEP recording to separate the signal content above and below 100 Hz. A clear separation of the EEG signal and high-frequency neural activity is obtained. Examination of the high-frequency signal reveals the action potential waveforms, most of which are too small to distinguish and are thus classified as neural noise, and some that could possibly be identified individually. The waveform contains spikes of both negative and positive polarity because the two electrodes of the telemeter are located in the cortex near active neurons. The expanded detail graph shows some spikes that could be the result of single action potentials occurring near a peak of the evoked response.

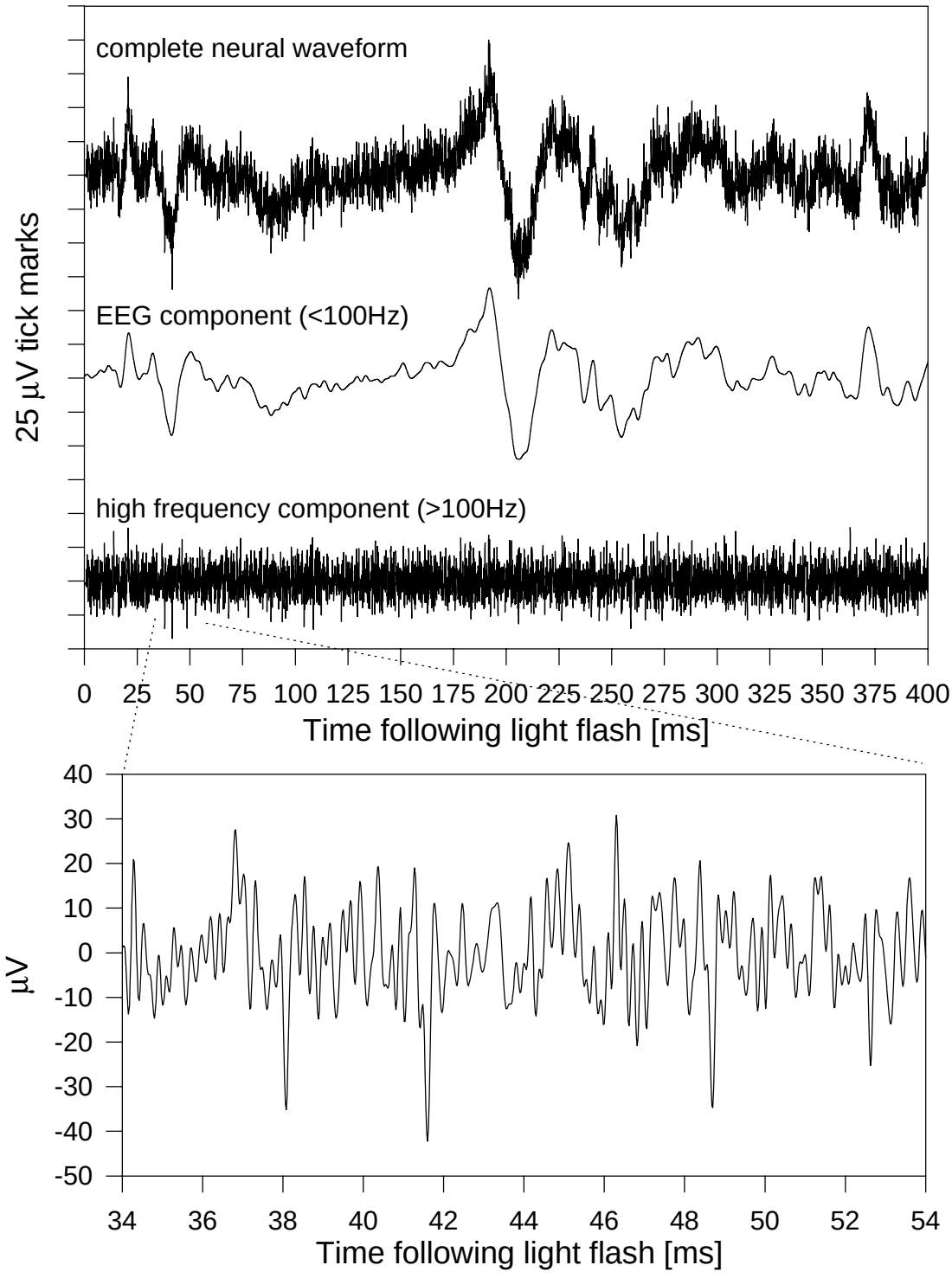

Figure 6.17: Filtering of EEG component from high-frequency content of a single VEP recording reveals action potential signals.

Since the electrodes of this implant are quite large compared to the size of the neurons, they are able to detect the electrical activity of many neurons, but have the disadvantage

that the amplitude of the recorded signals from the individual cells is small. This makes it difficult to distinguish the action potentials, but ensures that the activity of some cells will be observed. To test the assertion that the three large negative spikes in the detail graph of Figure 6.17 are discrete action potentials and not merely the result of fluctuations of a random signal, it is instructive to calculate the expected number of times that a purely random signal with the same spectral content would cross below –30 μV during this 20 ms interval. Following the analysis presented by Clark [29], if a random noise signal $v(t)$ and its time derivative $v'(t) = dv/dt$ have zero means and form a two-dimensional normal distribution, then the expected number of times per unit time that $v(t)$ will cross the negative threshold α with negative slope is given by:

$$\overline{N}_{\downarrow\alpha} = \frac{1}{2\pi}\left(\frac{d_{22}}{d_{11}}\right)^{1/2} e^{-\left(\alpha^2/2d_{11}\right)},$$

where

$$d_{11} = E\left[v^2(t)\right],$$

and

$$d_{22} = E\left[v'(t)^2\right].$$

The variances of the high-frequency component of the VEP in Figure 6.17 and its derivative can be used as generous values of d_{11} and d_{22}, respectively, to compute the expected number of purely random –30 μV crossings during a 20 ms period. Distribution plots of the recorded signal and its derivative were generated to verify that they were basically normal distributions, as required by the random signal analysis. They are presented in Figure 6.18.

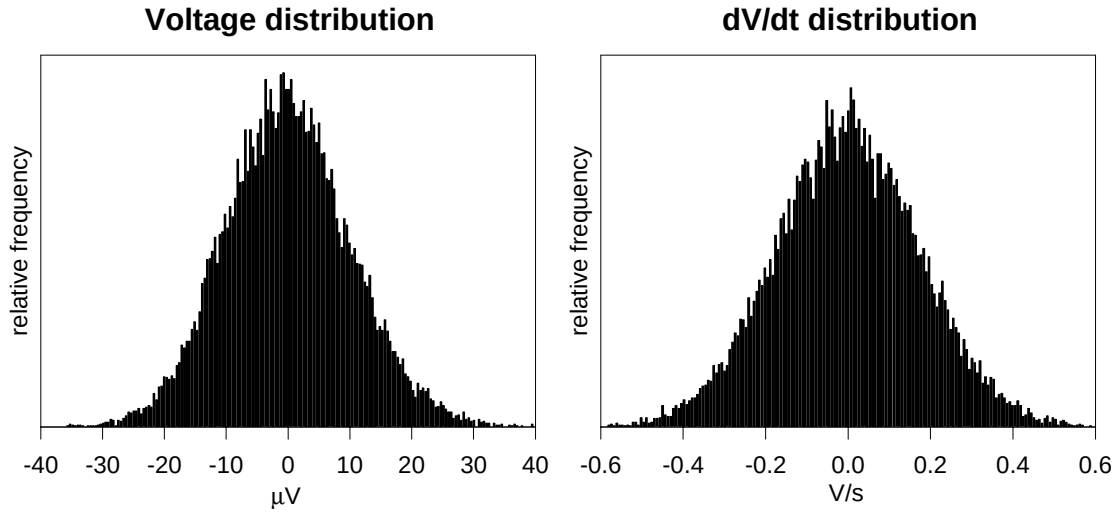

Figure 6.18: Distributions of the high-frequency neuroelectric signal and its time derivative are reasonably normal.

From the variances of the 400 ms high-frequency neuroelectric signal in Figure 6.17 we obtain:

$$d_{11} = 1.019 \cdot 10^{-10} \left[V^2 \right]$$

and

$$d_{22} = 3.022 \cdot 10^{-2} \left[V^2 / s^2 \right].$$

These values of d_{11} and d_{22} are generous because it is believed that the recorded signal contains spikes that are not purely random, and as a result the expected number of random threshold crossings may tend to err on the high side. The expected number of random negative crossings of –30 μV per unit time is:

$$\overline{N}_{\downarrow -30\mu V} = \frac{1}{2\pi} \left(\frac{3.022 \cdot 10^{-2}}{1.019 \cdot 10^{-10}} \right)^{1/2} e^{-\left(\frac{\left(-30 \cdot 10^{-6}\right)^2}{2\left(1.019 \cdot 10^{-10}\right)} \right)},$$
$$= 33.05 \left[s^{-1} \right]$$

so the expected number of crossings in any 20 ms period is 0.66. But in the recorded waveform we observe three such crossings. While this is not a strict statistical test, it does lend some confidence to the assertion that these spikes are not all random deviations in the signal, but rather are due to the firing of nearby neurons. As an additional test of the hypothesis that the observed signal is not purely random, the expected number of positive and negative voltage excursions during the entire 400 ms interval was computed as a function of threshold for comparison with the observed

neural waveform. This data is presented in Figure 6.19. It supports the hypothesis because the observed number of excursions is considerably lower than the expected number in certain voltage ranges, and higher in other ranges. The uneven distribution of crossings suggests that some voltage excursions may be due to the activity of particular neurons. Even though the spike amplitudes are not well defined because of the addition of many small overlapping action potential waveforms, the increased occurrence of crossings in the +30 μV range may be due to the firing of one or more neurons near to the "reference" (inverting differential input) electrode.

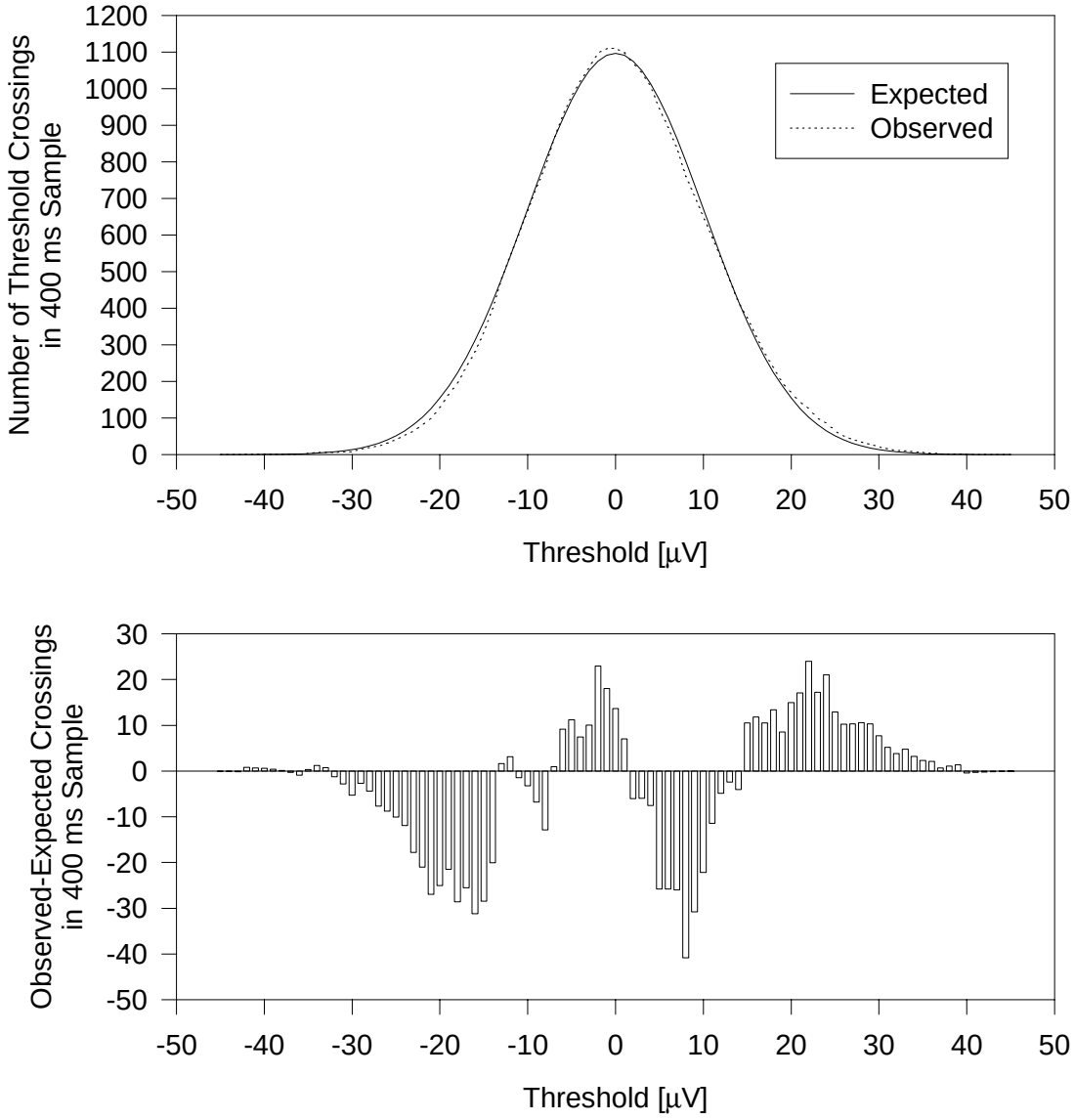

Figure 6.19: Difference in the expected and observed number of threshold crossings in high-frequency VEP recording.

6.2.2.2.3 Verification of proper telemeter function

Unfortunately, the only way to fully verify that the telemeter circuit of VA19 is still functioning correctly is to surgically remove the implant from the rabbit and test it as was done prior to implantation. But since much of the value of this prototype implant experiment is to test the long term in-vivo performance and stability of the implant, its surgical removal will probably not be performed until it is clear that the circuit has failed to operate properly or the rabbit has died of natural causes. So other means must be used to assess the functioning of the implant, in-vivo. Perhaps the most sensitive indicator of the telemeter circuit's integrity is simply its average LED pulse rate. Any leakage currents through the encapsulation or changes in circuit component values would be expected to cause the average pulse rate of the telemeter to change from its design value. Therefore the average pulse rate has been monitored with a sensitive digital frequency meter at regular intervals since the implant was accomplished. It remains stable at 37.7 kHz at the time of this writing (more than 28 months after implantation). VEP recordings provide another good test of the implant's operation. Because the visual evoked response is quite repeatable, the transmission of these characteristic neural waveforms is readily verified. The presence of possible action potential spikes are noted, as they provide a high-frequency input to the system to further test its performance. In any case, the background neural activity has the same spectral content as the action potential spikes, and can be used to test frequency response. Finally, the rms level of the neural waveforms in the absence of visual stimuli has been monitored. As noted previously, the rms level of this "neural noise" varies from day to day, probably with the ambient lighting conditions and mental state of the animal during the experiments. However, no trends that might indicate degradation of the implant have been observed. Absence of changes in the circuit performance, as indicated by these measures, suggests that the implant is still functioning properly and that telemetered signals above the level of the electronic and electrode noise (~14 μV_{rms}) are attributable to the rabbit.

6.3 Photodetector circuits

The first photodetector circuits were developed by crude calculations and experimentation, until there was time for the thorough analysis of photodetector performance in the context of pulse detection (Chapter 5). Consequently, the initial photodetector designs were far from optimal, and required that the detector be

positioned with great care, tight against the skin directly over the telemeter output LED. These designs were unforgiving for alignment error, and frequent loss of signal reception would occur during animal experiments as the rabbit moved its head. It was primarily these experimental difficulties that motivated the in-depth study of photodetector noise and the issues of pulse detection. While the analysis of Chapter 5 focused on the photodetector circuit that is necessary to receive particularly high-bandwidth multiplexed pulse-position encoded data, the results were applied to the design of a photodetector circuit optimized for the telemeter in rabbit VA19.

6.3.1 Optimized photodetector for VA19 telemeter

In order to optimize a second-order photodetector circuit with high-pass filtering (as discussed in section 5.2) for this single-channel neural waveform telemeter, the necessary photodetector circuit bandwidth had to be determined. The acceptable interaction between successive pulses places the minimum limit on the bandwidth. The shift in pulse detection time due to the tail of the preceding pulse response is

$$\underset{\max}{\Delta T_{interaction}} \approx 2.16 \cdot \omega_p \left(\left(T_{i,ave} - \Delta T_{\max} \right)^2 - \left(T_{i,ave} - \Delta T_{\max} - T_f \right)^2 e^{\omega_p T_f} \right) e^{-\omega_p \left(T_{i,ave} - \Delta T_{\max} \right)}$$

for this photodetector circuit. Assuming a maximum input signal range of ±250 μV (based on the actual VEP recordings), the minimum time between pulses $\left(T_{i,ave} - \Delta T_{\max} \right)$ is 20.8 μs. If it is desired to reconstruct the encoded neural waveforms with 5 μV accuracy, the shift in pulse detection time due to interaction must be less than 79 ns (the difference in pulse periods for –245 μV and –250 μV input signals). Since the light flash duration T_f is 3.5 μs, the expression above can be numerically solved for this condition:

$$2.16 \cdot \omega_p \left(\left(20.8 \cdot 10^{-6} \right)^2 - \left(17.3 \cdot 10^{-6} \right)^2 e^{\omega_p \left(3.5 \cdot 10^{-6} \right)} \right) e^{-\omega_p \left(20.8 \cdot 10^{-6} \right)} \le 79 \cdot 10^{-9} ,$$

yielding $\omega_p \ge 455 [krad/s]$. The minimum value $\omega_p = 455 [krad/s]$ can be used since it satisfies $\omega_p > 0.586 / T_f$.

Following the design example in section 5.2.4 of the photodetector for an 8-channel neural waveform telemeter, and using the same op-amp and photodetector so that $K = 1000$, $\tau = 8 \cdot 10^{-7}$, and $C_d \approx 70 [pF]$, the feedback resistor for the circuit of {Figure 13 of Chapter 5} would be

$$R_f \approx \left(\frac{K}{\tau C_d}\right)\left(\frac{1}{\omega_p}\right)^2 - \left(\frac{2}{C_d}\right)\left(\frac{1}{\omega_p}\right) + \frac{\tau}{KC_d} \cdot$$
$$\approx 86.2[M\Omega]$$

The compensation resistor for critical damping with this feedback resistance would be

$$R_c = \left(\frac{2}{C_d}\right)\left(\frac{1}{\omega_p}\right) - \frac{R_f}{K} - \frac{\tau}{KC_d},$$
$$\approx -23.4[k\Omega]$$

which clearly indicates an oversight in this design approach. The negative compensation resistance arises because the pole of the op-amp is beyond the cross-over frequency of the loop gain in this case. These equations are designed to produce a critically damped second-order closed-loop response, so the negative compensation resistance creates the second pole.

Since the OPA655 op-amp has constant gain over the desired bandwidth of this photodetector, no compensation resistor is necessary. The single pole produced by the feedback resistor and photodiode capacitance will dominate, giving a first-order closed-loop response. Because it was shown that the photodetector performance is improved by second-order response, a low-pass filter can be used at the output of a first-order photodetector circuit to add a second pole to the system. This circuit is sketched in Figure 6.20, with the addition of high-pass filtering.

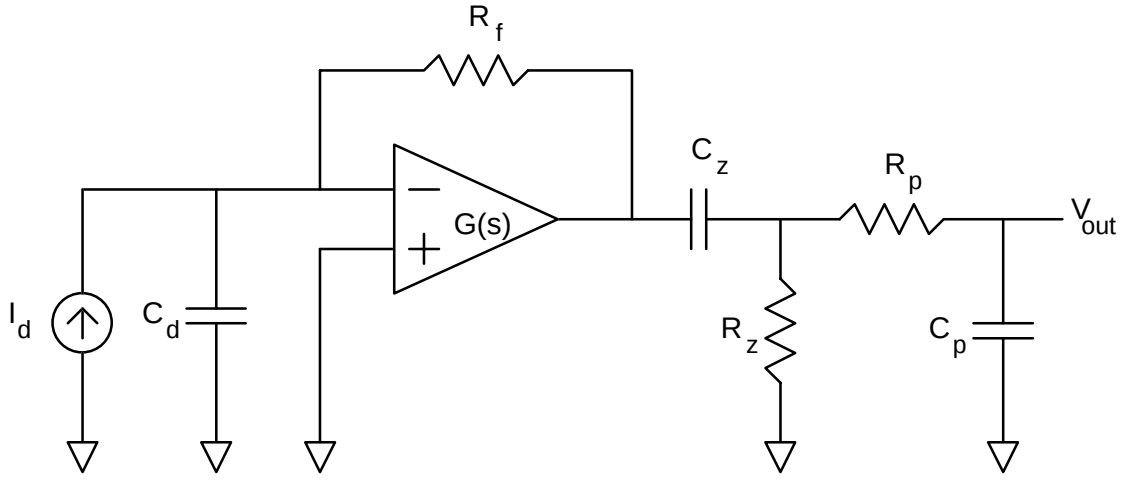

Figure 6.20: First-order transimpedance amplifier photodetector with band-pass filter to achieve second-order high-pass response.

First-order closed-loop transimpedance amplifier response with pole at $\omega_p = 455[krad/s]$ will be obtained by setting the feedback resistance so that the loop gain cross-over occurs at this frequency (approximately). The loop gain of the transimpedance amplifier is

$$L(s) = \frac{K}{s(R_f C_d) + 1},$$

since $G(s) \approx K$ for $L(s) \geq 1$. The feedback resistor that makes the loop gain magnitude equal to unity at $\omega_p = 455[krad/s]$ is approximately:

$$\begin{aligned} R_f &\approx \frac{K}{\omega_p C_d} \\ &\approx 31.4[M\Omega] \end{aligned} .$$

To obtain the desired system transfer function with a zero-frequency zero and three poles at ω_p, we can choose the components of the output bandpass filter so that

$$\frac{1}{R_z C_z} = \frac{1}{R_p C_p} = \omega_p ,$$

and

$$C_z >> C_p .$$

The constraint on the capacitor values permits the high- and low-pass parts of the filter to be designed independently, and avoids unnecessary attenuation of the signal. Also, it is desirable to keep the filter resistances much smaller than the feedback resistance so that their noise contribution can be neglected. Reasonable component values that satisfy these requirements are $R_z = 100[\Omega]$, $C_z = 22[nF]$, $R_p = 10[k\Omega]$, and $C_p = 220[pF]$. The complete schematic of this photodetector circuit is given in Figure 6.21.

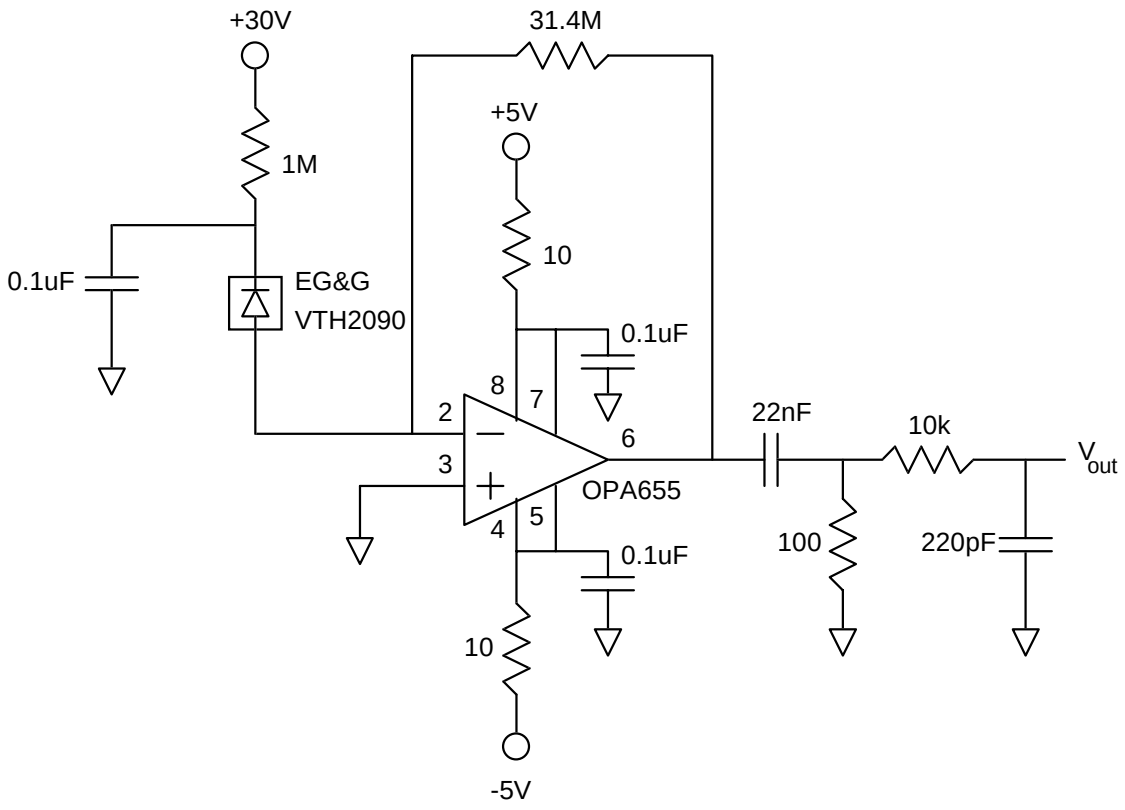

Figure 6.21: Photodetector circuit optimized for VA19 neural waveform telemeter.

In the dark, the input-referred noise of this photodetector is

$$S_{I_{eqTotal}}(\omega) \approx 2qI_{diode} + S_{I_{n,opamp}}(\omega) + \frac{4kT}{R_f} + \left(\frac{\omega^2 {R_f}^2 {C_d}^2 + 1}{{R_f}^2}\right) \cdot S_{V_{n,opamp}}(\omega)$$

$$\approx 3.2 \cdot 10^{-27} + 9 \cdot 10^{-28} + 5.27 \cdot 10^{-28} + 1.76 \cdot 10^{-37}\omega^2 + 3.65 \cdot 10^{-32},$$

$$\approx \underbrace{4.63 \cdot 10^{-27}}_{{I_{n,eq}}^2_{white}} + \underbrace{1.76 \cdot 10^{-37}}_{{I_{n,eq}}^2_{blue}}\omega^2$$

which is dominated by shot noise of the photodiode current at low frequency, and by the voltage noise of the op-amp at frequencies greater than about 162 krad/s (25.8 kHz). At the output of the circuit, the rms voltage noise is:

$$V_{\substack{n,out \\ rms}} = \frac{R_f}{4\sqrt{2}} \sqrt{{I_{\substack{n,eq \\ white}}}^2 \omega_p + 3{I_{\substack{n,eq \\ blue}}}^2 {\omega_p}^3}\ .$$

$$\approx 1.27[mV]$$

If the pulse detection threshold is set to the point of maximum slope, the rms error in the time of pulse detection will be:

$$\Delta T_{\substack{noise \\ rms,\min}} = \frac{V_{\substack{n,out \\ rms}}}{0.231 \cdot I_p R_f \omega_p} \approx \frac{3.83 \cdot 10^{-16}}{I_p}.$$

For 5 μV accuracy in decoding the telemetered neural waveforms, the pulse detection timing error must be less than 79 ns, so the minimum signal current in the photodiode must be:

$$I_p \geq 4.85[nA].$$

At this photocurrent, and with the detection threshold set to its optimal value of $V_{th} \approx 0.096 \cdot I_p R_f \approx 14.6[mV]$, the expected rate of spurious pulse detections would be

$$\overline{N}_{\uparrow V_{th}} \approx \left(\frac{3 I_{\substack{n,eq \\ white}}^{\ 2} + (32/\pi) \omega_p \omega_{pu} I_{\substack{n,eq \\ blue}}^{\ 2}}{I_{\substack{n,eq \\ white}}^{\ 2} + 3 \omega_p^{\ 2} I_{\substack{n,eq \\ blue}}^{\ 2}} \right)^{\frac{1}{2}} \frac{\omega_p}{2\pi} e^{-V_{th}^{\ 2} / 2 V_{\substack{n,out \\ rms}}^{\ 2}} \approx 3.65 \cdot 10^{-24} \left[s^{-1} \right],$$

where the extra pole $\omega_{pu} \approx 1.25 \cdot 10^6$ is from the op-amp.

Dividing the minimum photocurrent by the radiant sensitivity $\gamma_{diode} = 0.4[A/W]$ and the active area of the photodiode $A_{diode} = 0.8464[cm^2]$ yields the minimum acceptable light intensity at the detector:

$$L_{p,\min} = 14.3\left[\frac{nW}{cm^2}\right].$$

About 10.6 μW of light is emitted from the VA19 telemeter during the output pulses, since the quantum efficiency of the LED used is 16%. Making the crude approximation that this light is radiated uniformly over a hemispherical surface and is attenuated 70% by the rabbit skin and 45% by the optical filter, this photodetector should be able to receive the light pulses up to 4.4 cm from the telemeter.

Adapting the threshold detector developed for the 8-channel neural waveform telemeter for this application requires that the photodetector output peak by determined. The photodetector will reach its maximum (negative) output at the end of the pulse since $T_f < 2/\omega_p$. The light pulse from VA19 is 3.5 μs long, so the peak photodetector output voltage will be:

$$v_{out,peak} = -\frac{1}{2} I_p R_f {\omega_p}^2 t^2 e^{-\omega_p t}$$
$$\approx -8.1 \cdot 10^6 \cdot I_p$$

The optimal pulse detection threshold, where the slope of the photodetector output signal is greatest, is:

$$V_{th} \approx 3 \cdot 10^6 \cdot I_p$$
$$\approx 0.37 \cdot v_{out,peak}$$

Also, the comparator that disables the pulse detector output when the received signal is too weak should be set to cut off when $I_p < 4.85[nA]$, or:

$$\left| v_{out,peak} \right| \leq 39[mV].$$

The threshold detector circuit that incorporates these changes is shown in Figure 6.22.

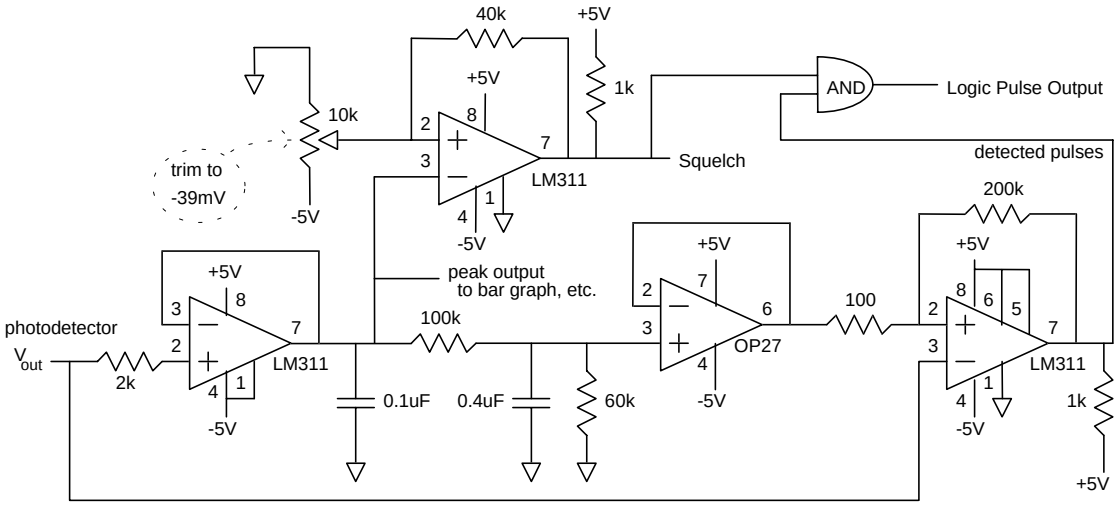

Figure 6.22: Threshold detector to complement the photodetector for VA19.

6.4 Decoder circuits

Decoding of the pulse-period-encoded neural signals was accomplished through a number of different techniques during the development of this technology, each with increasing success.

6.4.1 Analog frequency-to-voltage conversion

The first method attempted was to reverse the encoding technique in an analog circuit. In the single channel neural waveform encoders, the time it took for a constant amount of charge to be collected was inversely proportional to the input voltage signal. The first

decoder exploited this relationship by simply placing a fixed amount of electrical charge onto a capacitor every time a light pulse was detected from the telemeter. A resistor in parallel with the capacitor allowed charge to bleed off continuously, so that the average voltage on the capacitor was proportional to the frequency of encoded pulses, or inversely proportional to the time between them. The drawback to this method was that the time constant of the capacitor/resistor combination had to be small enough to accurately track the changes in the originally encoded signal, and this gave a saw-tooth output waveform as the capacitor voltage decayed rapidly after each charge packet was deposited on it. With extensive low-pass filtering the encoded signal could be reconstructed cleanly, but the electronics required to perform this high-order filtering were not practical. Instead, the saw-tooth output waveforms were oversampled and digital filtering was performed on the computer. This was time-consuming and necessitated the storage of excess information, so alternative decoding methods were investigated.

6.4.2 Digital counter decoders[14]

6.4.2.1 8-bit, 5 MHz

Recognizing that the signal information was encoded entirely in the timing between pulses, and that it was generally desirable to have recorded neural waveform data in digital form for processing, the next decoder circuit measured the time between pulses digitally. It utilized a digital counter to count the number of clock cycles between the detected light pulses. Every time a light pulse occurred, the counter was read and then reset to zero. The count value was input to a digital-to-analog converter to provide a real-time analog display, and a parallel-port interface was designed to send the count values to a computer. The first implementation of the digital decoder used a 5 Mhz clock to get 0.2 μs timing resolution, and an 8-bit counter to give 256 possible output values (corresponding to a maximum measurable time between pulses of 51.2 μs). At first, the system relied on the computer's speed to read the data from the parallel-port interface fast enough to catch every count value, but this became a limitation when using slower computers or a multitasking operating system such as Windows. On these computer systems there were unacceptable gaps in the acquired data. To remedy this problem, a

[14] Digital decoders designed and constructed primarily by Sean Sexton at MIT Lincoln Laboratory, with input and modifications by Bruce Larson

buffer memory was incorporated into the parallel-port interface portion of the digital decoder that would store the counter data until the computer could read it. The buffer memory circuit was designed to stop acquiring data when it reached its capacity, and to wait for the computer to empty it. The buffer would not acquire more data until the computer had emptied it and issued a command to resume data acquisition. In this manner any gaps in the decoded data would be known. Initially, a 4 kilobyte memory buffer was used which would store an average of 108 ms of data from the implant used in VA19. This was subsequently replaced by a 16 kilobyte buffer that would store approximately 434 ms of data.

A number of shortcomings in the first digital decoder led to the development of an improved version. Primarily, the 0.2 μs timing resolution quantized the data more than was desired, giving a resolution of about 6 μV for small signals when used with the encoder of VA19. This was well below the neural noise floor of recordings from VA19, but the data compression inherent in the encoding process (because the time between pulses is inversely proportional to the input voltage) decreased this resolution for large negative input signals and increased it for large positive signals. So for negative input voltage swings, the quantization of the decoded signal became more pronounced -- for example, a –250 μV signal has a 12.6 μV quantization. Also, the 8-bit counter limited the dynamic range of signals that could be decoded. As stated earlier, the maximum time that could be measured directly was 51.2μs, and inter-pulse intervals greater than this caused the counter to “wrap around” and start counting up from zero again, leading to discontinuities in the decoded signal. Finally, the real-time analog output provided by the D/A converter gave a reasonable approximation of the original signal only for small signals, since it was only a first-order approximation. From the Taylor series of the decoding equation (developed in Chapter 4):

$$
\begin{aligned}
v_{in} &= -\left(\frac{\left(\Delta t_{base} - T_{delay}\right)}{\left(\Delta t_{measured} - T_{delay}\right)} - 1 \right) \frac{R_g}{R_b} V_b \\
&= \underbrace{\left(\frac{\frac{R_g}{R_b} V_b}{\left(\Delta t_{base} - T_{delay}\right)} \right)}_{K_1} \left(\Delta t_{measured} - \Delta t_{base}\right) - \underbrace{\left(\frac{\frac{R_g}{R_b} V_b}{\left(\Delta t_{base} - T_{delay}\right)^2} \right)}_{K_2} \left(\Delta t_{measured} - \Delta t_{base}\right)^2 + \ldots, \\
&= K_1 \left(\Delta t_{measured} - \Delta t_{base}\right) - K_2 \left(\Delta t_{measured} - \Delta t_{base}\right)^2 + \ldots
\end{aligned}
$$

a first-order approximation for the encoded input voltage v_{in} may be taken:

$$v_{in} \approx K_1 \Delta t_{measured} - \underbrace{K_1 \Delta t_{base}}_{\text{constant}}$$

This is the approximation made by putting the counter output directly into a D/A converter, and considerable distortion of large signals resulted. Of course, signals stored in the computer were properly reconstructed according to the decoding equation.

6.4.2.2 16-bit, 20 MHz with decoding ROM

These problems were solved in the latest version of the digital decoder, which uses a 20 Mhz clock for 50 ns time resolution (corresponding to 1.5 μV quantization for small signals encoded by the implant in rabbit VA19), and a 16-bit counter that cures the dynamic range limitation by measuring pulse periods up to 3.3 ms long. To provide an undistorted analog output, the count value is used to address a ROM "lookup table" of properly decoded values, which are then sent to the D/A converter (rather than the raw count values). This decoder has been used for the majority of the prototype implant testing.

6.4.3 Analog integrator "counter" with decoding function circuit

Subsequent to the construction of this digital decoder, it was felt that a simpler and physically smaller decoder would be desirable for field use. This motivated us to re-examine the possibilities of analog decoder circuits. The use of an integrated circuit switched-capacitor filter enabled the problems of the first analog decoder (the frequency-to-voltage converter) to be resolved quite satisfactorily by providing a simple high order low pass filter to remove almost all of the saw-tooth artifact from the decoded waveform. Another analog decoder was devised using a circuit that integrates a constant current for the period between successive pulses, giving a voltage representation of the time between them. This voltage is captured by a sample-and-hold amplifier, and the integrator is quickly reset so that it can measure the time until the next pulse occurs, at which time this new voltage is sampled. The output of the sample-and-hold is thus a stair-step waveform whose amplitude is directly proportional to the time between the most recent pair of pulses. Accordingly, the waveform is *inversely* proportional to the originally encoded neural signal voltage (plus an offset). To complete the decoding, an "analog function chip" was used to invert the signal again to properly recontruct the input signals. This decoding system was also relatively simple and compact, and gave high-

quality output that required very little filtering. Computer-based analog-to-digital conversion of these decoder outputs enabled the data to be digitally processed and stored more efficiently by decreasing the number of samples required to that dictated by the Nyquist rate, about 20 kHz for a single channel of neural information.

Chapter 7: Integrated circuit neural waveform telemeters

Integrated circuits designed specifically for the acquisition and optical telemetry of biomedical signals can yield substantial improvements in the most critical aspects of the implant by reducing power consumption, size, and mass. Also, the noise characteristics of the circuits can be tailored for specific applications to give the best balance between signal quality and power consumption.

In this research, integrated circuits were developed for the transduction and telemetry of neural waveforms. The first part of this design process was the development of an input stage to detect and amplify the small extracellular potentials associated with the activity of individual neurons. Since the electrodes typically used for these recordings are small, their impedance is correspondingly large. MOS field-effect transistors are well-suited to recording from these electrodes because of the extremely high DC input impedance (and negligible leakage current) of their gates. Custom CMOS integrated circuits can also be obtained from several commercial sources at nominal cost, making this an attractive technology for this application.

7.1 Telemeter noise considerations – design of the input amplifier stage

A study of the noise and power consumption trade-offs for analog circuits produced by one such process, the Orbit Semiconductor 2 μm N-well CMOS process (through the MOSIS prototyping service), was recently conducted [90]. The results of this theoretical and empirical noise analysis were applied to the design of an integrated-circuit input stage for an implantable neural signal transducer. Since the noise of all subsequent stages in the telemeter system are divided by the signal gain of the input stage to determine their contribution to the input-referred noise (and thus the signal-to-noise ratio), their noise performance is less severely constrained. So once the input stage was designed to have sufficiently low noise to acquire the anticipated signals, the design effort for the rest of the system focused on minimizing its power consumption.

The recordings of neural signals from rabbit VA19 indicated a background neural noise level of approximately 23 μV_{rms}, so an input-referred noise level of 10 μV_{rms} over a bandwidth of 10 Hz to 10 kHz was chosen as the design goal for the input stage of the integrated-circuit neural signal transducer. With reasonable design of the rest of the system, this will be approximately the input-referred noise of the complete neural signal

transducer, so the combination of neural noise and circuit noise will be only 25 μV_{rms} (an increase of only 10% over the level of the observed neural noise).

The input stage of the integrated circuit is the same circuit that was used as the design example at the end of the theoretical noise analysis [90]. The schematic of the circuit is shown in Figure 7.1, and the equations that were developed in the design example are repeated below.

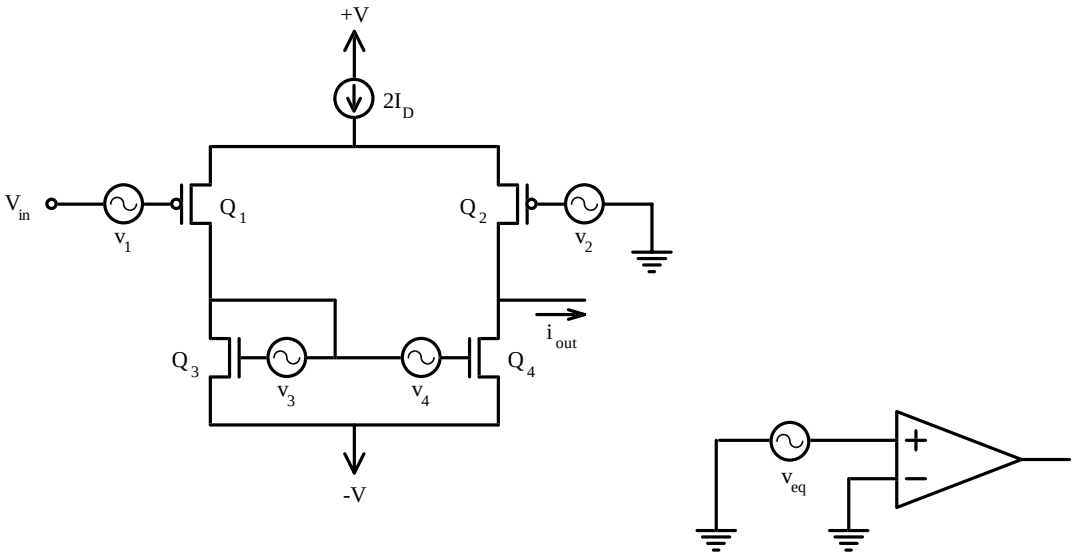

Figure 7.1: Differential amplifier circuit with transistor noise sources, modeled by noiseless amplifier with equivalent input noise source.

If transistors Q_1 and Q_2 are matched and have transconductance $g_{m_{1,2}}$, and transistors Q_3 and Q_4 are matched with transconductance $g_{m_{3,4}}$, the equivalent voltage noise spectral intensity at the input to the amplifier will be:

$$S_{v_{eq}} = S_{v_1} + S_{v_2} + \left(\frac{g_{m_{3,4}}}{g_{m_{1,2}}} \right)^2 \left(S_{v_3} + S_{v_4} \right),$$

where for each transistor i,

$$S_{v_i} \equiv S_{V_{GSi},\text{thermal}} + S_{V_{GSi},\text{flicker}}.$$

Expressing these noise components in terms of the design parameters of transconductance and transistor width and length, the gate-referred noise sources of the transistors may be approximated by:

$$S_{V_{GS},\text{thermal}} \approx \frac{K_t}{g_m}$$
$$S_{V_{GS},\text{flicker}} \approx \frac{K_f}{WLf}$$

Substituting these approximations into the equation for $S_{v_{eq}}$ yields the total noise of the amplifier:

$$S_{v_{eq}} \approx \underbrace{2\frac{K_{t_{1,2}}}{g_{m_{1,2}}} + 2\left(\frac{g_{m_{3,4}}}{g_{m_{1,2}}}\right)^2 \frac{K_{t_{3,4}}}{g_{m_{3,4}}}}_{\text{thermal}} + \underbrace{2\frac{K_{f_{1,2}}}{W_{1,2}L_{1,2}f} + 2\left(\frac{g_{m_{3,4}}}{g_{m_{1,2}}}\right)^2 \frac{K_{f_{3,4}}}{W_{3,4}L_{3,4}f}}_{\text{flicker}}$$
$$\approx \underbrace{\frac{2}{g_{m_{1,2}}}\left(K_{t_{1,2}} + \left(\frac{g_{m_{3,4}}}{g_{m_{1,2}}}\right)K_{t_{3,4}}\right)}_{\text{thermal}} + \underbrace{\frac{2}{f}\left(\frac{K_{f_{1,2}}}{W_{1,2}L_{1,2}} + \left(\frac{g_{m_{3,4}}}{g_{m_{1,2}}}\right)^2 \frac{K_{f_{3,4}}}{W_{3,4}L_{3,4}}\right)}_{\text{flicker}},$$

where the transistors in each matched pair are assumed to have the same noise characteristics, and the $1/f$ and thermal components have been grouped. If transistors Q_3 and Q_4 are designed to have a much lower width/length ratio than transistors Q_1 and Q_2, their transconductance will be much lower as well, so

$$\frac{g_{m_{3,4}}}{g_{m_{1,2}}} << 1,$$

and the equivalent input noise of the amplifier may be further approximated by neglecting the noise of transistors Q_3 and Q_4:

$$S_{v_{eq}} \approx \underbrace{\frac{2K_{t_{1,2}}}{g_{m_{1,2}}}}_{\text{thermal}} + \underbrace{\frac{2K_{f_{1,2}}}{W_{1,2}L_{1,2}f}}_{\text{flicker}}.$$

The mean-square noise voltage that this equates to over the 10Hz to 10kHz system bandwidth is:

$$\int_{10}^{10000}\left(S_{v_{eq}}\right)df \approx \underbrace{\int_{10}^{10000}\left(\frac{2K_{t_{1,2}}}{g_{m_{1,2}}}\right)df}_{\text{thermal}} + \underbrace{\int_{10}^{10000}\left(\frac{2K_{f_{1,2}}}{W_{1,2}L_{1,2}f}\right)df}_{\text{flicker}}$$
$$\approx \underbrace{\frac{2K_{t_{1,2}}}{g_{m_{1,2}}}(10000)}_{\text{thermal}} + \underbrace{\frac{2K_{f_{1,2}}}{W_{1,2}L_{1,2}}\ln(1000)}_{\text{flicker}}.$$

If the transistors in the amplifier circuit are operated in saturation, the coefficients $K_{t_{1,2}}$ and $K_{f_{1,2}}$ can be determined from the measured noise data that was presented in the empirical study of the Orbit Semiconductor 2 μm N-well CMOS process transistors [90]. Generously estimating the thermal and $1/f$ coefficients from the measured data yields:

$$\begin{aligned} K_{t_{1,2}} &\approx 1.2(4kT) \\ &\approx 2\times10^{-20}\left[\tfrac{\text{VA}}{\text{Hz}}\right], \end{aligned}$$

and

$$K_{f_{1,2}} \approx 5\times10^{-10}\left[\text{V}^2\mu\text{m}^2\right].$$

Other empirical parameters needed for the design were the transconductance/current ratio and the relationship between threshold current and width/length ratio. The study of noise and power consumption concluded that the best performance would be obtained if the input transistors Q_1 and Q_2 were operated in weak inversion, because the transconductance is greatest for a given drain current in subthreshold operation. The $I_D - V_{GS}$ curves indicated that for every unit of width/length ratio, the p-channel transistors will operate in weak inversion for saturated drain currents less than 10 nA. For example, a width/length ratio of 100 is necessary for the transistors to operate in weak inversion at currents up to 1 μA. The transconductance in weak inversion was found to be:

$$\begin{aligned} g_{m_{1,2}} &\approx \frac{I_D}{1.5\left(\frac{kT}{q}\right)}. \\ &\approx 25.6I_D \end{aligned}$$

Substituting these values into the mean-square voltage noise equation and equating it to the design goal of 10 μV_{rms} squared gave the following design trade-off between bias current and transistor size:

$$\left(10^{-5}\right)^2 = \underbrace{\frac{2\left(2\times10^{-20}\right)(10000)}{25.6I_D}}_{\text{thermal}} + \underbrace{\frac{2\left(5\times10^{-10}\right)(6.9)}{W_{1,2}L_{1,2}}}_{\text{flicker}}.$$

Splitting the noise evenly between the two sources gave some indication of the trade-off, and a place to start developing an acceptable balance between power consumption and chip area. For thermal noise to contribute less than half of the total noise requires

$$I_D \geq 0.3125\times10^{-6}\left[\text{A}\right],$$

and for flicker noise to contribute less than half,

$$W_{1,2}L_{1,2} \geq 138\left[\mu\mathrm{m}^2\right].$$

This happened to be a reasonable solution, at least for the prototype integrated circuits, because each input stage will require only 0.625 μA bias current and the transistor area is not excessively large. The width/length ratio necessary for the input transistors to operate in weak inversion was 31.25, so a transistor of width 70 μm and length 2 μm would satisfy this requirement and provide the desired area. Making transistors Q_3 and Q_4 have length 12 μm and width 12 μm would make them compact with comparable gate area (to keep their flicker noise low as well), and should force them to operate in strong inversion at the 0.3125 μA current level, giving them much lower transconductance than transistors Q_1 and Q_2. This should make their contribution to the total noise of the input stage negligible.

While these transistor geometries should have been adequate for an input amplifier with the minimum noise performance, it was deemed wise to exceed the minimum design requirements in order to provide a safety margin to account for other sources of noise in the circuit and fabrication process variations. Also, the study of the Orbit Semiconductor 2 μm N-well CMOS process transistors revealed somewhat deviant behavior of the shorter channel transistors, particularly the minimum length (2 μm) devices. The flicker noise of these transistors was higher than that predicted by the noise equation with the constant $K_{f_{1,2}}$ used above. At the time of the study, this was attributed to presumably different energy distribution of charge-trapping sites in the gate oxide of the short transistors. It was conceivable that charge traps near the source and drain edges of the gate had different density and distribution than traps in the rest of the gate oxide due to fabrication and electric field differences, and that these traps could dominate the flicker noise of short channel devices. However, it was more recently discovered that the difference in drawn and fabricated channel length is significant. It ranges from -0.1 μm to -0.7 μm, with a typical value of -0.4 μm. Thus the typical channel length of a minimum length transistor, drawn 2 μm, is only 1.6 μm! This introduces a +25% error in the calculation of gate area and a -20% error in the calculation of width/length ratio, based on the drawn dimensions of minimum length transistors. These errors could well account for the difference in characteristics observed during the empirical study of transistors fabricated by this process.

At the time of the design of the input amplifier stage, the geometry error was not known, so transistors Q_1 and Q_2 were given a gate length of 5 μm to avoid the aberrant behavior altogether. To ensure that these transistors would operate in weak inversion, a gate width of 200 μm was used for a width-length ratio of 40 and theoretical weak inversion limit of 0.4 μA. The larger area of these transistors was also expected to afford better matching of the differential pair. Because the flicker noise of the n-channel transistors was considerably greater than the p-channel devices, transistors Q_3 and Q_4 were made with larger dimensions of 32 μm by 32 μm to minimize their contribution to the total noise of the system. The larger area of the four transistors should also reduce the total $1/f$ noise component, permitting the circuit to be operated at somewhat lower current without exceeding the design noise specification. Once the input stage had been designed for adequate sensitivity, other challenges in the design of the complete system were finding ways to compensate for slow drifts in electrode potential that are often much larger than the signals of interest, and a means to encode multiple channels of recording data.

7.2 Integrated Circuit Development

The preferred integrated circuit development process would have been to first do a conceptual design, followed by computer simulation, then fabrication and testing of the circuits. Based on the experimental results, the process would be repeated to correct any deficiencies in the initial design. Unfortunately, several factors prevented this orderly development process from being followed. First, the circuit simulation tools available throughout most of this research effort were cumbersome to use, and the MOSFET models were not very accurate for simulating circuits with transistors operated in weak inversion. Also, because of the nonlinear nature of pulse-position encoding circuits, only transient response simulations could be used to simulate many aspects of their operation. Transient response simulations are computationally intensive and can have convergence problems, particularly for oscillatory circuits without any steady-state operating point. The simulation difficulties were compounded by the fact that operation of the encoder circuits entails relatively long periods of slow state changes interspersed with brief periods of rapid change. This necessitated that a fine time resolution be used for long transient response simulations, with the consequence that successful simulations often took several minutes or more to complete.

Another factor complicating the integrated circuit development process was the fixed fabrication schedule (closing every three months, approximately) and the 10-12 week turn-around time for submitted designs to be fabricated and delivered. It was sometimes necessary to submit designs which had been only partially simulated in order to meet fabrication deadlines. Often, circuits submitted for one production run were not received in time to test them before submitting the next design. So a 6 month or greater delay existed between the completion of one design and the time when the next version could be submitted based on the experimental results of the first. Fully custom transistor-level designs were used in an effort to optimize performance, so no standard CMOS library designs were used, and all mask layouts were completely original. A flaw in the layout editor's circuit extraction tool prevented the verification of the mask designs, so layout errors impaired circuit function in some designs.

The integrated circuit designs that were fabricated are presented in the following sections along with the results of their experimental testing. After the last set of integrated circuits were received from the foundry, better computer simulation tools became available for use in this research. This enabled the recent designs to be properly simulated, producing data in agreement with the experimental results, and providing some likely explanations for unexpected behavior. Utilizing this additional asset, the flaws in the previous designs were corrected, and the final version of a complete 8-channel neural waveform telemeter was submitted for fabrication at the conclusion of this research effort.

7.3 IC test chips

The first test chip was primarily an attempt to integrate the prototype optically-coupled neural waveform telemeter circuit that had been developed from discrete components. In addition, the basic components of this circuit were made available individually on the chip for evaluation. The second test chip was intended to test additional concepts and components needed for a multi-channel telemeter. Some of the components on the first test chip were common to this multi-channel circuit. But since the second design was submitted for fabrication before the first test chip was available for evaluation, several assumptions about the performance of the circuit components on test chip one had to be made. However, the multiplexing and switching circuits new to this design were provided separately on the chip for testing, so that it would be possible to combine the knowledge gained from the two test chips to isolate any problems or deficiencies that

existed in the multi-channel design. Based on the experimental results of these two test chips, three versions of an improved 8-channel neural waveform telemeter IC were designed. These designs incorporated the same basic multiplexer and encoder circuits, but used different input offset correction techniques to reject low-frequency electrode potential drift.

7.3.1 Test Chip One:

The single-channel neural waveform telemeter circuit sketched in Figure 7.2 was the design goal of the first test chip. This circuit uses *pulse-period encoding* where the timing between pulses is inversely proportional to the derivative of the input voltage. To accomplish this, the current flowing onto integration capacitor C_i is modulated by the input voltage, and when the capacitor voltage exceeds the Schmitt trigger high threshold, the capacitor is reset to the Schmitt trigger low threshold. During the integration capacitor reset period, the LED drive switch is closed to transmit a pulse of light, and the inverting input of the input amplifier is connected to its output. Connecting the amplifier as a voltage follower in this manner was intended to cause the output current to be close to zero at the instantaneous input voltage. Bias capacitor C_b maintains the voltage on the inverting input during the next sampling/integration phase, so that the next sample will reflect only the change in the input voltage. This takes the derivative of the input signal, which was expected to null DC and low frequency offsets (from electrode potential drift, etc.) that could otherwise overwhelm the small AC input signals of interest.

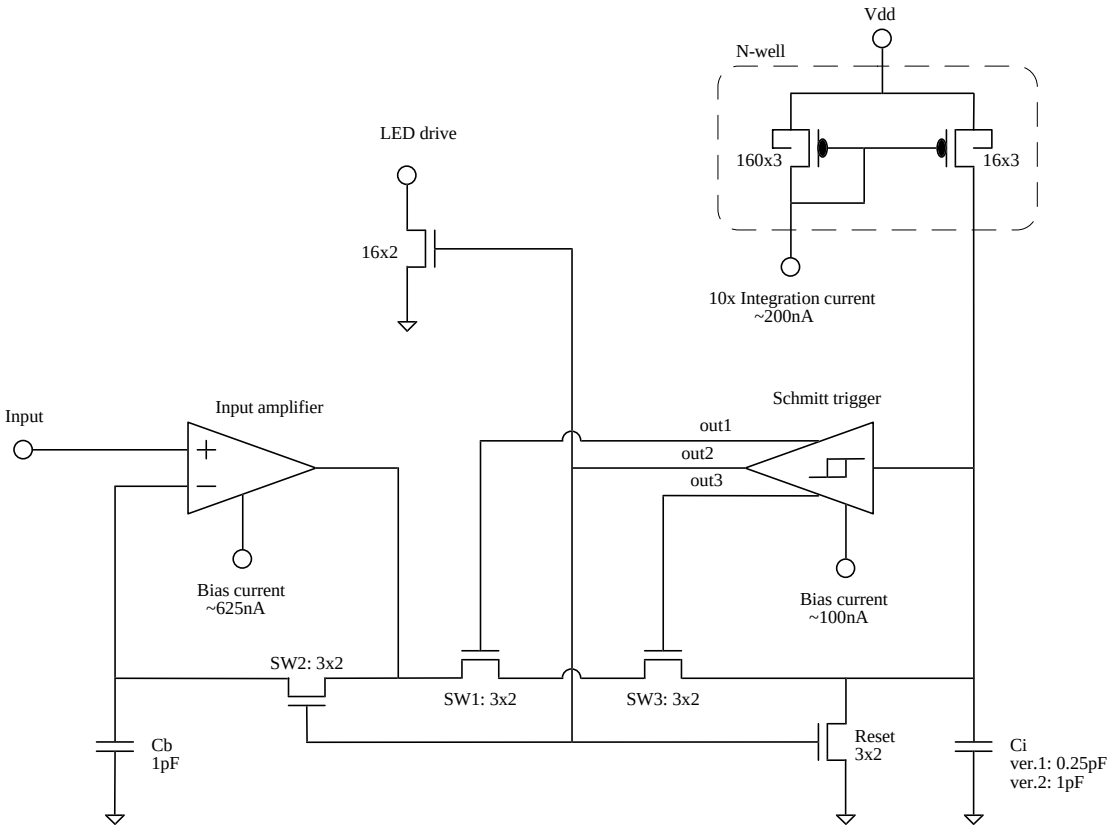

Figure 7.2: Single channel neural waveform telemeter integrated circuit.

The schematic of the input amplifier is given in Figure 7.3. Since the input amplifier functions as a transconductance amplifier, the current-to-voltage converter circuit shown in Figure 7.4 was used to test it.

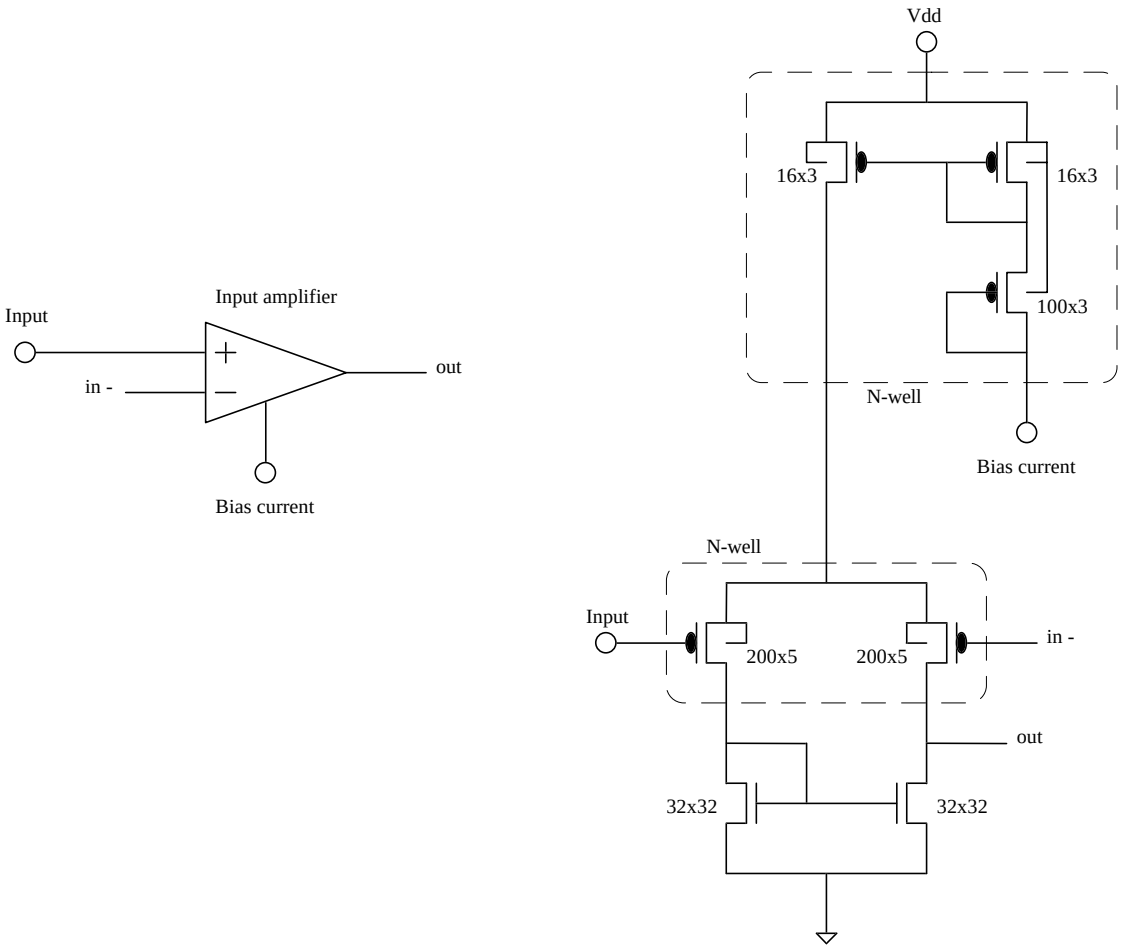

Figure 7.3: Input amplifier stage of integrated circuit neural waveform telemeter.

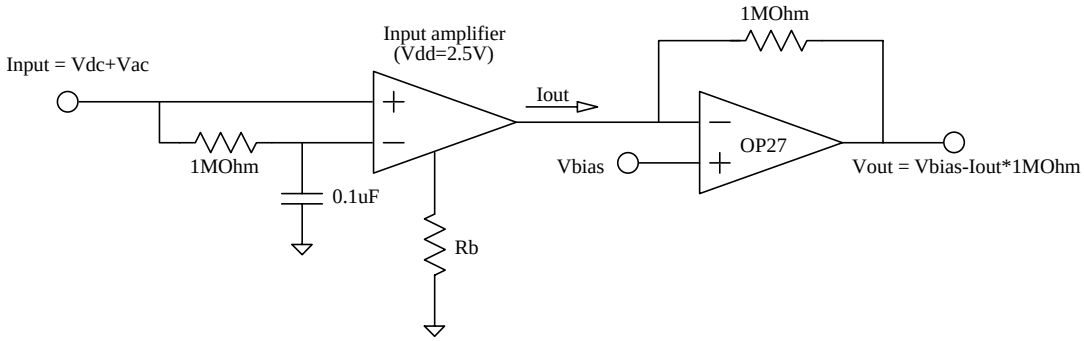

Figure 7.4: Input amplifier test circuit.

In general, a 2.5 V supply (V_{dd}) was used for the input amplifier tests, and the current-to-voltage converter connected to its output was biased with V_{bias} = 0.5 V. Using R_b = 1 MΩ, the current draw from the bias current node was approximately 0.336 μA. Forcing the non-inverting amplifier input to 2.5 V (its positive supply rail) and the inverting input to 0.5 V directed all of the amplifier current to its output, permitting the true bias current

to be determined. This was found to be 0.335μA, demonstrating excellent matching of the bias current mirror transistors. The small-signal transconductance was measured with a 10 mV_{p-p} sinewave (V_{ac}), and found to be 4 μA/V for DC common-mode inputs (V_{dc}) from 0 V to about 1.5 V. The transconductance was reduced by 20% at the upper limit of this range. A DC output current of –32 nA existed for zero differential input voltage, suggesting a –8 mV effective input offset. The DC output resistance of the amplifier was estimated by changing the output bias voltage (via V_{bias} on the current-to-voltage converter) and measuring the change in output current. Varying V_{bias} from 0.25 V to 0.75 V resulted in a change in the output current of 7.5 nA, indicating an output resistance of 66.7 MΩ.

Most of the tests described above were repeated for the case of R_b = 510 kΩ, which drew 558 nA current from the bias node. The measured bias current through the amplifier was 529 nA, for a current mirror error of about 5%. Transconductance was 6.35 μA/V. For comparison, a SPICE simulation predicted that with 500 nA bias current the transconductance of the input amplifier would be 5.8 μA/V, which is in good agreement considering the difference in bias. The measured DC common-mode input range (with V_{bias} = 0.5 V) still extended from 0 V to 1.5 V, with approximately 20% reduction in the transconductance at the extremes. The output current for zero differential input when V_{dc} = 0.5 V and V_{bias} = 0.5 V was –48 nA, consistent with a -7.4 mV effective input offset. Output resistance determined by changing V_{bias} from 0.25 V to 0.75V was 48.7 MΩ.

The details of the Schmitt trigger are shown in Figure 7.5. The input of this Schmitt trigger is the inverting input of a differential amplifier. The non-inverting input and the output of this amplifier are connected to the middle of a string of “diode-connected” transistors Q1-Q4 (borrowing bipolar junction transistor terminology), where the transistor drains are connected to their respective gates. With V_{dd} = 2.5 V, very little current will flow directly through the four transistors in this series. When the differential amplifier output is sinking current, it draws current through the two p-channel transistors Q1 and Q2, thereby setting the Schmitt trigger low threshold to approximately V_{dd}-2V_{GS}. Early computer simulations predicted this to be 0.745 V. Very little current flows through the two n-channel transistors Q3 and Q4 because of the low voltage across them in this case. Since the current through Q1 is mirrored by transistor Q5 and the current through Q3 is mirrored by transistor Q6, the voltage at the drains of Q5 and Q6 will be close to

V_{dd}. This signal goes through three inverters to create the control signals out1, out2, and out3, which are “low”, “high”, and “low” logic levels, respectively. This corresponds to the reset/pulse output phase of the encoding process. In the other state, when the differential amplifier output is sourcing current that flows through the two n-channel transistors, the high threshold of the Schmitt trigger is set to about $2V_{GS}$ (1.566 V, according to computer simulation). Outputs out1, out2, and out3 take on their complementary values, and the encoder is in the sampling/integration phase.

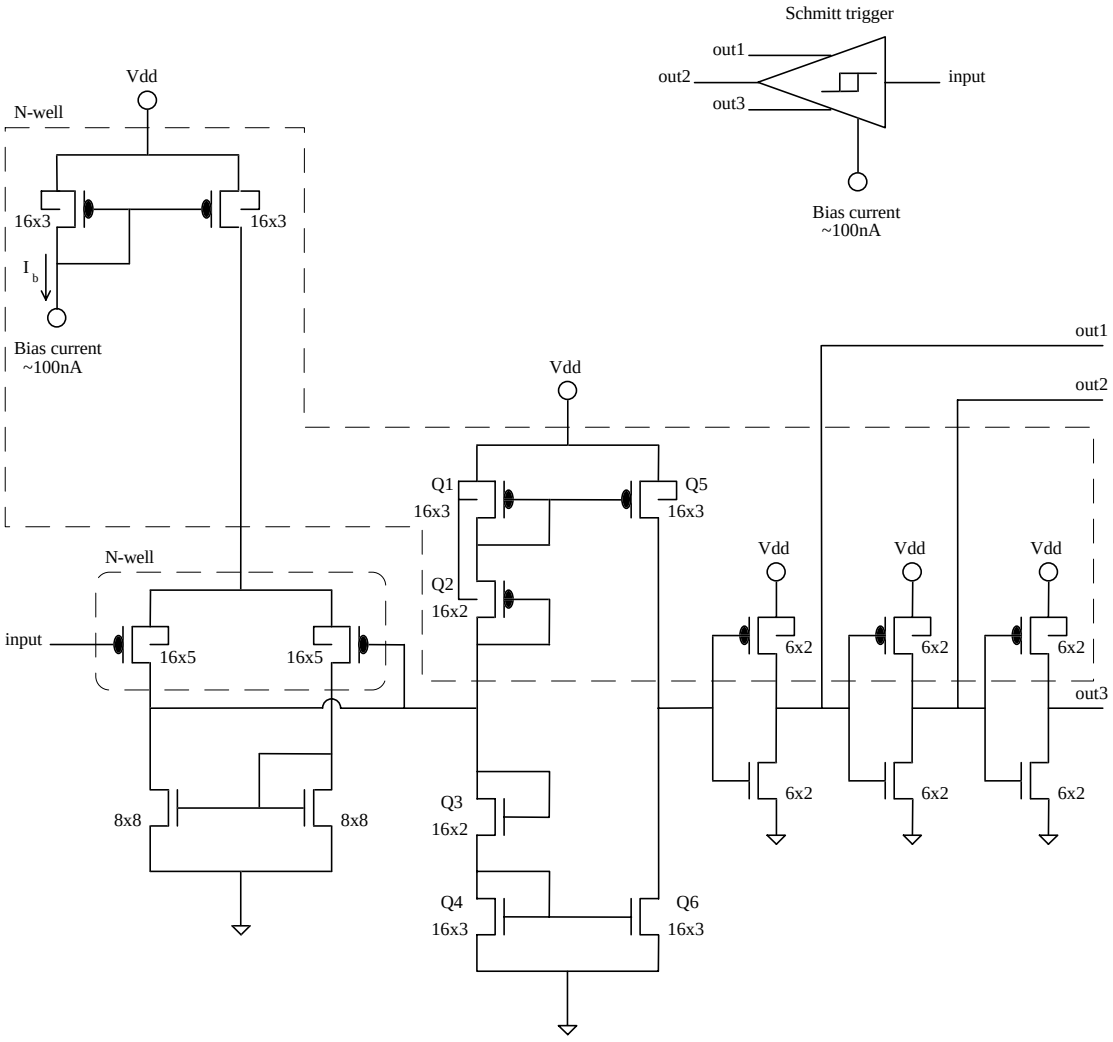

Figure 7.5: Schmitt trigger circuit.

Testing of the Schmitt triggers revealed that in order to reduce propagation delays to acceptable levels, it was necessary to operate at higher bias currents than predicted by the preliminary computer simulations. The discrepancy between the predicted and measured speed of the Schmitt trigger was mostly thought to be the result of poor

modeling of subthreshold transistor operation by the original SPICE simulator. Early simulations predicted propagation delays of 0.9 μs in response to a step input from 0 V to 2.5 V and 2.2 μs in response to a step input from 2.5 V to 0 V, with only 100 nA bias current. However, measured propagation delays with a 2.5 V supply and 150 nA bias current (supplied by a 10 MΩ resistor connecting the bias pin to ground) were 65 μs in response to a step input from 0 V to 2.5 V and 20 μs in response to a step input from 2.5 V to 0 V. Biased at 297 nA by a 5.1 MΩ resistor, the Schmitt trigger had propagation delays of 32 μs for the rising step input, and 2 μs for the falling step input. The thresholds where 0.55 V and 1.45 V with this bias current.

Propagation delays of the Schmitt trigger running at 2.5 V with 1.4 μA bias current (provided by a 1 MΩ resistor connecting the bias pin to ground) were 7 μs for a rising step input and 2 μs for a falling step input. Both delays were measured from the step transition to the time when the first inverter output crossed 1.25 V (50%). Delay through two inverters (from out1 to out3) was approximately 2 μs. But it should be mentioned that the stray capacitance introduced by connecting out1, out2, and out3 to the external pins of the IC package was much larger than the capacitances intrinsic to the integrated circuit. The capacitance between the pins in the test setup was probably greater than 1 pF, compared to less than 100 fF total capacitance at each of these nodes in the IC. And the pins for out1, out2, and out3 were adjacent, so the Miller effect could increase the impact of the capacitance between the pins, increasing the delay through the three inverters. It was also noted that the inverter outputs fell faster than they rose due to the lower “on” resistance of the n-channel transistors compared to the p-channel devices. Thresholds of the Schmitt trigger in this configuration were 1.5 V for slowly rising ramp inputs and 0.4 V for falling ramp inputs.

One possible explanation for the long propagation delays at low bias levels was motivated by an observation made during the experiments. Interestingly, the measured propagation delay for the rising input was *decreased* in all cases when the step amplitude was reduced. Using step inputs smaller than 2.5 V reduced the delay significantly (up to 50% for the low bias current cases). This effect suggested that the input differential pair and current source limit when its output is high (the input is low). When a large rising step input is used, the transistors in the differential pair both tend to shut off. The drain-source voltage of the current mirror transistor supplying the differential pair is too small to saturate the transistor, so it does not supply the intended

bias current. In this mode, the voltage across the series pair of n-channel transistors that provide the high threshold voltage must decay naturally to the point that the differential pair is turned back on again. This is a slow process compared to the active pull-down on the same node when the current through the differential amplifier is not shut off. A smaller input step might not shut off the differential pair and its current source as completely, allowing it to actively draw current from the threshold-setting node, thereby rapidly lowering its voltage and changing the Schmitt trigger output state. The dependence of propagation delay on input amplitude could probably be remedied by modifying the circuit to ensure that the input differential amplifier never shuts off, but instead always flows its intended bias current. This could be accomplished by increasing the supply voltage, or increasing the width of the differential pair transistors so that they operate with a lower gate-source voltage. Also, the threshold-setting transistors could be changed to lower the high threshold voltage so that it does not drive the differential pair and bias current mirror out of their operating range.

This explanation seemed quite plausible before the improved circuit simulations were performed, but these did not entirely support this theory. While recent computer simulations with the improved software were in closer agreement with the 1.4 μA bias current test case, predicting a 4 μs propagation delay in response to a 2.5 V rising step input and 2 μs delay in response to a falling step input, they still did not account for the very long delays observed at low bias levels. Even when the parasitic capacitances of the test setup were included in the circuit model, the simulator predicted delays of only 5 μs for rising step inputs and 7 μs for falling step inputs with 100 nA bias current! While the simulations of the circuit with 100 nA bias current show the source voltage of the input differential pair rise to almost 2.5 V for about 3 μs following a rising step input, which would shut off the bias current mirror as explained in the previous paragraph, the simulated circuit recovers after this and the output changes state 2 μs later. This finding is rather difficult to reconcile with the experimental results, so either the simulation is still inadequate, or there is another phenomenon or aspect of the circuit that has been overlooked in the model. It is now thought that the input transistor gate was damaged by electrostatic discharge (ESD), and that this damage impaired the Schmitt trigger circuit without totally preventing its operation. Great care was taken in handling the integrated circuit because its gates were unprotected and therefore extremely vulnerable to ESD, but it is possible that even during packaging at the foundry that the circuit was damaged.

Combining the results of the preceding experiments, the complete encoder circuit was tested. Using a 2.5 V supply, the input amplifier stage was biased at 558 nA with a 510 kΩ resistor and the Schmitt trigger stage was biased at 1.4 μA with a 1 MΩ resistor. Without the stray capacitance of the package pins connected to the Schmitt trigger, the propagation delay for a fast falling input was was only 0.5 μs, as evidenced by the LED drive output. In order to determine the proper integration bias current, the input amplifier stage was temporarily disabled by open-circuiting its bias pin. This prevented amplifier output current from influencing the base period of the integrator cycle. Integration bias current of 246 nA provided by a 6.6 MΩ resistor set the base period to 30 μs as desired. Since the circuit is designed to self-bias so that there is zero DC current output from the input stage, the base period should be unchanged when the input amplifier is operating. However, the base period was in fact highly dependent on the DC input voltage. For inputs less than about 1.2 V, the period was less than 10 μs, and there was no detectable change in the period for small-signal inputs. Increasing the input voltage from 1.2 V to 1.35 V caused the period to lengthen to a maximum of about 20 μs, and the period became quite jittery. In this input range, there was some period change corresponding to small-signal inputs. It is suspected that charge injection from switch SW2 is the cause of these problems. When NMOS transistor SW2 connecting the output of the input amplifier to its inverting input is switched off, the bias capacitor on the inverting input is supposed to hold the voltage on this node. Because the input amplifier was connected as a voltage follower before the switch was opened, the bias capacitor voltage was set to approximately the amplifier input voltage, so that there was zero current output from the amplifier. Apparently, as the NMOS transistor gate is changed from 2.5 V to 0 V to switch the transistor off, it injects enough (negative) charge onto the bias capacitor to lower its voltage by a non-negligible amount. At low DC input voltages (less than 1.2 V), where the input amplifier is functioning properly, this offset voltage on the inverting input causes an unwanted current to flow from the input stage onto the integration capacitor resulting in a decreased period of oscillation. Since the period of integration is very small, it is almost entirely set by the propagation delays of the Schmitt trigger, and AC small-signal inputs have negligible effect on the period. Only when the input voltage exceeds 1.2V, and the input amplifier begins to limit, does the period begin to increase again. This is because the current source (mirror circuit) supplying the input differential pair begins to shut off, limiting the ability of the input stage to supply *any* output current, including the unwanted offset current. For a small DC bias range (1.2 V

to 1.35 V), the input stage operates in a severely impaired manner to modulate the integration period. At higher input voltages, the circuit ceases to function entirely.

Various approaches could be taken to address the problem of charge injection from switch SW2. The simplest solution might be to decrease the integration bias current so that the input amplifier offset current provides the primary source of DC integration current. The charge-injection induced offset voltage is not large enough to take the input stage out of its small-signal amplifier operating range if the input is biased correctly (less than 1.2 V), so the signal current that depends on the AC input voltage will still change the period as intended. It may be necessary to decrease the input amplifier bias current to achieve the desired base period, at the expense of some signal gain. Alternatively, a "dummy" switch could be connected to the bias capacitor and switched to complement SW2, tending to cancel the charge injection. Continuous, non-switching techniques might be used to bias the input amplifier, eliminating the need for SW2 entirely. These concepts were not tested in the context of the single-channel telemeter, because after this initial design the research effort shifted to multi-channel telemeters. Techniques to improve the function of the various circuit components were explored in the development of multi-channel telemeters.

7.3.2 Test Chip Two:

An 8-channel neural waveform telemeter was designed for the second test chip. The circuit is sketched in terms of its functional component blocks in Figure 7.6. This circuit is designed to sample 8 input channels simultaneously, then use a pulse-period encoder to sequentially output the signal information. In the same manner as the single channel encoder of test chip one, the initial offset of each channel is nulled before each sample by connecting the outputs of the amplifier stages to their inverting inputs during the readout. Thus the derivative of the input signal is encoded, as before. Unlike the single-channel encoder, the periods between the readout pulses of this telemeter are *directly* proportional to the derivative of the corresponding input voltage.

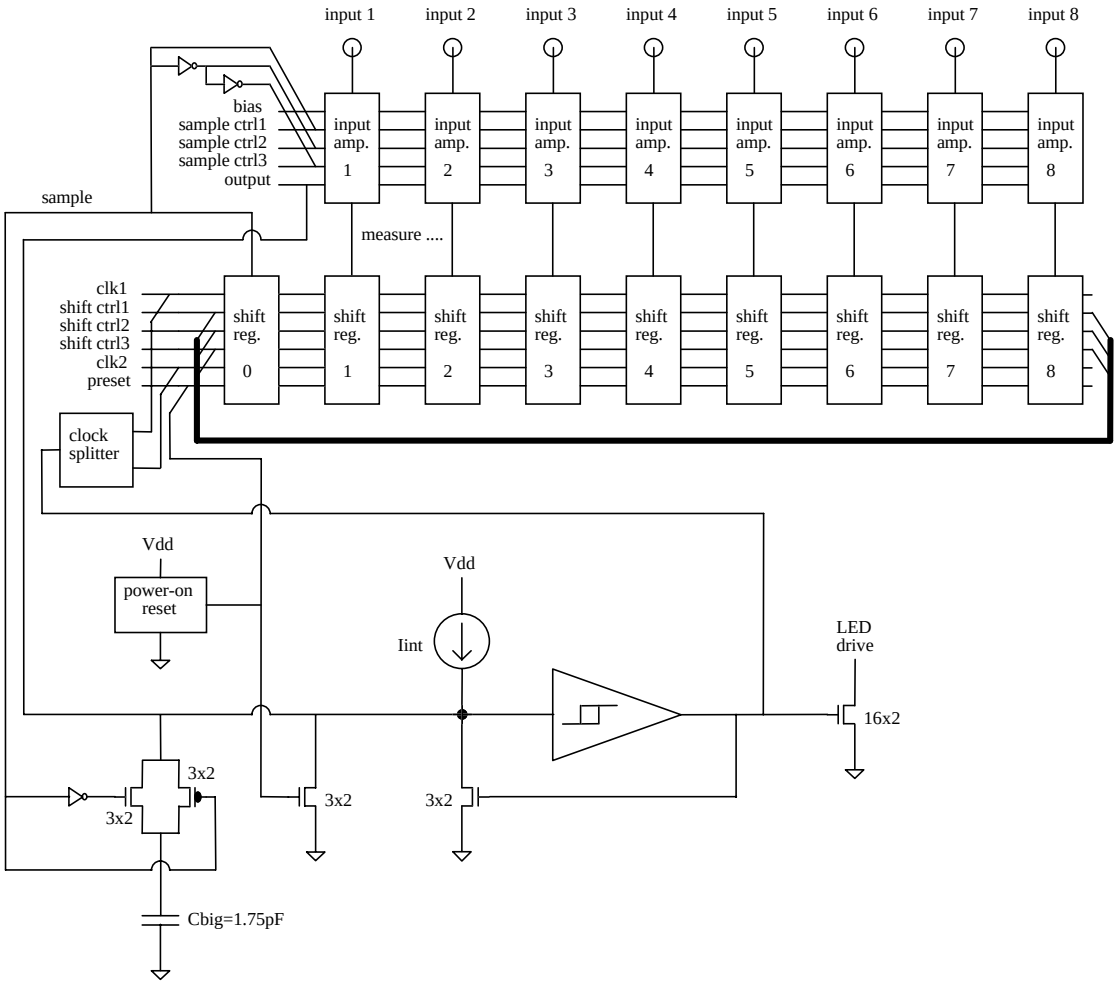

Figure 7.6: First design of an 8-channel telemeter circuit.

7.3.2.1 Theory of operation of first 8-channel telemeter

The circuit operates in two modes during each sampling cycle: one in which the sample is acquired, and one in which the data is serially encoded and transmitted. During the sample (acquire) mode, the outputs of the amplifiers are disconnected from their inverting inputs, where storage capacitors maintain the bias voltages. Then, any change in the input voltages will cause currents to flow from the corresponding input stages. The output current from each stage is integrated onto a sampling capacitor for a fixed amount of time, approximately 20μs, so the charge stored on the capacitors will be proportional to the change of the integral of the input voltage over this sampling time. But if the *rate* of change of the input voltage is relatively constant over this small sampling time, then the change of the integral over this interval will simply be

proportional to the total change of the input voltage. The amount of charge stored on each capacitor during the sampling period is therefore:

$$q_s = \int_{t_0}^{t_0+T_s} g_m\left(v_{in}(t) - v_{in}(t_0)\right)dt \approx \underbrace{\left(g_m T_s\right)}_{\text{constant}} \Delta v_{in} ,$$

where g_m is the transconductance of the input amplifier and Δv_{in} is the change in the channel input voltage over the sampling period from time t_0 to $t_0 + T_s$. At the end of the sampling period, the sampling capacitors are disconnected from the input amplifier outputs, which are then re-connected to the inverting inputs with their bias storage capacitors. To mark the beginning of the read-out period, the output LED drive switch is closed momentarily to emit a pulse of light. The sampling capacitors are then connected one at a time to a current source and Schmitt trigger. The voltage on the connected sampling capacitor rises at a constant rate, and when it exceeds the Schmitt trigger high threshold, the Schmitt trigger output changes state. The time it takes for the capacitor to charge up to the Schmitt trigger's high threshold depends on the amount of charge initially on the capacitor, so the time will be linearly related to the derivative of the input signal for the channel being read out. When the Schmitt trigger output changes state, it closes the LED output drive switch, and it closes a switch which resets the capacitor voltage to the Schmitt trigger's low threshold. At the same time, a shift register is advanced to connect the next sampling capacitor to the current source so that it may be read out. Thus the time between each flash of light and the previous one is linearly related to the sampled time derivative of the input voltage of the corresponding channel. Figure 7.7 may help to illustrate this data sampling technique.

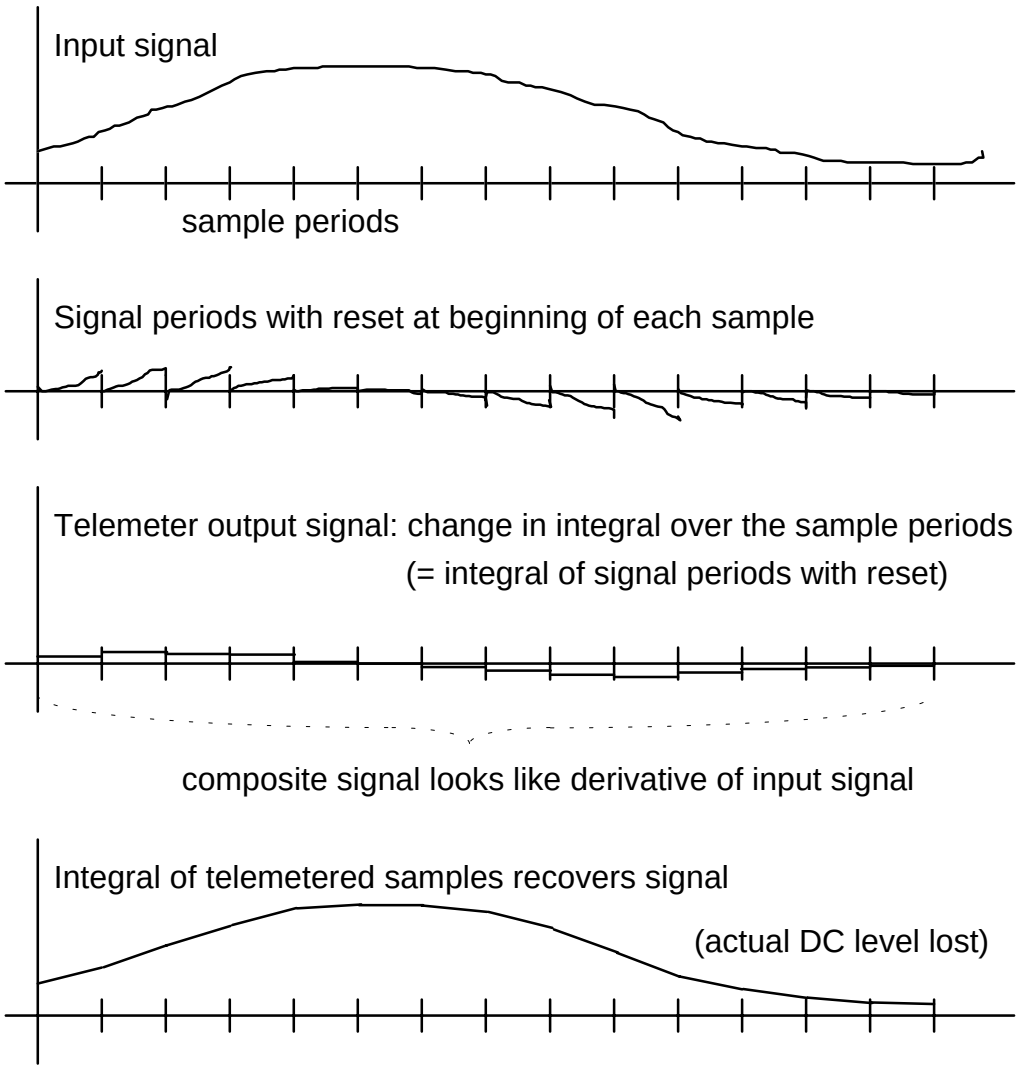

Figure 7.7: Illustration of data sampling technique used by the first 8-channel telemeter design.

The first trace gives a hypothetical input signal for one channel. The second trace shows what the signal looks like when the input amplifier is reset at the beginning of each sample. Each of these signal periods is then integrated, yielding the levels shown on the third trace (which have been expanded to fill the whole period just for ease of presentation). These levels represent the voltage on the sampling capacitor at the end of each sampling period, which is then pulse-period encoded. The pulse periods for this one channel are actually multiplexed with the other channel output signals in a repetitive sequence. Finally, once the data for the different channels are received and separated, the periods corresponding to one channel output can be converted to a voltage signal which once again looks like the third trace in Figure 7.7. This can be integrated to reconstruct the input signal information for this channel (except for the DC level of the

signal), as shown in the final trace. Note that if the sample rate is sufficiently fast (twice the Nyquist rate would be a good value), the rate of change of the input signal will be relatively constant over the sampling period, and higher frequency noise will be filtered by the sample integration process. Further beneficial smoothing of the data will occur when the telemetered signals are integrated to reconstruct the input signals.

The quantitative relationship between the input signal and the pulse period modulation was approximated as follows for the purposes of this design. Since the integration capacitors were supposed to be reset to the low Schmitt trigger threshold voltage, which early simulation and hand calculation indicated to be about 0.75 V, a maximum modulation of the capacitor voltage of ±0.5 V was desired. This would ensure a drain-source voltage of at least 0.25 V across the n-channel transistor at the output of the input amplifier, and would make the maximum capacitor voltage 1.25 V, a reasonable amount below the high Schmitt trigger threshold of 1.56 V. The maximum input signal for which the system was designed is a nerve action potential recording of amplitude 10 mV that peaks in approximately 0.1 ms. This corresponds to an input slew rate of about 100 V/s. Assuming the input amplifier has a transconductance of 7.5 μA/V at 0.625 μA total bias current, this input signal will create an output current that increases at 750 μA/s. Because of the input amplifier reset used in this design, the output current at the beginning of the sampling period should be zero. So if the sampling period is 20 μs long, the integral of the current should be 150 fC, which is the total charge output during the sample. A 250 fF integrating capacitor was included in the design, so if this was the total capacitance at the output of the amplifier, its voltage would change by 0.6 V. However, there is probably more than 350 fF stray capacitance at the output of the amplifier that cuts the voltage change during the integration to 0.25 V. This is less than desired for the maximum input signal, but decreasing the integration capacitor would not significantly improve the situation because of the parasitics. In retrospect, a cascode circuit could have been used to decrease the effect of the input amp's stray capacitance (which is large because of the size of the input transistors). The change in capacitor voltage is divided by the hysteresis voltage of the Schmitt trigger (~0.81 V) to estimate the fractional change in readout period. Accordingly, the maximum input signal should produce a ±30% change in the readout period.

The whole read-out process was designed to take approximately 30 μs for the 8 channels, allotting an average of 3.75 μs for each channel readout. This design was

developed before the harsh trade-off between photodetector bandwidth and sensitivity was well understood, so the small time between pulses may make signal reception unnecessarily difficult. Subsequent designs took this into consideration. The long delay between flashes (20 μs) that occurs while the circuit is in the sampling mode serves as a marker for the beginning of the read-out sequence. The sample timing is accomplished by an extra stage in the shift register chain that connects a large capacitor to the read-out current source and switches the system into sample mode. The time it takes the large capacitor to charge up sets the sampling time, which should be constant since the capacitor voltage is always reset to the low threshold and not changed during the read-out period.

The input amplifier stage is almost the same circuit used for the single-channel encoder, as shown in Figure 7.8.

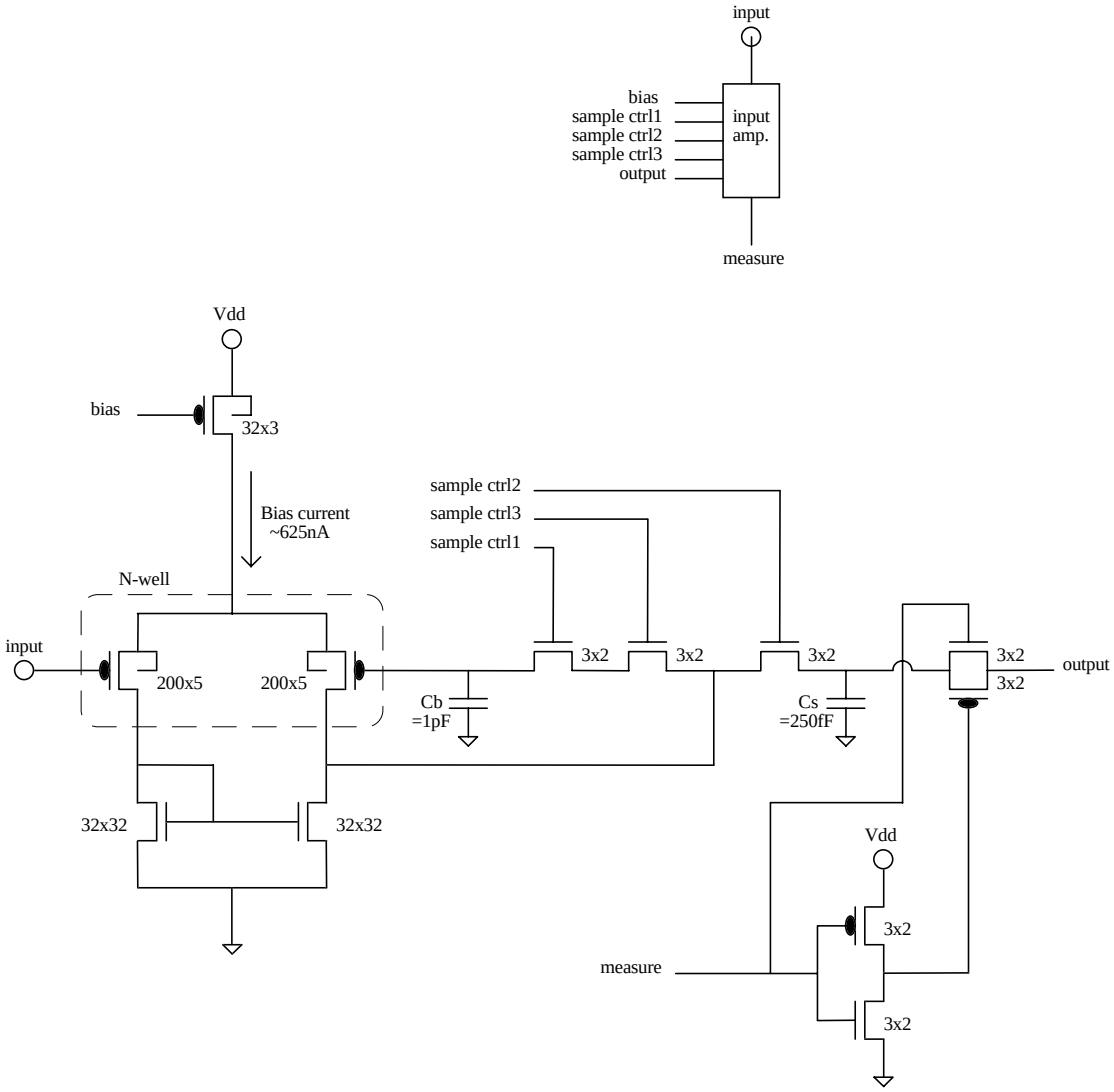

Figure 7.8: Input amplifier stage.

Figure 7.9 gives the schematic for a typical stage of the shift register, and Figure 7.10 shows the first stage.

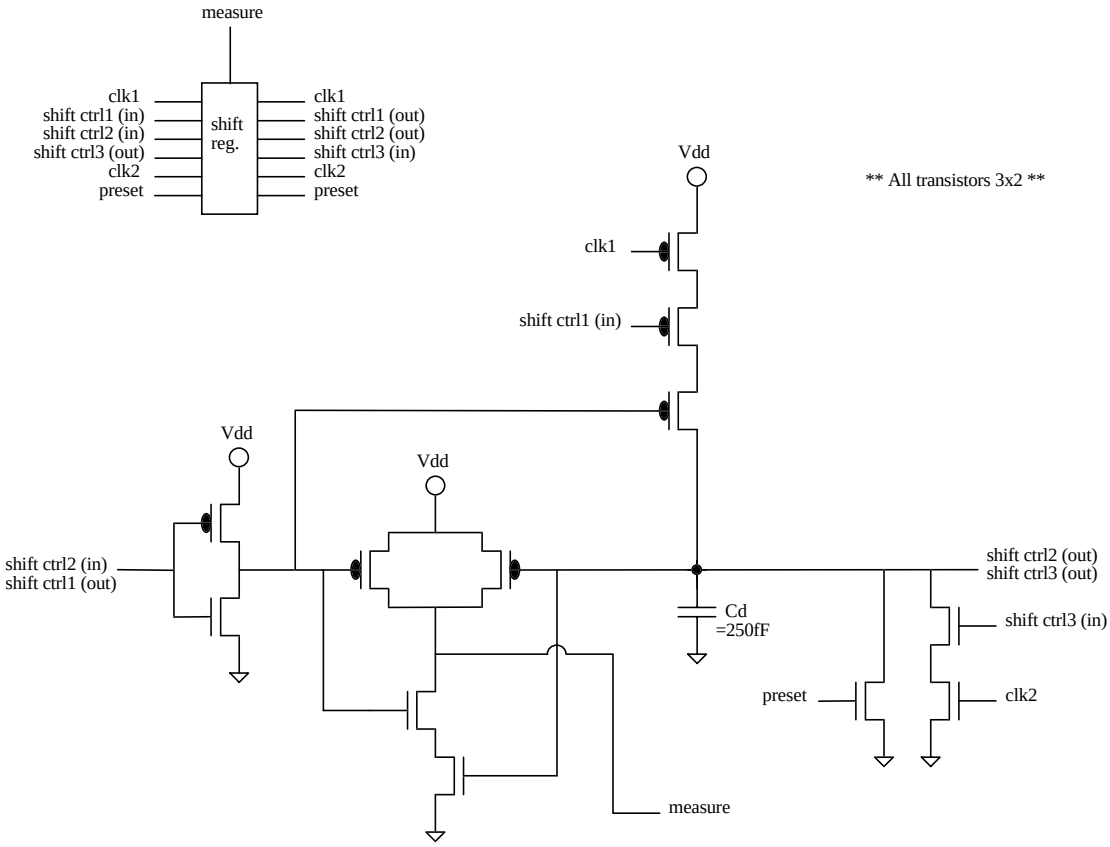

Figure 7.9: Standard shift register stage.

The shift register is a dynamic memory of sorts, where a capacitor stores the logic state information. The logic state of each stage is shifted to the next stage in the shift register with every clock pulse. The first stage differs from the other stages by a preset control which sets the storage capacitor voltage high, rather than low. The shift register is connected in a loop, so this single "high" bit is shifted around the register repeatedly. As the single high data bit is shifted through the register, it determines if the system is sampling the inputs or transmitting data. When the high bit is in the first stage (0), the inputs are being sampled, and when the high bit is in another stage, the corresponding channel is being read out.

Two clock phases are required for this shift register, referred to as "clk1" and "clk2". The "shift control" signals communicate state information between the stages. The shift process starts when clk2 goes low, preventing any storage capacitor from subsequently being pulled low. The capacitors hold their previous value until clk1 goes low. If the register was initialized properly, only one capacitor holds a high bit (V_{dd}), so only two stages will be affected by the data shift. Signals "shift ctrl1 (in)" and "shift ctrl2 (in)"

come from the storage capacitors of the two previous stages in the register and serve to move the high bit forward. Shift ctrl1 (in) is the storage capacitor two stages back in the register, and shift ctrl2 (in) is the storage capacitor one stage back. In order for a stage to be changed to the high state, shift ctrl1 (in) must be low, and shift ctrl2 (in) must be high. The one stage for which this is true will be pulled high when clk1 goes low. So when both clk1 and clk2 are low, two capacitors in the register will be high. Clk1 returns to the high state, followed by clk2. Shift ctrl3 (in), which is the storage capacitor of the next stage in the register, is able to pull the "old" high value stage low when clk2 goes high. This leaves only one stage high, completing the data shift. The primary output of each stage, used to control sampling and readout, is the "measure" signal. This is simply the state of each stage (the storage capacitor voltage) NANDed with the inverted state of the previous stage. This prevents overlap when clk1 and clk2 are low and two capacitors are in the high state. Only when one stage has the high bit will its "measure" output be low.

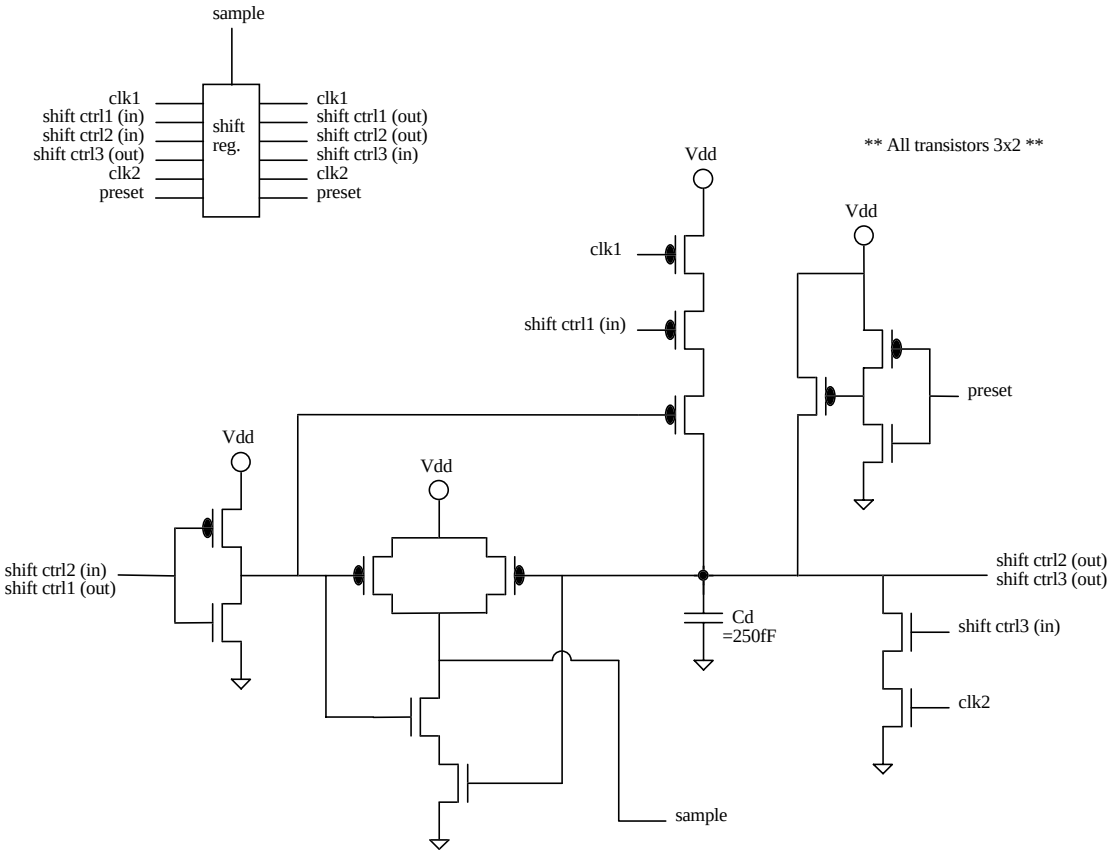

Figure 7.10: First stage of shift register.

The circuit that generates the two phases of the clock signal for the shift register is given in Figure 7.11. The input clock signal is the brief high pulse when the readout Schmitt trigger resets the integration capacitor and flashes the LED. This signal goes through two inverters to introduce a small delay. Then the normal and delayed clock pulses are NANDed and NORed to generate clk1 and clk2, respectively. Thus clk2 goes low before clk1, and returns high after clk1. The only reason that clk2 is returned to the high state before clk1 is to prevent a direct current path from the positive supply to ground in the case that the shift register is in a funny state (after start-up, for example). Otherwise the clock splitter could be replaced by simply three inverters in series. The output of the first inverter would provide clk2, and the output of the third inverter would be clk1.

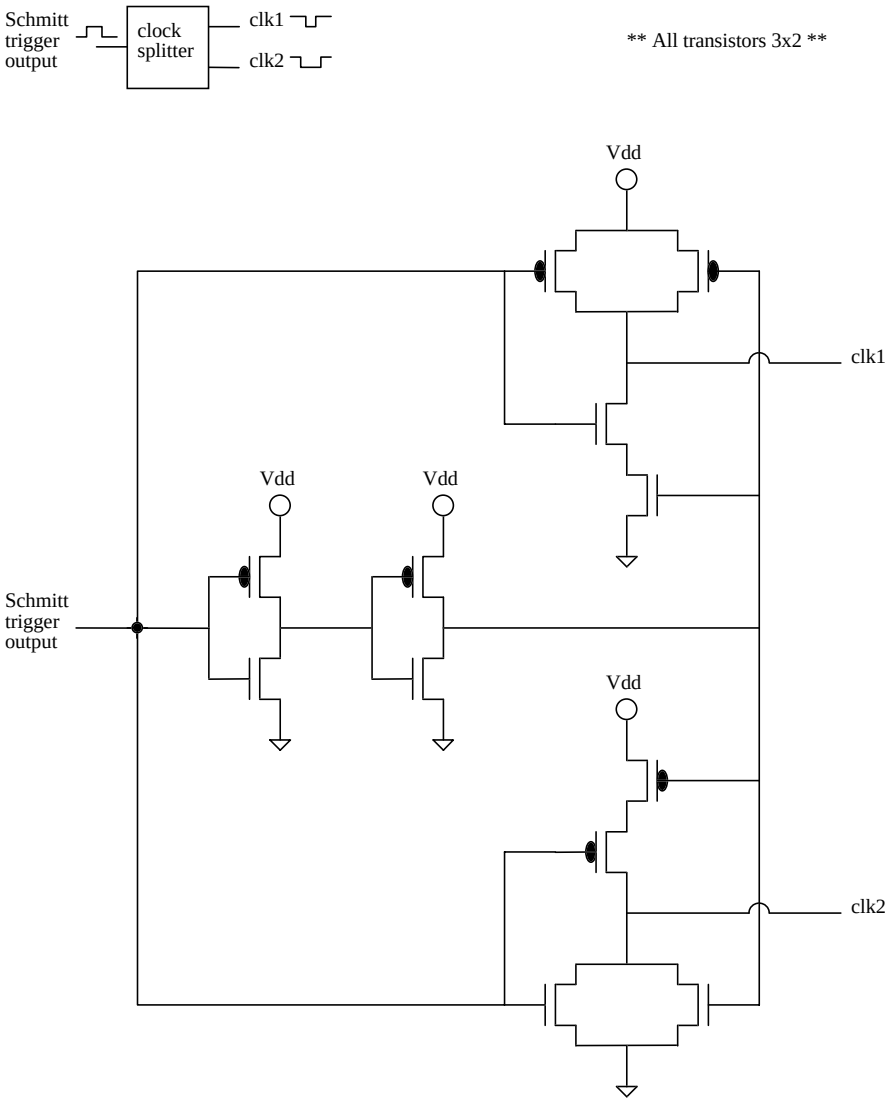

Figure 7.11: Clock splitter circuit.

Figure 7.12 provides the details of various other components of this prototype circuit. The power-on reset circuit was designed to provide a brief high logic signal for the shift register preset when the circuit was powered up. It was expected that the capacitor would initially pull the voltage across the reverse-biased well diode high, and that the leakage current through the diode would lower the voltage over a brief interval, less than one second. The inverters are to buffer the diode voltage and sharpen the transitions.

Input Amplifier Bias:

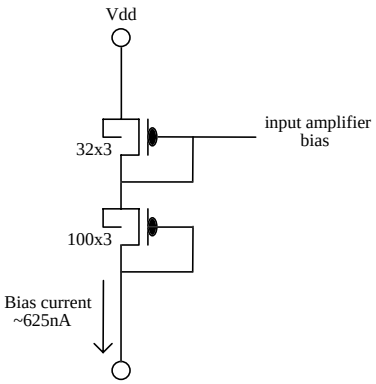

Power-On Reset (Preset):

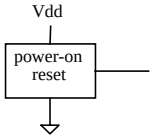

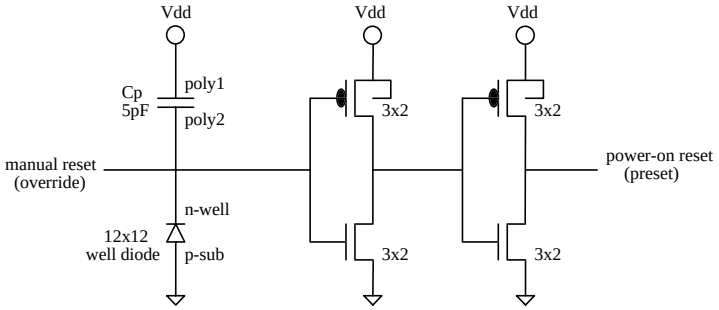

Integration Current Source:

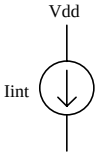

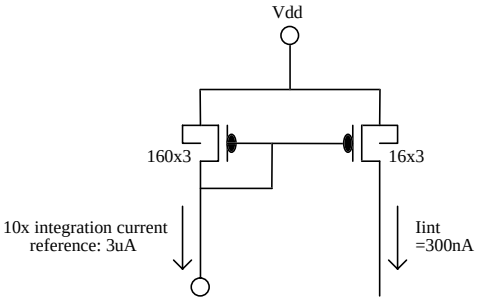

Standard Inverter:

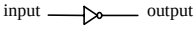

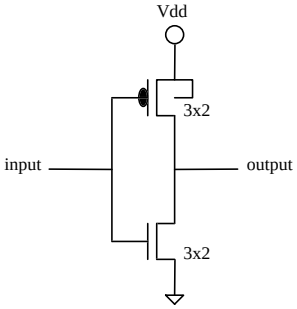

Figure 7.12: Miscellaneous 8-channel encoder components.

The Schmitt trigger is essentially the same as used for the single-channel encoder (Figure 7.5), except that “out2” is the only output used, as shown in Figure 7.13.

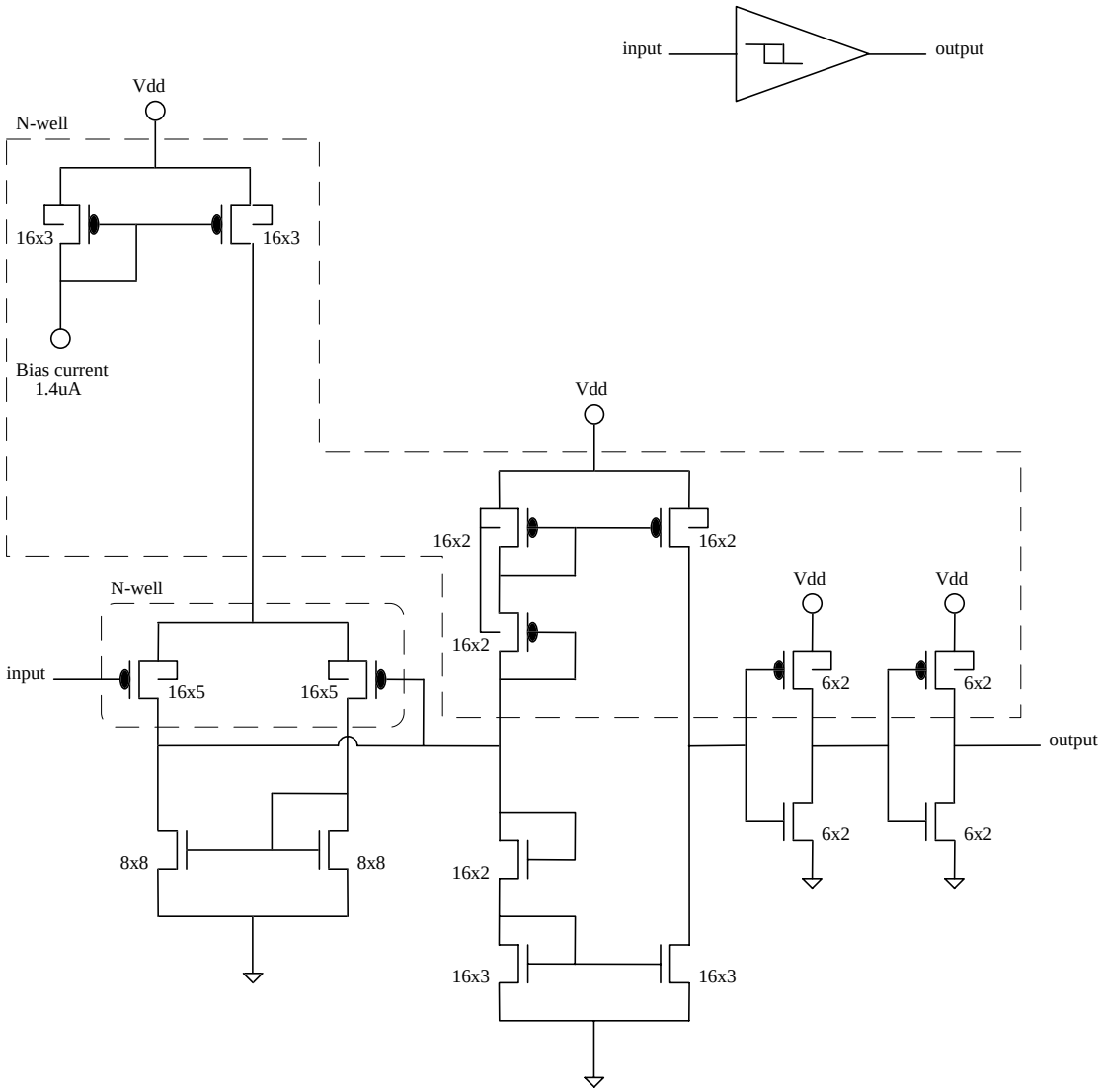

Figure 7.13: 8-Channel encoder Schmitt trigger.

7.3.2.2 Testing of first 8-channel telemeter circuit

The basic operation of the 8-channel telemeter circuit was according to design, but the readout period modulation by the input signals was much less than expected, and the relative timing of the sampling and readout periods were not as predicted. Also the power-on reset circuit did not pull the preset line low and had to be manually over-ridden. Leakage current through either the capacitor or the package leads evidently held the diode voltage at some intermediate level. The 8-channel encoder was tested with a 2.5 V positive supply (V_{dd}), the input amplifiers biased at about 594 nA (by a 510 kΩ resistor in series with the two p-channel bias transistors), the Schmitt trigger biased at 1.37 μA (by a 1 MΩ resistor), and the integration current set to approximately 295 nA (by

a 510 kΩ resistor flowing 2.95 μA on the 10x reference input). The DC voltage on the channel inputs was 0.75 V for most of the measurements. The sampling time, as indicated by the longest period in the 9-period output cycle, was 16.2 μs. In order from first to last, the eight periods corresponding to the input channels were approximately 6.2 μs, 6.15 μs, 6.15 μs, 6.15 μs, 5.8 μs, 5.9 μs, 6 μs, and 6.15 μs. These periods include the LED output pulses which last approximately 0.5 μs. The complete 9-period cycle averaged 64.5 μs, somewhat longer than desired. While increasing the integration current shortened the cycle time, this rate was acceptable for evaluation purposes.

Applying various small-signal AC waveforms to the channel inputs demonstrated that the encoder did basically function as a differentiator, changing the output periods in relationship to the derivative of the corresponding input signals. For example, applying a 2500 Hz triangle wave with 120 mV_{p-p} amplitude to input 8 made its corresponding output period (normally 6.15 μs) alternate between 5.95 μs and 6.35 μs. Applying a 5000 Hz triangle wave with 60 mV_{p-p} amplitude gave the same change in the period. Although the modulation is much less than predicted, this is the expected result to the extent that both inputs have the same derivatives of ±600 V/s. Changing the signal amplitude at a constant frequency had a proportional effect on the change in period, i.e. doubling the amplitude at 5000 Hz to 120 mV_{p-p} resulted in twice the deviation in the output periods, which were then 5.75 μs and 6.55 μs. Square wave inputs resulted in output periods that were mostly at their DC values, with two main deviations at equal increments above and below the DC value. These main deviations probably correspond to the step response of the input amplifier. Increasing the frequency of the input caused the deviations to become more prominent, as more of the step transitions occurred during the sampling phase of the cycle and were thus detected. A 20 mV_{p-p} square wave at 2500 Hz on channel 8 gave output periods mostly at 6.15 μs, with deviations out to 5.85 μs and 6.45 μs. No cross-talk between channels was observed, within the limitations of the decoding circuit.

A component of the period modulation that was proportional to the input signal became evident when the 8-channel decoder was used to reconstruct the encoded signals. As described in section 7.5, this decoder integrates a constant current for the time between each received pulse, so that at the instant each pulse is received the integrator voltage is proportional to the time since the previous pulse. This voltage is then sampled and demultiplexed to reconstruct the eight input signals. Figure 7.14 shows the output

voltage of the decoder integrator during operation of the 8-channel telemeter when no input signals were applied. The marker channel period creates the long ramps in the waveform (and the correspondingly large peak voltages) that are used by the decoder circuit to synchronize with the data transmission cycle. Following the marker period, each of the eight shorter ramps ends in the voltage representation of the corresponding input channel sample. Thus each cycle gives one sample of each channel. Note the consistency of the sample periods when no input signal is applied.

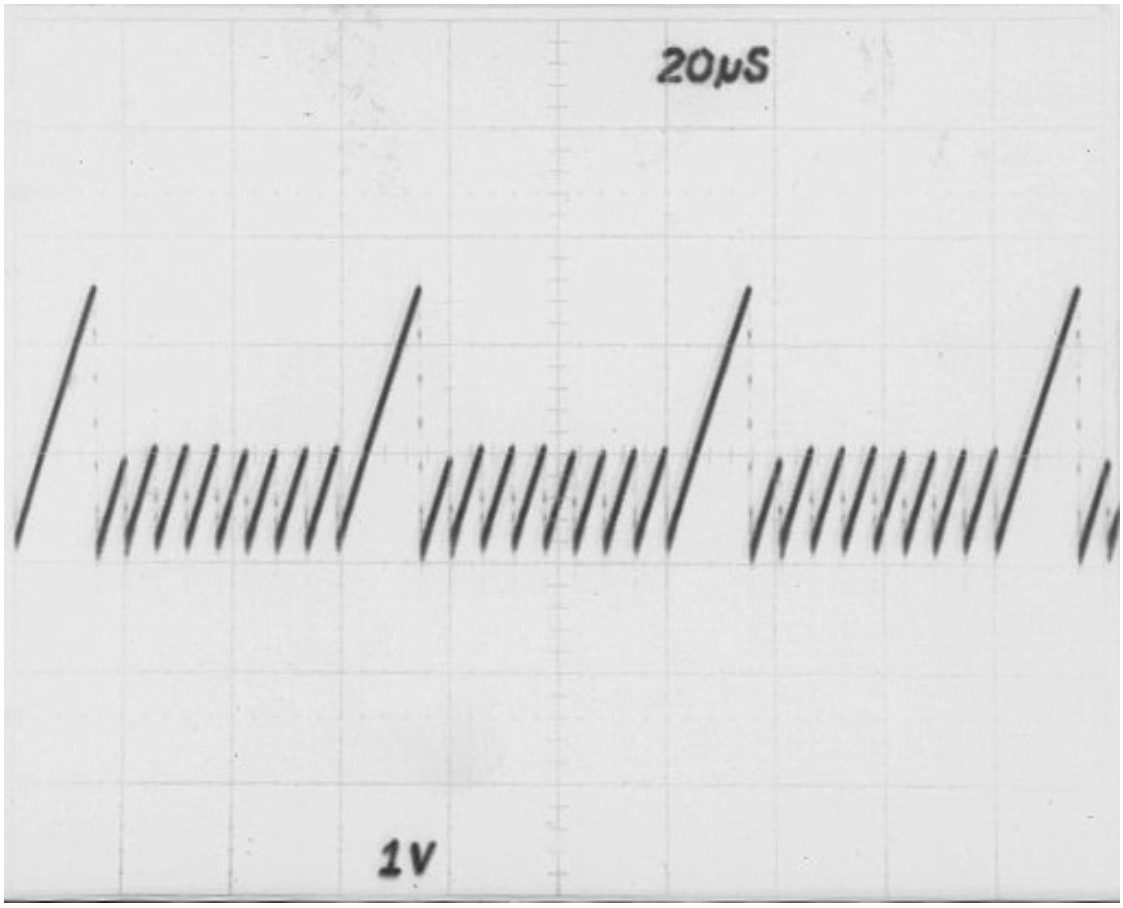

Figure 7.14: Output voltage of integrator in 8-channel decoder circuit (oscilloscope photo). Long ramps represent the marker period, and eight shorter ramps end in the representation of the corresponding channel sample. Each cycle reconstructs one sample of all eight channels.

Figure 7.15 shows the output of decoder channel eight when a 2 kHz sinewave was applied to the channel eight input of the telemeter. The top trace shows the input signal, the bottom trace shows the output of the sample-and-hold amplifier that acquires the integrator voltage at the end of the eighth signal period in the pulse sequence, and the middle trace is the sample-and-hold output filtered to reconstruct the transmitted signal.

Each step in the stair-step waveform seen at the output of the sample-and-hold corresponds to a sample of the encoder input signal.

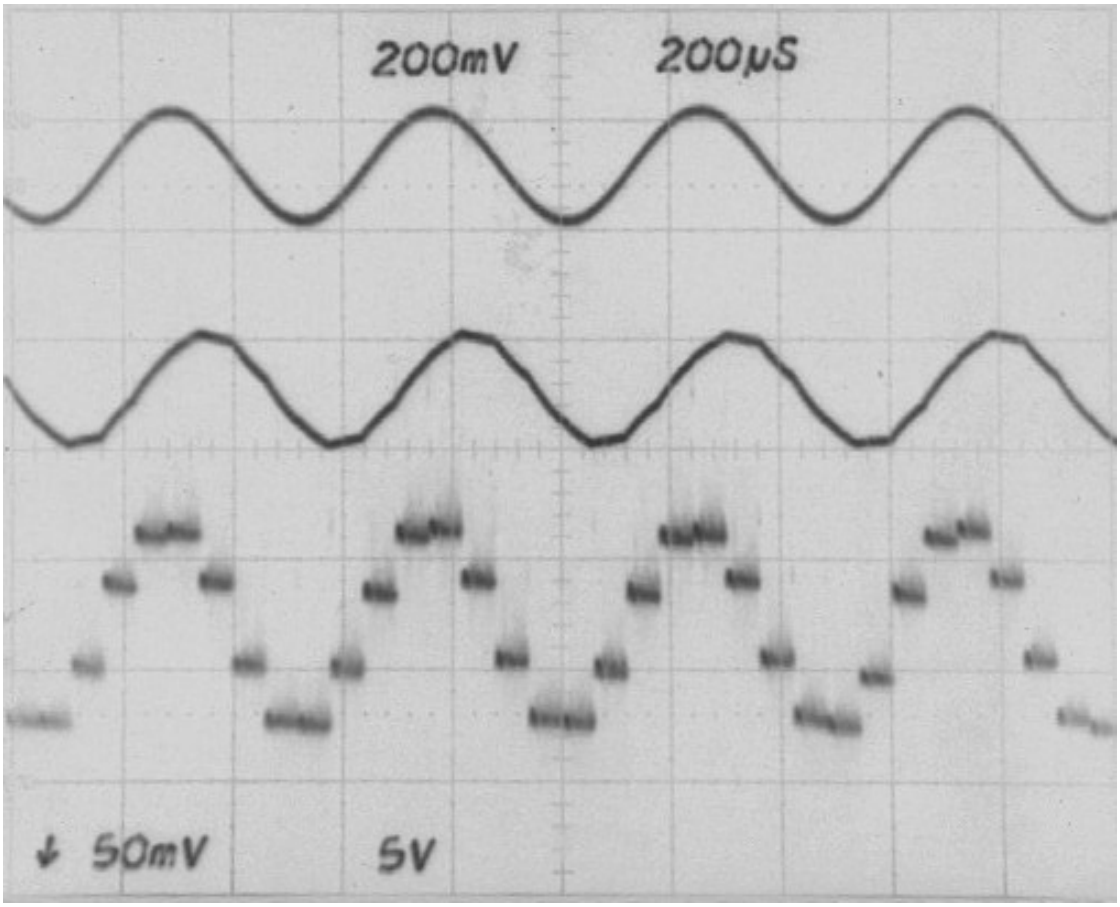

Figure 7.15: TOP: Telemeter channel eight input signal, 200 mV/div. MIDDLE: Telemetered signal reconstructed by decoder and low-pass filter, 5 V/div. BOTTOM: Partially reconstructed signal samples seen at output of decoder channel 8 sample-and-hold, 50 mV/div.

The same system voltages are shown in Figure 7.16 for the case when a triangle wave was input to channel eight of the telemeter. In the bottom trace of this figure (showing the raw decoder sample-and-hold voltages that are proportional to the pulse periods corresponding to the samples of channel eight), the two components of the period modulation are evident. The component that is proportional to the *derivative* of the input signal produces the expected large step changes in the sample-and-hold output voltage as the input triangle wave changes slope. But there is also a component of the period modulation that is directly proportional to the input voltage, as seen by the rising and falling of the decoder samples during the regions of constant input slope. This component is attributable to an incomplete reset of the input amplifier between samples.

Evidently, the bias capacitor on the input amplifier does not quite reach the input voltage. Nonetheless, the crude signal reconstruction seen in the middle trace can be performed with only a simple low-pass filter.

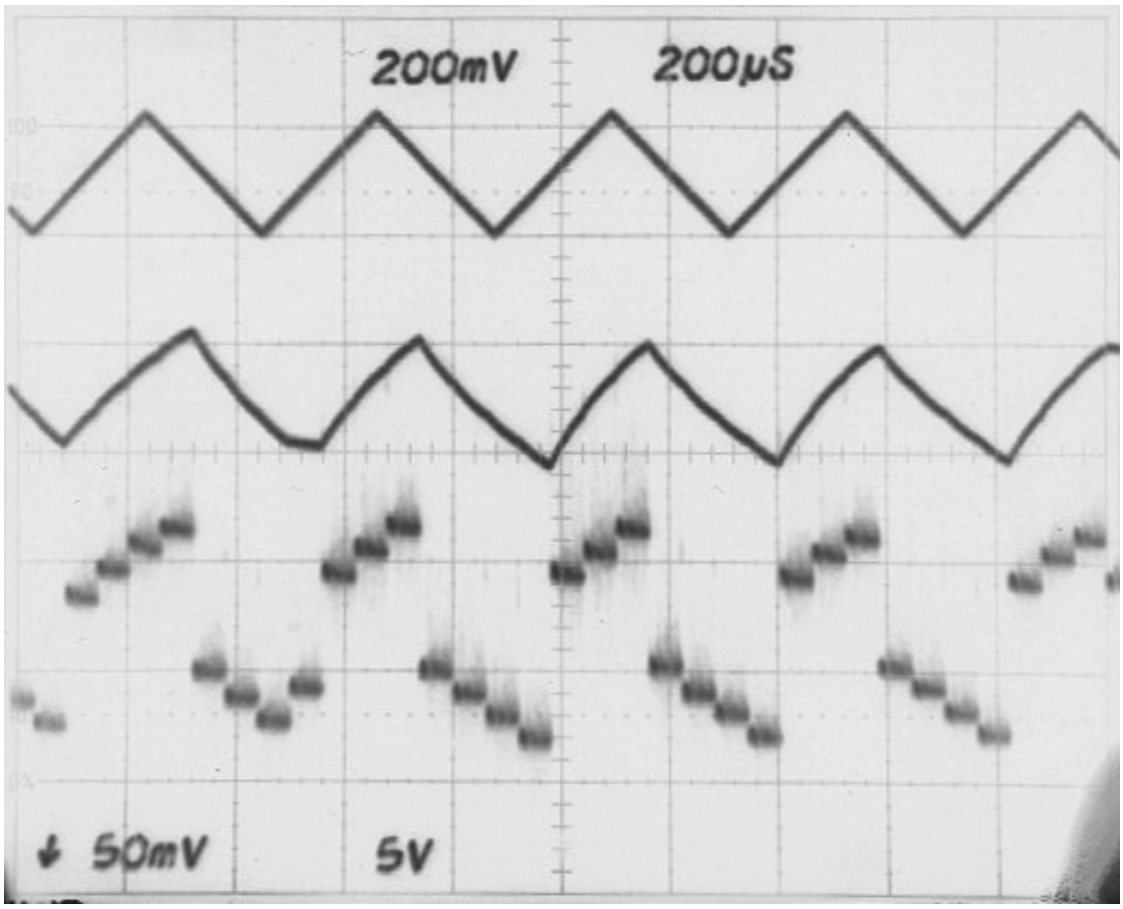

Figure 7.16: TOP: Telemeter channel eight input signal, 200 mV/div. MIDDLE: Telemetered signal reconstructed by decoder and low-pass filter, 5 V/div. BOTTOM: Partially reconstructed signal samples seen at output of decoder channel 8 sample-and-hold, 50 mV/div. Note large step changes corresponding to slope changes in input signal, and small step changes directly proportional to the input voltage.

A square wave input signal also illustrates the combination of derivative and proportional components of the pulse period modulation performed by this integrated circuit telemeter. In Figure 7.17, the decoded signal has large spikes when the telemeter's sample period happened to capture the step transitions in the square wave input signal. Only during these transitions is the derivative of the input signal not equal to zero. The rest of the time, the pulse periods are only modulated by the small factor that is directly proportional to the input voltage.

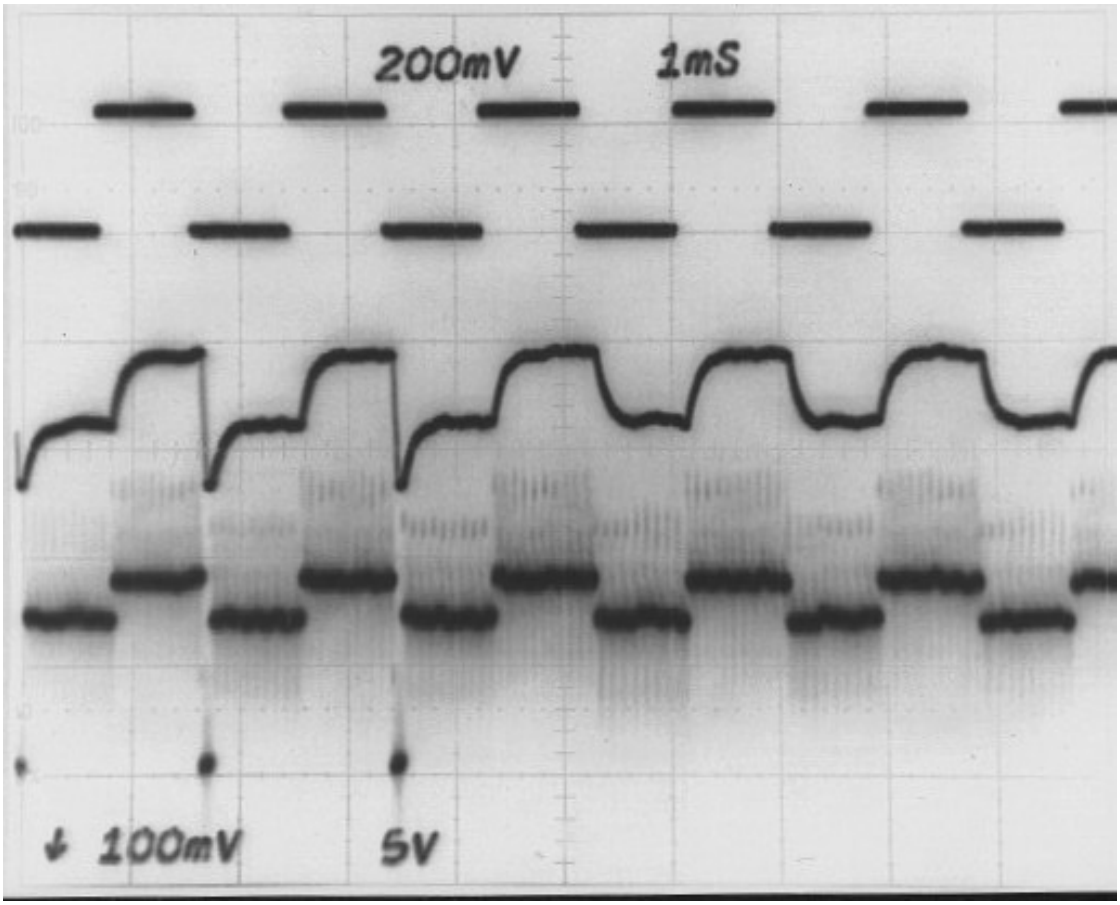

Figure 7.17: TOP: Telemeter channel eight input signal, 200 mV/div. MIDDLE: Telemetered signal reconstructed by decoder and low-pass filter, 5 V/div. BOTTOM: Partially reconstructed signal samples seen at output of decoder channel 8 sample-and-hold, 100 mV/div. Note large negative single-sample deviations when the telemeter samples and encodes step changes in the input signal.

Four factors are believed to contribute to the low signal "gain" (the period modulation) of the encoder. First, the sampling period as tested is about 20% shorter than the design value, so input signals are integrated for less time, resulting in less change in the capacitor voltages. Second, measurements of the Schmitt trigger from test chip 3 showed that delays were much longer than initial computer simulations had predicted. Even at the higher bias current used to speed up the Schmitt trigger circuit, it is quite possible that the propagation delay for rising input signals is 4 μs or more. If this is the case, then the true *signal* portion of the readout periods measured above are only 2 μs or so. Only this part of the period is modulated by the input signal, so what might be a reasonable fractional change in this 2 μs becomes a small fractional change (divided by almost 3) when the 4 μs constant delay is added to the period. Third, an oversight in this design was that the time constant of the integration capacitor reset (about 15 ns) is

much smaller than the propagation delays of the Schmitt trigger. Therefore the capacitor reset, which is a switch connecting it to ground, brings the capacitor voltage to zero rather than to the Schmitt trigger low threshold voltage. When this is connected to the input stage, it pulls the output voltage below its small signal operating range. The bias current of the amplifier should quickly charge the capacitor up to the point that the n-channel transistor is saturated, and the amplifier will resume operation, but the starting voltage on the integration capacitor is quite a bit lower than intended. Also, the effective transconductance of the amplifier is limited at this extreme of its output voltage range, especially for negative input signals, so the signal charge stored on the capacitor will be decreased. Since the voltage on the integrating capacitor is shifted to a lower average value, it takes longer for the readout current to bring the voltage up to the high threshold of the Schmitt trigger. This has the effect of further decreasing the modulation depth of the readout period because the signal voltage on the capacitor is a smaller fraction of the average voltage transition. The fourth factor that has been implicated in the weak period modulation of this encoder is the stray capacitance at various points in the circuit. A factor of two or more signal attenuation resulting from parasitic capacitances is quite conceivable. Particularly suspect is the capacitance associated with the bus and switches that connect the various input stages to the readout circuit.

The consequence of the decreased period modulation is that switching noise becomes a significant contributor to the input-referred noise of the system. The input-referred noise of the complete telemeter system is illustrated by Figure 7.18, which shows a 5 mV input sinewave (100 Hz) in comparison to the reconstructed output signal. Note that the noise is dominated by high frequency content from switching noise in the encoder circuit. The input-referred noise appears to be approximately 10 mV_{p-p} on this oscilloscope photo, but most of it is high frequency. Filtered at 7 kHz, the input-referred noise is approximately 7 mV_{p-p}.

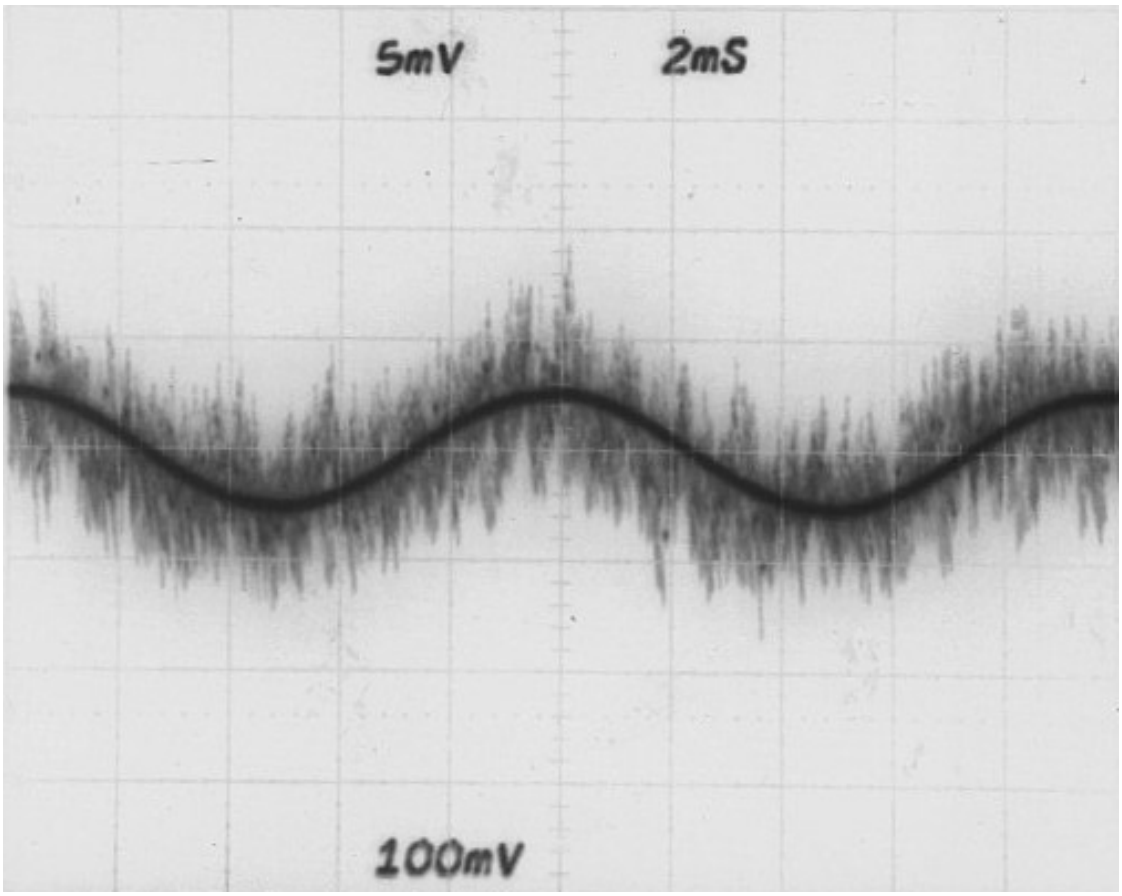

Figure 7.18: Input sinewave (dark line), 5 mV and 100 Hz, compared to reconstructed signal (fuzzy waveform) for estimation of input-referred noise of complete telemeter system.

The operating range of DC inputs extended from 0.25 V to 1.05 V with full small-signal performance. At the lower voltage, the sampling time extended slightly to 16.4 μs and the cycle time increased to 69 μs, and at the upper end of the input range the sample time was 16 μs and the cycle took 61.5 μs. This demonstrates the high stability of the sampling time, and the ability of the input amplifiers to self-bias effectively over a wide range of input voltage.

Power consumption of the 8-channel telemeter was measured with the LED driver open-circuited, in order to assess the efficiency of the control logic (mainly the shift register) and the input amplifiers. Only 12.5 μA current was drawn from the 2.5 V supply in this configuration, for a total circuit power consumption of 31.25 μW. The LED driver has the desired on-resistance of 10.4 kΩ, so the current drive through the LED should be approximately 100 μA during each pulse. Pulse duration is about 0.5 μs, so the average current through the LED (assuming 9 pulses every 64.5 μs) should be 7 μA. This brings

the total power for the 8-channel telemeter, including signal transmission, to 48.7 μW. This does not include any external power supply conditioning circuitry.

Recognizing that the performance of this telemeter was hindered by the Schmitt trigger circuit, with its long propagation delays, this component was redesigned for subsequent telemeters. And in order to have longer data readout periods for the same sample rate, a sequential sampling/readout scheme was adopted in which each channel is sampled and immediately read out. A dedicated simultaneous sample period was not used, so a marker period just long enough to be easily distinguishable from the readout periods was used to synchronize the decoder to the data readout cycle. Instead of taking the derivative of the input signals to cancel input offset and electrode potential drift, three different techniques for input offset nulling were attempted in versions of this second-generation telemeter circuit. Also, anticipating use of these circuits in an actual optically-coupled telemeter implant, all second-level metal interconnects were replaced with polysilicon interconnects. This allowed the second-level metal layer to be used as a shield covering the entire chip area, blocking out light and adding an extra layer of protection from the harsh biological environment.

7.3.3 Test Chip Three

Basic operation of the 8-channel neural waveform telemeter of the third test chip is described by the component schematic of Figure 7.19. The input stabilization used for this telemeter is similar to the design of test chip two in that the input amplifiers can be connected as voltage followers to set the bias voltage on their inverting inputs. A capacitor holds the bias voltage for each stage while the feedback is disconnected and the amplifier is used to provide voltage gain for the input signal. The technique differs in that the reset operation is not performed before every sample, and a larger capacitor is relied on to hold the bias voltage for longer times. The reset can be performed during power-up by connecting its control to the power-on reset circuit, or it could be triggered periodically.

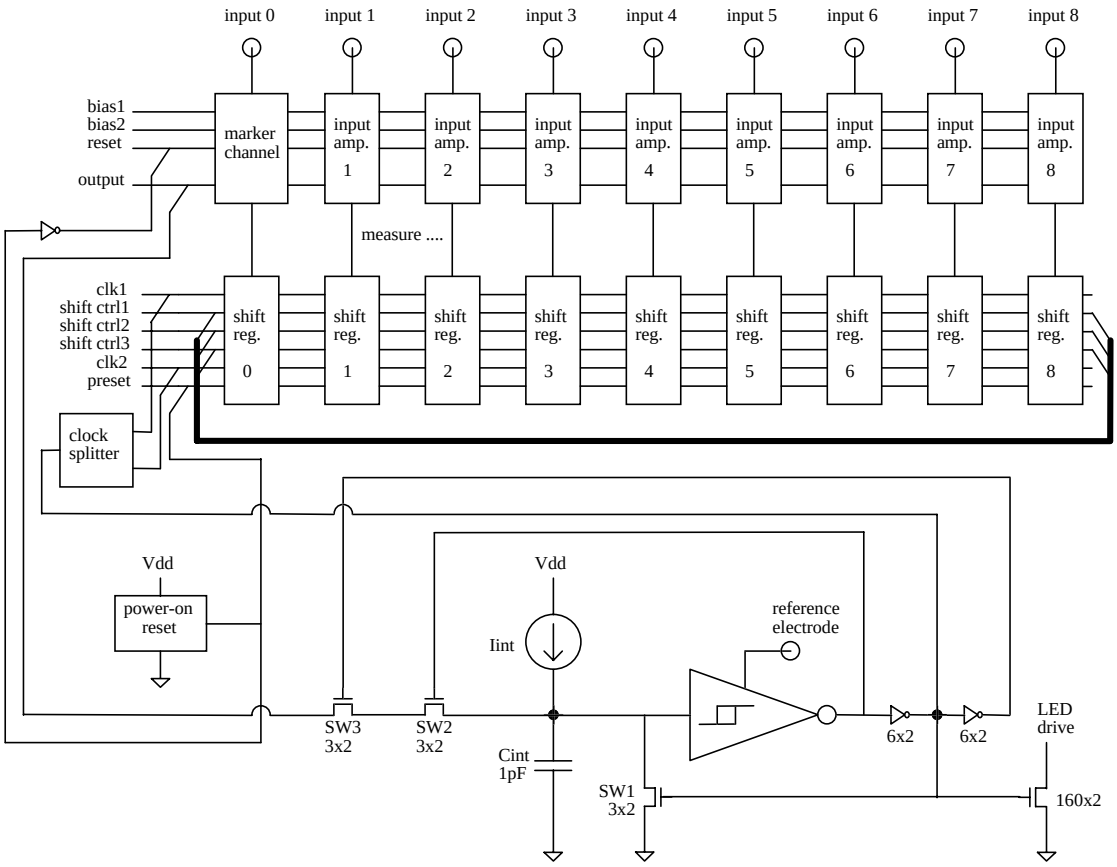

Figure 7.19: Improved 8-channel telemeter circuit design with input offset cancellation.

7.3.3.1 Theory of telemeter operation

A constant current flowing from source I_{int} onto capacitor C_{int} causes the voltage at the input of the Schmitt trigger to rise until the high threshold voltage of the Schmitt trigger is exceeded. When this happens, the inverting output of the Schmitt trigger goes low, open-circuiting the n-channel MOSFET switch SW2. An instant later, the first inverter after the Schmitt trigger changes to the high state, providing the first edge of the shift register clock pulse. The gates of the n-channel transistors SW1 and the LED driver are pulled high, closing these switches. The LED driver draws current through the output LED (which is also connected to V_{dd}), and SW1 discharges the integrating capacitor (C_{int}). Next, the second inverter output goes low, opening switch SW3. As the voltage across C_{int} rapidly falls to zero (about 120 ns 10-90% fall time), the Schmitt trigger's low threshold is crossed, and it begins to change state again. The output of the Schmitt trigger goes high after its propagation delay time, and switch SW2 is closed. The first inverter returns to the low output state, turning off the LED drive and opening switch SW1. This is also the end of the shift register clock pulse, completing the data shift that

controls the input stage multiplexing. Finally, the second inverter output goes high, closing switch SW3. This connects capacitor C_{int} to the output bus. One shift register stage will have a low "measure" output at a time, and the input amplifier associated with it will be connected to the output bus. The input amplifier circuit is illustrated in Figure 7.20.

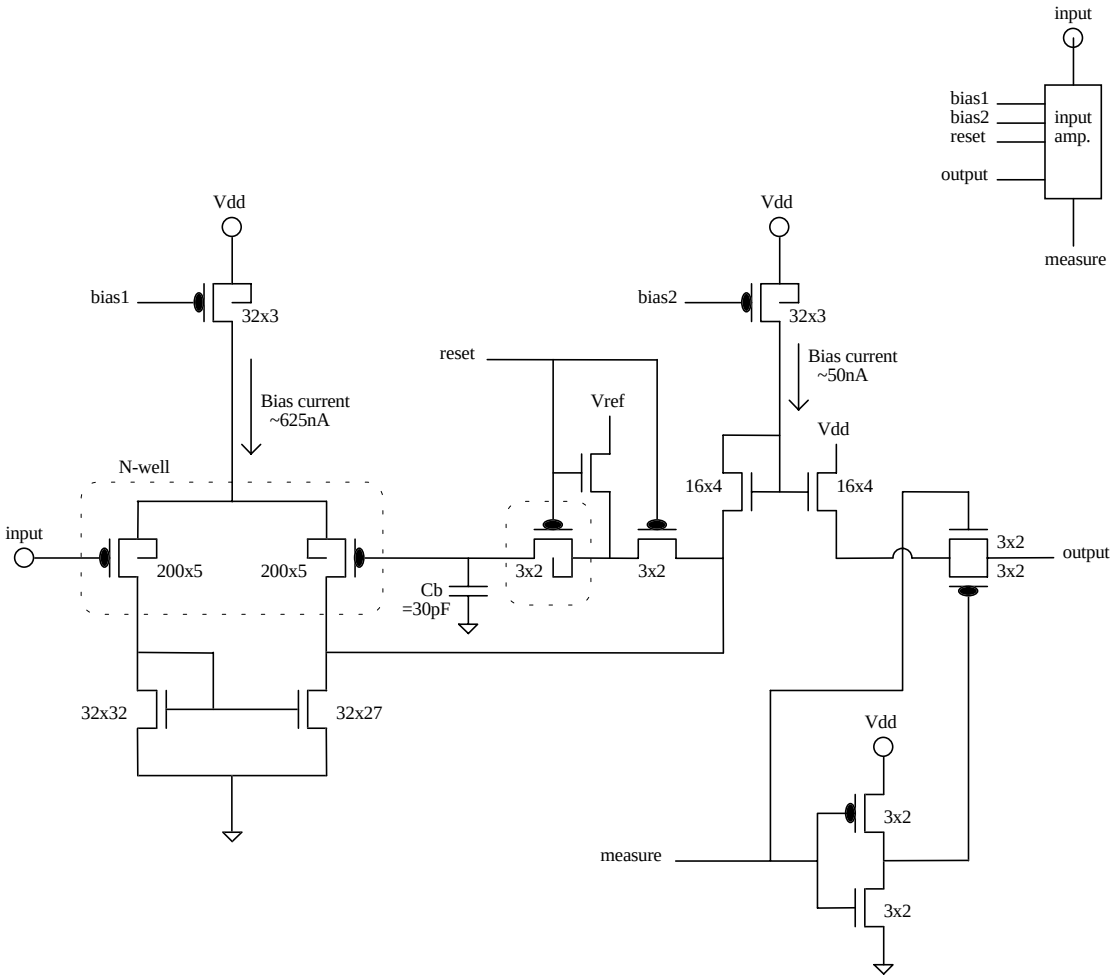

Figure 7.20: Input amplifier stage with bias setting capacitor for improved telemeter.

As seen in this schematic, the "measure" control line opens a pass gate when it is pulled low. This pass gate connects the source-follower circuit that buffers the amplifier output to the output bus. Via the output bus, connection is made to the readout integration capacitor C_{int} in Figure 7.19. Voltage on C_{int} is initially close to zero, so the n-channel transistor voltage follower quickly charges the capacitor until the voltage on it is close to the amplifier output. Since the follower circuit is unidirectional, it turns off as current I_{int} continues to raise the capacitor voltage at a slower, constant rate. Thus the change of the capacitor voltage can be approximately described by two phases: a rapid jump up to

the output voltage of the input amplifier, followed by a slower constant rate of rise. In this manner, the time required for the capacitor voltage to exceed the Schmitt trigger high threshold is modulated by the input signals. If the ramping phase dominates the time, the period will be linearly related to the input signal voltage. In normal operation the reset line in Figure 7.20 is in the high state, so the biasing feedback is disconnected, and input signals are multiplied by the open-loop gain of the input amplifier of about 240. This increases the modulation of the pulse period. In reset mode, when the reset line is low, the amplifier is connected with unity feedback to set the bias capacitor voltage. The elaborate switching that performs this is intended to maintain the bias voltage for a longer time by minimize leakage currents. When the reset line is high, the n-well that contains the open-circuit switch connected to the bias capacitor is held near the bias voltage in an attempt to decrease junction leakage currents.

Switching noise (kT/C noise) is a concern in all of these input amplifier circuits that use a capacitor to store a bias voltage. A 1 pF capacitor, such as used for bias in the integrated single-channel and first 8-channel telemeter designs, would have a random voltage error with a standard deviation of about 64 μV after switching. This would clearly exceed the desired rms noise specification of the neural waveform telemeter, except that it was not clear what effect the negative feedback around the amplifier would have on this noise. When a capacitor is disconnected from a constant voltage source, the thermal noise of the switch resistance is “aliased” down to DC. The rms variation in the final capacitor voltage is obtained from the total integral of the thermal noise of the switch resistor low-pass filtered by the capacitor. The actual value of the resistance drops out of the equation because the voltage noise and filter bandwidth are opposing functions of resistance. But in the case where the voltage source connected to the capacitor is not constant, and instead varies in proportion to the capacitor voltage with a negative gain, perhaps the feedback will tend to cancel the error voltage left on the capacitor when the switch opens. It appears to be a more complex problem to compute the rms variation of the capacitor voltage in this case, since the transfer function and dynamics of the amplifier and the switch opening speed may have to be considered. This analysis was deemed beyond the scope of this work, and since integrated circuit capacitors consume a relatively large amount of chip space, it was decided to try the small capacitor in the first two designs (test chips one and two). In later designs, larger capacitors were used for a variety of reasons, and have the added benefit of ensuring that the switching noise is not a problem. The 30 pF capacitor used for the telemeter

presented in this section was large primarily to hold the bias voltage for a long time. But strict kT/C noise (if it holds for this feedback case) would leave a random offset on the bias capacitor after an input reset with standard deviation of less than 12 μV. This is small enough not to interfere with amplifier operation.

The schematic of the marker channel at stage zero of the shift register is given in Figure 7.21. The measure control line simply connects an n-channel source-follower in this circuit. By properly biasing the input, the source voltage can be set so that it will always be slightly lower than any of the amplifier channel outputs. This creates a readout pulse period that is longer than all of the rest and is therefore easily identified. The decoder demultiplexer can be synchronized to this marker period to sort out the eight signal periods. It is anticipated that the marker period will be adjusted via the voltage on "input 0" to be approximately twice the average signal period.

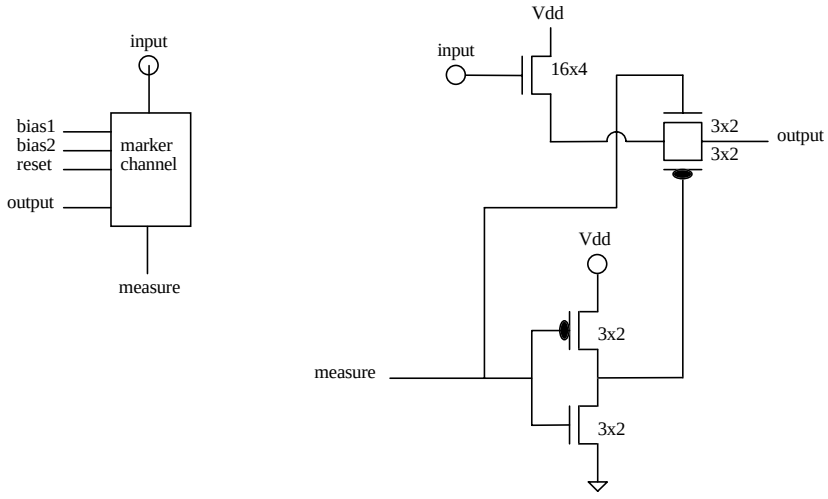

Figure 7.21: Marker channel circuit.

The redesigned Schmitt trigger for this telemeter is shown in Figure 7.22. The main difference in this circuit is that the hysteresis is set by varying the current through a single "diode-connected" transistor (Q1) rather than the series of transistors in the previous design. A differential amplifier forms the input of this Schmitt trigger, and its output current either increases or decreases the current through Q1. A constant current source provides the DC bias for this diode-connected n-channel transistor, so this Schmitt trigger circuit can be operated over a wider range of supply voltage. The ideal mirrored currents are labeled on Figure 7.22 to give some indication of how the voltages in the circuit will change with the state of the Schmitt trigger. As used in the telemeter circuit, the Schmitt trigger will operate in the high output state, as the input voltage is

ramped up to the high threshold. This threshold voltage is set by the gate-source voltage of Q1 flowing approximately twice the bias current (I). The current flowing through Q1 would be mirrored by Q2 except that Q2 is supplied by a constant current I. Thus the voltage at the drain of Q2 will be low, and the following inverter makes the output voltage high. When the input voltage exceeds the high threshold, the differential amplifier steers current away from Q1. The gate-source voltage of Q1 should fall to approximately the drain-source saturation voltage of Q3. This sets the low Schmitt trigger threshold voltage, which is not critical because the input voltage quickly falls to zero anyway when the integration capacitor of the telemeter is reset. When the current through Q1 approaches zero, so does the current through Q2. The constant current driving Q2 then causes its drain voltage to climb to almost V_{dd}, and the inverter output goes low. Since the differential amplifier works as a current-steering circuit, and the voltage changes during operation are much smaller than in the previous version, this circuit should operate much faster. Simulations with the original software predicted propagation delays of about 1 μs with bias current of 250 nA.

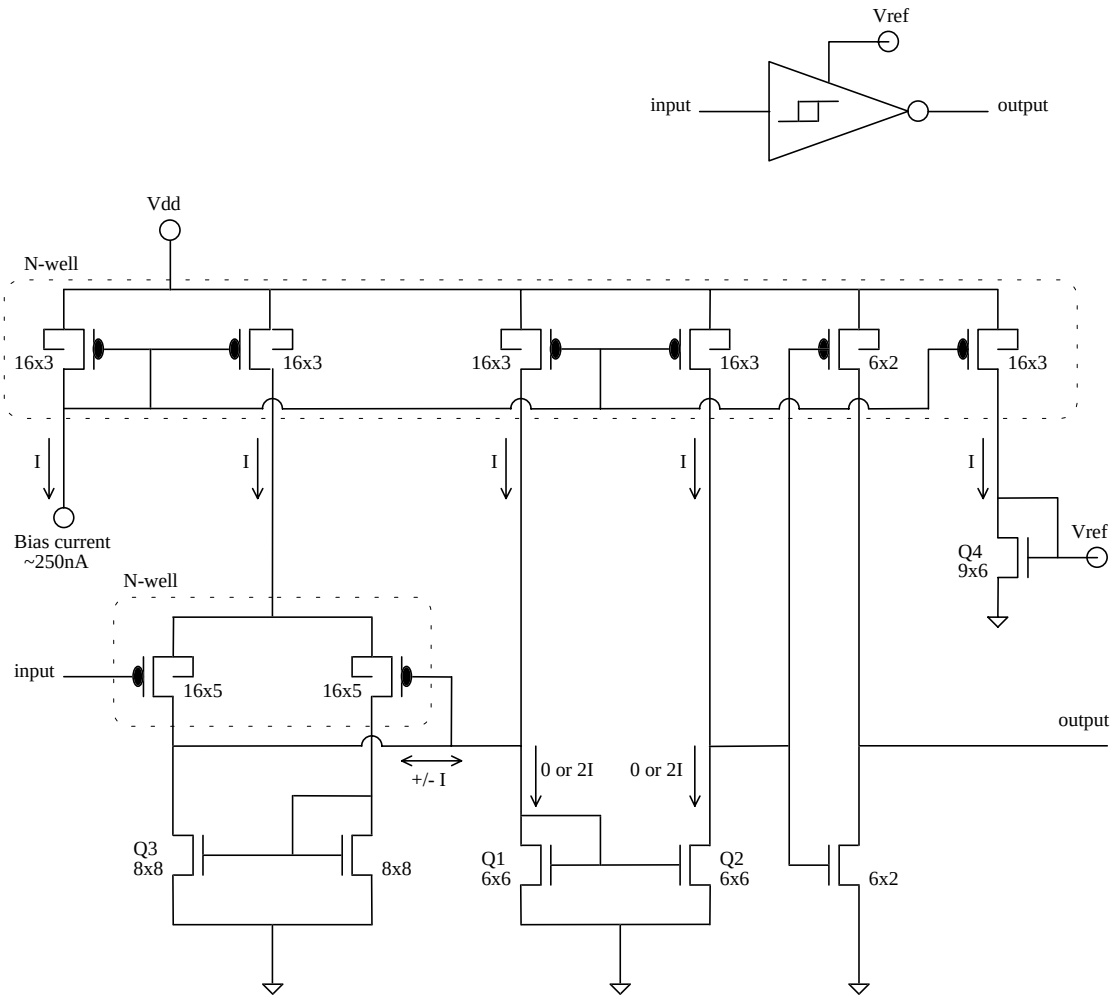

Figure 7.22: Improved Schmitt trigger circuit.

Transistor Q4 provides a reference voltage for the telemeter input amplifiers that should be slightly lower than the Schmitt trigger high threshold regardless of the bias current level. Early computer simulations predicted a reference potential of 0.81 V and a high threshold of 0.93 V when the Schmitt trigger was biased at 250 nA. The 120 mV difference will be the average ramp that the integrating capacitor voltage will go through during the readout periods. A 100 μV input signal amplified by a gain of 240 would change this ramp by 24 mV, modulating the integration period by 20%. If the maximum pulse period modulation is to be 50%, a ±250 μV input signal can be encoded. Integration current of 30 nA (I_{int} in Figure 7.19) should yield an average pulse period of about 5 μs, so that the sample rate of the eight channels will be approximately 50 kHz.

Aside from the replacement of second-level metal interconnects with polysilicon, the shift register stages were the same as for test chip two, shown in Figure 7.9 and Figure 7.10,

except that the data storage capacitor C_d was increased from 250 fF to 1 pF to give the dynamic memory a greater hold time. This was done so that the new telemeter circuits could be operated at lower sample rates for monitoring different biomedical signals (such as EEG, EMG and EKG signals that have lower bandwidth). The clock splitter circuit was also the same as in Figure 7.11.

Other changes to this telemeter are improved circuits for the power-on reset and LED drive. The LED drive transistor was made ten times as wide to 160x2 μm. This reduces its on resistance (with the 2.5 V power supply) to about 1 kΩ, increasing LED pulse current to approximately 1 mA. This increases light pulse intensity by a factor of almost ten. Figure 7.23 gives the schematic of the new power-on reset circuit. This circuit uses the same concept to generate a delayed start-up signal as before, where the reverse leakage current of a diode is intended to slowly charge a capacitor. However, this design uses a transistor gate for the capacitor, since this oxide is formed from single-crystal silicon and is thus expected to have the lowest leakage current per unit capacitance (in a reasonable area). Instead of buffering the capacitor voltage with an inverter, a low-power Schmitt trigger circuit is used. In the old circuit, if the capacitor voltage settled to some intermediate value between ground and V_{dd}, the first inverter could flow significant quiescent current (up to 10 μA with only a 2.5 V supply), dramatically increasing the power consumption of the telemeter. The Schmitt trigger consumes a small amount of power regardless of the capacitor voltage. The hysteresis of the Schmitt trigger keeps its output in either the high or low state so that the subsequent inverters do not flow quiescent current.

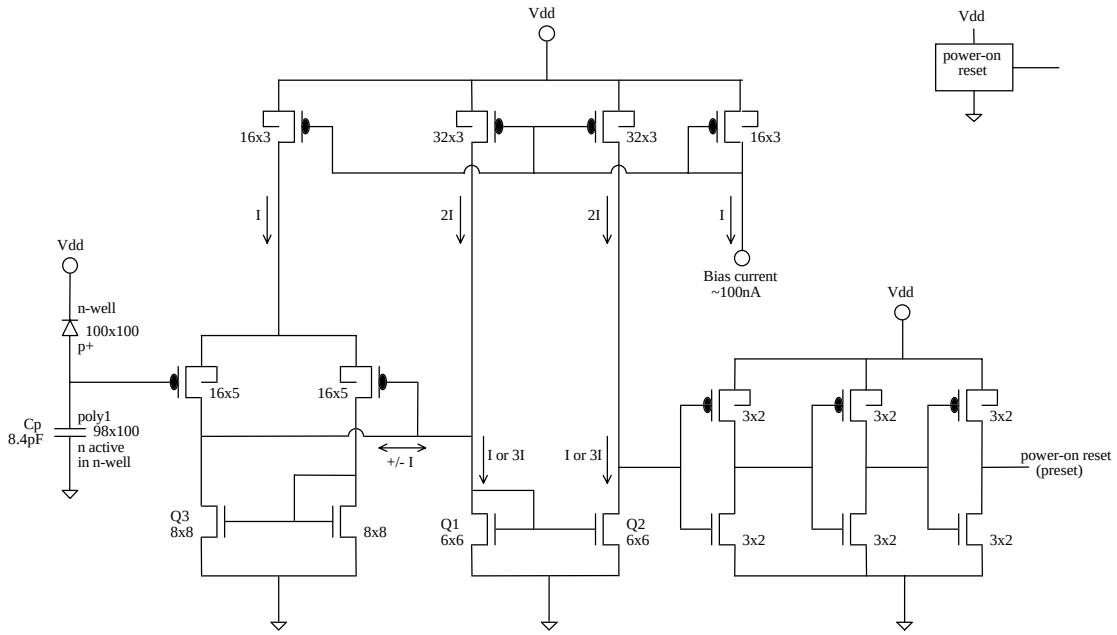

Figure 7.23: Improved power-on reset circuit.

7.3.3.2 Testing of second 8-channel telemeter circuit

The input amplifier of Figure 7.20 was tested independently prior to the complete telemeter circuit. Unfortunately, the early computer simulations had again led to design choices that ended up compromising circuit performance. Specifically, the simulations overestimated the leakage current through p-n junctions and the switch transistors in the off state. This led to the adoption of the more complicated switching circuit that was hoped to minimize leakage current from the amplifier bias storage capacitor. This in itself should not have posed a problem, but the simulator also underestimated the "on" resistance of the p-channel switches that had to be used in this design. When the reset control line is pulled low, it is supposed to connect the amplifier with unity-feedback and thereby set the bias capacitor voltage. But both p-channel switches do not in fact "close" for gate-source voltages much less than 1 V. So the input amplifier cannot adjust to DC input voltages in the range of 0.81 V, which is required for telemeter operation. The input amplifier performs as designed for slightly higher input voltages (the output follower circuit limits for inputs above 1.4 V unless the supply voltage is increased), but this will not work with the 8-channel telemeter circuit because the amplifier output voltage must always be less than the Schmitt trigger high threshold of about 0.93 V. Over the range for which the input amplifier did operate properly, the voltage gain was about 300, and the 3 dB bandwidth was 10 kHz.

No attempt was made to operate the 8-channel telemeter because there was no indication that it would work, given the known limitations of the input stage design. Versions of this telemeter circuit with different input stage designs were fabricated concurrently, so the test effort was turned to these.

7.3.4 Test Chip Four

An 8-channel neural waveform telemeter circuit that uses a switched-capacitor technique to cancel electrode potential drift and amplifier offset was fabricated on test chip four. The block schematic of this circuit is presented in Figure 7.24. Each input amplifier circuit of this telemeter uses a small capacitor to transfer a small amount of charge from the amplifier output onto a large bias capacitor at the inverting input after every sample. This creates a feedback path. At DC, the feedback is unity, while at higher frequencies the feedback is much smaller. Signal amplification is therefore greater at higher frequencies than at DC, as desired.

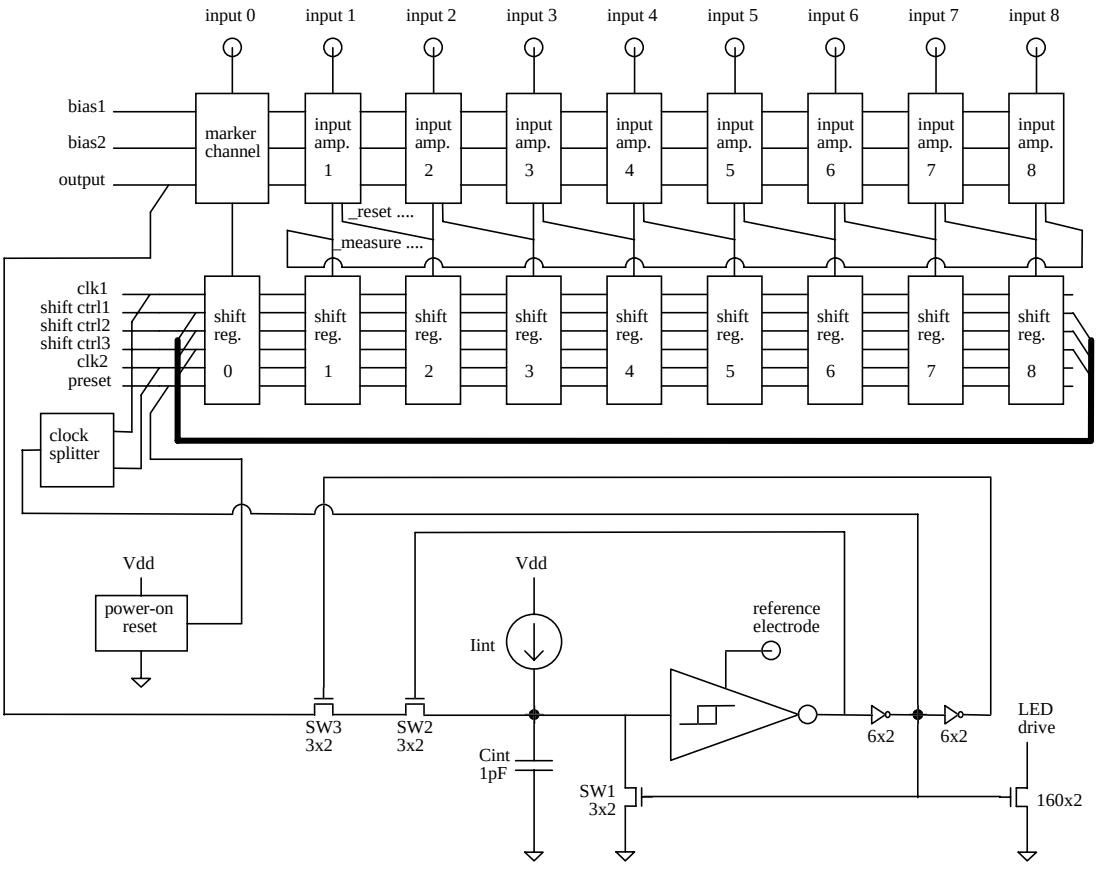

Figure 7.24: Improved 8-channel telemeter circuit design with switched capacitor input stabilization.

7.3.4.1 Theory of telemeter operation

All components of this telemeter are the same as the circuit of test chip three except the input amplifier stage. Consequently, the general principles of the encoder operation are the same. The input amplifier circuit of this version of the second-generation telemeter is given in Figure 7.25.

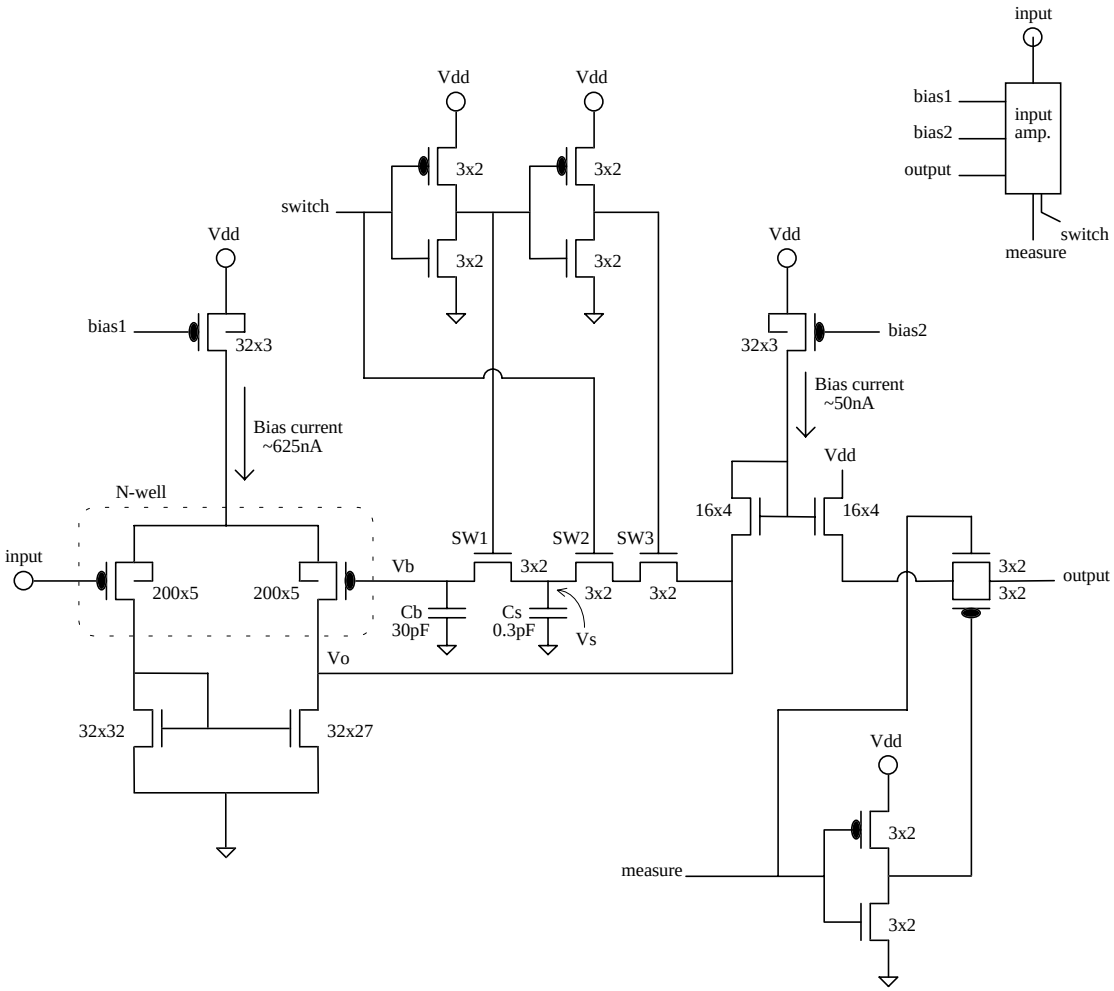

Figure 7.25: Input amplifier stage with switched-capacitor offset cancellation.

The “switch” control line is connected to the “measure” control line of the following stage. Most of the time, the measure lines are in the high state so n-channel switches SW2 and SW3 are closed and SW1 is open. The 0.3 pF switch capacitor C_s is therefore connected to the amplifier output during most of the sampling cycle, and when the stage’s measure line is pulled low to read it out. When the pulse-period readout for the channel is complete, and the next measure control line in the shift register is pulled low to read out the following channel, the switches change state. First, switch SW2 opens to

disconnect C_s from the amplifier output, then SW1 closes to connect C_s to the 30 pF bias capacitor C_b. In order to prevent a continuous conduction pathway by timing overlap when the switches change back to their normal state, switch SW3 is also opened. By opening SW2 before SW3, charge injection onto C_s is minimized. When the shift register advances again, SW2 closes, SW1 opens, and SW3 closes to reconnect C_s to the amplifier output.

Feedback provided by the switched capacitor can be approximated by a large resistor as long as the switching rate is fast compared to the voltage changes at the output of the amplifier. Since the switching rate is the same as the sample rate, which must be greater than the Nyquist rate, this condition is satisfied. The circuit of Figure 7.26 is helpful in deriving the feedback equivalent.

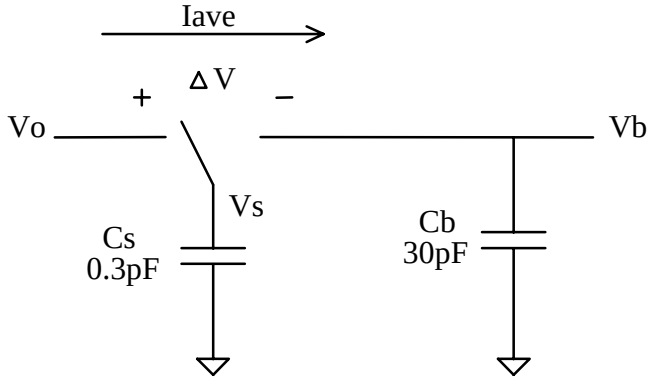

Figure 7.26: Switched-capacitor feedback.

In order to approximate the feedback through switched capacitor C_s by a resistor, the average current flow through the pathway must be related to the voltage difference across it, $\Delta V = V_o - V_b$. Before each switching operation, C_s is connected to the amplifier output, so $V_s = V_o$. When the switch is flipped to connect C_s to C_b, the change in the charge on C_s is given by:

$$\Delta Q_s = C_s V_o - C_s \left(\frac{C_s V_o + C_b V_{b,old}}{C_s + C_b} \right),$$

where $V_{b,old}$ is the bias voltage prior to switch. Of course, the change in the charge on C_s is the amount of charge transferred to C_b. In the case that $C_s << C_b$, as it is here, the charge transfer can be approximated by:

$$\begin{aligned}\Delta Q_s &= C_s\left(1+\frac{C_s}{C_s+C_b}\right)V_o - C_s\left(\frac{C_b}{C_s+C_b}\right)V_{b,old} \\ &\approx C_s V_o - C_s V_{b,old} \\ &\approx C_s \Delta V\end{aligned} \quad .$$

Since this amount of charge is transferred after every time the channel is sampled, the average current flow is equal to:

$$\begin{aligned}I_{ave} &\approx \frac{\Delta Q_s}{T_{s,ave}} = \frac{C_s \Delta V}{T_{s,ave}} \\ &\approx \frac{\Delta V}{\left(T_{s,ave}/C_s\right)}\end{aligned} \quad ,$$

where $T_{s,ave}$ is the average sample period. From this expression, the equivalent feedback resistance is obtained:

$$R_{eq} \approx T_{s,ave}/C_s \; .$$

For recording neural waveforms, the average sample period will be about 50 μs, so the equivalent feedback resistance will be 167 MΩ. Substituting the equivalent feedback resistor for the switched capacitor network in the input amplifier circuit facilitates the calculation of the amplifier transfer function. Figure 7.27 shows this equivalent circuit.

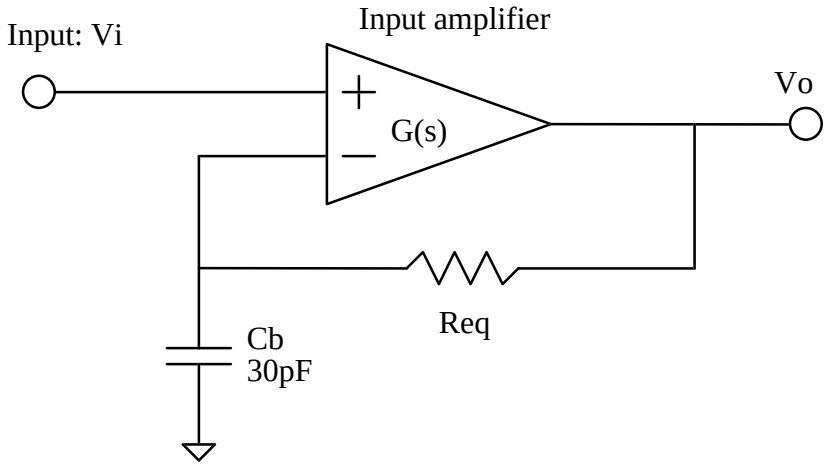

Figure 7.27: Equivalent circuit of switched-capacitor input amplifier stage.

With the bias currents of Figure 7.25, the amplifier transfer function should be approximately:

$$G(s) \approx \frac{240}{s/48000+1},$$

where the dominant pole frequency is set by the output resistance of about 32 MΩ and the switching and stray capacitance totaling about 0.65 pF. The feedback function is:

$$H(s) = \frac{1}{sR_{eq}C_b + 1} \approx \frac{1}{s/200 + 1}.$$

Loop gain of this system is

$$L(s) = G(s)H(s) \approx \frac{240}{(s/200+1)(s/48000+1)},$$

which has unity magnitude just below the frequency of the second pole, so the system is stable. The closed-loop transfer function of this system is sketched in the Bode magnitude plot of Figure 7.28.

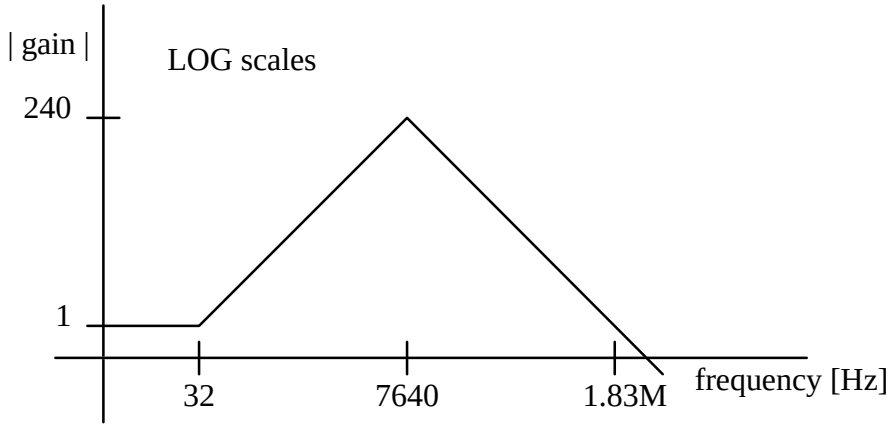

Figure 7.28: Switched-capacitor input amplifier transfer function.

At low frequency the gain is about 1, and above 32 Hz the gain rises at 20 dB per decade of frequency until approximately 7640 Hz, where the gain peaks at about 240 and begins to decrease at 20 dB per decade. This transfer function is acceptable for amplifying neural waveforms, since the gain is adequate over the most important frequency range, and an equalizing filter can be used to correct the spectrum of the received and decoded signals.

7.3.4.2 Testing of 8-channel telemeter circuit with switched-capacitor input stage

The input stage was first tested by itself. An input amplifier stage separate from the 8-channel telemeter was included on the test chip for this purpose. In addition to the bias, input, and output nodes, the capacitor switch control line was pinned out, and a p-

channel transistor source follower was used to monitor the bias capacitor voltage. A 20 kHz clock was used for the switching signal, and the bias currents were set to approximately the values specified in Figure 7.25. It was discovered that a supply voltage greater than 2.5 V was necessary for proper operation. Charge injection from the switches and higher transistor thresholds probably accounted for this by limiting the range over which the switched-capacitor feedback was effective. At 2.5 V, the input voltage range for *any* small-signal amplification was very limited, from 0.74 V to 0.75 V. Increasing the supply voltage to just 2.8 V yielded amplification of small signals inputs biased between 0.25 V and 0.70 V. Gain at 1 kHz was approximately 160, considerably higher than expected. The DC tracking range extended from about 0.15 V to 0.70 V, with long settling times near the upper voltage limit that probably reflects increased on-resistance of the feedback switches. Because the bias capacitor of this circuit could be monitored by a p-channel source follower, another valuable experiment was performed. After allowing the capacitor voltage to settle to about $\frac{1}{2}V_{dd}$ (1.35 V), while the switching line was clocked at 20 kHz, the switch signal was held low so that the bias capacitor would hold its value. The droop rate measured over a period of one minute was only 30 μV/s. Thus leakage current off of the 30 pF bias capacitor is only 0.9 fA! Early computer simulations had predicted leakage currents more than 1000 times greater. A double-layer structure that utilizes both the poly1 gate oxide and poly1-poly2 capacitor oxide was used to fabricate this 30 pF capacitor in as small an area as possible. Clearly the leakage through the oxides is quite small, since the switch transistor's p-n junction reverse current probably accounts for most of the measured leakage.

When the complete 8-channel telemeter circuit was tested with all bias values set to the design specifications, except for the power supply voltage which was set to 2.8 V, the output LED driver did pulse but the shift register did not appear to cycle. Even after a shift register preset was performed, the pulse periods were uniform. Changing the input bias voltage had no affect on the pulse periods either. Increasing the shift register current or the readout integration current caused the pulse rate to increase. Holding the shift register preset line high forced the system to sample the marker channel input continuously, and then voltage signals on the this input modulated the pulse periods as would be expected.

The reason for the failure of the shift register was revealed by circuit simulations made practical by the improved software. Two factors were responsible: first, the shift register

storage capacitance had been increased from 250 fF to 1 pF as mentioned earlier. Second, the improved Schmitt trigger has a very small propagation delay in response to a falling step input voltage. As indicated by the LED drive response, this propagation delay is about 100 ns (evidently the changes to the circuit had the desired effect!). As a result, the shift register memory capacitors do not have sufficient time to change to the high state when required. To demonstrate the proper operation of the shift register, a computer simulation of the shift register with 250 fF storage capacitors was performed. To duplicate the operating conditions of the real telemeter circuit as closely as possible, the correct encoder circuit was used in the simulation. Schmitt trigger bias current was set at 250 nA. Rather than including all the input stages, a single follower circuit from an input amplifier was biased at the Schmitt trigger reference potential to provide the input to the encoder. Thus all the pulse periods in the simulation are identical, including the marker. Figure 7.29 plots the voltage on the integrating capacitor, the clk1 control line, the first four storage capacitors in the shift register, and the first three measure control lines. The simulation starts with the power-up of the telemeter and a 10 μs preset signal. Note how the high logic state voltage is advanced through the shift register storage capacitors as required. Accordingly, the measure control lines fall low with every ninth output pulse, sequencing through the one marker channel and eight signal channels.

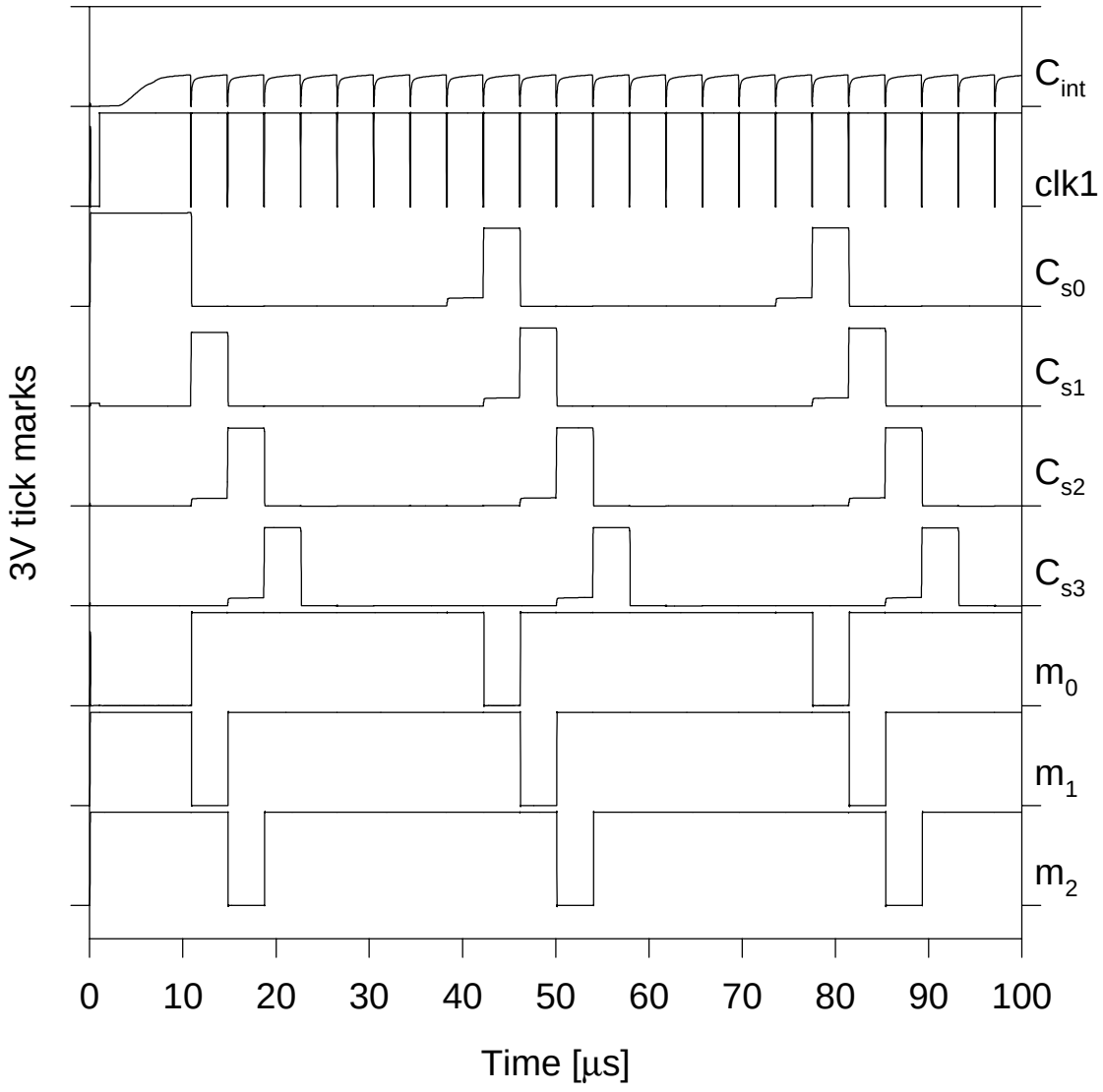

Figure 7.29: Simulation of the proper operation of shift register with 250 fF memory storage capacitor. This shift register design was proven to work in test chip two.

Unfortunately, with the 1 pF storage capacitors, the shift register fails to advance the high logic state, and the measure control lines quickly become inactive (all high) after the preset. Figure 7.30 plots the simulated voltages on the first five storage capacitors in the shift register and the first four measure control signals. The shift register control logic does not operate correctly, as evidenced by the stair-step voltages on the first few storage capacitors that span three or more clock pulses. The high data bit never even makes it to the fourth stage of the shift register.

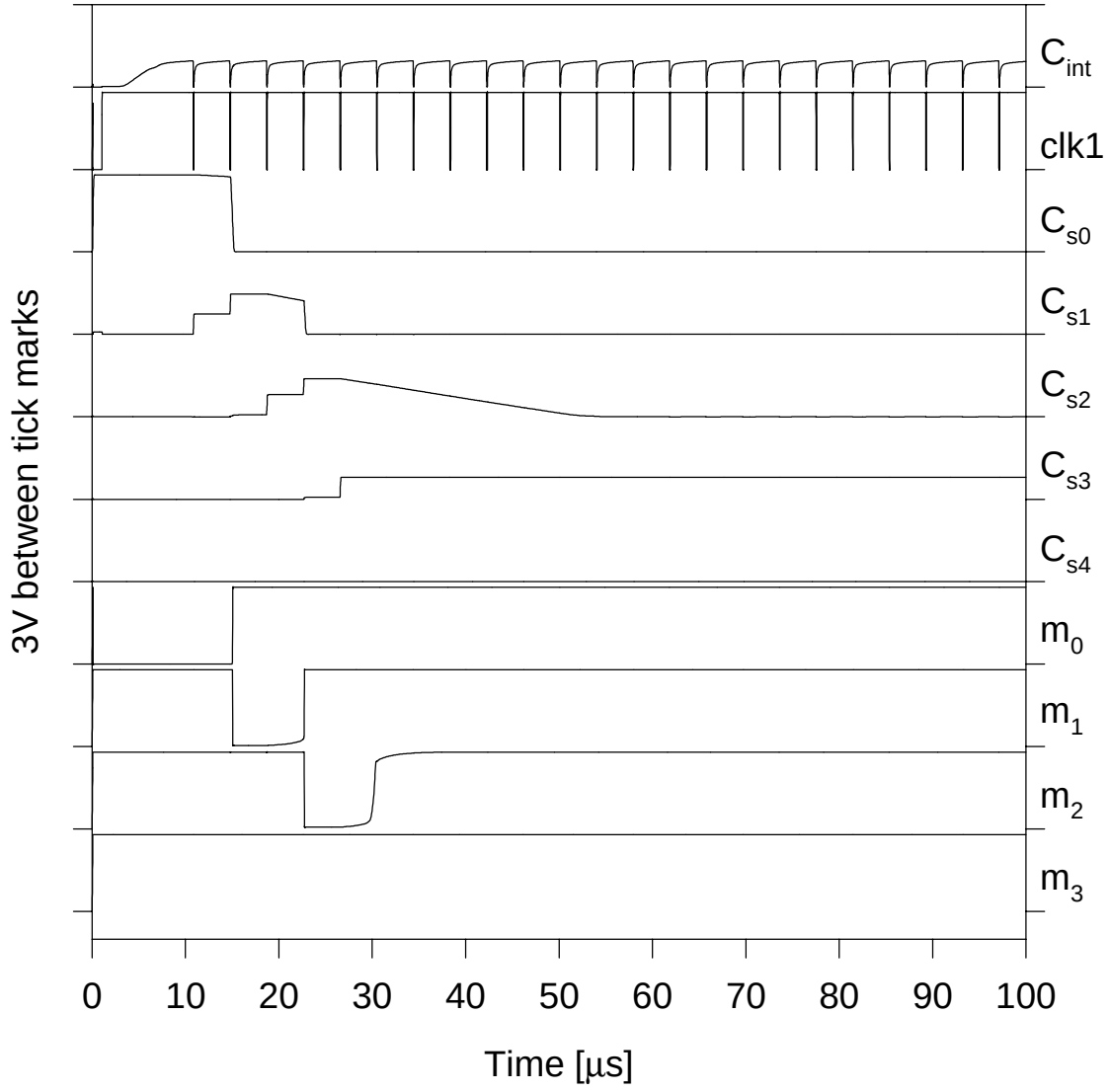

Figure 7.30: Simulated failure of shift register operation with 1 pF memory storage capacitor.

It appears from the simulations that the larger storage capacitors do not have time to charge to the high logic state during the short (80 ns) clock pulses. It was hypothesized that the clock pulses could be lengthened by slowing the Schmitt trigger circuit. Decreasing the Schmitt trigger bias current from 250 nA to 50 nA in the simulation increased the clock pulse width to 180 ns, returning proper function to the circuit as shown in Figure 7.31. Integration current could be increased to shorten the pulse periods if necessary. Unfortunately, attempts to restore proper function by reducing Schmitt trigger current were not successful in the laboratory. Evidently the clock pulse

width could not be increased sufficiently to advance the shift register state (while maintaining proper operation of other circuit components). Another solution that could be implemented in future versions of the telemeter is to increase the width/length ratio of the three series-connected p-channel transistors in each shift register stage (Figure 7.9 and Figure 7.10) that are used to pull the storage capacitor high. This would decrease the on-resistance of these switches, thereby decreasing the charging time. Or, considering the small leakage current that was measured in the tests of this telemeter's input amplifier circuit, the 250 fF storage capacitor may be adequate to hold the shift register data for long periods of time. With 0.9 fA leakage, it would take almost 140 seconds for the voltage on a 250 fF capacitor to drop by 0.5 V! This should enable sampling rates much slower than would be useful for most biomedical signals.

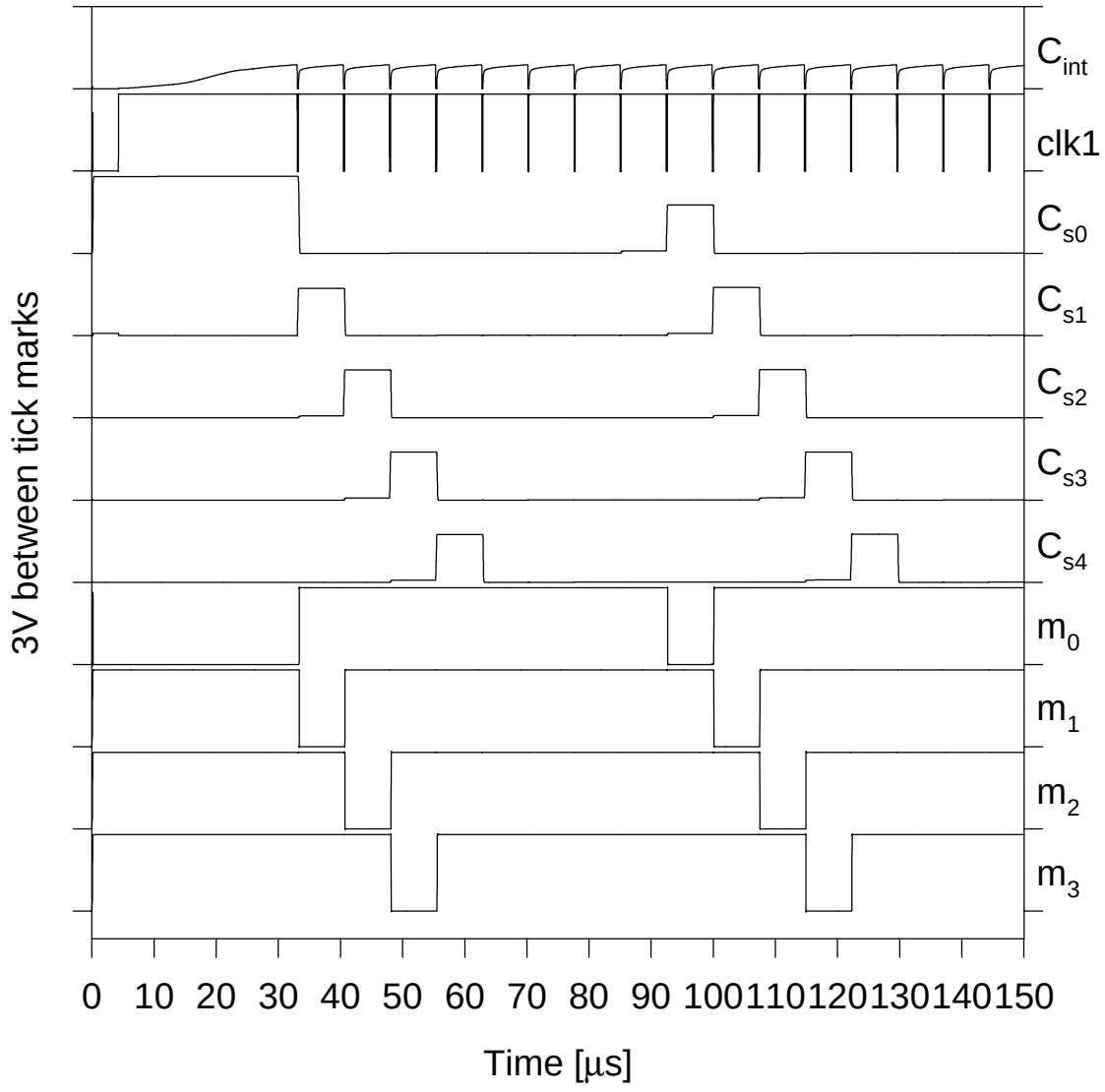

Figure 7.31: Simulated operation of shift register with 1 pF memory storage capacitor restored to proper function by decreasing Schmitt trigger speed.

7.3.5 Test Chip Five

This version of the second-generation 8-channel telemeter was fabricated concurrently to test a third input offset cancellation technique. Figure 7.32 illustrates the connection of the basic elements of this circuit. For this telemeter, an additional amplifier operating at extremely low current was used in each input stage to provide low-frequency feedback around the main input amplifier. This low-frequency feedback was intended to cancel amplifier offsets and electrode drift by actively biasing each amplifier so that its

DC output voltage is driven to a preferred reference voltage. This reference voltage can be set relative to the high threshold of the readout Schmitt trigger to adjust the signal range and sensitivity (modulation depth) of the pulse-position encoding process. A small capacitor was used to provide a high-frequency feedback path to set a more well-defined gain (approximately 100) at important signal frequencies.

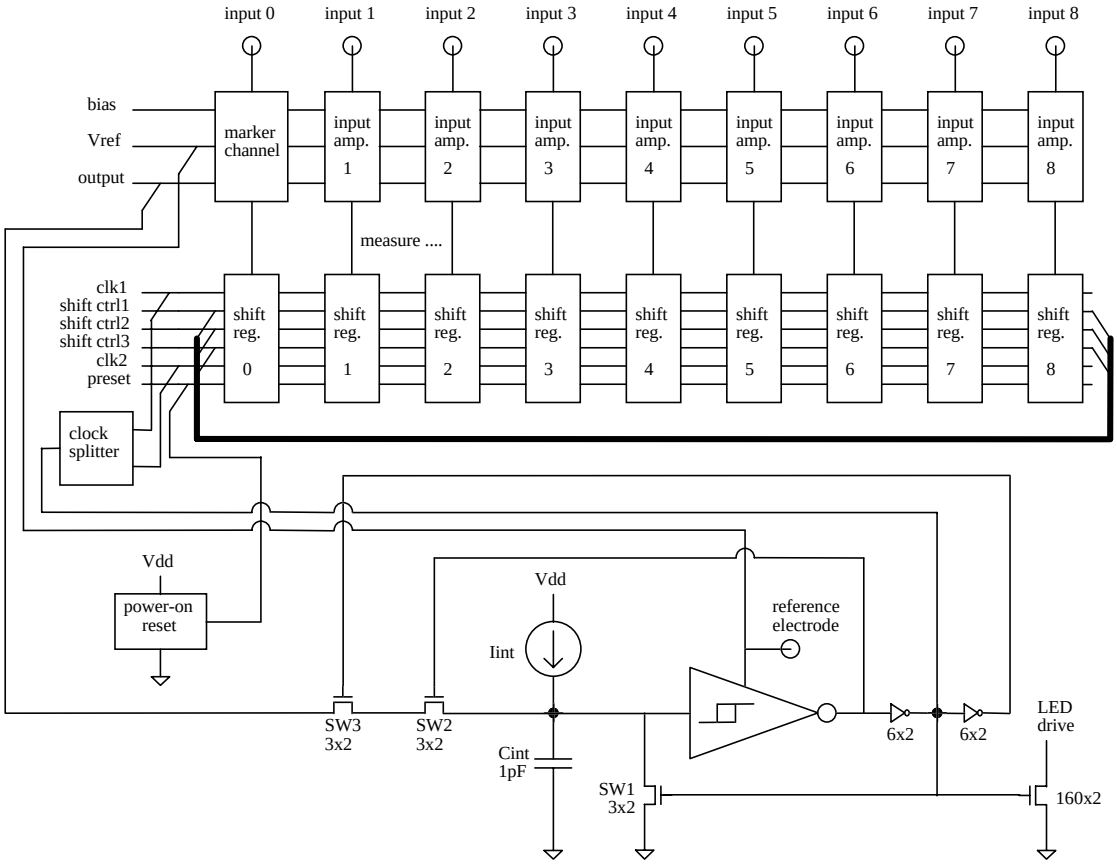

Figure 7.32: 8-Channel telemeter circuit with feedback amplifier offset correction.

7.3.5.1 Theory of telemeter operation

Except for the input amplifier circuit, the components of this telemeter are the same as for test chips three and four, so the general operation of the encoder is the same. The schematic of the input amplifier circuit is presented in Figure 7.33. The differential amplifier labeled “Amp1” is the usual input amplifier, and “Amp2” provides the low-frequency feedback.

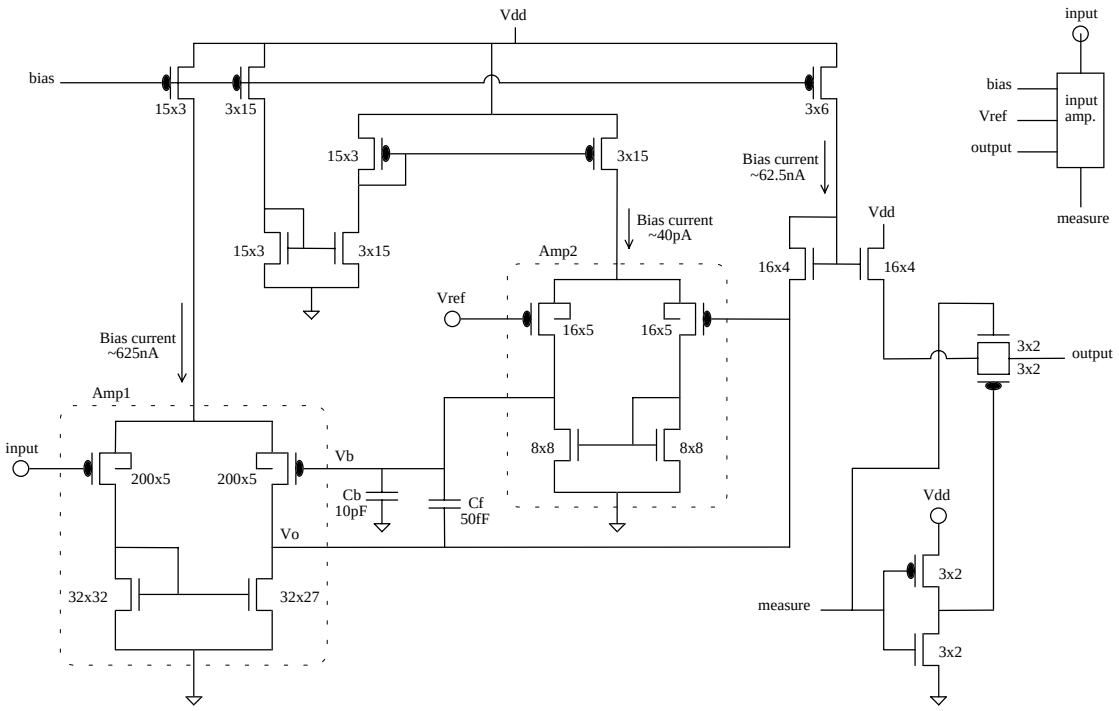

Figure 7.33: Input amplifier stage with low-frequency feedback amplifier offset cancellation.

Neglecting the 50 fF feedback capacitor at first, the input stage can be represented by the block diagram of Figure 7.34. Transfer function G(s) describes Amp1 since it is responsible for the forward signal path, and H(s) describes Amp2 since it is in the feedback path.

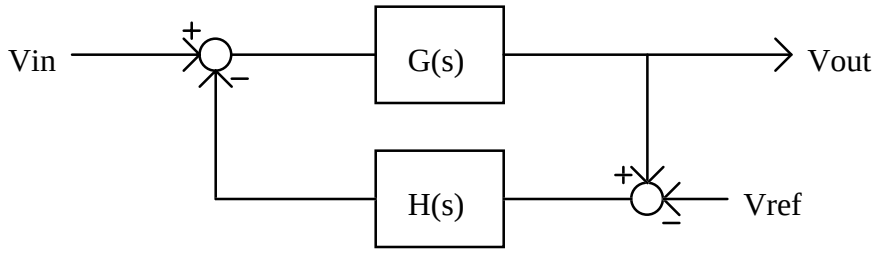

Figure 7.34: Block diagram of input amplifier stage with low-frequency feedback amplifier, neglecting 50 fF feedback capacitor.

The transfer function of Amp1 can be approximated by:

$$G(s) \approx \frac{g_{m1} r_{o1}}{s r_{o1} C_{o1} + 1},$$

where g_{m1} is the transconductance of the amplifier, and r_{o1} and C_{o1} are its output resistance and capacitance, respectively. These values were estimated to be

$$g_{m1} \approx 7.5\left[\tfrac{\mu A}{V}\right]$$
$$r_{o1} \approx 40[M\Omega].$$
$$C_{o1} \approx 350[fF]$$

Likewise, the transfer function of Amp2 is approximately

$$H(s) \approx \frac{g_{m2} r_{o2}}{s r_{o2} C_b + 1},$$

where

$$g_{m2} \approx 0.48\left[\tfrac{nA}{V}\right]$$
$$r_{o1} \approx 625[G\Omega].$$
$$C_{o1} \approx 10[pF]$$

Substitution yields

$$G(s) \approx \frac{300}{s/71400 + 1},$$

and

$$H(s) \approx \frac{300}{s/0.16 + 1}.$$

Loop gain of the system,

$$L(s) = G(s)H(s) \approx \frac{90000}{(s/71400 + 1)(s/0.16 + 1)},$$

is plotted in Figure 7.35.

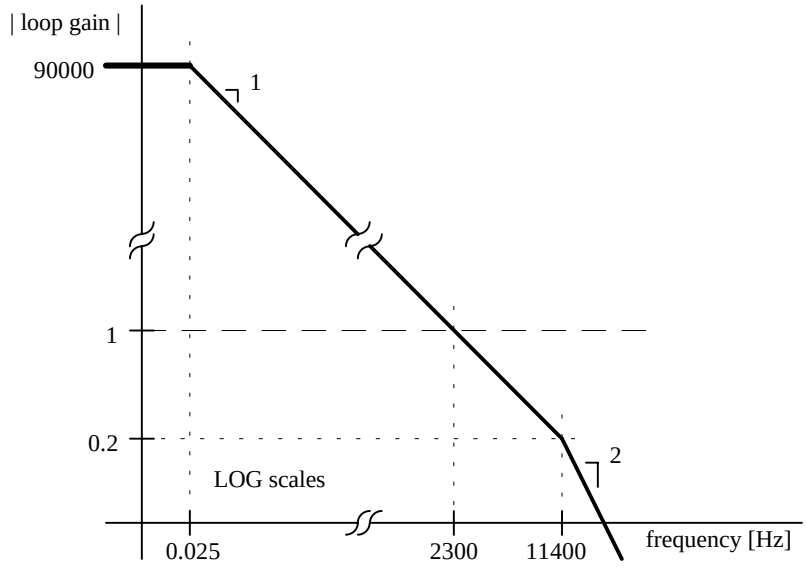

Figure 7.35: Bode magnitude sketch of loop gain of input stage with feedback amp.

Because the second pole in the loop transmission (11.4 kHz) occurs beyond the unity gain frequency (2300 Hz), the closed-loop system should be stable with almost 80 degrees of phase margin. The closed-loop transfer function between V_{ref} and V_{out} describes how well the output voltage tracks the reference voltage. There is unity feedback between these signals, so the gain magnitude will be approximately one below the unity gain frequency of the loop transmission. At higher frequencies the frequency response will follow the loop gain function. Modifying Figure 7.35 yields the Bode plot of this transfer function as shown in Figure 7.36.

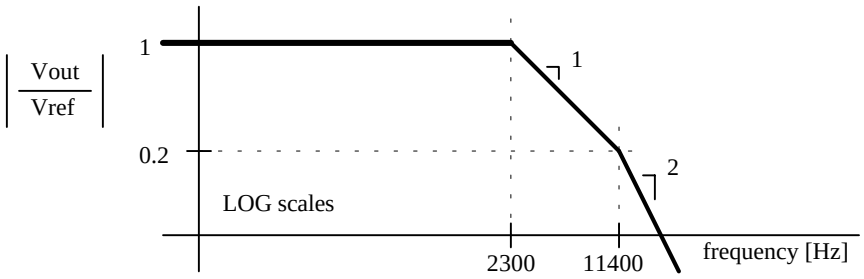

Figure 7.36: Bode magnitude sketch of reference voltage tracking function.

Of primary interest is the transfer function relating the input voltage and output voltage, since this will amplify the neuroelectric signals. This transfer function can be approximated from the feedback and forward gain functions according to Black's formula as follows:

$$\frac{V_{out}}{V_{in}} = \frac{G(s)}{1+G(s)H(s)}$$

$$\approx \begin{cases} \dfrac{1}{H(s)}, & G(s)H(s) >> 1 \\ G(s), & G(s)H(s) << 1 \end{cases}$$

yielding the Bode plot of Figure 7.37.

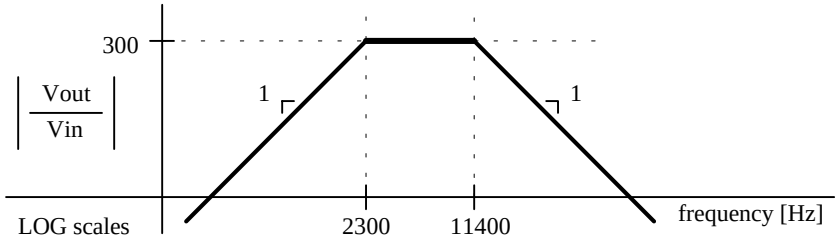

Figure 7.37: Bode magnitude sketch of neuroelectric signal amplification.

The passband of the amplifier covers the most important frequency range for neuroelectric potential recording, but it was desired to have a somewhat wider

passband, and some of the gain could be sacrificed for this purpose. The 50 fF capacitor in Figure 7.33 was added to flatten the gain of the amplifier over a wider frequency range. This capacitor provides negative feedback around the primary amplifier (Amp1), but also adds some positive feedback around the reference tracking amplifier (Amp2). The positive feedback could have been easily avoided by buffering the voltage signal that is applied to the 50 fF capacitor, as shown in the revised schematic of Figure 7.38. However, this is not necessary because the total gain around the positive feedback loop is less than unity.

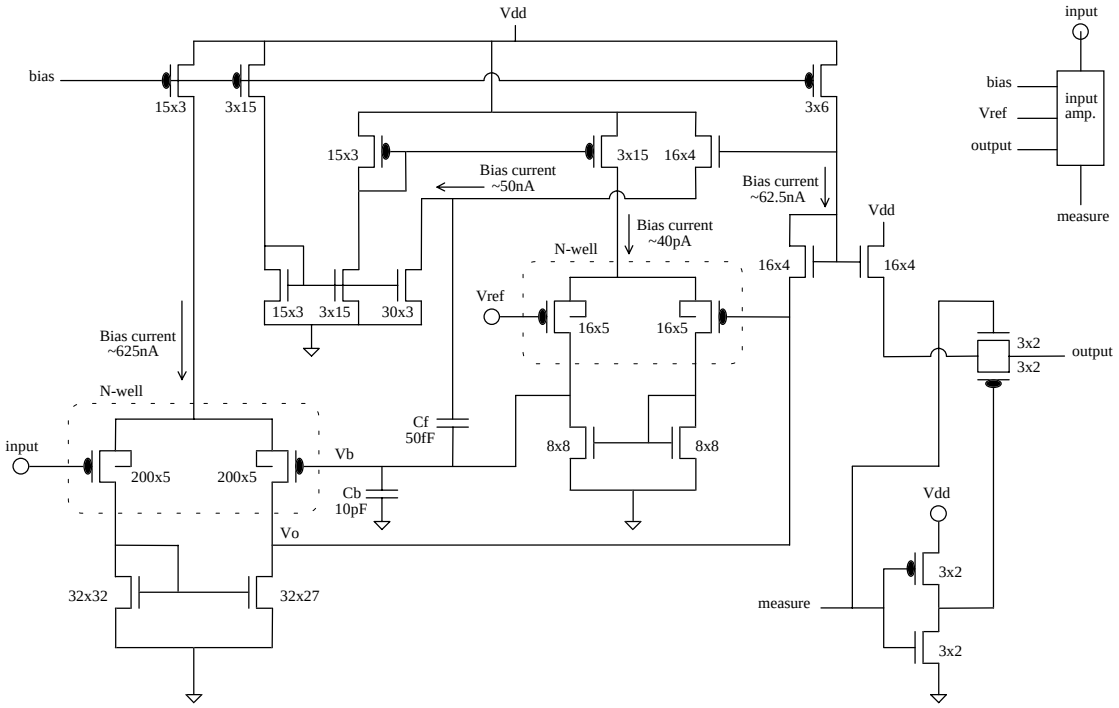

Figure 7.38: Elimination of positive feedback pathway in input amplifier stage by buffering signal to 50 fF feedback capacitor.

A total feedback capacitance of 100 fF to the 10 pF bias capacitor should yield a closed-loop gain of about 100 in the passband. Capacitance between the drain and gate of the 200x5 μm p-channel transistor that forms the inverting input of Amp1 was originally estimated to be 50 fF, so an additional 50 fF capacitor was fabricated to achieve the design value. More recent models suggest that drain-gate capacitance of this transistor is almost 63 fF, so the closed-loop gain of the system should be closer to 88. The Bode plot of the gain flattened by the feedback capacitor is shown in Figure 7.39.

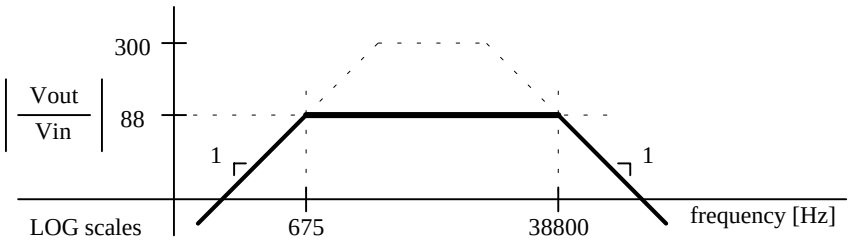

Figure 7.39: Bode magnitude sketch of neuroelectric signal amplification, with addition of feedback capacitor.

Recent computer simulations are in reasonable agreement with these calculations, as shown by the computer generated Bode plots presented in Figure 7.40.

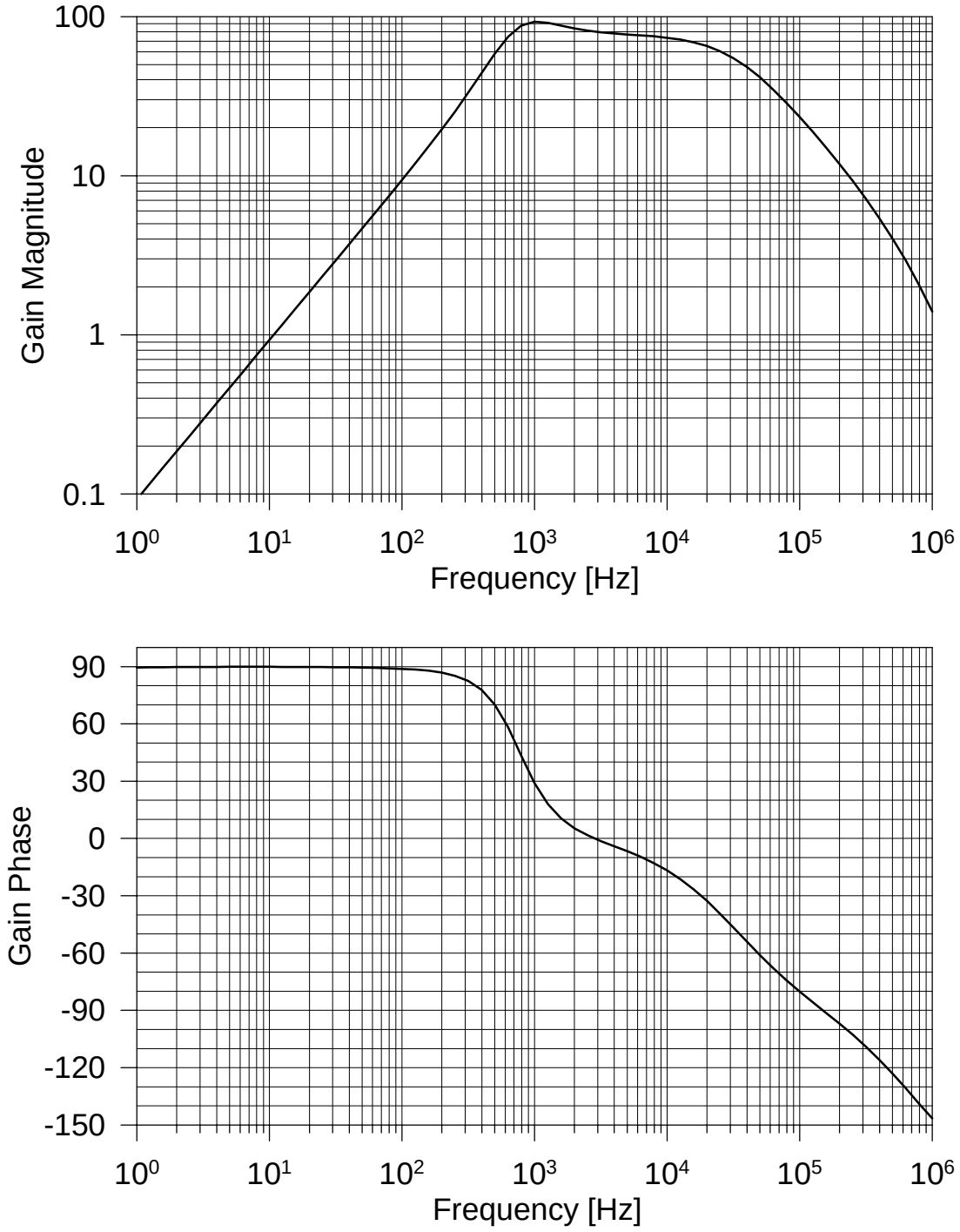

Figure 7.40: Computer simulation Bode plots of input stage with low-frequency feedback amplifier offset cancellation.

To verify that the complete input stage would be stable, a transient simulation was performed. This forced the simulator to use complete transistor models, not just small-

signal AC approximations. A power-up simulation showed the bias capacitor voltage rise to the designated reference voltage (0.85 V) over about 200 ms, then the small-signal amplification began as the system settled in to its steady-state condition. A 500 ms long simulation starting at the operating point of the circuit is shown in Figure 7.41. Note that the perturbation caused by the square wave does not cause the system to go unstable. Also, the expanded portion of the graph shows the step response (to a 100uV step on V_{in}) of the amplifier. The fast rise and (relatively) slow decay times are consistent with the two poles in the closed-loop transfer function.

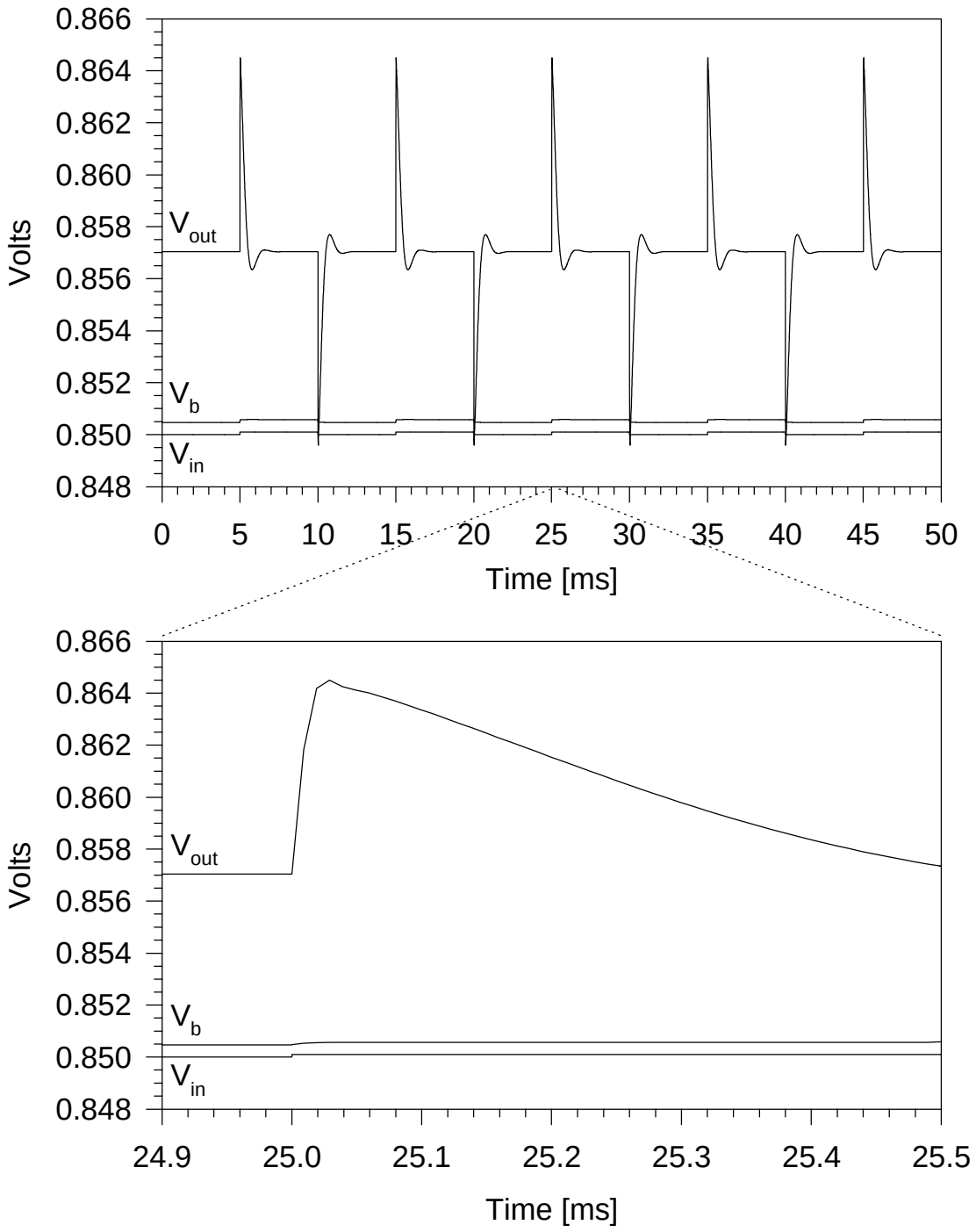

Figure 7.41: Computer simulated square wave (step) response of input stage with low-frequency feedback amplifier offset cancellation.

7.3.5.2 Testing of 8-channel telemeter circuit with feedback amplifier input stage

The input stage was tested independently of the 8-channel telemeter, but exhibited very strange behavior. The amplifier output voltage drifted and occasionally made step-like transitions to intermediate voltages. The output voltage did not oscillate with a fixed frequency, nor did it limit at the supply voltages as might be expected from an unstable system. Similarly confusing signals were observed at the bias capacitor, which was designed with a source-follower circuit connected for testing purposes. Perhaps some unmodeled parasitic capacitance or resistance caused the system to have conditional stability that depended on the gain of the two amplifiers. As the voltages in the two amplifiers change, their gains and pole frequencies could also change as the transistors go between saturated and linear operation. A decrease in gain could give the system temporary stability until the amplifiers settled and gain increased, causing renewed instability to drive the system out of its normal operating range, where stability could again be restored temporarily. Or perhaps the circuits were damaged by ESD or stress in the metal2 shield. Stress in the continuous metal2 layer could possibly cause mechanical failure of contacts or interconnects. While the solid metal2 shield did not violate the design rules provided by MOSIS, it was later discovered to violate the design rules specified by the fabricator (Orbit Semiconductor). Design rules for the process from Orbit Semiconductor recommended that stress relief slots be included in any wide metal interconnects. Since microscopic inspection of the integrated circuits did not reveal any obvious defects, more investigation is needed to determine if the metal2 shield is an acceptable way to protect the circuit from light. Also, it should be possible to model more of the circuit parasitics by extracting the circuit model directly from the integrated circuit layout file. This would include most of the small interlayer capacitances that were not included in the basic circuit analysis.

7.4 Conclusions from the IC test chips, and attempts to resolve problems

The known successes and failures of the tested integrated circuit designs provide directions for new versions of the telemeter. The input amplifier design has been demonstrated to be appropriate for the detection of low-amplitude neuroelectric potentials. Subsequent to the fabrication of test chips three, four, and five, but before these devices were available for testing, a complete telemeter IC was constructed from

the same basic circuit elements for related research in insulating biomaterials[15]. It was recently received from the foundry and tested (January 1999), and works almost perfectly according to design. The circuit measures leakage currents ranging from below one femtoAmp up to a few picoAmps through 13 different integrated test structures continuously[16]. It accomplishes this with less than 4 μA total supply current. The slow sampling rate used for this telemeter (~6 Hz) helps to achieve this, but careful design was required to keep the static current consumption low. This design also includes its own supply-independent biasing circuit, so that no external reference must be provided.

Input stages consist of autonomous current integration amplifiers with automatic reset circuitry, rather than neural signal amplifiers, but the channel multiplexing and readout techniques are the same as in the neural waveform encoder designs. The shift register circuit is identical. The main difference that allowed this circuit to work when the others failed is that the readout Schmitt trigger is operated at much lower current levels (~10 nA) because this circuit did not need to cycle as fast. Also, the circuit is operated at a higher supply voltage, so "diode-connected" transistors could be used in the positive feedback loop to increase hysteresis in the Schmitt trigger. These differences result in longer propagation delays through the readout Schmitt trigger, and a correspondingly longer clock pulse (~1.5 μs) which is able to operate the shift register. The pulse-period encoded output of this circuit is shown in Figure 7.42, where the marker channel and 13 signal periods can be seen clearly.

[15] Circuit design and initial layout by Bruce Larson, final layout by David Edell

[16] Leakage current test structures and measurement concept developed by David Edell

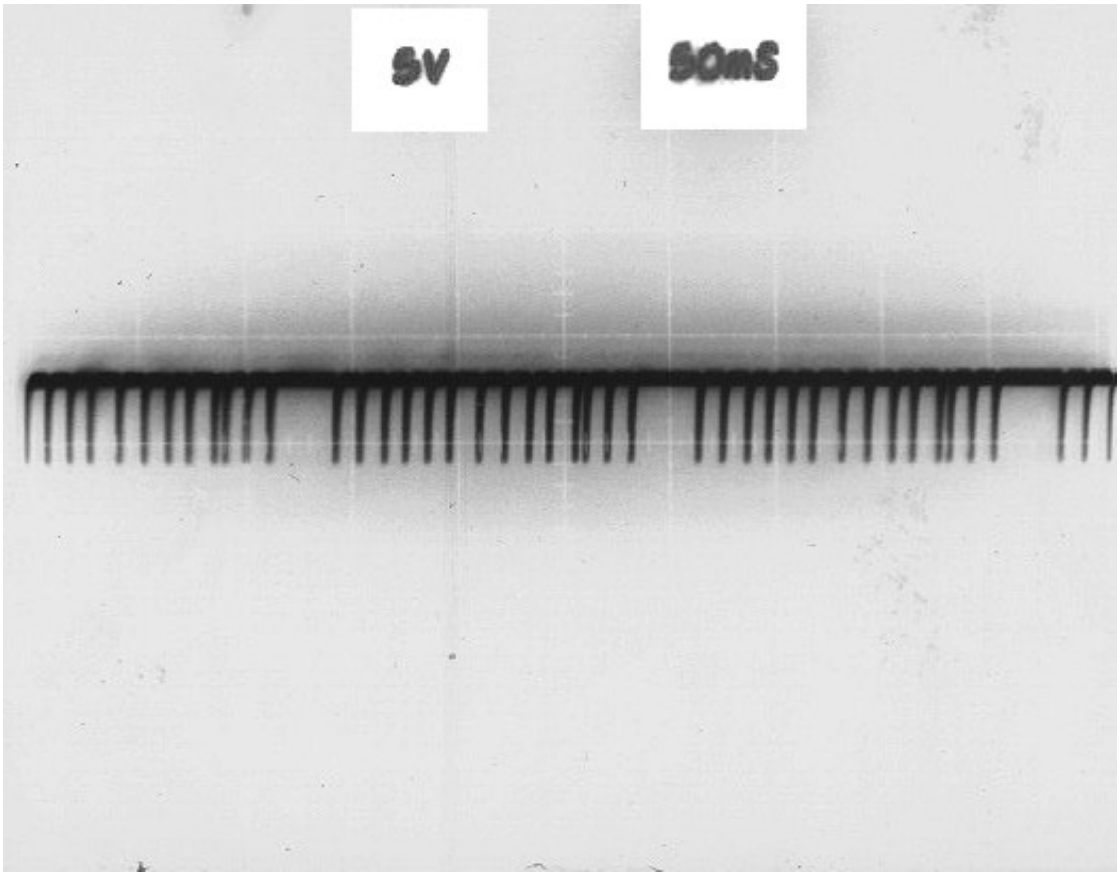

Figure 7.42: Pulse period encoded output from 13 channel insulating biomaterials test chip.

The pulse periods from this circuit are proportional to samples of the outputs of the leakage current integrators. By continuously transmitting the output voltage of each integrator, small changes in the integrator outputs can be detected over many samples to determine the current leaking onto each channel. The reconstructed channel voltages are expected to fall slowly as the integrators collect leakage current. Each integrator on the telemeter has its own reset circuit that draws current off when the integrator output voltage reaches a certain limit. The reset current is disconnected once the integrator output voltage reaches a specified level, so that it may continue to measure leakage current. The decoded output for one channel is shown in Figure 7.43. This channel was measuring a relatively large leakage current of about 300 fA.

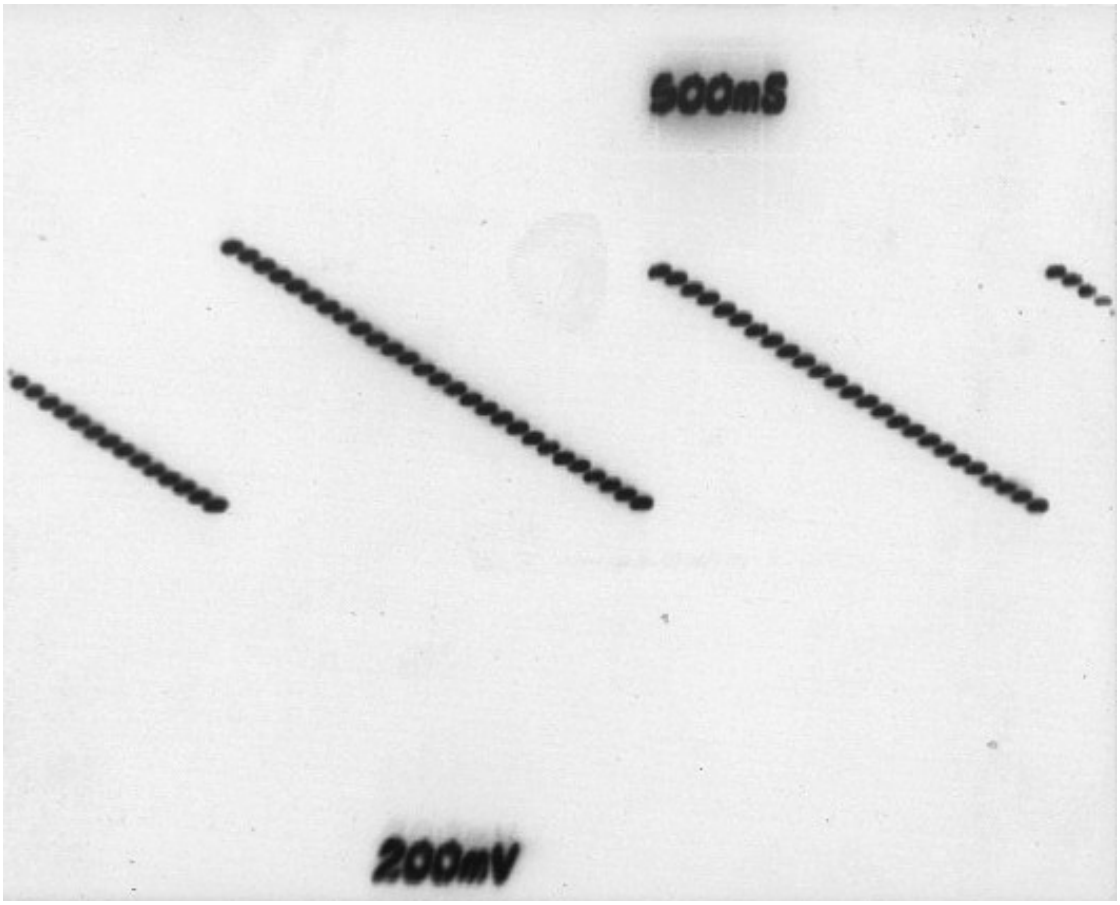

Figure 7.43: Decoded signal for one channel of insulating biomaterials test chip. Signal represents the leakage current integrator output voltage for this channel. It ramps down as it integrates about 300 fA leakage current, and is reset periodically by its circuit to keep it in its proper operating range.

From the success of this telemeter, it was learned that the shift register should operate if the clock pulse can be made wide enough. Also, it was learned that the channel multiplexing and readout technique, using a single capacitor connected sequentially to the voltage follower outputs of the input stages, works quite well. It encodes the channel output voltages fairly linearly, and without noticeable switching noise.

Problems that came to light through improved circuit simulations and laboratory testing were corrected for the designs of test chips three, four, and five. Provisions were also made for more basic testing of these designs, in case unforeseen problems arise. Because of the considerable success of test chip two (the first 8-channel telemeter IC design), the subsequent three designs did not include access to as many circuit nodes as would have been enjoyed in retrospect. Given the limited number of connections (40) in the packaging available with these test chips, the choice had been made to include

more circuit components with fewer external connections. In light of the difficulties encountered with these designs, more test nodes were “pinned out” in the last iterations. Also, given the possibility that the metal2 shield could be responsible for some of the aberrant circuit behavior, it was removed from these submissions. One version was submitted for fabrication both with and without this layer, to determine more conclusively if it is problematic. In light of the successful operation of the insulating biomaterials test chip, it is not likely that the metal2 shield is culpable. However, there is still the possibility that there was a fabrication error in run that produced test chips three, four, and five. Aspects of the integrated circuit that had been shown to work, such as the input amplifier, Schmitt trigger, pulse period encoding technique, switched capacitor feedback, and shift register, were not changed for the final designs.

To correct the problem of the shift register clock pulse being too small, a one-shot circuit was created that mimics the charging of the memory storage capacitors in the shift register. This circuit is shown in Figure 7.44.

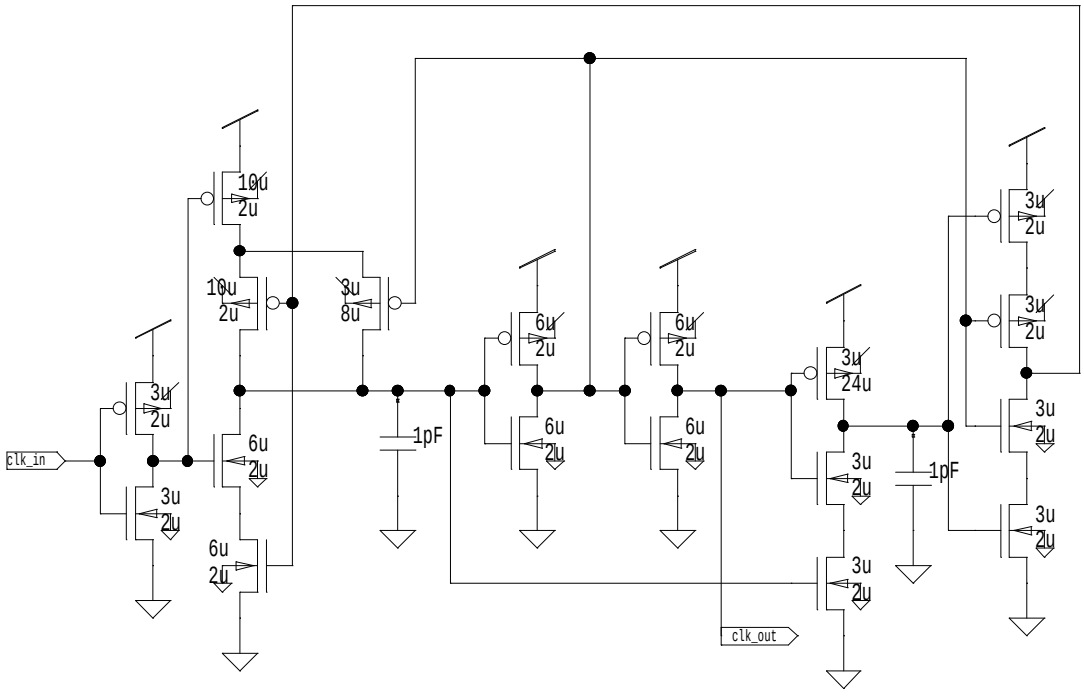

Figure 7.44: One-shot circuit to provide longer clock pulse for shift register.

This one-shot circuit was inserted between the output of the Schmitt trigger and the first inverter in the revised versions of the telemeters (shown in Figure 7.19, Figure 7.24, and

Figure 7.32). It can be triggered by a short “low” pulse on the input labeled “clk_in” in Figure 7.44 when the Schmitt trigger resets the readout integration capacitor, and produces a longer (about 0.5 μs) low logic pulse at the output labeled “clk_out”, which is connected to the first inverter in the switching network of the telemeters. Operation of the one-shot is as follows. The Schmitt trigger output, connected to clk_in, will be at the positive supply voltage during a readout integration period, and the first capacitor in the circuit (on the left in Figure 7.44) will be charged to the positive supply voltage. Accordingly, the inverters that follow the first capacitor keep clk_out in the high state and the second capacitor grounded. Also, the pathways connecting the first capacitor to ground and the positive supply are all open, so the capacitor is storing the high logic state voltage. When the voltage on clk_in falls (as the Schmitt trigger initiates a reset of the readout integration capacitor), the first capacitor in the one-shot is quickly discharged to zero volts. The inverters that follow it drive clk_out to ground, and connect the second capacitor to the positive supply through a high resistance switch. The voltage on the first capacitor, and thus clk_out, remain low until the voltage on the second capacitor rises to the high logic level. When this happens, the first capacitor is charged high again, clk_out rises, and the second capacitor is discharged. During the period when clk_out is low, the shift register is changing state, and one of its memory capacitors is connected to the positive supply through other high resistance switches. But the same capacitors are used in the one-shot as in the shift register, and the resistance of the switch in the one-shot is four times greater than the network that charges the memory capacitor. Thus the shift register memory capacitors will always have ample time to settle to the next state. Switches in the one-shot circuit that at first may appear redundant or unnecessary prevent overlap conditions where excess current could flow between the positive supply and ground.

To help ensure that at least one multiplexed neural waveform telemeter can be assembled for prototype animal testing, the simple telemeter design from test chip three was revised. The p-channel switch networks, intended to unity-feedback connect the input amplifiers to set the bias capacitor potentials, were replaced with minimum-size n-channel switches (3 μm wide by 2 μm long). This should allow the input amplifiers to bias properly at lower input voltages. In addition, the output and inverting input of each amplifier are pinned out in the new design, so that external feedback resistors and capacitors can be connected if necessary. Continuous drift and offset rejection can then be achieved with normal low-pass feedback that cannot be accomplished on-chip. Also,

channel output signals can be directly measured or injected to test the function of the pulse period encoder. This telemeter design was submitted for fabrication both with and without the metal2 shield. If the metal2 shield does not cause problems, then it will provide protection from light and chemical intrusion for implant purposes.

The telemeter designs from test chip four and five were submitted with the addition of the one-shot clock circuit, and without the metal2 shield. It is anticipated that the switched-capacitor feedback design of test chip four will function when the shift register problem is resolved. And since there was no apparent explanation for the failure of the input stages of test chip five, removal of the metal2 shield and simply re-fabrication may allow it to function. Finally, additional test nodes were connected for all three revised telemeter circuits, so that more debugging information may be gathered if they still do not function properly.

The laboratory verification of most subsystems of the improved designs, and the encouraging results of the first 8-channel telemeter circuit and the recent insulating biomaterials test chip, indicate that the complete system for a free floating, multi-channel neural telemeter will likely be functional when the next set of fabricated devices is available.

7.5 Decoder for the 8-channel telemeter

A decoder circuit that could synchronize to the pulse sequence (from the photodetector circuit) and separate and decode the multiplexed signal information was designed and built to complement the 8-channel telemeters. The fundamental design can be expanded to make a decoder for higher channel-count telemetry systems.

7.5.1 Design

The simplified schematic of the 8-channel decoder is presented in Figure 7.45. Details of the functional blocks in Figure 7.45 are provided in the four figures that follow it. To generate a voltage that is proportional to the time between the light pulses from the telemeter, a constant current is integrated for the period between each successive pulse. The integration current is set by the reference voltage V_{ref} and resistor R_i. A 0.5 mA current and 2.2 nF integrating capacitor were used in the test configuration, which yields a 1.14 V integrator output for a 5 μs pulse period. The integrator is quickly reset after each received pulse in preparation for the next integration period, so a peak detector is used to hold the final integrator output voltage that corresponds to the last pulse period.

While the integrator is measuring the next pulse period, the one-shot circuits cause one of the sample-and-hold amplifiers to sample and then reset the peak detector. The sample-and-hold amplifier that captures the voltage is selected by the counter/decoder logic that sequences through the eight sample-and-hold amplifiers to demultiplex the eight signal periods coming from the telemeter. Since the integrator output voltage corresponding to the long marker period will be larger than all the signal periods, a comparator is used to detect this period. When the marker period is received, the integrator voltage will exceed V_{marker}, and the counter is reset to its highest count value (15). When the pulse at the end of the marker period occurs, the counter is held in this state (because the reset/load condition overrides the clock input), and the integrator is reset as usual. But the most significant bit of the counter (which is not needed for the count to 8) is used to disable the decoder so that none of the sample-and-holds will capture this period voltage. The next pulse that arrives corresponds to the end of the first signal channel period, and it advances the counter, causing it to "wrap around" to zero, so that the decoder selects the first sample-and-hold to capture the integrator voltage. The next seven pulses increment the counter and decoder to sample the other channel signal voltages. Each sample-and-hold output is therefore instantaneously proportional to the periods in the sequence that correspond to one of the telemetered signal channels. The sample-and-hold outputs change in a stair-step fashion once every cycle of pulse periods (because each cycle transmits one sample of each channel). Smoothing and equalizing filters can be added at the output of each sample-and-hold to finish the reconstruction of the encoded signals, or these outputs can be sampled by a computer-based data acquisition system for the greater flexibility of digital signal processing.

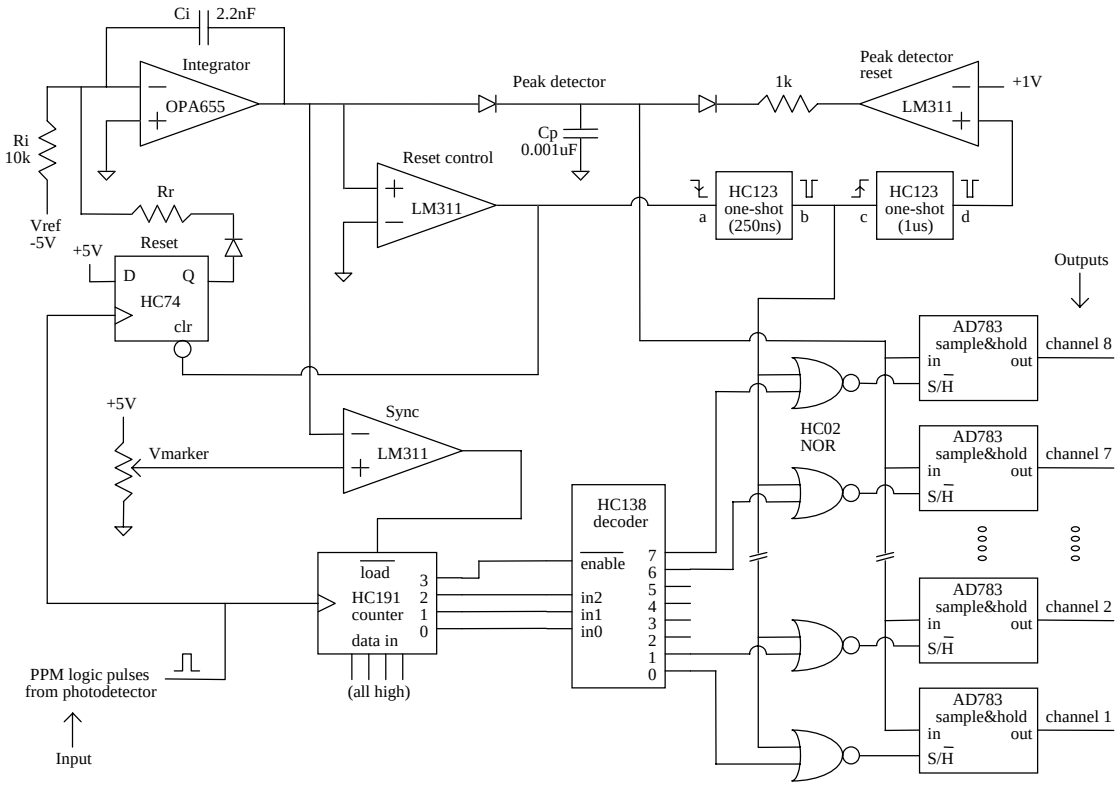

Figure 7.45: Decoder for 8-channel telemeters.

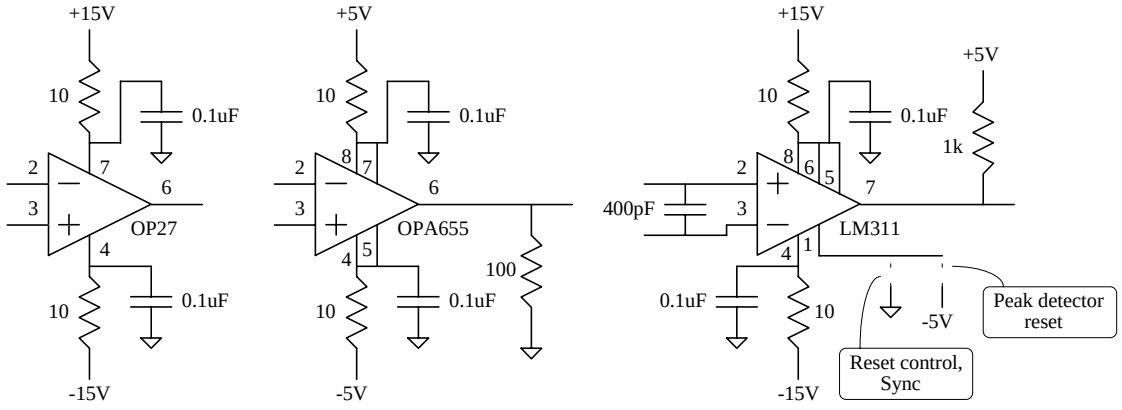

Figure 7.46: Operational amplifier and comparator connections.

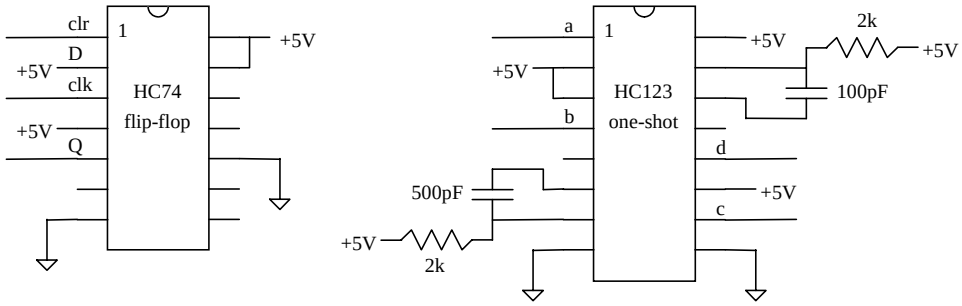

Figure 7.47: Flip-flop and one-shot connections.

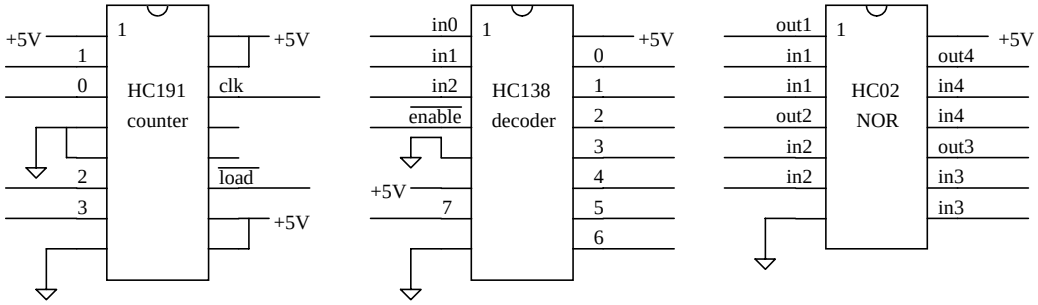

Figure 7.48: Counter, decoder, and NOR gate connections.

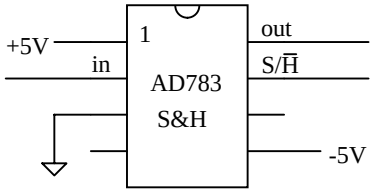

Figure 7.49: Sample-and-hold amplifier connections.

7.5.2 Testing

The original design of the 8-channel decoder relied on the fast sample-and-hold amplifiers to capture the peak integrator voltage just before it was reset, without the aid of the peak detector circuit. With a 6 μs digital clock as the input pulse signal, and a single sample-and-hold amplifier wired to sample the integrator every period (rather than demultiplexing this dummy signal), the output exhibited about 30 $mV_{p\text{-}p}$ noise. This corresponded to 135 ns peak-to-peak "jitter" in the pulse period measurement. After the addition of the peak detector circuit in the final decoder design of Figure 7.45, the sample-and-hold output noise was reduced to approximately 0.8 $mV_{p\text{-}p}$ with the digital clock input, corresponding to only 3.6 ns peak-to-peak measurement jitter!

With the negligible pulse period measurement error introduced by this decoder, it should be possible to reconstruct signals within the noise limits of any of the proposed telemeter

circuits. Because the noise of the decoder is so low, it can be used to characterize the noise of the telemeter circuits directly. For example, decoding signals from the 8-channel telemeter of test chip two with inputs connected to AC ground revealed approximately 7 mV_{p-p} noise over a 7 kHz bandwidth on each decoder output channel, corresponding to about 31.5 ns peak-to-peak jitter in the pulse period encoding by this telemeter.

Chapter 8: Conclusions

The primary objective of this research was the development of a technology base for optically-coupled systems that would permit in-vivo transmission of biomedical signals across the skin. It was also desired that the system be small and lightweight so that it could potentially be implanted on the surface of the brain to allow mechanically stable connections to microelectrode arrays.

The two most important goals for the design of the optical telemetry system were that it operate on the minimum amount of optical power, and that it be capable of transmitting information at the highest possible rate. These factors go together in the sense that decreasing the power needed by the implant electronics would allow more information to be acquired, encoded, and transmitted. The less power required by the implant for a given number of channels and bandwidth, the easier it is to provide the power optically. If a smaller optical power supply can be used, a smaller and lighter implant will result. Thus these two considerations are foremost in the design of maximally useful telemeters.

Careful design of the complete system was necessary to accomplish these goals. The specific tasks involved in the system design were:

- Selection of an encoding scheme for efficient optical transmission of signals.
- Design of ultra low power implant electronics to acquire and encode desired biomedical signals.
- Identification of light wavelengths and sources for efficient transmission of power and signals across the skin.
- Specialized design of a photodetector system to receive the transmitted signals with the highest sensitivity, so that less power is required for signal telemetry by the implant.
- Development of optical power supplies optimized to provide the voltage and current requirements of the implant with as little incident light as possible for a given size.

These tasks were completed successfully. A pulse-period encoding technique was developed for the optical transmission of signals. This technique gave robust signal transmission with minimal power because the signal is encoded entirely in the timing between intense but brief pulses of light. Multiple channels of information were encoded in this technique by multiplexing the pulse periods, and by using a marker period that was different from the others to synchronize the receiver so that the transmitted signals

could be decoded. This encoding was accomplished with less complicated and lower power electronics than necessary for traditional analog-to-digital conversion. Using a low power design methodology developed in prior work [90], integrated circuit input amplifiers were designed to measure biomedical signals with only as much power as necessary to achieve sufficiently low noise. An amplifier suitable for recording small neuroelectric potentials was developed that had less than 10 μV_{RMS} input-referred noise over a 10 kHz bandwidth while consuming only 625 nA.

A literature review and experiments with cadaver skin and in-vivo experiments led to the selection of LEDs with optimal performance for transmitting data and power. Skin was found to transmit light best at longer wavelengths and in the near infrared. An LED suitable for the telemeter output device was found that generates 660 nm red light with high efficiency. A mounting technique was developed for this chip LED that incorporates a reflector to increase light transmission across the skin. It provided up to 104% improvement over flat mounts. Power was transmitted at 880nm because it was less absorbed than 660nm light, thereby minimizing tissue heating effects. The safety of optical power transmission at 880nm was demonstrated in an experiment that measured tissue heating when the power illumination was applied.

A design methodology for optimizing detection of the timing of light pulses from low amplitude sources was developed and applied to the problem of detection of pulses from an implanted multichannel neural signal telemeter. A transimpedance amplifier photodetector circuit was optimized for sensitive detection of pulse period encoded signals. Optical filters were found that reduced most background and powering illumination by a factor of more than 10,000 compared to the signal transmission wavelength. These improved photodetector performance by minimizing the interference and noise associated with the unwanted light.

Maximally efficient optical power supplies were designed similar to solar panels. The optimal number of photodiodes to connect in series was determined, and panels smaller than 2.5 mm x 2.5 mm were fabricated. A six-diode silicon panel provided 2.5 V and 75 μA when illuminated by 880 nm infrared light at 50 mW/cm^2 (half of overhead sunlight intensity). Its power conversion efficiency was up to 13.6%. GaAlAs panels were up to 41.3% efficient. A four-diode GaAlAs panel fitting in the same area would produce 3 V and 280 μA under the same illumination. Panel layouts that reduce the effects of non-uniform illumination were developed along with fabrication techniques.

The accomplishment of these individual, but interrelated, goals enabled the primary research objectives to be achieved. A technology base was developed enabling optical transmission of data from, and power to, implanted electronics for readout of biological information. As a demonstration, a prototype telemeter that recorded one channel of high-frequency extracellular neuroelectric signals was constructed and implanted in a rabbit. It was still functional at the time of this writing, more than 28 months after implantation. This telemeter was bulky and thus was subcutaneously placed because the integrated circuits developed in this research were not available when it was built. However, it incorporated many of the same low power signal detection, signal encoding, data transmission, and power transmission concepts.

Integrated circuits were fabricated using the developed technology concepts that can encode eight channels of biomedical information. These designs are expandable to an arbitrary number of channels, limited only by available power and signal bandwidth. The initial 8-channel design had approximately 10 mV_{p-p} input-referred noise when operated at 15 kHz/channel sample rate. It consumed only 12.5 μA current from a 2.5 V supply for signal amplification, encoding, and multiplexing, and used another 7 μA for the optical output. Improved circuit designs were then developed and are now being fabricated which should permit much smaller signals to be encoded (limited by the noise level specified in the input amplifier design) with less power. Most subsystems of the improved designs were fabricated and verified in the laboratory indicating that the complete system for a free floating, multi-channel neural telemeter will likely be functional when the next set of fabricated devices is available. The technology base developed in this thesis work can now be exploited for many challenging applications. This optical telemetry technology will be especially useful whenever biological data must be acquired from small implanted sensors for long periods of time.

References

[1] R. Kadefors and J. Reswick, “A percutaneous electrode for long-term monitoring of bio-electric signals in humans,” *Med & biol Engng*, vol. 8, pp. 129-135, 1970.

[2] G. D. Winter, “Transcutaneous implants: Reactions of the skin implant interface.,” *J. Biomed. Mater. Res. Symp.*, vol. 5, pp. 99-113, 1974.

[3] J. Miller and C. E. Brooks, “Problems related to the maintenance of chronic percutaneous electronic leads,” *J. Biomed. Mater. Res. Symposium*, vol. 2, pp. 251-67, 1971.

[4] A. F. v. Recum and J. B. Park, “Permanent percutaneous devices,” *CRC Crit. Rev. Bioengineering*, vol. 5, pp. 37-77, 1981.

[5] S. Al-Nakeeb, P. T. Pearson, and N. R. Cholvin, “A thoracic percutaneous lead system: development and evaluation,” *J. Biomed. Mater. Res.*, vol. 6, pp. 245-65, 1972.

[6] H. Aoki, M. Akao, Y. Shin, T. Tsuzi, and T. Togawa, “Sintered hydroxyapatite for a percutaneous device and its clinical application,” *Medical Progress through Technology*, vol. 12, pp. 213-20, 1987.

[7] K. Akazawa, M. Makikawa, J. Kawamura, and H. Aoki, “Functional neuromuscular stimulation system using an implantable hydroxyapatite connector and a microprocessor-based portable stimulator,” *IEEE Transactions on Biomedical Engineering*, vol. 36, pp. 746-52, 1989.

[8] V. Mooney, D. B. Hartmann, D. McNeal, and J. Benson, “The use of pure carbon for permanent percutaneous electrical connector systems,” *Arch. Surg.*, vol. 108, pp. 148-53, 1974.

[9] T. Akin, K. Najafi, and R. M. Bradley, “An implantable multichannel digital neural recording system for a micromachined sieve electrode,” , 1995.

[10] D. C. Jeutter, “Biomedical telemetry techniques,” *CRC Critical Reviews in Bioengineering*, 1982.

[11] I. C. Forster, “Preliminary development of a radiotelemetry system for biological applications,” *Medical & Biological Engineering & Computing*, 1986.

[12] Z. Hamici, R. Itti, and J. Champier, “A high-efficiency power and data transmission system for biomedical implanted electronic devices,” *Measurement Science & Technology*, 1996.

[13] R. S. MacKay, “Biomedical telemetry: the formative years,” *IEEE Engineering in Medicine and Biology Magazine*, 1983.

[14] J. D. Meindl and A. J. Ford, “Implantable telemetry in biomedical research,” *IEEE Transactions on Biomedical Engineering*, 1984.

[15] Y. Taenaka, T. Masuzawa, F. Tatsumi, H. Anai, K. Toda, H. Akagi, T. Nakatani, Y. Baba, K. Fya, Y. Wakisaka, and et al., “Development and evaluation of components for a totally implantable artificial heart system,” *Asaio J*, vol. 40, pp. M314-8, 1994.

[16] S. J. Gshwend, J. W. Knutti, H. V. Allen, and J. D. Meindl, “A general-purpose implantable multichannel telemetry system for physiological research,” *Biotelemetry Patient Monitoring*, vol. 6, pp. 107-17, 1979.

[17] J. S. Brugler, D. H. LaForge, J. Lee, F. K. Beering, J. S. Jassawalla, and P. M. Portner, “Transcutaneous power transmission and electronic control of a ventricular assist system,” presented at IEEE/Eighth Annual Conference of the Engineering in Medicine and Biology Society, 1986.

[18] M. Nardin and K. Najafi, “A multichannel neuromuscular microstimulator with bi-directional telemetry,” , 1995.

[19] Z. Tang and P. H. Peckham, “Multichannel implantable stimulation and telemetry system for neuromuscular control,” presented at Proceedings of 16th Annual International Conference of the IEEE Engineering in Medicine and Biology Society, Baltimore, MD, USA, 1994.

[20] D. B. McCreery, “Studies of the feasibility of a central nervous system auditory prosthesis,” Huntington Medical Research Institute, Pasadena, NIH NINDS Contract Quarterly Report NO1-DC-2400, 1995.

[21] G. E. Loeb, C. J. Zamin, and J. H. Schulman, “Injectable microstimulator for functional electrical stimulation,” *Med. & Biol. Eng. & Comput.*, vol. 29, pp. NS13-NS19, 1991.
[22] D. J. Edell, “Development of a Chronic Neuroelectric Interface,” in *Biomedical Engineering*. Davis: University of California, 1980.
[23] D. J. Edell, J. N. Churchill, and I. M. Gourley, “Biocompatibility of a silicon based peripheral nerve electrode,” *Biomat Med Dev Art Org*, vol. 10, pp. 103-122, 1982.
[24] D. J. Edell, “A peripheral nerve information transducer for amputees: long-term multichannel recordings from rabbit peripheral nerves,” *IEEE Trans. Biom. Eng.*, vol. 33, pp. 203-213, 1986.
[25] D. J. Edell, L. D. Clark, and V. M. McNeil, “Optimization of electrode structure for chronic transduction of electical neural signals,” presented at IEEE-EMBS 8th Annual Conference, 1986.
[26] D. Edell, “Design of Chronically Implantable Microelectronic Devices for Rehabilitation,” presented at Southern Biomedical Engineering Society Meeting, Philadelphia, 1993.
[27] D. Edell, “Minisymposium: Chronically Implantable Neural Information Transducers,” presented at IEEE EMBS Meeting, Amsterdam, 1996.
[28] D. Edell, “Minisymposium: Tomorrow's Implantable Electronic Systems,” *EMBS 1996: "Bridging disciplines for biomedicine"*, pp. 497-498, 1996.
[29] L. D. Clark, “A system for chronic neural signal transduction, processing, and control.,” in *Electrical Engineering*. Cambridge: MIT, 1990, pp. 195.
[30] G. T. A. Kovacs, C. W. Storment, and J. M. Rosen, “Regeneration microelectrode array for peripheral nerve recording and stimulation,” *IEEE Transactions on Biomed. Eng.*, vol. 39, pp. 893-902, 1992.
[31] G. T. A. Kovacs, C. W. Storment, M. Halks-Miller, J. C.R. Belcynski, C. C. D. Santina, E. R. Lewis, and N. I. Maluf, “Silicon-Substrate microelectrode arrays for parallel recording of neural activity in peripheral and cranial nerves,” *IEEE Transactions on Biomed. Eng.*, vol. 41, pp. 567-577, 1994.
[32] C. W. Selvidge, A. C. Malamy, and L. A. Glasser, “Power and Communication Techniques for Physically Isolated Integrated Circuits,” in *Advanced Research in VLSI*, P. Losleben, Ed. Cambridge: MIT Press, 1987, pp. 231-248.
[33] J. C. Jarvis and S. Salmons, “A family of neuromuscular stimulators with optical transcutaneous control,” *Journal of Medical Engineering & Technology*, vol. 15, pp. 53-7, 1991.
[34] G. D. Summers, “Implant monitoring by optical telemetry,” , 1968.
[35] K. Hagi, M. Makikawa, and H. Iizumi, “Transcutaneous digital communication by pulse-code-modulated infrared rays,” *Japanese Journal of Medical Electronics and Biological Engineering*, 1995.
[36] H. P. Kimmich, “Biotelemetry, based on optical transmission,” *Biotelem Patient Monit*, vol. 9, pp. 129-43, 1982.
[37] F. F. Klein, W. E. Thornton, D. A. Davis, L. A. Dowell, and L. W. Burton, “An eight channel surgical patient monitoring telemetry system utilizing infrared light as the transmitting medium,” , 1979.
[38] V. I. Lebedev and V. G. Munyakin, “8-channel telemetry system of IR band,” , 1987.
[39] A. Santic, “Theory and application of diffuse infrared biotelemetry,” *CRC Critical Reviews in Biomedical Engineering*, 1991.
[40] A. Santic, “Application of infrared radiation in medicine,” *Automatika*, 1985.
[41] B. Hok, V. Bythell, and M. Bengtsson, “Development of a wireless stethoscope for auscultatory monitoring during anaesthesia,” *Medical & Biological Engineering & Computing*, 1988.
[42] M. Takahashi and V. Pollak, “Near infra-red telemetry system (for biomedical research),” *Medical & Biological Engineering & Computing*, 1985.
[43] M. Yamashita, K. Shimizu, and G. Matsumoto, “Threshold evaluation of electric field perception using optical telemetry technique,” , 1994.
[44] J. Black, M. Wilkins, P. Atanasov, and E. Wilkins, “Integrated sensor-telemetry system for in vivo glucose monitoring,” *Sensors and Actuators B*, 1996.

[45] T. Kobayashi, T. Sugita, T. Sasaki, T. Iwase, R. Sassa, and M. Iio, “A windowless Si radiation detector and biomedical telemetry system for studying the function of organs of free-ranging animals,” *IEEE Transactions on Nuclear Science*, 1974.
[46] R. Maestri, M. Marzegalli, M. Bernasconi, A. Di Cesare, and G. D. Pinna, “Assessment of the fidelity of pacemaker telemetric signals,” , 1995.
[47] R. S. Mackay, “Recent advances in biotelemetry and their applications to measurements of pressure and electrical changes in the oviduct in vivo,” *Biotelemetry*, 1974.
[48] Z. McCreesh, N. E. Evans, and W. G. Scanlon, “Vaginal temperature sensing using UHF radio telemetry,” *Medical Engineering & Physics*, 1996.
[49] D. E. Olsen, A. Firstenberg, S. W. Huston, L. R. Dutcher, and W. R. Adey, “An eight channel micropowered PAM/FM biomedical telemetry system,” , 1971.
[50] Z. K. Salman, S. H. Jones, R. M. Weikle, J. H. Aylor, J. D. Meindl, P. R. Mukund, T. Gabara, and R. Sridhar, “An integrated, wireless microinstrument for monitoring skin temperature,” , 1996.
[51] K. Van Schuylenbergh and R. Puers, “Self-tuning inductive powering for implantable telemetric monitoring systems,” *Sensors and Actuators A*, 1996.
[52] Z. Tang, B. Smith, J. H. Schild, and P. H. Peckham, “Data transmission from an implantable biotelemeter by load-shift keying using circuit configuration modulator,” *IEEE Transactions on Biomedical Engineering*, 1995.
[53] A. Boos, M. H. Jagger, G. W. Paret, and J. W. Hausmann, “A new, lightweight fetal telemetry system,” *Hewlett Packard Journal*, 1995.
[54] E. S. Hochmair, “System optimization for improved accuracy in transcutaneous signal and power transmission,” *IEEE Transactions on Biomedical Engineering*, vol. BME-31, pp. 177-86, 1984.
[55] R. R. Anderson and J. A. Parrish, “The optics of human skin,” *J Invest Dermatol*, vol. 77, pp. 13-9, 1981.
[56] W. Cheong, S. A. Prahl, and A. J. Welch, “A review of the optical properties of biological tissues,” *IEEE Journal of Quantum Electronics*, vol. 26, pp. 2166-85, 1990.
[57] J. B. Dawson, D. J. Barker, D. J. Ellis, E. Grassam, J. A. Cotterill, G. W. Fisher, and J. W. Feather, “A theoretical and experimental study of light absorption and scattering by in vivo skin,” *Phys Med Biol*, vol. 25, pp. 695-709, 1980.
[58] H. R. Eggert and V. Blazek, “Optical properties of normal human intracranial tissues in the spectral range of 400 to 2500 nm,” in *Optical Imaging of Brain Function and Metabolism*, U. Dimagl, et al., Ed. New York, NY: Plenum Press, 1993, pp. 47-55.
[59] H. R. Eggert and V. Blazek, “Optical properties of human brain tissue, meninges, and brain tumors in the spectral range of 200 to 900 nm,” *Neurosurgery*, vol. 21, pp. 459-64, 1987.
[60] S. T. Flock, B. C. Wilson, and M. S. Patterson, “Monte Carlo modeling of light propagation in highly scattering tissues -- II: Comparison with measurements in phantoms,” *IEEE Transactions on Biomedical Engineering*, vol. 36, pp. 1169-73, 1989.
[61] M. J. C. Van Gemert, S. L. Jacques, J. C. M. Sterenborg, and W. M. Star, “Skin optics,” *IEEE Transactions on Biomedical Engineering*, vol. 36, pp. 1146-54, 1989.
[62] Z. F. Gourgouliatos, A. J. Welch, and K. R. Diller, “Microscopic instrumentation and analysis of laser-tissue interaction in a skin flap model,” *Journal of Biomechanical Engineering*, vol. 113, pp. 301-7, 1991.
[63] H. Kolarova and D. Ditrichova, “Contribution to the measurement of optical characteristics of the skin,” *Acta Univ Palacki Olomuc Fac Med*, vol. 125, pp. 215-24, 1990.
[64] J. L. Leveque, P. Corcuff, J. de Rigal, and P. Agache, “In vivo studies of the evolution of physical properties of the human skin with age,” *Int J Dermatol*, vol. 23, pp. 322-9, 1984.
[65] R. Marchesini, C. Clemente, E. Pignoli, and M. Brambilla, “Optical properties of in vitro epidermis and their possible relationship with optical properties of in vivo skin,” *J Photochem Photobiol B*, vol. 16, pp. 127-40, 1992.
[66] J. M. Schmitt, G. X. Zhou, E. C. Walker, and R. T. Wall, “Multilayer model of photon diffusion in skin,” *J Opt Soc Am [A]*, vol. 7, pp. 2141-53, 1990.

[67] R. Splinter, W. Cheong, M. v. Gemert, and A. Welch, “In vitro optical properties of human and canine brain and urinary bladder tissues at 663 nm,” *Lasers in Surgery and Medicine*, vol. 9, pp. 37-41, 1989.
[68] J. Torres, A. Welch, and M. Motamedi, “Tissue optical property measurements: Overestimation of absorption coefficient with spectrophotometric techniques.,” *Lasers in surgery adn medicine*, vol. 14, pp. 249-257, 1994.
[69] A. Vogel, C. Dlugos, R. Nuffer, and R. Birngruber, “Optical properties of human sclera , and their consequences for transscleral laser applications,” *Lasers in Surgery and Medicine*, vol. 11, pp. 331-340, 1991.
[70] J. Whitton and J. Everall, “The thickness of the epidermis,” *British Journal of Dermatology*, vol. 89, pp. 467-476, 1973.
[71] B. Wilson, M. Patterson, and S. Flock, “Indirect versus direct techniques for the measurement of the optical properties of tissues,” *Photochemistry and photobiology*, vol. 46, pp. 601-608, 1987.
[72] S. Igarashi, R. L. Trelstad, and A. H. Kang, “Physical chemical properties of chick cartilage collagen,” *Biochim Biophys Acta*, vol. 295, pp. 514-9, 1973.
[73] T. S. Melo, L. Dubertret, P. Prognon, A. Gond, G. Mahuzier, and R. Santus, “Physicochemical properties and stability of anthralin in model systems and human skin,” *J Invest Dermatol*, vol. 80, pp. 1-6, 1983.
[74] R. M. Sayre and H. S. Black, “Beta-carotene does not act as an optical filter in skin,” *J Photochem Photobiol B*, vol. 12, pp. 83-90, 1992.
[75] J. M. Schmitt, A. Knuttel, and J. R. Knutson, “Interference of diffusive light waves,” *J Opt Soc Am [A]*, vol. 9, pp. 1832-43, 1992.
[76] S. Wan, R. R. Anderson, and J. A. Parrish, “Analytical modeling for the optical properties of the skin with in vitro and in vivo applications,” *Photochem Photobiol*, vol. 34, pp. 493-9, 1981.
[77] D. J. Edell, “Insulating Biomaterials,” MIT, Cambridge, Quarterly Report NO1-NS-3-2301, 1996.
[78] R. C. Neville, *Solar Energy Conversion: The Solar Cell*. Amsterdam: Elsevier Scientific, 1978.
[79] L. Cromwell, F. Weibell, and E. Pfeiffer, *Biomedical instrumentation and measurements*, 2nd ed. Englewood Cliffs, N.J.: Prentice-Hall, Inc., 1980.
[80] J. Roberge, “Technique for capacitive feedback compensation of photodetector circuit,” Personal communication, Oct. 26, 1998.
[81] E. Kandel, J. Schwartz, and T. Jessell, *Principles of neural science*, 3rd ed. Norwalk, CT: Appleton & Lange, 1991.
[82] L. Geddes and L. Baker, *Principles of applied biomedical instrumentation*, 2nd ed. New York: John Wiley & Sons, 1975.
[83] R. Doty, “Potentials evoked in cat cerebral cortex by diffuse and by punctiform photic stimuli,” *J. Neurophysiol.*, vol. 21, pp. 437-464, 1958.
[84] B. P. Choudhury, “Visual cortex in the albino rabbit,” *Exp Brain Res*, vol. 66, pp. 565-71, 1987.
[85] K. L. Chow, R. H. Masland, and D. L. Stewart, “Receptive field characteristics of striate cortical neurons in the rabbit,” *Brain Res*, vol. 33, pp. 337-52, 1971.
[86] N. Lesevre and J. P. Joseph, “Modifications of the pattern-evoked potential (PEP) in relation to the stimulated part of the visual field (clues for the most probable origin of each component),” *Electroencephalogr Clin Neurophysiol*, vol. 47, pp. 183-203, 1979.
[87] T. Uchida and N. Suzuki, “Origin of the secondary response induced by flash stimulation under barbiturate anesthesia in the rabbit,” *Jpn J Physiol*, vol. 27, pp. 399-411, 1977.
[88] M. Steriade and D. Ionescu, “Specific potentiation of photically evoked activity in the visual cortex,” *Exp Brain Res*, vol. 4, pp. 256-74, 1967.
[89] K. E. Bignall and L. T. Rutledge, “Origin of a Photically Evoked Afterdischarge in Cat Visual Cortex,” *J Neurophysiol*, vol. 27, pp. 1048-62, 1964.
[90] B. C. Larson, “Design considerations for minimizing noise in micropower CMOS integrated circuits,” in *Electrical Engineering and Computer Science*. Cambridge: Massachusetts Institute of Technology, 1996.

About the Author

Bruce Larson grew up in Omaha, Nebraska. After graduating from Creighton Preparatory School in 1987, he entered the University of Houston as a National Merit Scholar. There he was named the Outstanding Senior Engineering Student in the both the Department of Electrical Engineering and the Cullen College of Engineering in 1992. He graduated Summa Cum Laude with a Bachelor of Science degree in Electrical Engineering in May of 1992, and began attendance at the Massachusetts Institute of Technology in September of that year. He received his Master of Science degree in the Department of Electrical Engineering and Computer Science in May of 1996. His research interests include low noise, low power analog circuit and system design, optical power and communication techniques, and chronic neural interface technology.

Acknowledgments

I wish to thank David Edell for guiding the research that went into this thesis, and for providing a stimulating and enjoyable work environment. I also appreciated his friendship, which made long days spent in the lab or writing at the computer bearable.

Special thanks to my thesis readers, Professor Jim Roberge and Professor George Pratt for all their time, thoroughness, and highly constructive criticism.

I thank the Department of Veteran's Affairs and the National Institutes of Health for the funding which made this research possible. More importantly, I thank the taxpayers and private contributors who fund these organizations.

I would like to thank Sean Sexton for fun lunchtime companionship and cheerful help with myriad instrumentation issues.

I thank all the people of the EECS Graduate Office for their "encouragement" to get things done on time, and for their understanding when they weren't.

I thank Don, Lisa, and Niall Devaney for their encouragement and for providing much-needed recreation that helped me get through my final years of graduate school.

Finally, I wish to thank my wife, Lisa, for her encouragement and patience, and my parents for 29 years of complete and unwavering support.